JSST2023

The 42nd JSST Annual International Conference on Simulation Technology

Conference Proceedings

Niigata University, Niigata, Japan
August 29 — 31, 2023

Supporting Companies

CYBERNET

HOLDINGS
SOFT CREATE

Session Schedule

Day 1: Tuesday, 29th August, 2023				
Time	Room A	Room B	Room C	Room D
10:00 – 10:15	Opening Ceremony			
10:15 – 11:15	Plenary Talk 1 (Symposium 3)			
11:15 – 11:30	Group Photo			
11:30 – 12:30	Symposium 3: Invited Talks Session 1 (2)	OS6 ① Session 5 (3)	OS1 ① Session 9 (3)	
12:30 – 14:00	Lunch Time			
14:00 – 15:00	Symposium 3 ① Session 2 (3)	OS6 ② Session 6 (3)	OS1 ② Session 10 (3)	OS7 ① Session 13 (3)
15:00 – 15:15				
15:15 – 16:15	Symposium 3 ② Session 3 (3)	OS5 ① Session 7 (3)	Symposium 2 ① Session 11 (3)	OS7 ② Session 14 (3)
16:15 – 16:30				
16:30 – 17:10	Symposium 1 ① Session 4 (3)	OS5 ② Session 8 (2)	Symposium 2 ② Session 12 (3)	OS7 ③ Session 15 (2)
17:10 – 17:30				

Day 2: Wednesday, 30th August, 2023

Time	Room A	Room B	Room C	Room D
9:00 – 10:00	Plenary Talk 2 (Symposium 2)			
10:00 – 10:15				
10:15 – 10:55	Symposium 2: Invited Talks Session 16 (2)	OS4 ① Session 19 (3)	OS1 ③ Session 22 (2)	RS ① Session 25 (3)
10:55 – 11:15				
11:15 – 11:30				
11:30 – 12:30	Symposium 2 ③ Session 17 (3)	OS4 ② Session 20 (3)	OS1 ④ Session 23 (3)	RS ② Session 26 (3)
12:30 – 14:00	Lunch Time			
14:00 – 14:40	Symposium 2 ④ Session 18 (3)	OS4 ③ Session 21 (2)	OS1 ⑤ Session 24 (2)	RS ③ Session 27 (2)
14:40 – 15:00				
15:00 – 15:15				
15:15 – 16:00	Shotgun Presentation			
16:00 – 16:15				
16:15 – 18:00		Poster Session		

Day 3: Thursday, 31st August, 2023

Time	Room A	Room B	Room C	Room D
9:00 – 10:00	Plenary Talk 3 (Symposium 1)			
10:00 – 10:15				
10:15 – 11:15	Symposium 1: Invited Talks Session 28 (2)	OS2 ① Session 31 (3)	OS3 ① Session 33 (3)	Symposium 2 ⑤ Session 36 (3)
11:15 – 11:30				
11:30 – 12:10	Symposium 1 ② Session 29 (3)	OS2 ② Session 32 (3)	OS3 ② Session 34 (2)	Symposium 2 ⑥ Session 37 (3)
12:10 – 12:30				
12:30 – 14:00	Lunch Time			
14:00 – 14:40	Symposium 1 ③ Session 30 (3)		OS3 ③ Session 35 (2)	Symposium 2 ⑦ Session 38 (3)
14:40 – 15:00				
15:00 – 15:15				
15:15 – 15:45	Closing Ceremony			

Symposium1

Plenary Talk

Presenter:

Prof. Ryusuke Ae

Division of Public Health, Center for Community
Medicine, Jichi Medical University

Title:

Data analysis project in medical and engineering collaboration by big data in Kawasaki Disease

Abstract:

Half a century has passed since Dr. Tomisaku Kawasaki first reported patients with Kawasaki disease (KD) from Japan. Recently, KD has been reported worldwide and in children of all races and ethnicities. Some patients with KD develop coronary artery abnormalities, which is a global issue as it is the current leading cause of acquired heart disease in children. Nevertheless, the cause of KD remains unidentified.

In Japan, a nationwide KD survey has been conducted since 1970, aiming to provide evidence that may suggest clues that could help identify KD pathogenesis. To date, the database contains approximately 420 thousand patients with KD; this is one of the largest patient registration databases worldwide. We have established an interdisciplinary research team to analyze KD database as an example of medical-engineering collaboration with effective programming techniques for big data analysis. In this lecture, we talk about the collaboration work with some informative results from big data analysis.

Biography:

Dr. Ryusuke Ae is currently a professor at Jichi Medical University. After graduating from Jichi Medical University in 2003, he was engaged in primary healthcare in rural communities in Hyogo prefecture as a physician for ten years. His medical specialty is general internal medicine (Fellow of the

Japanese Society of Internal Medicine) and geriatrics (Board certified Geriatrician: the Japan Geriatric Society). After his clinical experience, he has been an epidemiologist at Jichi Medical University since 2013. While a Regular Research Fellow at the Centers for Disease Control and Prevention (CDC) during 2018–2019, he received several awards for skilled analysis of complex Kawasaki disease data and a relevant publication. He is interested in practical medical-engineering collaboration to find epidemiological evidence that may result in identifying the etiology of Kawasaki disease.

Invited Talk

Presenter:

Prof. Satoshi Yokojima

School of Pharmacy, Tokyo University of Pharmacy
and Life Sciences

Title:

Theoretical investigation of reversible fluorescent photoswitching molecules upon irradiation with visible light

Abstract:

One of the problems of conventional photoswitches is in the use of UV light as the trigger of the switch in at least one direction. Since UV light induces harmful reactions and since UV light is absorbed at the surface in most materials, it is preferable to use visible or IR light for controlling a photoswitch. Thus, the development of photoswitches controlled by visible or IR light is recently quite active. We theoretically investigated the mechanism of a switch of one of such photoswitching organic molecules, a fluorescent dye attached diarylethene. We show the photoswitching reaction upon irradiation with green light occur due to multiplicity conversion based on intramolecular energy transfer from the excited singlet state of the fluorescent dye to the triplet state of diarylethene.

Biography:

Satoshi Yokojima studied field theory in physics at Keio Univ.. He received PhD in 1995 supervised by Prof. R. Fukuda. He then worked on optical response with Prof. S. Mukamel at Univ. of Rochester. He moved to Univ. of Hong Kong and developed a linear scaling method with Prof. G.H. Chen. After working with Prof. Y.J. Yan on dissipative systems, he studied a charge transfer in DNA with Dr. A. Okada at Univ. of Tsukuba. He joined Dr. S. Nakamura’s group at Mitsubishi Chemical and worked on photochromic systems. He moved to Tokyo Univ. of Pharm. and Life Sci. in 2011 and promoted to Professor in 2016.

Invited Talk

Presenter:

Dr. Hiroshi Yokota

Graduate School of Human and Environmental
Studies, Kyoto University

Title:

Simulation study on “torsion” and local structure of chromosome: Loop structure via one side loop extrusion with twist deformation

Abstract:

In eucaryotic cell, during cell division, genome DNA condenses into the rod-like shape so called chromosome. The rod-like shape comes from consecutive loop structures constructed by condensin (protein complex).

Experiments show that condensin binds with DNA through the two binding sites, and then, pushes (extrudes) either of the binding sites. Such a one side loop extrusion creates DNA loops. Molecular dynamics simulations, however, show the fails of the chromosome condensation by only a one side loop extrusion.

In this talk, we would like to talk about loop structures by one side loop extrusion with twist deformation (a kind of “torsion” deformation) based on coarse-grained molecular dynamics simulation. Moreover, each structure is compared with some experiments in vivo and in vitro.

Biography:

Hiroshi Yokota is currently a postdoctoral researcher in Graduate School of Human and Environmental Studies, Kyoto University. He received his Dr. in Department of physics, Tohoku University in 2019. After he received his Dr., he had been working as a postdoctoral researcher at RIKEN 2019-2023. He has theoretically studied chromosome condensation and polymer crystallization based on soft matter physics.

Note:

The full paper of this presentation has been published in Journal of Advanced Simulation in Science and Engineering (JASSE).

`https://doi.org/10.15748/jasse.11.54`

Symposium2

Plenary Talk

Presenter:

Prof. Masayuki Yokoyama

Sensing and Intellectualization unit / Rokkasho Research Center,
National Institute for Fusion Science / National Institutes of Natural Sciences

Title:

Statistical-mathematical thinking in fusion research

Abstract:

“Statistical-mathematical thinking in fusion research” has been proposed, which complements conventional thinking based on plasma-physics. Its main concept is to acquire a model that “fits to the data”, rather than trying to explain the data. It does not necessarily have to be a “big data” but has a strong implication of maximizing data utilization. It can be said that this viewpoint is different from AI, which assumes the existence of big data. A few examples of such thinking will be described in the talk. It will be possible to share issues in fusion research with the statistical mathematics community and challenge them by widening the viewpoints such as plasma physics and statistical mathematics. It is also timely to consider this approach since the measurement becomes limited towards the fusion reactor and the need for estimation of necessary parameters will be increasing.

Biography:

I was born in Niigata in 1969. I completed the doctoral program at Kyoto University (Graduate School of Nuclear Engineering) and became an assistant professor of National Institute for Fusion Science (NIFS) in Jul. 1996. I conducted research mostly related to thermal transport issues of helical plasma (Large Helical Device) and then promoted the initiative to formulate the integrated transport analysis suite, so called TASK3D-a. Based on the accumulated results by TASK3D-a, I have got the interest to implement a data-science approach and then have proceeded to propose “Statistical-mathematical thinking in fusion research” (this talk). I am currently the director of Rokkasho Research Center of NIFS.

Invited Talk

Presenter:

Prof. Kazuo Kashiyama

Civil and Environmental Engineering, Chuo University

Title:

Simulation and Visulaization Using XR technology
～Application to Safety and Environmental Problems～

Abstract:

In recent years, the development of XR (VR/AR/MR) has been remarkable, and it is effectively used not only in the field of science and engineering but also in various fields. In this presentation, the simulation and visualization using XR technique for safety and environmental problems are presented.

For the application to safety problem, Tsunami disaster problem is investigated. Tsunamis kill many human beings and damages economic activities seriously, such as the tsunami caused by the Great East Japan Earthquake in 2011. It is very important to develop useful modelling, simulation and visualization methods for tsunami waves in order to perform the planning and design for the community development and the mitigation of disaster. Especially, the visualization is important to understand the power of tsunami and to improve the consciousness of disaster mitigation. In this presentation, the modelling, simulation and visualization methods for tsunami waves are presented. For the modelling method, several GIS, CAD and AUV data are employed. The stabilized finite element method is employed for tsunami based on the shallow water equation. We also propose a visualization system linked to the evacuation simulation to understand the power of tsunami and the importance of the evacuation. The present modelling, simulation and visualization methods are shown to be useful tools for disaster mitigation education.

On the other hand, for the application to environmental problem, noise problem in urban area is investigated. Since noise may affect the human body such as psychological discomfort and sleep disturbance, it is necessary to quantitatively evaluate the noise level when planning and designing soundproofing measures in urban area. In the conventional studies, the

computed noise level is described by the visualization using computer graphic such as iso-surface. Although the visualization is a powerful tool to understand the distribution of noise, it is difficult to recognize the noise level intuitively. In this presentation, noise evaluation systems based on both acoustic wave theory and geometrical acoustic theory are developed. The system exposes to the users the computed noise level with both the auditory information using sound source signal and the visual information using CG image. In order to investigate the validity and efficiency of the method, the present method is applied to several noise problems. The present system is useful for planning and designing tool for various facilities in an urban area, and also for consensus building for designers and the local residents.

Biography:

Dr. Kazuo Kashiyama obtained his PhD at Chuo University, Department of Civil Engineering, in 1987. He is currently a professor of the Department of Civil and Environmental Engineering of Chuo University and the director of AI and Data Science Center of Chuo University. His research interests cover many areas of computational mechanics, such as shallow water flow, free surface flow, noise simulation, wind flow, fluid-structure interaction, high performance computing and application of VR/AR/MR in pre and post processing.

He received the encouragement award of computational mechanics JUSE (Japan Union of Science and Engineering) in 1990, the Kawai medal from JSCES (The Japan Society for Computational Engineering and Science) in 2008 and Computational Mechanics Award (Asian-Pacific Association for Computational Mechanics) in 2013, JSCES Achievement Award and IACM (International Association for Computational Mechanics) Fellow Award in 2016 and Achievement Award for Applied Mechanics (Japan Society of Civil Engineers) in 2021.

He is the past President of the JSCES and an executive council member of IACM since 2012. He also serves as the advisory board member of the International Journal for Numerical Methods in Fluids, International Journal for Numerical Methods in Engineering and International Journal of Computational Methods.

Invited Talk

Presenter:

Dr. Emi Narita

Graduate School of Engineering,
Kyoto University

Title:

Development of a neural-network-based turbulent transport model DeKANIS and its application to integrated simulations of fusion plasmas

Abstract:

Fusion power is severely affected by plasma density and temperature, which are usually predicted by integrated codes. Such codes solve transport equations with turbulent fluxes provided by turbulent transport models embedded in the codes. First-principle-based turbulent transport models give reasonable agreement with experiments, but they consume large computational resources. To accelerate integrated simulations, neural-network (NN) based turbulent transport models have been developed, which predict turbulent fluxes about 10^3 times faster than the conventional models. While most NN based models work as surrogate models that mimic the existing ones, our model named DeKANIS is founded on gyrokinetic calculations performed on supercomputers and experimental data. DeKANIS has the feature that reveals the dominant transport processes in the predicted density and temperature based on the gyrokinetic calculations.

Biography:

PhD in Engineering from Osaka University in 2015. Emi Narita started her career at Naka Fusion Institute of QST. She has been engaged in experimental analysis of turbulent transport in fusion plasmas with gyrokinetic codes, transport modelling utilizing machine learning techniques, and development of integrated codes. She moved to the Graduate School of Engineering at Kyoto University in 2023.

Symposium3

Plenary Talk

Presenter:

Prof. Hisashi Morishita

Department of Electrical and Electronic Engineering,
National Defense Academy

Title:

An innovative decoupling method for MIMO antenna element

Abstract:

Recently, the Internet of things (IoT) has become prevalent with applications in countless areas of life. Along with the significant annual increase in the number of IoT devices, data traffic will increase, especially mobile data traffic. Therefore, large channel capacity and high-speed communication is required to satisfy the needs of all users of these devices. Multiple input multiple output (MIMO) is an attractive technique that can achieve a large channel capacity and high-speed communication by using multiple antenna elements in the same system. However, when MIMO antennas are closely placed in a limited space, one important issue is the strong mutual coupling that adversely affects the antenna efficiency. Thus, to improve the antenna efficiency, a reduction in mutual coupling (hereinafter referred to as decoupling) is required.

To date, many decoupling methods have been proposed. Among them, the method using a bridge line (BL) to directly connect antenna elements is considered as one of the simplest and most effective decoupling methods. However, the resonant frequency shifts to a different frequency when the antenna elements are connected directly by a BL. Hence, to shift the resonant frequency toward the desired frequency, the original size of the antenna elements must be adjusted individually. This is considered to be disadvantageous if the methods are applied under design conditions that hinder the implementation, for example, for small wireless modules with antenna. Therefore, to easily decouple the antennas in such cases, an

approach that does not require the adjustment of the original antenna sizes or structure is required.

A simple idea to implement a decoupling method that meets the above requirements is to use parasitic elements (PEs), since PEs will electromagnetically couple the antenna if they are placed in suitable locations close to the antenna. And thus, the antenna characteristics can be adjusted using PEs instead of directly redesigning the original antenna. Based on this idea, this study will utilize the combination of PEs and BLs to reduce the mutual coupling between multiple planar inverted-F antennas (PIFAs), without having to adjust the original antenna sizes or structure. In this study, PIFA was chosen as the research object because it is the type of antenna widely used in compact mobile terminals. Moreover, the design target of this study is to reduce and maintain all the reflection coefficient and mutual coupling for less than −10 dB, which are acceptable levels for MIMO antennas.

Firstly, the proposed method is investigated for two PIFAs with the feeding pins facing each other as a primary study. Using the proposed decoupling method, the mutual coupling decreased from −6.6 to −14.1 dB, and good impedance matching is maintained simultaneously at the desired resonant frequency of 2.0 GHz without having to adjust the original sizes of the PIFAs. Therefore, the total antenna efficiency is improved from 77.4% to 94.6%.

Next, the proposed method is developed to increase the operating frequency band and decouple the two PIFAs at these frequency bands. First, a dual-band design for 1-element PIFA using PE is performed. The PEs are then connected by a BL to decouple the two PIFAs in dual band. By loading the proposed PEs and BL onto the two PIFAs, two resonances with good impedance matching can be obtained at 2.0 and 2.4 GHz. Moreover, the mutual coupling at these frequencies is reduced to −14.6 dB and −14.4 dB, respectively. Therefore, the total antenna efficiency is improved from 77.4% to 95.2% at 2.0 GHz, and from 66.9% to 90.0 % at 2.4 GHz.

Finally, the PEs and BLs are investigated to reduce the mutual coupling between four PIFAs. As the number of PIFAs increases from two to four, decoupling becomes considerably more complicated, and impedance mismatch is also an issue to be considered. Therefore, PEs and BLs are functionally developed to simultaneously achieve low mutual coupling and improved impedance matching of the four PIFAs. The simulated results showed that the proposed method could reduce and maintain all mutual coupling for less than −10 dB, and simultaneously improve the impedance matching at 2.0 GHz. Although the bandwidth is narrow, the antenna efficiency at 2.0 GHz could be significantly improved from 64.2% to 84.8% for

PIFA1 and PIFA4 and from 35.9% to 74.2% for PIFA2 and PIFA3. Therefore, the design target of this study is achieved.

Biography:

Hisashi Morishita received the B.S. degree from National Defense Academy of Japan in 1980, the M.S. and Dr. Eng. Degrees from University of Tsukuba in 1987 and 1980, respectively. From 1990 to 1992, he worked as a research and development officer of JASDF. Since 1992, he has been with National Defense Academy and is currently a Professor in the Department of Electrical and Electronic Engineering. From 1996 to 1997, he was a Visiting Researcher at Communications Research Laboratory, McMaster University, Canada, he was engaged in research on smart antenna system.

He served as a Technical Committee member of the IEICE TG on Antennas and Propagation between 2002 and 2003, a TC member of 2004 and 2007 International Symposium on Antennas and Propagation (ISAP), a Secretary of 2002 Interim ISAP and was a Chair of the IEEE AP-S Japan Chapter from 2007 to 2008. He is currently a chair of Research Committee on Multi-dimensional Mobile Communication Networks of JSST.

His research is concerned with mobile communications and small antennas, on which he has published many papers in various major technical journals. Dr. Morishita is a Fellow of IEICE and a Senior Member of IEEE.

Invited Talk

Presenter:

Prof. Tatsuya Yamazaki

Faculty of Engineering, Niigata University

Title:

Multi-Agent Simulation for Urban Disaster Evacuation

Abstract:

Urban-sized evacuation simulation provides us with various knowledge and suggestion before a real disaster happens. Therefore, multi-agent simulation experiments must be useful to verify urban resiliency against disaster and to design city functions to support the evacuees. This talk provides two types of innovative multi-agent simulation experiments. The first developed evacuation simulation model includes human psychological models for evacuee agents. The objective of this model is to make the simulation experiments more realistic and simulated experimental results show that the proposed model provides accurate evacuation behaviors. In the second simulation model, we propose a narrow-area specific messaging system using taxis as information transmitters. As the experimental results, it is found that decentralized and unbiased taxi allocation can accelerate evacuation completion.

Biography:

Tatsuya Yamazaki received the B.E., M.E. and Ph.D. degrees in information engineering from Niigata University, Niigata, Japan, in 1987, 1989 and 2002, respectively. He joined Communications Research Laboratory (at present, National Institute of Information and Communications Technology) as a researcher in 1989. Since August 2013, he has been with the Faculty of Engineering, Niigata University, Niigata, where he is currently a Professor. Currently, he is also the director at the Big Data Activation Research Center of Niigata University.

Invited Talk

Presenter:

Prof. Tomotaka Wada

Department of Electrical, Electronic and Information
Engineering, Faculty of Engineering Science,
Kansai University

Title:

Development of Emergency Rescue Evacuation Support System (ERESS) for Safe and Secure Life

Abstract:

In recent years, many victims have been caused by sudden disasters such as fires and terrorism all over the world. When disaster information cannot be obtained, evacuees may not be able to choose a safe evacuation route. For this reason, in a disaster, the damage will increase due to the delay in evacuating. In order to reduce the number of victims caused by such sudden disasters, it is very important to promptly provide disaster information to evacuees. Hence, there is a system that quickly detects disasters and provides evacuation guidance. Typical systems include systems using communications such as mobile phones and sensor networks. An example of the former is disaster navigation. This is an evacuation support system that acquires current location information using the GPS function and displays the route from the current location to the evacuation center. However, because information acquisition depends on the server, information cannot be acquired if the server is damaged during a disaster. In addition, it takes time to acquire information because the access to the server is concentrated immediately after the disaster. On the other hand, the latter sensor network is a system composed of multiple sensors and servers. The sensors to be installed are sensors that detect temperature, smoke, gas, etc., and the data acquired by each sensor is managed by the server. It detects the occurrence of a disaster from the acquired data and notifies the evacuees in the building after the detection. However, it is limited to use only where the sensor is installed. Also, if the sensors or servers are damaged, the system will stop functioning. In order to solve these problems, we are developing an emergency rescue evacuation support system (ERESS). ERESS is a system that automatically detects disasters at an early stage by collecting sensor information from

mobile terminals through an ad-hoc network. It provides evacuation support by giving real-time disaster information to evacuees. I explain an overview of the development of this system so far.

Biography:

Tomotaka Wada received B.E. and M.E. degrees in Electrical and Electronic Engineering from Osaka Prefecture University, Japan, in 1995 and 1997, respectively. He received his Ph.D. degree in Communications Engineering from Osaka University, Japan, in 1999. From 1999 to 2006, he was a research associate in the Faculty of Systems Engineering of Wakayama University. In 2006, he joined the Faculty of Engineering at Kansai University, where he is currently professor. His research interests are wireless communications, sensor networks, evacuation support systems, and Intelligent Transport Systems (ITS). He was serving as chair of the IEICE Technical Committee on Intelligent Transport Systems Technology (ITS) from 2019 to 2021, and Information and Communication Technologies for Safe and Secure Life (ICTSSL) from 2022 to 2023. He was also chair of IEEE Communications Society Kansai Chapter from 2020 to 2022. He is a senior member of IEEE and IEICE, and a member of IPSJ, JSST and JASDIS.

Committee

General Chair:

Susumu Fujiwara (Kyoto Institute of Technology)

Conference Chair:

Takahiro Kenmotsu (Doshisha University)

Local Committee Chair:

Keisuke Nakano (Niigata University)

Committee Members:

Kenichi Ito (Niigata Institute of Technology)
Akira Otsuka (Niigata Comprehensive Academy Graduate School of Business Creation)
Tatsuya Kabasawa (National Institute of Technology, Nagaoka College)
Naoyuki Karasawa (Kaishi Professional University)
Kazuyuki Miyakita (Niigata University of International and Information Studies)
Ryusuke Numata (University of Hyogo)
Shugo Yasuda (University of Hyogo)
Masakazu Sengoku (Niigata University / Niigata Comprehensive Academy Graduate School of Business Creation)
Hiroshi Tamura (Chuo University)
Seiki Saito (Yamagata University)
Yoshihisa Fujita (Nihon University)
Satoshi Togo (University of Tsukuba)
Chako Takahashi (Yamagata University)
Makoto Nakamura (National Institute of Technology, Kushiro College)
Masafumi Yoshida (National Institute of Technology, Ube College)
Fumihiro Tamura (National Institute of Technology, Nagaoka College)
Takashi Hara (National Institute of Technology, Kagoshima College)
Yuichi Tamura (Konan University)
Nobuaki Ohno (University of Hyogo)
Ryosuke Ueda (Tohoku University)
Yuki Uchida (National Institute of Technology, Nagaoka College)
Miyuki Yajima (National Institute for Fusion Science)
Hiroyuki Suzuki (Yamagata University)

Hiroaki Ohtani (National Institute for Fusion Science)
Tomoko Mizuguchi (Kyoto Institute of Technology)
Taku Itoh (Nihon University)
Masami Iwase (Tokyo Denki University)
Hiroto Tadano (University of Tsukuba)
Hideki Kawaguchi (Muroran Institute of Technology)
Hiroaki Nakamura (National Institute for Fusion Science)

Table of Contents

Day 1: Tuesday, 29th August, 2023

Plenary Talk 1 (Symposium 3: Multi-Dimensional Communication Networks)
Time: 10:15 – 11:15
Room: Room A
Chair: ***Keisuke Nakano (Niigata University)***

Symposium 3: Multi-Dimensional Communication Networks (Session 1, Invited talks)
Time: 11:30 – 12:30
Room: Room A
Chair: ***Naobumi Michishita (National Defense Academy)***

OS6: Numerical Harmonic Analysis and Signal Processing ① (Session 5)
Time: 11:30 – 12:30
Room: Room B
Chair: ***Kensuke Fujinoki (Kanagawa University)***

OS1: Numerical Simulation and Visual Analytics of Nonlinear Problems ① (Session 9)
Time: 11:30 – 12:30
Room: Room C
Chair: ***Ayumu Saitoh (Yamagata University)***

Symposium 3: Multi-Dimensional Communication Networks ① (Session 2)
Time: 14:00 – 15:00
Room: Room A
Chair: ***Kenichi Ito (Niigata Institute of Technology)***

OS6: Numerical Harmonic Analysis and Signal Processing ② (Session 6)
Time: 14:00 – 15:00
Room: Room B
Chair: ***Kensuke Fujinoki (Kanagawa University)***

OS1: Numerical Simulation and Visual Analytics of Nonlinear Problems ② (Session 10)
Time: 14:00 – 15:00
Room: Room C
Chair: ***Teruou Takayama (Yamagata University)***

OS7: Computational electromagnetics and its applications ① (Session 13)
Time: 14:00 – 15:00
Room: Room D
Chair: ***Yoshihisa Fujita (Nihon University)***

Symposium 3: Multi-Dimensional Communication Networks ② (Session 3)
Time: 15:15 – 16:15
Room: Room A
Chair: ***Kazuyuki Miyakita (Niigata University)***

OS5: Complex Networks and Complex Systems ① (Session 7)
Time: 15:15 – 16:15
Room: Room B
Chair: ***Atsushi Tanaka (Yamagata University)***

Symposium 2: Simulation, machine learning and/or XR for science and technology ① (Session 11)
Time: 15:15 – 16:15
Room: Room C
Chair: ***Yuichi Tamura (Konan University)***

OS7: Computational electromagnetics and its applications ② (Session 14)
Time: 15:15 – 16:15
Room: Room D
Chair: ***Hideki Kawaguchi (Muroran Institute of Technology)***

Symposium 1: Advanced Concept and Methodology in Bioscience ① (Session 4)
Time: 16:30 – 17:30
Room: Room A
Chair: ***Susumu Fujiwara (Kyoto Institute of Technology)***

OS5: Complex Networks and Complex Systems ② (Session 8)
Time: 16:30 – 17:10
Room: Room B
Chair: ***Tetsuo Imai (Hiroshima City University)***

Symposium 2: Simulation, machine learning and/or XR for science and technology ② (Session 12)
Time: 16:30 – 17:30
Room: Room C
Chair: ***Hiroaki Ohtani (National Institute for Fusion Science)***

OS7: Computational electromagnetics and its applications ③ (Session 15)
Time: 16:30 – 17:10
Room: Room D
Chair: ***Kazuhiro Fujita (Saitama Institute of Technology)***

Day 2: Wednesday, 30th August, 2023

Plenary Talk 2 (Symposium 2: Simulation, machine learning and/or XR for science and technology)

Time: 9:00 – 10:00
Room: Room A
Chair: ***Seiki Saito (Yamagata University)***

(**Plenary**) Statistical-mathematical thinking in fusion research
Masayuki Yokoyama

Symposium 2: Simulation, machine learning and/or XR for science and technology (Session 16, Invited Talks)

Time: 10:15 – 11:15
Room: Room A
Chair: ***Nobuaki Ohno (University of Hyogo)***

(**Invited**) Simulation and Visulaization Using XR technology ∼Application to Safety and Environmental Problems∼
Kazuo Kashiyama

(**Invited**) Development of a neural-network-based turbulent transport model DeKANIS and its application to integrated simulations of fusion plasmas
Emi Narita

OS4: Advanced Numerical Analysis and Software in Multiphysics ① (Session 19)

Time: 10:15 – 11:15
Room: Room B
Chair: ***Hiroshi Kawai (Toyo University), Amane Takei (University of Miyazaki)***

OS1: Numerical Simulation and Visual Analytics of Nonlinear Problems ③ (Session 22)
Time: 10:15 – 10:55
Room: Room C
Chair: ***Taku Itoh (Nihon University)***

Regular Session ① (Session 25)
Time: 10:15 – 11:15
Room: Room D
Chair: ***Ryosuke Ueda (Tohoku University)***

Symposium 2: Simulation, machine learning and/or XR for science and technology ③ (Session 17)
Time: 11:30 – 12:30
Room: Room A
Chair: ***Masayuki Yokoyama (National Institute for Fusion Science)***

OS4: Advanced Numerical Analysis and Software in Multiphysics ② (Session 20)
Time: 11:30 – 12:30
Room: Room B
Chair: ***Daisuke Ishihara (Kyushu Institute of Technology)***

OS1: Numerical Simulation and Visual Analytics of Nonlinear Problems ④ (Session 23)
Time: 11:30 – 12:30
Room: Room C
Chair: ***Hiroto Tadano (University of Tsukuba)***

Regular Session ② (Session 26)
Time: 11:30 – 12:30
Room: Room D
Chair: ***Seiki Saito (Yamagata University)***

Symposium 2: Simulation, machine learning and/or XR for science and technology ④ (Session 18)
Time: 14:00 – 15:00
Room: Room A
Chair: ***Emi Narita (Kyoto University)***

OS4: Advanced Numerical Analysis and Software in Multiphysics ③ (Session 21)
Time: 14:00 – 14:40
Room: Room B
Chair: ***Akihiro Kudo (National Institute of Technology, Tomakomai College)***

OS1: Numerical Simulation and Visual Analytics of Nonlinear Problems ⑤ (Session 24)
Time: 14:00 – 14:40
Room: Room C
Chair: ***Kyoko Hasegawa (Ritsumeikan University)***

Regular Session ③ (Session 27)
Time: 14:00 – 14:40
Room: Room D
Chair: *Chako Takahashi (Yamagata University)*

Day 3: Thursday, 31st August, 2023

Plenary Talk 3 (Symposium 1: Advanced Concept and Methodology in Bioscience)
Time: 9:00 – 10:00
Room: Room A
Chair: ***Takahiro Kenmotsu (Doshisha University)***

(**Plenary**) Data analysis project in medical and engineering collaboration by big data in Kawasaki Disease
Ryusuke Ae

Symposium 1: Advanced Concept and Methodology in Bioscience (Session 28, Invited Talks)
Time: 10:15 – 11:15
Room: Room A
Chair: ***Takahiro Kenmotsu (Doshisha University)***

(**Invited**) Theoretical investigation of reversible fluorescent photoswitching molecules upon irradiation with visible light
Satoshi Yokojima

(**Invited**) Simulation study on “torsion” and local structure of chromosome: Loop structure via one side loop extrusion with twist deformation
Hiroshi Yokota

OS2: Design and Simulations for System Integration ① (Session 31)
Time: 10:15 – 11:15
Room: Room B
Chair: ***Shunsuke Nansai (Akita University)***

OS3: Verified Numerical Computations ① (Session 33)
Time: 10:15 – 11:15
Room: Room C
Chair: ***Kazuaki Tanaka (Waseda University)***

Symposium 2: Simulation, machine learning and/or XR for science and technology ⑤ (Session 36)
Time: 10:15 – 11:15
Room: Room D
Chair: ***Hideo Miyachi (Tokyo City University)***

Symposium 1: Advanced Concept and Methodology in Bioscience ② (Session 29)
Time: 11:30 – 12:30
Room: Room A
Chair: ***Hiroaki Nakamura (National Institute for Fusion Science)***

OS2: Design and Simulations for System Integration ② (Session 32)
Time: 11:30 – 12:30
Room: Room B
Chair: ***Koki Jimbo (Tokyo Denki University)***

OS3: Verified Numerical Computations ② (Session 34)
Time: 11:30 – 12:10
Room: Room C
Chair: ***Katsuhisa Ozaki (Shibaura Institute of Technology)***

Symposium 2: Simulation, machine learning and/or XR for science and technology ⑥ (Session 37)
Time: 11:30 – 12:30
Room: Room D
Chair: ***Masafumi Yoshida (National Institute of Technology, Ube College)***

Symposium 1: Advanced Concept and Methodology in Bioscience ③ (Session 30)
Time: 14:00 – 15:00
Room: Room A
Chair: ***Takahiro Kenmotsu (Doshisha University)***

OS3: Verified Numerical Computations ③ (Session 35)
Time: 14:00 – 14:40
Room: Room C
Chair: ***Katsuhisa Ozaki (Shibaura Institute of Technology)***

Symposium 2: Simulation, machine learning and/or XR for science and technology ⑦ (Session 38)

Time: 14:00 – 15:00
Room: Room D
Chair: ***Ryosuke Ueda (Tohoku University)***

JSST2023

Multi-Agent Simulation for Urban Disaster Evacuation

Tatsuya Yamazaki[1*]

[1]Big Data Activation Research Laboratory, Niigata University

*`yamazaki.tatsuya@ie.niigata-u.ac.jp`

Abstract. Urban-sized evacuation simulation provides us with various knowledge and suggestion before a real disaster happens. Therefore, multi-agent simulation experiments must be useful to verify urban resiliency against disaster and to design city functions to support the evacuees. This paper provides two types of innovative multi-agent simulation experiments. The first developed evacuation simulation model includes human psychological models for evacuee agents. The objective of this model is to make the simulation experiments more realistic and simulated experimental results show that the proposed model provides accurate evacuation behaviors. In the second simulation model, we propose a narrow-area specific messaging system using taxis as information transmitters. As the experimental results, it is found that decentralized and unbiased taxi allocation can accelerate evacuation completion.

Keywords: Multi-agent system, Disaster evacuation, Urban area simulation

1. Introduction

Evacuation drills are important to reduce possible panic occasions when a disaster happens. A building-size or community-size evacuation drill is often carried out normally, because the number of participants is limited and the evacuation drill can be easily notified of them in advance. On the other hand, evacuation drills in an urban area are not so easy, because not only the number of evacuees is relatively large but also a crowd of evacuees consists of various types of people with different ages, physical property, knowledge and so on. Therefore, the role of computer simulation is becoming more and more important to evaluate how the crowd of people behave in the case of emergency instead of the real evacuation drills.

For computer simulations, MAS (Multi-Agent System) is often used as a powerful scheme to simulate human behaviors on a computer platform. MAS contains an environment, objects, and agents, where an agent plays a roll of an evacuee. The autonomous agent can perceive its environment, and communicate with other agents [1].

This paper provides two types of MAS-based simulation experiments. The first one focuses on an evacuee agent model including human psychological models for evacuee. The purpose of this model is to make the simulation experiments more realistic. The second one focuses on a messaging system for evacuee agents. We propose a narrow-area messaging system using taxis that transmit specific evacuation information depending on the location of individual agents.

2. Agent model incorporating human psychology

An agent model with human psychology has been implemented in the first MAS-based simulation. The simulation system was linked with GIS (Geographic Information System) data and the agents looked for the evacuation stations in an urban area. The size of the urban area that was about 1.0 km by 1.2 km.

Three kinds of human psychological biases were included in the evacuee agent model: normalcy bias, emotional contagion bias, and sympathy behavior bias. The normalcy bias is the initial evacuation delay caused by a belief that abnormal events rarely happen. The emotional contagion bias is the effect of one person's emotional state on the emotional state of people around him/her both explicitly and implicitly. The sympathy behavior bias means that people instinctively take care of others, especially the weak such as elderly persons, injured persons, and so on.

The proposed agent model has been implemented in the evacuation simulation system based on MAS and GIS for urban disaster situation. The simulation experiment results showed that the normalcy and emotional contagion biases induced delayed evacuation. On the other hand, it was found that the sympathy behavior bias does not show any negative effect in evacuation time. The sympathy behavior is important to support the weak-side people such as the elderly persons [2].

3. Narrow-area messaging system using taxis

The second MAS-based simulation was situated for Tsunami evacuation, in which specific evacuation information needed to be transmitted to each evacuee. The simulation model included a proposed narrow-area specific messaging system. In the proposed messaging system, taxis played a role of information transmitters. Once an evacuee entered in the narrow-area communication region of the taxi, he/she could receive route information to the nearest evacuation site.

To evaluate effectiveness of the narrow-area messaging system using taxis, MAS-based simulation experiments were conducted. A 500 m by 500 m virtual city area was the experimental environment and 50 agents were located arbitrarily in the environment. The agents had no knowledge about the evacuation sites, so they executed random walk. When they came into the taxi’s communication region, they received evacuation information and moved toward the nearest evacuation site. In the experiments, the number of taxis was fixed as 5. The experimental results showed that a decentralized and unbiased taxi allocation could accelerate evacuation completion [3].

4. Conclusion

This paper briefly described two MAS-based evacuation simulation models.

References

[1] J. Ferber: Multi-Agent System: An Introduction to Distributed Artificial Intelligence. Addison-Wesley Professional, Boston, (1999).

[2] T. Yamazaki, H. Tamai, Y. Owada, K. Hattori, S. Taira, K, Hamaguchi: Urban Disaster Simulation Incorporating Human Psychological Models in Evacuation Behaviors, *the First IFIP Conference on Information Technology in Disaster Risk Reduction*, (2016).

[3] N. Kobayashi, T. Yamazaki: A Narrow-Area Specific Messaging System for Tsunami Evacuation, *IEEE Global Conference on Consumer Electronics*, (2019).

Development of Emergency Rescue Evacuation Support System (ERESS) for Safe and Secure Life

Tomotaka Wada[1,*]

[1]Department of Electrical, Electronic and Information Engineering, , Faculty of
Engineering Science, Kansai University

*`wadat@kansai-u.ac.jp`

The full paper of this paper has been published in Journal of Advanced Simulation in Science and Engineering (JASSE).

DOI: `https://doi.org/10.15748/jasse.11.236`

JSST 2023

An improvement for image compression using the discrete wavelet transform and the linear quantization

Kouta Yamamoto[1,*], Toshio Suzuki[2], Emiko Ishiwata[2]

[1]Graduate School of Science, Tokyo University of Science
[2]Faculty of Science Division I, Tokyo University of Science

*`1422544@ed.tus.ac.jp`

Abstract. In this study, we consider the quantization of coefficients obtained by the discrete wavelet transform for image compression. Specifically, we focus on the linear quantization method and propose an improved method that degrades image quality less than the conventional linear quantization method.

Keywords: Wavelet transform, linear quantization, image compression

1. Introduction

Image compression is frequently used in the various fields. One method is quantization. For example, when sending and receiving image data, compressing the images reduces their capacity and speeds up the transmission and reception. In this study, we focus on the discrete wavelet transform and try to improve the image compression technique. The wavelet transform is a time-frequency analysis technique that analyzes signals using a wavelet function which has a strong localization. The discrete wavelet transform can decompose a signal into low-frequency and high-frequency components, which enables compression and feature extraction. Specifically, we improve linear quantization for image compression and apply it to detail coefficients obtained by the discrete wavelet transform . There are two main types of quantization: linear quantization and nonlinear quantization. The linear quantization method sometimes degrades image quality significantly, while the nonlinear quantization method involves optimization and is computationally expensive. In this study, we focus on the linear quantization method and propose an improved method that does not degrade image quality as much as the conventional linear quantization method.

2. Discrete wavelet transform

First, we explain the discrete wavelet transform. Let φ be an orthonormal scaling function and ψ be an orthonormal wavelet function satisfying $\varphi(x) = \sum_{k=-\infty}^{\infty} 2a_k\varphi(2x-k), \psi(x) = \sum_{k=-\infty}^{\infty} 2b_k\varphi(2x-k)$. a_k and b_k are called the two-scale coefficients. Let $\varphi_k^j(x) = 2^{j/2}\varphi(2^jx-k)$

and $\psi_k^j(x) = 2^{j/2}\psi(2^j x - k)$ $(j, k \in \mathbb{Z})$. $f_j(x, y)$ is called the approximation function of level j if the image is expressed as $f_j(x, y) = \sum_{k=-\infty}^{\infty} \sum_{l=-\infty}^{\infty} C_{k,l}^j \varphi_k^j(x)\varphi_l^j(y)$. $C_{k,l}^j$ are called the approximation coefficients, where $C_{k,l}^j = \int_{-\infty}^{\infty} \int_{-\infty}^{\infty} \overline{\varphi_k^j(x)\varphi_l^j(y)} f_j(x, y) dx dy$. $f_j(x, y)$ can be decomposed as $f_j(x, y) = f_{j-1}(x, y) + g_{j-1}(x, y) + p_{j-1}(x, y) + q_{j-1}(x, y)$. Here, for the vertical, horizontal and diagonal detail coefficients $D_{k,l}^j$, $E_{k,l}^j$, and $F_{k,l}^j$,

$$
\begin{aligned}
f_{j-1}(x, y) &= \sum_{k=-\infty}^{\infty} \sum_{l=-\infty}^{\infty} C_{k,l}^{j-1} \varphi_k^{j-1}(x)\varphi_l^{j-1}(y), \;\; g_{j-1}(x, y) = \sum_{k=-\infty}^{\infty} \sum_{l=-\infty}^{\infty} D_{k,l}^{j-1} \varphi_k^{j-1}(x)\psi_l^{j-1}(y), \\
p_{j-1}(x, y) &= \sum_{k=-\infty}^{\infty} \sum_{l=-\infty}^{\infty} E_{k,l}^{j-1} \psi_k^{j-1}(x)\varphi_l^{j-1}(y), \;\; q_{j-1}(x, y) = \sum_{k=-\infty}^{\infty} \sum_{l=-\infty}^{\infty} F_{k,l}^{j-1} \psi_k^{j-1}(x)\psi_l^{j-1}(y). \quad (1)
\end{aligned}
$$

Let $\boldsymbol{C}_j = \left\{C_{k,l}^j\right\}_{k,l\in\mathbb{Z}}$, $\boldsymbol{D}_j = \left\{D_{k,l}^j\right\}_{k,l\in\mathbb{Z}}$, $\boldsymbol{E}_j = \left\{E_{k,l}^j\right\}_{k,l\in\mathbb{Z}}$, $\boldsymbol{F}_j = \left\{F_{k,l}^j\right\}_{k,l\in\mathbb{Z}}$. The discrete wavelet transform (DWT) is the mapping $\boldsymbol{C}_j \mapsto (\boldsymbol{C}_{j-1}, \boldsymbol{D}_{j-1}, \boldsymbol{E}_{j-1}, \boldsymbol{F}_{j-1})$ given by

$$
\begin{aligned}
C_{k,l}^{j-1} &= 2 \sum_{n=-\infty}^{\infty} \sum_{m=-\infty}^{\infty} \overline{a_{n-2k}}\, \overline{a_{m-2l}} C_{n,m}^j, \quad D_{k,l}^{j-1} = 2 \sum_{n=-\infty}^{\infty} \sum_{m=-\infty}^{\infty} \overline{a_{n-2k}}\, \overline{b_{m-2l}} C_{n,m}^j, \\
E_{k,l}^{j-1} &= 2 \sum_{n=-\infty}^{\infty} \sum_{m=-\infty}^{\infty} \overline{b_{n-2k}}\, \overline{a_{m-2l}} C_{n,m}^j, \quad F_{k,l}^{j-1} = 2 \sum_{n=-\infty}^{\infty} \sum_{m=-\infty}^{\infty} \overline{b_{n-2k}}\, \overline{b_{m-2l}} C_{n,m}^j. \qquad (2)
\end{aligned}
$$

By applying the DWT to $\boldsymbol{C}_{j-1}$, the approximation and detail coefficients $\boldsymbol{C}_{j-2}$, $\boldsymbol{D}_{j-2}$, $\boldsymbol{E}_{j-2}$, $\boldsymbol{F}_{j-2}$ can be computed sequentially. The inverse discrete wavelet transform (IDWT) is the mapping $(\boldsymbol{C}_{j-1}, \boldsymbol{D}_{j-1}, \boldsymbol{E}_{j-1}, \boldsymbol{F}_{j-1}) \mapsto \boldsymbol{C}_j$ given by

$$
\begin{aligned}
C_{n,m}^j &= 2 \sum_{k=-\infty}^{\infty} \sum_{l=-\infty}^{\infty} a_{n-2k} a_{m-2l} C_{k,l}^{j-1} + 2 \sum_{k=-\infty}^{\infty} \sum_{l=-\infty}^{\infty} a_{n-2k} b_{m-2l} D_{k,l}^{j-1} \\
&+ 2 \sum_{k=-\infty}^{\infty} \sum_{l=-\infty}^{\infty} b_{n-2k} a_{m-2l} E_{k,l}^{j-1} + 2 \sum_{k=-\infty}^{\infty} \sum_{l=-\infty}^{\infty} b_{n-2k} b_{m-2l} F_{k,l}^{j-1}. \qquad (3)
\end{aligned}
$$

3. Linear quantization and its modification

Quantization is a method of grading the distribution of pixel values. Quantization reduces the number of types of pixel values to be stored and enables image compression. A method of image compression using the DWT and quantization is given below. In Figure 1, $\boldsymbol{C}_{j-1}$, $\boldsymbol{D}_{j-1}$, $\boldsymbol{E}_{j-1}$, and $\boldsymbol{F}_{j-1}$ are first obtained. Next, quantization is applied to each detail coefficient $\boldsymbol{D}_{j-1}$, $\boldsymbol{E}_{j-1}$, and $\boldsymbol{F}_{j-1}$ to obtain $Q\left(\boldsymbol{D}_{j-1}\right)$, $Q\left(\boldsymbol{E}_{j-1}\right)$, and $Q\left(\boldsymbol{F}_{j-1}\right)$. Then the IDWT constructs $\widetilde{\boldsymbol{C}}_j$ from $\boldsymbol{C}_{j-1}$, $Q\left(\boldsymbol{D}_{j-1}\right)$, $Q\left(\boldsymbol{E}_{j-1}\right)$, and $Q\left(\boldsymbol{F}_{j-1}\right)$. Since quantization is applied to each detail coefficient, $\widetilde{\boldsymbol{C}}_j$ is a compressed image of $\boldsymbol{C}_j$.

There are several quantization methods, and the compression ratio varies depending on the quantization method. One well-known method is the linear quantization method. This is a method that grades the distribution of pixel values by placing rounding values at equal intervals. Specifically, the pixel value x is quantized to $Q(x)$ using the following staircase

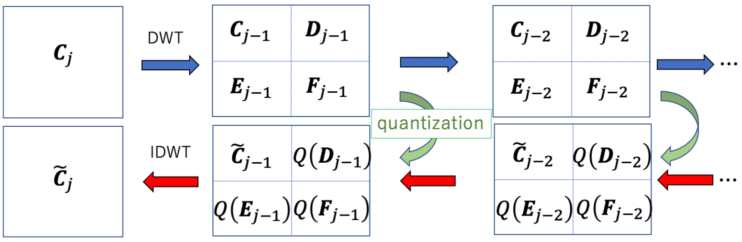

Fig 1: Compression process

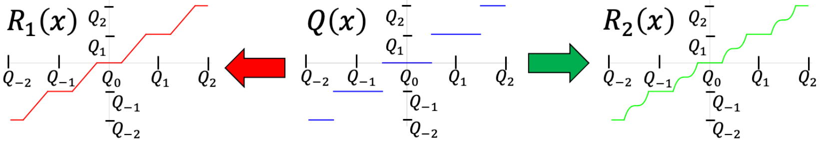

Fig 2: The graphs of $Q(x)$, $R_1(x)$ and $R_2(x)$

function $Q(x) = \sum_{n=N_1}^{N_2} Q_n \chi_{I_n}(x)$, where $\chi_{I_n}(x)$ denotes the characteristic function on $I_n = \left[Q_n - \frac{h}{2}, Q_n + \frac{h}{2}\right)$ and $Q_{n+1} = Q_n + h$, $Q_0 = 0$. h is a positive real number. N_1 and N_2 in the sum sign satisfy (minimum of pixel values) $\in I_{N_1}$ and (maximum of pixel values) $\in I_{N_2}$. One of the disadvantages of linear quantization is the large degradation of image quality, but the nonlinear quantization method overcomes it. The nonlinear quantization method is characterized by the use of optimization in the calculation to make $Q(x)$ smooth in order to suppress the degradation of image quality after compression. However, this method is complex and computationally expensive. Therefore, we propose a method that does not degrade image quality as much as the linear quantization method and is not as complex as the nonlinear quantization method.

4. Proposed method and experimental results

Based on the above, we consider the improvement to the linear quantization function $Q(x)$. The improvement is to make the staircase function $Q(x)$ be continuous, and in this study, we have tried two cases: $R_1(x)$ and $R_2(x)$.

$$R_1(x) = \sum_{n=N_1}^{N_2} l_{J_n}(x), \quad l_{J_n}(x) = \begin{cases} Q_n & (x \in J_{n,1}), \\ 2\left\{x - \left(Q_n + \frac{h}{4}\right)\right\} + Q_n & (x \in J_{n,2}), \\ 0 & (x \notin J_n), \end{cases} \tag{4}$$

$$R_2(x) = \sum_{n=N_1}^{N_2} c_{J_n}(x), \quad c_{J_n}(x) = \begin{cases} Q_n & (x \in J_{n,1}), \\ \frac{32}{h^2}\left\{x - \left(Q_n + \frac{h}{2}\right)\right\}^3 + Q_n + \frac{h}{2} & (x \in J_{n,2}), \\ 0 & (x \notin J_n), \end{cases} \tag{5}$$

where $J_{n,1} = \left[Q_n - \frac{h}{4}, Q_n + \frac{h}{4}\right)$, $J_{n,2} = \left[Q_n + \frac{h}{4}, Q_{n+1} - \frac{h}{4}\right)$, $J_n = J_{n,1} \cup J_{n,2}$. In this study, we use $R_1(x)$ and $R_2(x)$ to quantize and compress the images of Fig. 3 with $h = 100$. The compression results are shown in Fig. 5. The top rows show the compressed images using the proposed method, and the bottom rows show the histograms corresponding to the top images. The compression ratio (CR) and PSNR of the images are also shown. CR is calculated using entropy. The higher the value of CR, the more information is preserved in the original image. The higher the value of PSNR, the better the image quality. Next, we focus on the shading. The image quantized with the staircase function $Q(x)$ is whiter than the original image. This is because the distribution of the histogram is more centered. In the histogram of the original image, the first peak is around 10 and the second peak is around 170. The histogram of the image quantized with $Q(x)$ shows that the first peak is around 50 and the second peak is around 160. The two peaks in the histograms of the images quantized with $R_1(x)$ and $R_2(x)$ are closer to those in the histogram of the original image than to those with $Q(x)$. The shapes of the distributions of the histograms with $R_1(x)$ and $R_2(x)$ are almost the same as that with $Q(x)$. Quantizing with $R_1(x)$ and $R_2(x)$ gives higher CR and PSNR values than quantizing with $Q(x)$. These indicate that the proposed method has less image quality degradation than image compression using the linear quantization method.

Fig 3: Original image

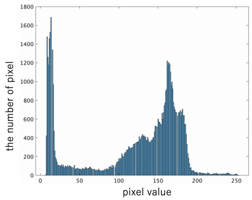

Fig 4: Histogram of Fig. 3

5. Conclusion

In this study, we focused on quantization in image compression using the DWT. We modified the linear quantization function to be continuous and applied it to image compression. The experimental results showed that the proposed method reduced the degradation of image quality compared to the linear quantization method.

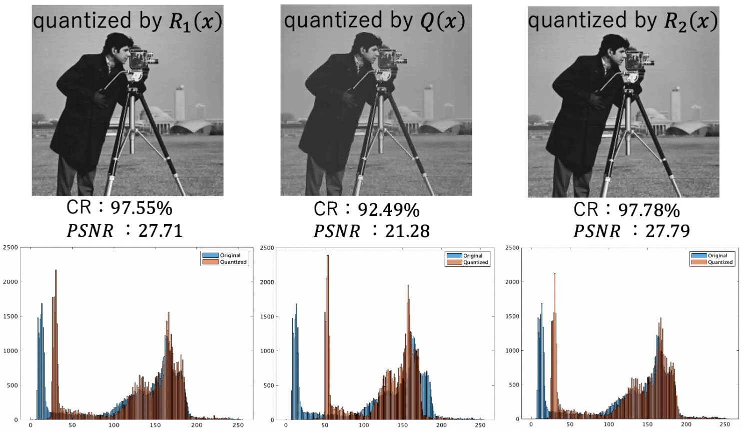

Fig 5: Quantized images and their histograms

References

[1] E. Hernández, and G. Weiss, A first course on wavelets, CRC press, 1996.

[2] D. Tyagi, R. Kumar and A. Gupta, Analysis of linear quantization based wavelet decomposition technique for electrocardiogram signal compression, **12**, No.1, pp. 118-130.

Feature Extraction Based on Curvelet for Defect Detection in a Sewer Pipe Image

Tomoki Suka[1,*], Hajime Omura[2], Teruya Minamoto[1]

[1]Graduate School of Science and Engineering, Saga University, Saga, Japan
[2]Fukuhaku Printing Co., Ltd., Saga, Japan

*`sukatomo@ma.is.saga-u.ac.jp`

Abstract. We propose a novel methodology for feature extraction, based on the curvelet transform, aimed at detecting defects in sewer pipe images. Traditional defect detection methods in sewer pipes typically require a manual inspection of video feeds, a labor-intensive and costly process. We utilize the curvelet transform for feature extraction to streamline this process and enhance detection eficiency, proving effective at extracting edge features within images. We apply various machine-learning techniques to evaluate the efficiency of our proposed method. Our experimental findings indicate that this approach significantly enhances defect detection, offering clear benefits over existing methodologies.

Keywords: Curvelet Transform, Sewer defect detection, Sewer pipe

1. Introduction

In Japan, regular inspections become increasingly crucial as sewer pipes approach their standard service lifespan of 50 years. These inspections often require an inspector to identify the presence or absence of defects using sewer pipe videos, a meticulous process that demands sustained concentration incurs substantial costs and is labor-intensive. Recent methodologies for defect detection have begun utilizing deep learning techniques [4, 6]. However, these methods have notable drawbacks, as they require extensive high-quality data for training and entail lengthy training periods.

This study aims to extract the features for detecting the defect from the sewer pipe image. As defective and normal regions present discernible visual differences, we apply the curvelet transform [1] to extract unique features of sewer pipe defects. The curvelet transform, recognized for its ability to capture the characteristics of curved lines, has been extensively employed in various image analysis studies [2]. Notably, the features extracted using our proposed method enable highly accurate classification via machine learning techniques, thus eliminating the need for large datasets.

2. Proposed method

As mentioned above, we used the curvelet transform in the proposed method. The curvelet transform is more adept at extracting edge features from curved lines than the conventional wavelet transform. Consequently, it can better capture edge features in sewer pipe images compared to the standard wavelet transform.

The procedure in the proposed method is shown below.

1. Convert the sewer color image to the grayscale.

2. Extract the features by the following three types (Step.A, B, and C) methods.

  A-1. Apply morphological transformation and normalization to the range of 0 and 255 to the grayscale image obtained in Step.1.

  A-2. After marking five types of thresholds, perform the region segmentation by the watershed algorithm. The thresholds for the range of markers are [0 25], [0 45], [0 65], [0 85], and [0 105].

  A-3. Compute the area ratio of the region to the convex hull and curvature of each region obtained by Step.A-2. The curvature is calculated from the contour of the region by Ref.[3] and then histogrammed and normalized into 7-dimensions.

  B. Compute the entropy and average value to each region obtained by Step.A-2.

  C-1. Apply the noise reduction and edge extraction based on the curvelet to the grayscale image obtained by Step.1.

  C-2. Perform the region segmentation in the same position as Step.A-2 to the edge image obtained by Step.C-1.

  C-3. Compute the number of zero points and root mean square to each region obtained by Step.C-2. Here, the number of zero points is calculated using the following equation.

$$Z[m] = \begin{cases} 1 & R[m] * R[m+1] \leq 0 \\ 0 & else \end{cases}$$

$$the\ number\ of\ zero\ counts = \frac{1}{M-1}\sum_{m=1}^{M-1} Z[m] \quad (M = Length\ of\ R),$$

  where R is a 1-D vector that vertically connects each region element.

4. Standardize the 12-dimensional features obtained by Steps.A, B, and C, and perform PCA.

5. Represent the features using up to the ninth principal components.

3. Experiment

The experimental method and results are presented in Section 3. To confirm the usefulness of the proposed method, we compared the existing method of detecting the defect concerning detection accuracy. We used the kernel-SVM, decision tree, and logistic regression as the classifiers based on the extracted features by the proposed method. We use SegNet[4] from VGG16 to compare the existing method, which trains and classifies sewer pipe defects using a model pre-trained on the CamVid dataset [5]. Figure.1 shows the schematic diagram of the detecting defect based on the proposed method.

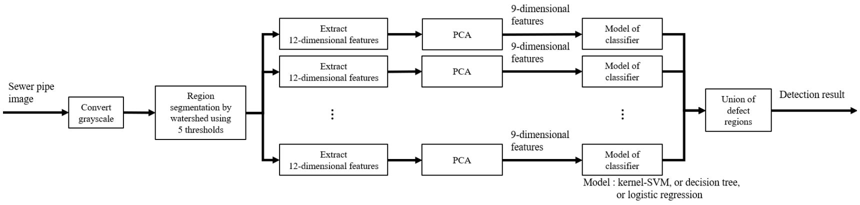

Figure 1: Schematic diagram of the detecting defect based on the proposed method

First, we prepared images of sewer pipes (720 x 343 pixels). We labeled each pixel separately for the sewer pipe attachment pipe, the region where the pipe is damaged, and the normal region. As a result, 542 images of sewer pipes are used. The ratio of training data to test data is 7:3, respectively.

To obtain the detection accuracy, we used three metrics. First, for each region that the model predicts as a defect based on the image, if equation (1) holds, it means that the prediction was correct, and we denote it as TP.

$$\frac{\text{Detected Region} \cap \text{Ground-truth Defect Region}}{\text{Detected Region}} > 0.1 \tag{1}$$

FP is assumed if the model predicts that the normal region is the defect. If the model cannot predict the defect region, it is set to FN. The reproducibility is calculated using the above as $Recall = TP/(TP + FN)$. Next, Pixel Accuracy (PA) and IoU are used as per-pixel evaluation indices: $PA = TP/(TP + FN)$ and $IoU = TP/(TP + FP + FN)$ are calculated by TP, FP, and FN for each pixel, and represent how accurately a defect is detected.

Table 1 shows the detection accuracy of SegNet and our proposed method using three evaluation metrics in 162 test data. The Recall of the SVM based on the proposed method is higher than the logistic regression and is almost the same as the decision tree. In addition, the Recall and IoU of the SVM based on the proposed method are higher than SegNet.

Table 1: Result of evaluation metrics in our proposed method and SegNet

	SegNet	Proposed Method		
		SVM	Decision Trees	Logistic regression
Recall	0.6923	**0.7692**	**0.7885**	**0.7115**
PA	**0.9119**	0.6578	0.6271	0.5465
IoU	0.2127	**0.2842**	0.0712	0.2082

As shown in Figure 2, SegNet's detection results are inaccurate because of the large defect region compared to the image with the ground-truth label. This is the reason for the high PA and low Recall of SegNet. On the other hand, the SVM based on the proposed method can accurately detect the defect region.

Figure 2: Example of detection results (Left:SegNet, Center:Proposed Method(SVM), Right:Ground-truth defect label)

4. Conclusion

We proposed a feature extraction method founded on the curvelet transform to detect defective regions within sewer pipe images. The proposed method has shown higher accuracy in defect detection compared to SegNet. In future work, we plan to refine the features extracted by our proposed method to enhance the precision of defect detection further.

5. Acknowledgements

This work was partially supported by JSPS KAKENHI Grant Number 22K03417.

References

[1] Candes, E., Demanet, L., Donoho, D., Ying, L Fast discrete curvelet transforms, *Multiscale Model. Simul. 5 (3), (2006), 861–899*,

[2] Jumpei Yamaguchi, Akihiko Yoneyama, Teruya Minamoto Automatic detection of early gastric cancer from endoscopic images using fast discrete curvelet transform and wavelet transform modulus maxima, *Advances in Intelligent Systems and Computing, 800 Part F1, (2019), pp. 379-383*,

[3] MathWorks (Matlab Central Community),
`https://jp.mathworks.com/matlabcentral/fileexchange/69452-curvature-of-a-1d-curve-in-a-2d-or-3d-space.`

[4] Min He, Qinnan Zhao, Huanhuan Gao, Xinying Zhang, Qin Zhao Image Segmentation of a Sewer Based on Deep Learning, *Sustainability, 14(11), 6634, (2022)*,

[5] Brostow, G. J., J. Fauqueur, and R. Cipolla. Semantic object classes in video: A high-definition ground truth database, *Pattern Recognition Letters. Vol. 30, Issue 2, (2009), pp 88-97*,

[6] Jiawei Zhang, Xiang Liu, Xing Zhang, Zhenghao Xi, Shuohong Wang Automatic Detection Method of Sewer Pipe Defects Using Deep Learning Techniques, *Appl. Sci, 13(7), 4589, (2023)*,

Watermarking Using Gyrator Transform and Dyadic Lifting Schemes

Junya Noda[1,*], Hajime Omura[2], Teruya Minamoto[1]

[1]Graduate School of Science and Engineering, Saga University, Saga, Japan
[2]Fukuhaku Printing Co.,Ltd., Saga,Japan

*`nodajun@ma.is.saga-u.ac.jp`

Abstract. This paper presents a refined approach to digital watermarking, an innovative technique that subtly embeds information into digital content for copyright protection, origin identification, and tamper detection. Our method enhances the previously proposed blind digital watermarking approach based on Dyadic Wavelet Transform (DYWT) and Gyrator Transform (GT) with higher perceptibility and robustness. The novelty lies in adopting Dyadic Lifting Schemes (DLS), utilizing its free parameters to build filters encapsulating critical image features. The process involves learning these parameters using watermark-free and watermarked images. The improved method enhances the quality of the watermarked images and bolsters their resilience against various digital attacks, such as cropping and rotation.

Keywords: Digital watermarking, Gyrator transform, Dyadic Lifting Schemes, Dyadic Wavelet Transform

1. Introduction

Digital watermarking is a technique that subtly incorporates invisible data, known as a watermark, into digital content like images, sound, and videos for copyright protection, origin identification, and tampering detection, without affecting the original data. It requires a balance between perceptibility and ensuring the watermark is invisible to humans. It does not impact the original data and robustness, ensuring the watermark endures despite potential data modifications or attacks, like compression, filtering, or noise addition.

In Ref. [1], a blind digital watermarking method based on the Dyadic Wavelet Transform (DYWT) and the Gyrator Transform (GT)[2], offering high perceptibility and robustness was proposed. This paper proposes a modified version of this method that improves perceptibility and robustness. We incorporate the Dyadic Lifting Schemes (DLS) alongside the DYWT. The DLS has free parameters, which enable us to construct filters possessing significant image features [3]. Our method involves learning these free parameters based on some training images, both with and without a watermark. Consequently, we successfully improved the image quality of the watermarked image, making it robust against various attacks such as cropping and rotation.

2. Proposed Method

This section describes our watermarking method that incorporates the GT, DYWT, and DLS. We begin with a ternary-valued watermark, denoted as W, consisting of the values -1, 0, and 1. The initial filter condition is considered when $m = 0, r = 1$ as mentioned in Ref. [4].

The embedding procedure, which utilizes the DLS, is inspired by the process outlined in Ref. [5]. Owing to page limitations, we briefly describe our watermarking process below.

The embedding algorithm includes the following steps:

1. Apply the GT to the original grayscale image.
2. Apply the DYWT to the image obtained from Step 1, resulting in the low-frequency and three high-frequency components. These high-frequency components correspond to the horizontal, vertical, and both directions.
3. Compute relation (1) for the horizontal, vertical, and diagonal high-frequency components, where M and N represent the image size, S_i represents the high-frequency component where the watermark is embedded, and K and L are fixed natural numbers.

$$\underline{S_i}[m,n] = \mathrm{sgn}(S_i[m,n]) \cdot \frac{1}{2K+1}\frac{1}{2L+1}\sum_{\mu=-K}^{K}\sum_{\nu=-L}^{L}|S_i[m+\mu, n+\nu]| \tag{1}$$

4. Embed the watermark W into $\underline{S_i}$ by computing $\widetilde{S}_i[m,n] = \underline{S_i}[m,n] + \alpha W[m,n]$ for a positive number α.
5. The DLS updates the filter corresponding to the component where the watermark is embedded, following the same procedure as in Ref. [5]. This process involves the construction of two filters: one aligns closely with the high frequency of the original image, and the other aligns with the high frequency of the watermarked image, deviating from the procedure in Ref. [5].
6. Decompose the image obtained from Step 1 using the two types of filters updated in Step 5.
7. Apply the inverse DYWT to the target frequency components to reconstruct the image, creating a watermarked image.

The watermark extraction algorithm proceeds as follows:

1. Apply the GT and DYWT sequentially to the watermarked image.
2. Compute the values in (1) for the target high-frequency components.
3. Extract the watermark based on the difference between $\widetilde{S}_i$ and the frequency components obtained in the previous step.

3. Experimental results

We evaluated the performance of the proposed method by conducting experiments on 256 × 256 pixel images. The original images used were SIDBA's GIRL, WOMAN, and BARBARA, with the watermarked image on the right. The sliding window's width parameters were set to $K = L = 20$. Additionally, the rotation angle of the gyrator transform was assigned a value of $\pi/1000$. The parameter α, which signifies the strength of the watermark embedding, was set to 20.

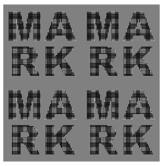

We used the Peak Signal-to-Noise Ratio (PSNR) as the evaluation metric to assess the quality of watermarked images. As Figure 1 indicates, our proposed method effectively enhances both the quality and robustness of images. Specifically, subplot (a) represents our proposed method, subplot (b) corresponds to the method described in Ref. [1], and subplot (c) depicts the results of using the Dyadic Lifting Schemes and Dyadic Wavelet Transform (DLS-DYWT) for watermark embedding. Figures 2 and 3 show the watermarks extracted after a crop attack, rotation attack, JPEG compression attack, and Gaussian filter attack were applied to the watermarked image.

Figure 1: Watermarked image (upper row) and extracted watermark (lower row)

Figure 2: Cropping : (a) – (c) and Rotation : (d) – (f)

These figures confirm the robustness of the extracted watermark, even when the watermarked image has undergone various types of attacks.

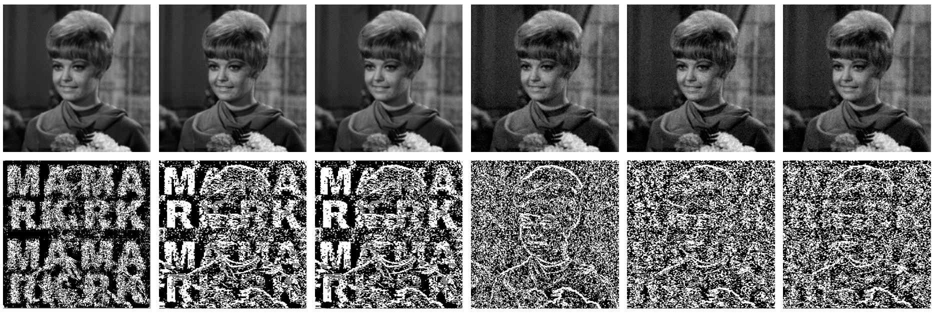

Figure 3: JPEG compression : (a) – (c) and Gaussian filtering : (d) – (f)

4. Conclusion

We proposed a blind digital image watermarking method that employs the Gyrator Transform (GT), Dyadic Wavelet Transform (DYWT), and Dyadic Lifting Schemes (DLS). The experimental results indicate that our proposed method improves the Peak Signal-to-Noise Ratio (PSNR) compared to existing methodologies. Furthermore, it demonstrates robustness against attacks such as cropping and rotation. Nonetheless, the robustness against other attacks remains a topic for future investigation.

Acknowledgement

This work was partially supported by JSPS KAKENHI Grant Number 22K03417.

References

[1] A. Ide, R. Ohura, T.Minamoto: Digital image watermarking method using the gyrator and dyadic wavelet transforms, *Proceedings of the 2020 International Conference on Wavelet Analysis and Pattern Recognition*, (2020), 84–89.

[2] J.A. Rodrigo, T. Alieva, M.L. Calvo: Gyrator transform: Properties and applications, *Optics Express*, 15:5 (2007), 2190 – 2203.

[3] Teruya. Minamoto, Keisuke. Tsuruta, Satoshi. Fujii: Edge-preserving Image Denoising Method Based on Dyadic Lifting Schemes, *IPSJ Transactions on Computer Vision and Applications*, 2 (2009), 283–294.

[4] Turghunjan.Abdukirim , Shigeru.Takano , Koichi. Niijima: Construction of Spline Dyadic Wavelet Filters, *Research Reports on Information Science and Electrical Engineering of Kyushu University*, 7 (2002), 1–6.

[5] R. Ohura, T. Minamoto: A recoverable visible digital image watermarking based on the dyadic lifting scheme, *Proceedings of the 2014 11th International Conference on Information Technology: New Generations*, (2014), 447–451.

JSST 2023

Comparison of Total-Field and Scattered-Field Physics-Informed Neural Networks for Impedance Simulations

Kazuhiro Fujita[1,*]

[1]Department of Information Systems, Faculty of Engineering, Saitama Institute of Technology

*`kfujita@sit.ac.jp`

The full paper of this paper has been published in Journal of Advanced Simulation in Science and Engineering (JASSE).

DOI: `https://doi.org/10.15748/jasse.11.73`

Parallel calculations of the extremely large number of MPI processes in Fugaku

Hiroki Nakano[1,*], Norikazu Todoroki[2], Hiroto Tadano[3]

[1]Graduate School of Science, University of Hyogo
[2]Chiba Institute of Technology
[3]Center for Computational Sciences, University of Tsukuba

[*]`hnakano@sci.u-hyogo.ac.jp`

Abstract. We carry out MPI-parallel calculations in Fugaku and observe the memory consumption when the total number of MPI processes is extremely large. We have carried out an eigenvalue calculation of quantum spin systems describing an insulating magnet and successfully confirmed the acceleration of the high MPI-parallelization jobs with more than two million MPI processes.

Keywords: Numerical diagonalization, Lanczos algorithm, Quantum lattice model, MPI Parallelization

1. Introduction

Specific cases of matrix eigenvalue problems appear in a variety of scenes of science and technology. When building a big building for example, it is necessary to compute the normal modes, which lead to information to clarify the stability of the building; the calculation is a kind of issues of matrix eigenvalue problems. In quantum physics, the Schrödinger equation $\mathcal{H}\Psi_n = E_n\Psi_n$ as a fundamental equation is a typical matrix eigenvalue problem, where $\mathcal{H}$ is the Hamiltonian matrix describing a target physical system. If one obtains an eigenvalue and its eigenstate, the results for E_n and Ψ_n can clarify various physical properties. For physical systems in which a lot of researchers are interested, on the other hand, the dimension of the matrix (d) has often been very large. To carry out a diagonalization for such a large-dimensional matrix is not so easy, even if one utilizes a modern powerful supercomputer. Then, there raises a question: what is the largest limit value of a dimension, the matrix with which can be diagonalized in a utilizable computer? Under the circumstances, we have been challenging such calculations of diagonalizing matrices with a very large dimension from the era of supercomputer K in Japan[1].

What happens when one achieves such calculations of diagonalizing matrices with a very large dimension in supercomputer Fugaku? Fugaku consists of over 150 thousand calculation nodes, each of which has 48 CPU cores and 32 GiB memory. A large number of nodes have to be used at the same time in a single job for an eigenvalue problem of such a large dimension. Therefore, it is necessary to carry out a parallel calculation with a total number of MPI processes ($N_{\rm MPIP}$) to be large. What then happens as a kind of adverse effects when $N_{\rm MPIP}$ is quite large? The purpose of this study is to clarify such an effect on the basis of the following two points. One is the memory use of a calculation job other than the use coming from the vectors that are explicitly determined in the user code. In particular, our primary focus is on the amount of memory used by MPI functions. The other point is whether or not the calculation jobs are carried out in a stable manner, even though complex communications occur between the large $N_{\rm MPIP}$.

2. Model system and calculation method

We explain the physical model here, namely, the quantum Heisenberg model. It is widely known that this model can describe insulating magnets. The Hamiltonian is given by $\mathcal{H} = \sum_{\langle i,j \rangle} J_{ij} \boldsymbol{S}_i \cdot \boldsymbol{S}_j$ where $\boldsymbol{S}_i$ is a spin-S spin operator at spin site i. Each spin takes $2S + 1$ states; therefore, a state of the N-spin system can be described by an N-digit integer in the base-($2S + 1$) notation. The total Hilbert space is divided into subspaces characterized by the sum of the value in each digit from the reason that the sum corresponding to the z-component of the total spin (M) is conserved. Our diagonalization of the matrix is carried out within each of such subspaces. When J_{ij} is positive, interactions in the studied model are antiferromagnetic. The quantum nature of the case with negative J_{ij} generally is larger than in a ferromagnetic case. In antiferromagnets, from the point of view of physical interests, the case of the subspace with the largest dimension is much attracted among all the subspaces. However, the dimension increases exponentially with respect to N. The increase makes it difficult to study large systems, particularly by numerical diagonalizations. Here, we treat the $S = 1/2$ Heisenberg chain model under the periodic boundary condition.

Our numerical diagonalizations were carried out based on the Lanczos algorithm. Calculations using this algorithm provide us with the precise eigenvalue of the lowest-energy state. However, it is difficult to treat large systems within studies using this algorithm due to the fact that the dimensions of the matrices are extremely large. In order to treat systems with sizes that are as large as possible, under the circumstances, one of the present authors developed an MPI-parallelized code of numerical diagonalization using the Lanczos algorithm in the study of Haldane's gaps[2]. It is widely known that in an MPI-parallelized calculation, data transfer between the computational nodes becomes a bottleneck as a cause of delay. In the code of our group, a growth of cost concerning time owing to the data transfer is suppressed. Thus, our code makes us carry out efficient diagonalizations even in huge-scale parallel calculations. Our previous studies strongly suggest that our program can be carried out in large-scale parallelized calculations in various supercomputers. Note here that it is possible to realize efficient parallel calculations not only in the K computer[1] and Oakforest PACS (OFP)[3] but also in Fugaku. Note also that our code includes OpenMP directives to make it possible to carry out hybrid parallel calculations. When we challenge large-scale parallel calculations in a supercomputer like Fugaku, a computational job requires that $N_{\rm MPIP}$ is equal or larger than the number of nodes used in the job. Under the circumstances, the present study clarifies the behavior of jobs of the high MPI-parallelization.

We examine how large N_{MPIP} is in a single job that can be achieved. In particular, we focus on the memory consumption (MC) of such a job.

3. Results and discussions

Using the code explained above, we have challenged calculations of Lanczos diagonalization of $\mathcal{H}$ in a single job that consists of considerably large N_{MPIP}. We have successfully carried out the parallel calculations up to the case that N_{MPIP} is 2,097,152(= 2^{21}). Let us compare the behavior of the highly MPI-parallelized job with jobs that are carried out when N_{MPIP} is smaller. Figure 1(a) shows the case of $N = 45$ and $M = 1/2$ by changing N_{MPIP} when the number of MPI processes per node is fixed to be 16 and the number of threads is common to be three. Note here that the case $N = 45$ was able to be treated in K computer and OFP. One can observe a successful acceleration with respect to the elapsed time until N_{MPIP} is the largest. When N_{MPIP} is increased, on the other hand, the MC shows a nonmonotonic behavior. The MC decreases in the region where N_{MPIP} is small; on the other hand, in the region where N_{MPIP} is large, it increases contrary to our expectation. The upturn suggests the occurrence of MC, which is difficult for users to control in their source codes.

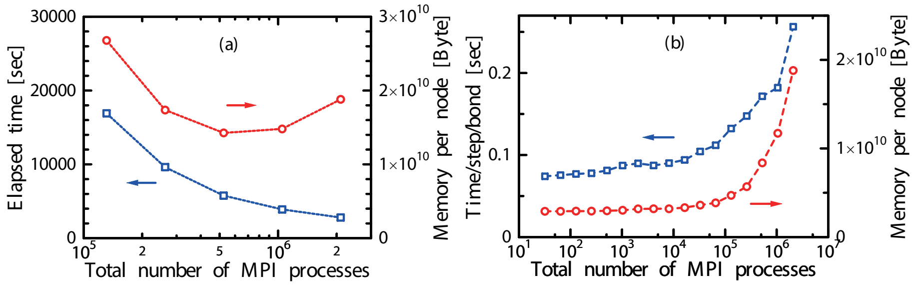

Figure 1: Parallel calculations of the eigenvalue problem for $\mathcal{H}$. (a) The target model is fixed to be $N = 45$ and $M = 1/2$. (b) N is varied under the condition that computational costs per node are maintained constant.

This study also examined another change when the treated sizes N are enlarged by the increase of N_{MPIP} while computational costs for time and memory are maintained constant. Results are depicted in Fig. 1(b). Let us observe the cases of changing N by changing N_{MPIP} under the condition that the number of MPI processes per node is fixed to be 16 and the number of threads is common to be three. Note that odd-N cases correspond to $M = 1/2$; on the other hand, an even-N cases correspond to $M = 0$. In the ideal situation for this change, the time for a single operation of $\mathcal{H}$ is proportional to the number of interaction bonds in the system. Thus, we plot the time per step per bond in Fig. 1(b). The results concerning the time show an increasing behavior; during N_{MPIP} is increased by multiplication of more than 60,000, the time per step per bond only increases by a factor of less than four. This suggests that the time per step per bond is almost constant during this change.

Let us, next, observe the MC during the change in Fig. 1(b). When N_{MPIP} is less than approximately 10^5, one finds almost constant MC. When N_{MPIP} is more than approximately 10^5, on the other hand, a significant increase of the MC occurs. The boundary in Fig. 1(b) between a region where the MC maintains and the region where it increases is consistent to the upturn in Fig. 1(a). We carried out parallel calculations in K computer and OFP; such a considerable increase of MC was not observed. It is difficult to compare the situations between the present results in Fugaku and those in K computer and OFP because jobs in K computer and OFP were carried out when N_{MPIP} were at most in the order of 10^4.

4. Conclusion and remarks

We have studied whether or not highly parallelized calculations can be carried out in Fugaku, using our code that was successfully used in K computer and OFP. We have successfully confirmed the acceleration in running of the practical code for the Heisenberg model up to the total number of MPI processes to be about two million. At present, we have achieved calculations of an eigenvalue problem with a very large matrix dimension in Fugaku to be $d = 18,252,025,766,941$ for $S = 1$, $N = 30$, and $M = 0$ in Ref.[4] and $d = 32,247,603,683,100$ for $S = 1/2$, $N = 48$, and $M = 0$ in Ref.[5]. In near future, we will challenge cases of even larger matrix dimensions in Fugaku. Our present information concerning jobs of large numbers of MPI processes contributes much to such a challenge.

Acknowledgement

This work was partly supported by JSPS KAKENHI Grant Numbers JP20K03866, JP20H05274, and JP23K11125. The computational resources of Fugaku were provided by RIKEN through the HPCI System Research projects (Project IDs: hp220043 and hp230114).

References

[1] H. Nakano, N. Todoroki, and T. Sakai: Haldane Gaps of Large-S Heisenberg Antiferromagnetic Chains and Asymptotic Behavior *J. Phys. Soc. Jpn.*, volume:91 (2019), 114702(1–4).

[2] H. Nakano, A. Terai: Reexamination of Finite-Lattice Extrapolation of Haldane Gaps, *J. Phys. Soc. Jpn.*, volume:78 (2009), 014003(1–9).

[3] H. Nakano and T. Sakai: Precise Estimation of the $S=2$ Haldane Gap by Numerical Diagonalization *J. Phys. Soc. Jpn.*, volume:91 (2018), 105002(1–2).

[4] H. Nakano, H. Tadano, N. Todoroki, and T. Sakai: The Haldane Gap of the $S = 1$ Heisenberg Antiferromagnetic Chain, *J. Phys. Soc. Jpn.*, volume:91 (2022), 074701(1–5).

[5] H. Nakano and T. Sakai: Large-Scale Numerical-Diagonalization Study of the Shastry-Sutherland Model, *JPS Conf. Proc.*, volume:38 (2023), 011166(1–6).

Estimating radiation source distribution from measured γ -ray energy spectra

Katsuhiko Yamaguchi[1*], Yuka Kumada[1], Taiyo Sato[1], Yuto Kondo[1], Kenji Suzuki[1],

Masaharu Matsumoto[2]

[1]Faculty of Symbiotic Systems Science, Fukushima University
[2] Information Technology Center, Fukushima University
*`yama@sss.fukushima-u.ac.jp`

Abstract. A machine learning algorithm was constructed to estimate the radiation source distribution by using the γ-ray energy spectrum around the radiation source. A large amount of spectral data obtained by simulation is used to train the neural network. We report that the estimation accuracy has improved dramatically by launching another neural network for machine learning that converts actual measurement data into simulation data.

Keywords: Machine learning, γ-ray, Radiation source distribution, Decommissioning

1. Introduction

In decommissioning and decontamination work, it is important to know the distribution of radioactive materials in advance in order to ensure safety and improve efficiency. However, it was difficult to identify the distribution from radiation dose data at remote locations. We have shown that this difficulty can be solved to some extent by machine learning using the γ-ray energy spectrum around the radiation source as input data [1]. At that time, the data for training the neural network in advance was generated by simulation. However, until now, inputting actually measured γ-ray energy spectrum data to the neural network after training has not improved the accuracy of radiation source distribution estimation. This is probably due to the difference in shape between the simulated spectrum and the measured spectrum. Therefore, in this research, we constructed another machine learning algorithm that learns the correspondence between the measured spectrum and the simulated spectrum, and decided to use the 1st neural network after learning as a filter to convert the measured spectrum to the simulated spectrum.

2. Method

4 x 4 meshes were placed on a two-dimensional plane with 7 cm x 7 cm squares per mesh to match the dimensions of the actual NaI spectrometer. Patterns in which multiple ^{137}Cs and ^{60}Co are arranged were set. A NaI spectrometer was placed 1 cm above a two-dimensional plane to measure the γ-ray energy spectrum on each mesh, and the spectra were also simulated using a particle transport Monte Carlo code (PHITS) for the same arrangement [2]. The 1st neural network was trained using the measured spectrum as input data and the simulated spectrum as answer data. After training, the 1st neural network was input with measured spectra for patterns not used during training, and the converted output spectra were compared with the simulated spectra. These converted spectra were input to the 2nd neural network for estimating the radiation source distribution, and the loss function was obtained from the difference from the original arrangement.

3. Results and Discussion

Consider a pattern in which two ^{137}Cs (red) and one ^{60}Co (green) are arranged as shown in Fig. 1(a). Figure 1(b) shows the γ-ray spectrum actually measured above the ^{60}Co (①) using a NaI spectrometer. This measurement data is input to the first neural network and converted as shown in Fig. 1 (c). It can be seen that the converted spectrum corresponds well with the spectrum calculated by PHITS shown in Fig. 1(d). Figure 2 shows the result of 2nd neural network estimation for the arrangement pattern in Fig. 1. The correct answer is the original. Only PHITS simulation data is used for 2nd neural network training. When simulation data is input to this trained neural network and the arrangement pattern is estimated, the loss function is 6.54×10^{-7}, indicating high estimation accuracy. However, when estimated from spectral data obtained by measurement, the loss function is 1.06, which is a significant drop in accuracy. Looking at the estimated position of the ^{137}Cs distribution, we can see that the accuracy is low because it is estimated that the ^{137}Cs is placed in the position where the ^{60}Co position and the radiation source are not placed. If we convert the spectral data measured by a 1st neural network and use that data for estimation, we can see that the accuracy is greatly improved to the loss function 7.83×10^{-6}. As shown in this study, the accuracy is improved by transforming the measured data so that it corresponds to the simulated data and then using it as the input data for the estimation algorithm. This method would be expected to be used for various other estimation techniques.

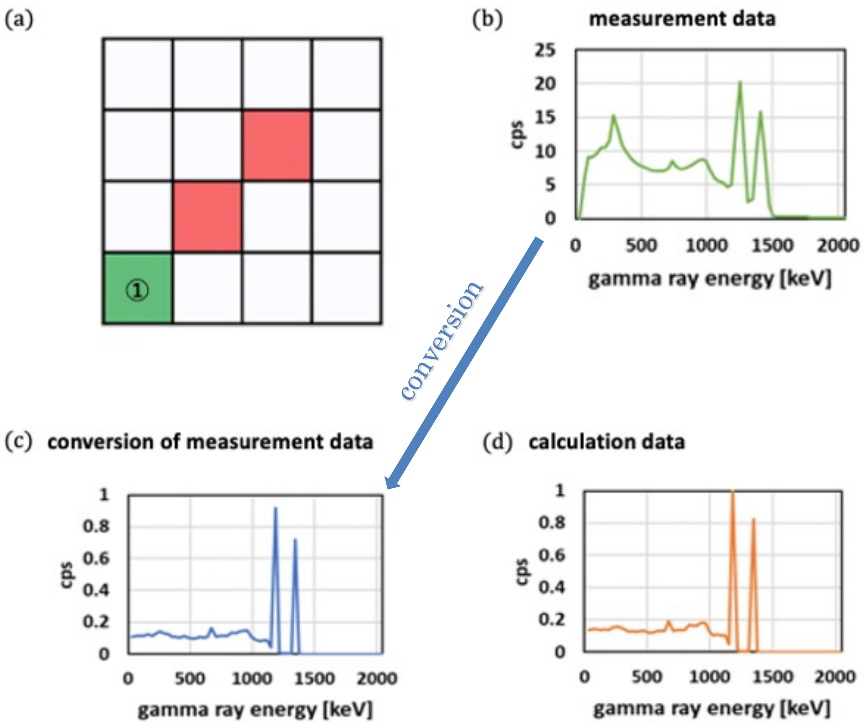

Fig.1 (a) A model in which two ^{137}Cs (red) and one ^{60}Co (green) are arranged. At position ①, γ-ray energy spectrum is measured. (b) γ-ray energy spectrum actually measured using a NaI spectrometer for the configuration in (a). (c) γ-ray energy spectrum data converted by inputting the spectrum shown in (b) into the first neural network. (d) γ-ray energy spectrum data simulated using PHITS for the configuration in (a). The spectrum in (c) agrees well with the simulation data.

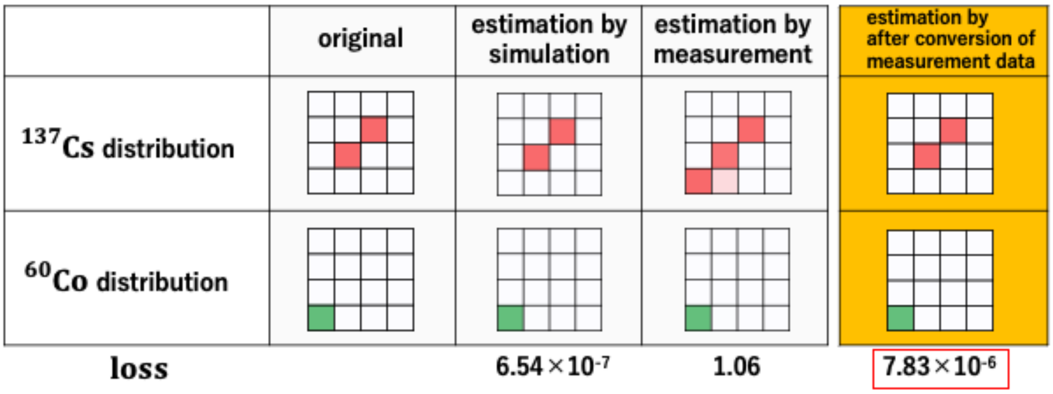

	original	estimation by simulation	estimation by measurement	estimation by after conversion of measurement data
^{137}Cs distribution				
^{60}Co distribution				
loss		6.54×10^{-7}	1.06	7.83×10^{-6}

Fig.2. Estimation results by machine learning when multiple nuclides are arranged on a two-dimensional plane. For the pattern with two ^{137}Cs (red) and one ^{60}Co (green) shown in the original, the estimation result from the simulation data (loss function L=6.54×10^{-7}) and the estimation result obtained from the measurement data (L=1.06) and the estimated result (L=7.83×10^{-6}) using the spectrum transformed from the measured data to fit the simulated data. Only simulation data is used for all pre-learning.

References

[1] T. Uemura, K Yamaguchi: Estimation of radiation source distribution using machine learning with γ ray energy spectra, *Journal of Advanced Simulation in Science and Engineering,* 7/1, pp71-81. (DOI) 10.15748/jasse.7.71.

[2] T. Sato, Y. Iwamoto, S. Hashimoto, T. Ogawa, T. Furuta, S. Abe, T. Kai, P. E. Tsai, N. Matsuda, H. Iwase, N. Shigyo, L. Sihver, K. Niita, Features of Particle and Heavy Ion Transport code System (PHITS) version 3.02, *Journal of Nuclear Science and Technology.* **55** (2018) 684-690.

Improvement of Efficiency of Simulation for Mobile Communication Networks

Kazuyuki Miyakita[1*], Naoyuki Karasawa[2], Keisuke Nakano[1]

[1]Niigata University

[2]Kaishi Professional University

*kmiyakita@ie.niigata-u.ac.jp, karasawa.naoyuki@kaishi-pu.ac.jp,
nakano@ie.niigata-u.ac.jp

Abstract. Simulation is often used to evaluate mobile multi-hop wireless networks. Simulation can be classified into time-driven simulation and event-driven simulation, depending on the timing for observing the states of the network. In this paper, we investigate the methods for improving the efficiency of simulation in the performance evaluation of mobile multi-hop wireless networks using simulation, and in particular, we propose methods for improving the efficiency of event-driven simulation.

Keywords: Mobile communication networks, Simulation, Efficiency improvement

1. Introduction

Simulation is one of the methods used to evaluate the performance of mobile multi-hop wireless networks [1,2], which are one of the methods of communication in disaster situations where communication infrastructure cannot be used. In simulation, node movements and processes of each communication layer are modelled, and communication characteristics such as throughput, packet loss rate, delay time, and mean length of a communication path are evaluated.

Simulation can be classified into time-driven simulation and event-driven simulation, depending on the timing for observing the states of the network [3]. Time-driven simulation is a method where the network state is updated every short constant time interval Δt and only each state is observed. In this simulation, if we use smaller Δt, we can observe more detailed network state and can obtain more accurate performance. However, a small Δt causes a long simulation time.

On the other hand, event-driven simulation updates the system state only at times when the network state changes, such as when the network topology changes or packets are transmitted. In this type of simulation, the possible times of occurrence of events are predicted in advance, and the network state is updated each time these events occur. In other words, there is no need to update the network state at times when no events are occurring. However, if there are too many events to observe, the simulation will take a long time.

Although the suitability of each type of simulation depends on the evaluation metric, if there are many different types of network parameters, or if the range of each parameter is large, the time required for simulation is enormous, regardless of the type of simulation used. Therefore, improving the efficiency of simulation is one of the most important issues in performance evaluation using simulation. In this paper, methods for improving the efficiency of simulation in performance evaluation of mobile multi-hop wireless networks using simulation are investigated and, in particular, a method for improving the efficiency of event-driven simulation is proposed.

2. Accuracy of time-driven simulation

First, as a basic evaluation of the time-driven simulation, we evaluate the accuracy of the time-driven simulation. In this paper, we refer to the time-driven and event-driven simulations as Method 1 and Method 2, respectively.

To do this, we consider a two-dimensional square service area of $[0, L] \times [0, L]$. There are N mobile nodes in the area, and these mobile nodes move according to a random waypoint model. Namely, a mobile node moves linearly at a constant speed v to a destination in the area, and as soon as it arrives at the destination, it randomly determines a new destination in the area and moves to the new destination. A Fixed source node S and a fixed destination node D are located in this area at (L/3, L/2) and (2L/3, L/2), respectively, and information is sent from S to D via a multi-hop path consisting of mobile nodes. The communication range of all nodes is r. Considering any two nodes, we call the link connection when the distance between these nodes decreases from a state greater than r to less than r, and we call the link disconnection when the distance between the two nodes decreases from less than r to greater than r. We consider the following two evaluation metrics.

- $E(T_{on})$: Mean time from the appearance of a multi-hop path between S and D to the disappearance of the multi-hop path between S and D.
- $E(T_{off})$: Mean time from the disappearance of a multi-hop path between S and D to the appearance of a new multi-hop path between S and D.

In Method 1, we observe whether there is a multi-hop path between S and D at every Δt and compute $E(T_{on})$ and $E(T_{off})$. In Method 2, we only observe the states when a link connection or a link disconnection occurs at any pair of two nodes, because other events do not affect $E(T_{on})$ and $E(T_{off})$. To do this, in Method 2, based on the current location and destination of each node, we compute the times at which link connections and disconnections occur in advance and observe whether there is a multi-hop path between S and D only at the times at which these events occur. Note that we can obtain the exact values of $E(T_{on})$ and $E(T_{off})$ using Method 2.

Figure 1 shows the simulation results of $E(T_{on})$ and $E(T_{off})$ for L = 150 m, r = 10 m, v = 1 m/s, and N = 200. We can see that as Δt increases, the accuracy of $E(T_{on})$ and $E(T_{off})$ for Method 1 becomes low. This is because if Δt is large, then the change in the observed state is also large, and the appearance and disappearance of multi-hop paths connecting S and D that occur during Δt may be missed.

3. Methods for improving the efficiency of event-driven simulation

Next, we propose methods to improve the efficiency of Method 2, which is an event-driven simulation. These methods omit the observation of some events that do not affect $E(T_{on})$ and $E(T_{off})$. Specifically, we propose the following four methods.

- Method 2-1: We omit observing the network state in the events of link connection that occurs when there is a multi-hop path between S and D, and link disconnection that occurs when there is no multi-hop path between S and D, because these events do not affect $E(T_{on})$ and $E(T_{off})$ obviously.
- Method 2-2: A multi-hop path between S and D exists only if there is at least one node in each of the communication ranges of S and D. Therefore, in Method 2-2, we omit observing the state in the events of the link connections and disconnections that occur during the time when there is no node in the communication range of S or that of D.
- Method 2-3: Consider three nodes n_1, n_2, and n_3 and suppose that n_3 is within both communication ranges of n_1 and n_2. In this case, the link connection and disconnection between n_1 and n_2 does not affect $E(T_{on})$ and $E(T_{off})$ because n_1 and n_2 are connected via a multi-hop path through n_3. Therefore, in Method 2-3, we omit observing the state in the events of the link connection and disconnection for such a case. Note that in Method 2-3, the observation of such events is omitted whether or not there is a multi-hop path between S and D, unlike in Method 2-1.
- Method 2-all: We apply all of Methods 2-1, 2-2, and 2-3 simultaneously.

Figure 2 shows the number of observations of the states for the four proposed methods, where the simulation time is 1000 s. For comparison, Fig. 2 also shows the results of Method 1 with $\Delta t = 0.05$ s, which means that the error between $E(T_{on})$ and $E(T_{off})$ is about 0.1% from Fig. 1, and those of Method 2. The results show that all the proposed methods are effective as they reduce the number of observations compared to Method 2. In particular, Method 2-1 is effective when there are few nodes, and Method 2-3 is effective when there are many nodes, while Method 2-2 is effective regardless of the number of nodes. In addition, Method 2-all significantly reduces the number of observations.

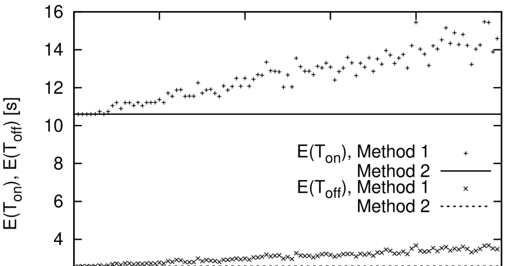

Figure 1: Accuracy of $E(T_{on})$ and $E(T_{off})$ for Methods 1 and 2.

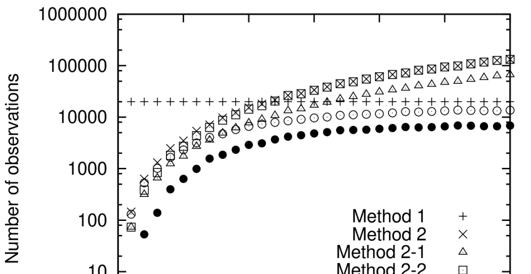

Figure 2: Number of observations.

References

[1] C.E.Perkins, Ad hoc Networking, *Addison-Wesley*, 2001.

[2] K. Nakano, K. Miyakita, et al., “Analysis and Relative Evaluation of Connectivity of a Mobile Multi-hop Networks,” *IEICE Trans. Commun.*, vol.E91-B, no.6, June 2008.

[3] S. Robinson, Simulation: The Practice of Model Development and Use, *John Wiley and Sons*, 2004.

Evaluation of Virtual Accumulation and Reaccumulation by Information Floating in a Crossroad Network

Keisuke Nakano[1*], Yuhei Nemoto[1], Kazuyuki Miyakita[1], Naoyuki Karasawa[2],
Hiroshi Tamura[3]

[1]Niigata University
[2]Kaishi Professional University
[3]Chuo University
*`nakano@ie.niigata-u.ac.jp`, `f23c031d@mail.cc.niigata-u.ac.jp`,
`kmiyakita@ie.niigata-u.ac.jp`, `karasawa.naoyuki@kaishi-pu.ac.jp`,
`tamura@elect.chuo-u.ac.jp`

Abstract. Information Floating (IF) is a method of delivering information to mobile nodes in target areas preventing unnecessary transmissions by permitting mobile nodes to transmit data via wireless direct links only in Transmittable Areas (TAs). IF can virtually accumulate data by making mobile nodes transmit multiple different data in the same TAs. In addition, the cooperation of multiple TAs reaccumulates temporarily lost data. In a past research, the performance characterization of virtual accumulation and reaccumulation by IF in a one-dimensional network has been done. In this paper, we consider a crossroad network as a more complicated network model and evaluate the performance of virtual accumulation and reaccumulation in the crossroad network.

Keywords: Information floating, Data accumulation, Reaccumulation, Crossroad

1. Introduction

In Delay Tolerant Networks (DTNs), mobile nodes can deliver information to mobile nodes in a target area in an epidemic manner utilizing wireless direct communication and the movement of nodes having information [1]. This epidemic information delivery causes unnecessary transmissions from mobile nodes in nontarget areas. To overcome this problem, various methods have been proposed [1]. Information Floating (IF) is one of these methods [1]-[6].

In IF, a mobile node transmits data only in a designated area called a Transmittable Area (TA). It is assumed that each mobile node can grasp its position using a positioning method, such as GPS, and that a mobile node receiving data in IF receives the location of the TA together with the data. These assumptions enable a mobile node to transmit data only in a TA to prevent unnecessary transmissions. A mobile node that receives data for IF transmits the data to other mobile nodes while it is in the TA. This process is repeated and the data appear to float in and around the TA.

While IF was originally considered as a method for dissemination of a single message, it has demonstrated the ability to virtually accumulate multiple data and disseminate the accumulated data [5]. The virtual accumulation is realized simply by letting mobile nodes transmit multiple data in the same TA. Suppose that each mobile node generates new data in real time and, in a TA, transmits the data generated by itself together with other data received from other nodes. The multiple data generated by the mobile nodes are then received by mobile nodes in and around the TA; this process seems to accumulate the multiple data into one place. We therefore call this process virtual accumulation.

As discussed in [5], the number of TAs is not always one and multiple TAs in different places are possible. As an interesting example of cooperation between multiple TAs, let us consider the virtual accumulation in two TAs (TA1 and TA2) on a road along which mobile nodes pass. Suppose that IF ends in TA2 and all data virtually accumulated in TA2 disappear from TA2. In this case, the data that disappeared from TA2 are carried from TA2 to TA1 by mobile nodes that received the data in TA2 before the end of IF, are accumulated in TA1, are carried backward by mobile nodes moving from TA1 to TA2, and are again accumulated in TA2. Namely, in the virtual accumulation with the two TAs, recovery of the lost data in a TA caused by the end of IF, namely reaccumulation, is possible [5].

In [6], the performance characterization of virtual accumulation and reaccumulation by IF in a one-dimensional network has been done. In this paper, we consider a crossroad network as a more complicated network model and evaluate the performance of virtual accumulation and reaccumulation in the crossroad network.

2. Definitions and assumptions

We consider a crossroad network model as shown in Fig. 1. Mobile nodes enter the crossroad network from four directions. Assume that the distribution of nodes from each of the four directions obeys a Poisson process with intensity λ. The velocity of each node is constant v. When a node arrives at the intersection, it goes straight, turns right, or turns left with probability 1/3.

There are four TAs in the crossroad. The length of each TA is quite small (ideally zero), as in [6]. The distance between each TA and the intersection is $d/2$, i.e. the distance between two TAs along the road is d. For simplicity, assume that only the nodes entering TA2 from the left direction generate the new data to be accumulated. A node having data transmits the data to other nodes within the communication range of the node only when the node is in a TA. The communication range of each node is constant r.

3. Simulation results and discussions

In Fig. 2, we show the simulation results of the amount of data accumulated in TA2, namely $|D(\mathrm{TA2}, t)|$. Figure 2 also shows $|G(t)|$ and $|D(\mathrm{SA}, t)|$, where $G(t)$ is the set of all generated data by time t and $D(\mathrm{SA}, t)$ is the set of data carried by the nodes in the service area at time t. Note that the data of $G(t)$ not included in $D(\mathrm{SA}, t)$ are the lost data that completely disappeared from the service area and can never be reaccumulated in TA2 after t. The parameters used in the simulation are as follows: $\lambda = 0.007\ \mathrm{m}^{-1}$, $v = 36$ km/h, $d = 2000$ m, and $r = 100$ m.

From Fig. 2, we can see that the data accumulation has been done to some extent when $\lambda = 0.007\ \mathrm{m}^{-1}$. However, some data are lost from the service area because $|D(\mathrm{SA}, t)| < |G(t)|$. For comparison, we also show the simulation results of $|D(\mathrm{TA2}, t)|$, $|D(\mathrm{SA}, t)|$, and $|G(t)|$ for a one-dimensional road model [6], where $\lambda = 0.007\ \mathrm{m}^{-1}$, $v = 36$ km/h, $d = 2000$ m, and $r =$

100 m, in Fig. 3. Comparing Figs. 2 and 3, a crossroad model can accumulate more data than a one-dimensional model. The reason for this is as follows. In a one-dimensional network, if IF ends in TA2, then the reaccumulation of the lost data in TA2 requires a support of the accumulation in only one TA, namely TA1, as mentioned. On the other hand, in a crossroad network, there are three TAs, namely TA1, TA3, and TA4, which can support the reaccumulation of the lost data in TA2.

Next, we show the relation between the accumulation performance and the density of nodes. To do this, we use a metric e_1, which is defined as follows [6]:

$$e_1 = \frac{1}{N_S}\sum_{i=1}^{N_S} \frac{|G_i(\tau_e)| - |D_i(SA,\tau_e)|}{|G_i(\tau_e)|}, \qquad (1)$$

where N_S is the number of simulations for a value of λ, τ_e is the time of the end of a simulation, and $D_i(\mathrm{SA}, \tau_e)$ and $G_i(\tau_e)$ are $D(\mathrm{SA}, \tau_e)$ and $G(\tau_e)$ in the i-th simulation, respectively. e_1 is the ratio of the amount of data that disappear from the service area to the total amount of generated data. Figure 4 shows the results of e_1 for a crossroad and a one-dimensional network, where v = 36 km/h, d = 2000 m, r = 100 m, N_S = 10, and τ_e = 6000 s. From this figure, we can see that the performance of accumulation and reaccumulation of a crossroad network is higher than that of a one-dimensional network, as mentioned.

However, if we focus on the boundary density of nodes with sufficiently high accumulation and reaccumulation performance (i.e., e_1 is sufficiently small), the boundary densities for both the crossroad and one-dimensional cases are not so different. Figure 4 also includes the numerical results of Pr($E1$'), which was theoretically analyzed in [6]. For one-dimensional networks, we can estimate the border density as the density where Pr($E1$') is very small. For example, if we find the value of λ that satisfies Pr($E1$') = 0.0005, we obtain $\lambda = 0.0217$ m^{-1}. From Fig. 4, we can confirm that the accumulation and reaccumulation work well when $\lambda >$ 0.0217 m^{-1} for both the crossroad and one-dimensional cases. From this result, we can estimate the boundary density for a crossroad network by using the theoretical result for a one-dimensional network derived in [6]. Note that it is considered that we have such a tendency because we assume the uniform density of nodes in the network. The analysis and discussion for the case of uneven node density is our future work.

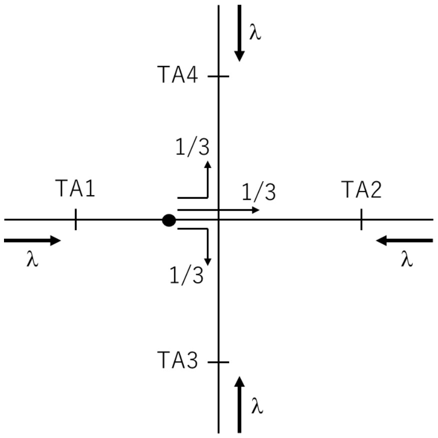

Figure 1: Crossroad network model.

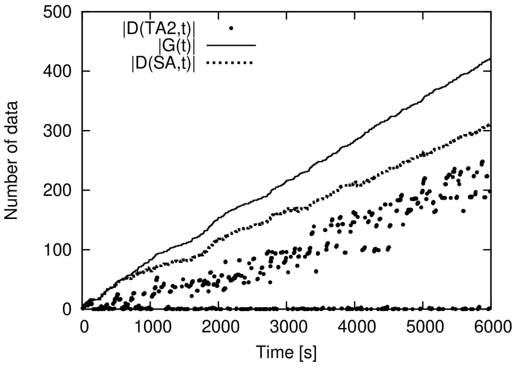

Figure 2: Number of accumulated data for a crossroad network, where $\lambda = 0.007$ m^{-1}.

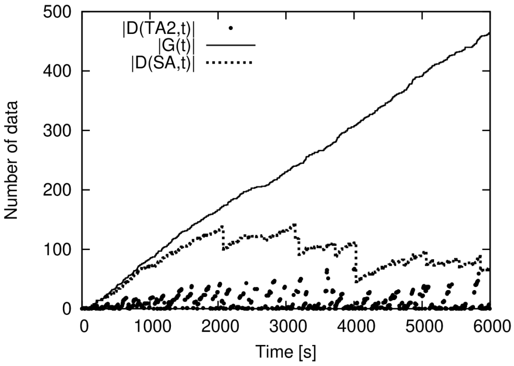

Figure 3: Number of accumulated data for a one-dimensional network, where $\lambda = 0.007$ m^{-1}.

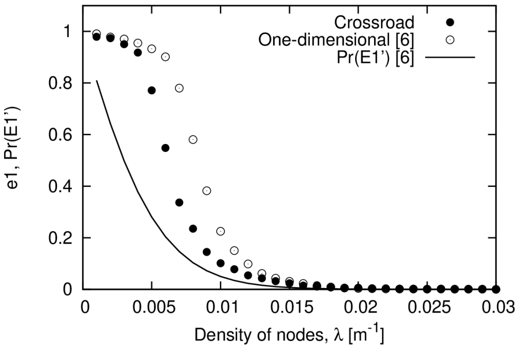

Figure 4: Simulation results of e_1.

References

[1] K. Nakano, “Epidemic Communication, Information Floating and Safety/Security,” *IEICE Fundamentals Review*, vol. 10, no. 4, pp.282–292, April 2017. (in Japanese)

[2] A. V. Castro, G. Di Marzo Serugendo, et al., “Hovering Information - Self-organising Information that Finds its Own Storage,” *Technical Report, School of Computer Science and Information Systems, Birkbeck College, London, UK*, BBKCS-07-07, 2007.

[3] K. Nakano, K. Miyakita, “Information Floating on a Road with Different Traffic Volumes Between Opposite Lanes,” *Journal of Advanced Simulation in Science and Engineering*, vol. 3, no. 1, pp. 97–113, Aug. 2016.

[4] K. Miyakita, N. Karasawa, Y. Inagawa, K. Nakano, “A Consideration on Traffic Guidance by Information Floating,” *IEICE Transactions on Communications (Japanese Edition)*, vol. J101-B, no.8, pp. 603–618, Aug. 2018. (in Japanese)

[5] N. Karasawa, K. Miyakita, Y. Inagawa, K. Kobayashi, H. Tamura, and K. Nakano, “Information Floating for Sensor Networking to Provide Available Routes in Disaster Situations,” *IEICE Transactions on Communications*, vol. E103-B, no. 4, pp. 321-334, Apr. 2020.

[6] K. Miyakita, H. Tamura, K. Nakano, “Performance Characterization of Virtual Accumulation and Reaccumulation by Information Floating,” *Transaction of the Japan Society for Simulation Technology*, vol.14, no.2, pp.104–113, Oct. 2022. (in Japanese)

Beam-steering in 4x4element 2port circular polarized antenna at 300 GHz-band

Seiji Nishi[1*], Kazuhiko Tamesue [1], Toshio Sato [1], San Hlaing Myint[1], Takuro Sato[1],

Tetsuya Kawanishi[2]

[1]Waseda Research Institute for Science and Engineering, Waseda University

[2] Faculty of Science and Engineering, Waseda University

*s.nishi3@kurenai.waseda.jp

Abstract. A 300 GHz-band 4x4 element 2-port right-handed circularly polarized antenna with dielectric substrate was developed. The design was done using an electromagnetic simulator, HFSS from Ansys. The antenna gains of 13 dBi were obtained for each port, which is consistent with the simulation results. When the two ports are used in-phase, the antenna gain increases by 3 dB to 16 dBi. The radiation patterns when the phase is changed in two ports were calculated by MATLAB using the radiation pattern of the one-element antenna calculated by HFSS. The beam angle that can be swung over a range of 6 dB decrease in antenna gain is ±23°, covering 46°.

Keywords: 300 GHz-band, circular polarized antenna, beam-steering

1. Introduction

The 300 GHz band is expected for applications in communications above 100 Gb/s [1], [2]. Antennas on dielectric substrates are considered to have good connectivity with RF sections. Circularly polarized waves are suitable for high-capacity communications because they can be multiplexed by polarization. We have developed a 300-GHz 4x4 element 2-port circular polarized antenna on a dielectric substrate [3]. The 2-port antenna is designed for power combining and beam steering.

The antenna design was based on Ansys HFSS. For beam steering, the radiation pattern of one element antenna obtained by HFSS was used to calculate the array factor in MATLAB and the radiation pattern were calculated when the phase is changed.

2. Antenna structure

Figure 1 shows the antenna structure and substrate configuration. 300 GHz band is a short wavelength and the substrate thickness is as thin as 50 μm. The wavelength is also short (about 1 mm), and the glass cloth in the dielectric substrate may appear discontinuous in the transmission line. Therefore, we considered using bonding film as a substrate. The antenna structure is a right-handed circularly polarized patch antenna with a strip line as the transmission line, and the transmission line and the patch antenna are coupled through a slot in the two-layer metal.

In the case of HFSS, the structure shown in Figure 1 can be calculated if the dielectric properties, relative permittivity and tanδ, are known.

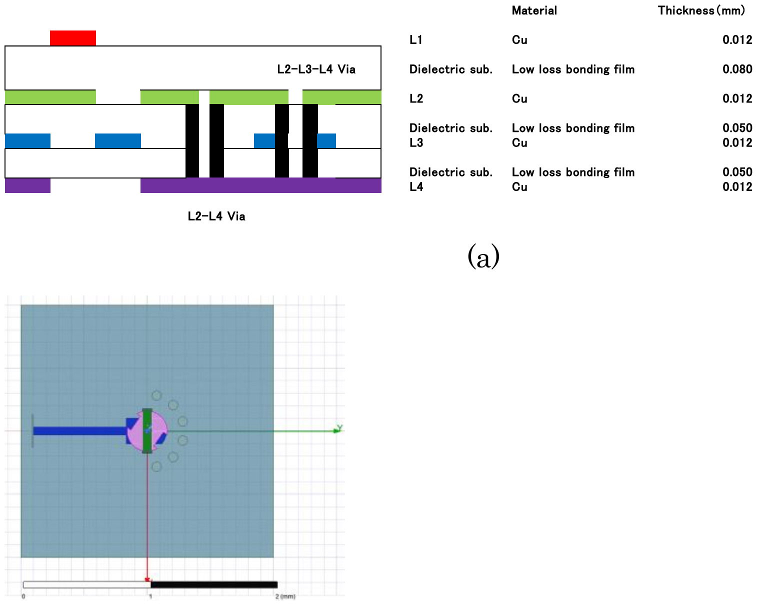

	Material	Thickness (mm)
L1	Cu	0.012
Dielectric sub.	Low loss bonding film	0.080
L2	Cu	0.012
Dielectric sub.	Low loss bonding film	0.050
L3	Cu	0.012
Dielectric sub.	Low loss bonding film	0.050
L4	Cu	0.012

(a)

(b)

Figure 1. Layer structure (a) and antenna structure (b) [3].

3. Prototype 4x4 element 2-port antenna

Figure 2 shows the pattern of the prototype 4x4 element 2-port antenna. The element spacing is 0.65λ in the x-direction and 0.75λ in the y-direction, where λ is the free-space wavelength at 287 GHz. The antenna consists of four 2x2-element subarrays, which are connected by double sequential connections to improve circular polarization characteristics [4]. 2-port design allows RF power synthesis and beam steering by controlling the phase. Back view of 4x4 element 2-port antenna is shown in Figure 3. The spacing of the waveguide ports in Figure 2 is very narrow, and in Figure 3 it can be seen that they can be connected with standard waveguide flanges spread out in a waveguide circuit.

Antenna gains of 13 dBi were obtained at each port, in good agreement with the calculations by HFSS [3]. The loss in the strip line of the antenna is expected to be 1.3dB for a strip line length of 3.76mm. If the two ports are used in-phase, a combined antenna gain of 16dBi is obtained.

The radiation pattern with the phase difference between the two ports controlled can be obtained by calculating the array factor in MATLAB using the radiation pattern of the one-element antenna calculated in HFSS.

Figure 4 shows the radiation pattern calculated in MATLAB when the phase of the two ports is changed. Figure 5 shows the relation between tilt angle and gain. The angle covered by a decrease of up to 6 dB from the peak is 46° with ±23°. The phase difference, $\emptyset$, and tilt angle, θ, can be expressed by the following relationship,

$$\emptyset = 1.3 * 360 * \sin\theta \tag{1}$$

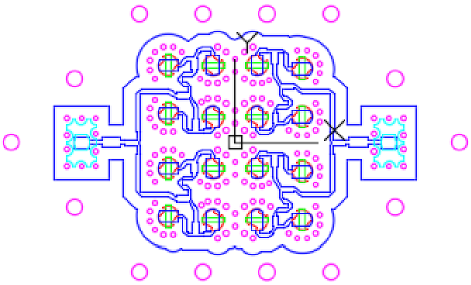

Figure 2. Pattern of 4x4 element 2-port antenna [3].

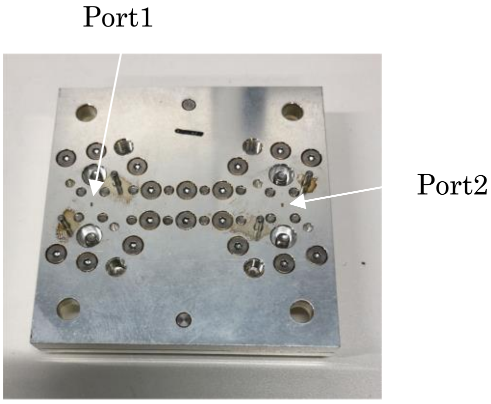

Figure 3. Back view of 4x4 element antenna [3].

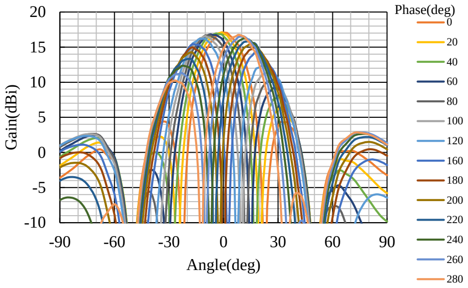

Figure 4. Radiation pattern when phase shifted between two ports.

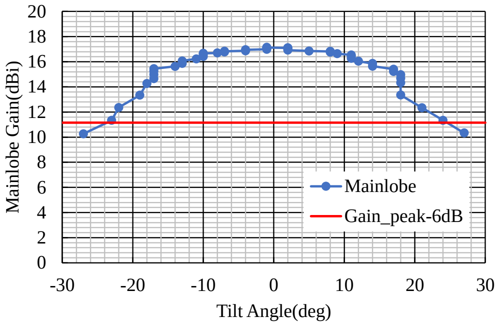

Figure 5. Relation between tilt angle and gain of main lobe.

5. Conclusion

A 300 GHz-band 4x4 element 2-port right-handed circularly polarized antenna with dielectric substrate was developed. The antenna gains of 13 dBi were obtained for each port, which is consistent with the simulation results. When the two ports are used in-phase, the antenna gain increases by 3 dB to 16 dBi. The radiation patterns when the phase is changed in two ports were calculated by MatLab using the radiation pattern of the one-element antenna calculated by HFSS. The beam angle that can be swung over a range of 6 dB decrease in antenna gain is ±23°, covering 46°. The calculations confirm that the proposed 4x4 element 2-port element structure is capable of beam scanning over an angular range of 46°.

ACKNOWLEDGMENT

This paper contains the results of a research project commissioned by the National Institute of

Information and Communications Technology (NICT), "Beyond 5G Research and Development Promotion Project", which is a research and development of wireless communication technology for realizing Beyond 5G ultra-high-speed and large-capacity communication using the terahertz band (task number 003).

References

[1] H. Hamada, T. Tsutsumi, H. Matsuzaki, T. Fujimura, I. Abdo A. Shirane, K. Okada, G. Itami H. Song H. Sugiyama, H. Nosaka: *300-GHz-Band 120-Gb/s Wireless Front-End Based on InP-HEMT Pas and Mixers, IEEE Jour. of Solid-State Circuits,* vol. 55, 2020, pp. 2316-2335

[2] D. Warana, L. John, B. Schoch, S. Wagner, I. Kallfass: *Sensitivity Analysis of a 280-312 GHz Superheterodyne Terahertz Link Targeting IEEE802.15.3d Applications,* IEEE Trans. Terahertz Science and Tech., vol. 12, 2022, pp. 325-333.

[3] S. Nishi, K. Tamesue, T. Sato, S. H. Myint, T. Sato, T. Kawanishi: *Bonding Film Based 280 GHz Circulary Polarized Antenna Array design,* IEEE WAMICON, 2023, pp. 33-36.

[4] S. Nishi, K. Tamesue, T. Sato, S. H. Myint, T. Sato, T. Kawanishi: *280 GHz Circular Polarized 4x4 Elements Antenna Array,* IEEE MAPE, 2022, pp. 132-136.

JSST 2023

Numerical analysis of nonlinear circuits with non-polynomial nonlinearity using Haar wavelet transform

Haruto Shitanaka[1] and Seiichiro Moro[1,*]

[1]Department of Electrical and Electronics Engineering, Faculty of Engineering, University of Fukui

*moro@u-fukui.ac.jp

The full paper of this paper has been published in Journal of Advanced Simulation in Science and Engineering (JASSE).

DOI: `https://doi.org/10.15748/jasse.11.116`

The Representation of p-adic Fourier Transform of a Locally Constant Test Function

Munehiro Kobayashi[1] and Toshio Suzuki[2,*]

[1]Schilf Institute Co., Ltd.
[2]Faculty of Science Division I, Tokyo University of Science

*`tosuzuki@rs.tus.ac.jp`

Abstract. p-adic numbers have applications in several areas of mathematics and physics. In this study, we consider the p-adic Fourier transform of the test function with compact support. We can obtain the matrix representation of the p-adic Fourier transform and this allows the Fourier transform to be computed efficiently.

Keywords: p-adic number, p-adic Fourier transform, locally constant

1. Introduction

Let p be a prime number. Every non-zero $x \in \mathbf{Q}$ can be represented by $x = p^{\mathrm{val}(x)} m/n$, where $m, n \in \mathbf{Z}$ are not divisible by p and val(x) is a unique integer. Then the p-adic norm of $x(\neq 0)$ is given by $|x|_p = p^{-\mathrm{val}(x)}$ and $|0|_p = 0$. The field of real numbers $\mathbf{R}$ is defined by the completion of the field of rational numbers $\mathbf{Q}$ with respect to Euclidean metric determined by the absolute value $|\cdot|$. On the other hand, the p-adic field $\mathbf{Q}_p$ is obtained by completing the field of rational numbers with respect to the p-adic norm. Every non-zero p-adic number $x \in \mathbf{Q}_p$ such that $|x|_p = p^{-\mathrm{val}(x)}$ can be uniquely represented in the canonical form

$$x = p^{\mathrm{val}(x)}(x_0 + x_1 p + x_2 p^2 + \cdots),$$

where $0 \leq x_k \leq p-1$, $x_0 \neq 0$. For $\gamma \in \mathbf{Z}$, the sphere S_γ and the ball B_γ with radius p^γ and centered on $a \in \mathbf{Q}_p$ are defined as

$$S_\gamma(a) = \{x \in \mathbf{Q}_p \mid |x-a|_p = p^\gamma\}, \quad B_\gamma(a) = \{x \in \mathbf{Q}_p \mid |x-a|_p \leq p^\gamma\}.$$

If $a = 0$, then we write $S_\gamma(0) = S_\gamma$, $B_\gamma(0) = B_\gamma$. For the p-adic number x, $\{x\}_p$ denotes the fractional part of the p-adic number $x \in \mathbf{Q}_p$, that is,

$$\{x\}_p = \begin{cases} 0 & \text{if } x \in B_0, \\ p^{\mathrm{val}(x)} \displaystyle\sum_{j=0}^{|\mathrm{val}(x)|-1} x_j p^j & \text{if } x \notin B_0. \end{cases}$$

The p-adic field is a field primarily used in number theory, but in recent years, it has been expected to find applications in various fields, including the time-frequency analysis [1, 2]. In this study, we give the p-adic Fourier transform of functions satisfying certain conditions and give another representation.

2. The p-adic Fourier Transform

A complex valued function on $\mathbf{Q}_p$ is called locally constant if for any $x \in \mathbf{Q}_p$ there exists $l \in \mathbf{Z}$ such that,

$$f(x + x') = f(x) \quad \text{for} \quad |x'|_p \leq p^l.$$

We call the largest number $l = l(f) \in \mathbf{Z}$ the parameter of constancy of a function f. A locally constant function with compact support is called a test function. We denote by $\mathcal{D}_N^l$ the set of locally constant functions with the parameter of constancy l and with support in B_N (see [3]).
For $f \in \mathcal{D}_N^l$, we define the Fourier transform as

$$\hat{f}(\xi) = \int_{\mathbf{Q}_p} f(x)\chi_p(x\xi)\,dx \tag{1}$$

where χ_p is an additive character on $\mathbf{Q}_p$, that is, $\chi_p(x) = \exp(2\pi i\{x\}_p)$. If $f \in \mathcal{D}_N^l$ is a function depending only the p-adic norm $|x|_p$, that is, $f(x) = f(p^{\mathrm{val}(x)})$, then its Fourier transform can be calculated as

$$\hat{f}(\xi) = \int_{\mathbf{Q}_p} f(x)\chi_p(x\xi)\,dx = \sum_{\gamma\in\mathbf{Z}} f(p^\gamma)\lambda(\xi,\gamma)$$

where $\lambda(\xi,\gamma) = \int_{S_{-\gamma}} \chi_p(x\xi)\,dx$ and we can obtain the Fourier transform $\hat{f}$ as the summation of f and λ. From this formula, we have that the Fourier transform of the function which depends only the norm becomes the function which depends only the norm.

3. The Fourier Transform of a Test Function

Let Ω be the characteristic function of B_0 and $\Pi(x) = \Omega(x) - \Omega(px)$. That is, Π is the characteristic function of S_0. For integers $0 \leq N < l$, we define the function $f \in \mathcal{D}_{-N}^{-l-1}$ depending only the norm as

$$f(x) = \sum_{N\leq\gamma\leq l} a_\gamma \Pi(p^{-\gamma}x).$$

It is known that

$$\lambda(\xi,\gamma) = \int_{S_{-\gamma}} \chi_p(x\xi)dx = \begin{cases} p^{\gamma-1}(p-1) & (\gamma \leq \mathrm{val}(\xi)), \\ -p^{\gamma-1} & (\gamma = \mathrm{val}(\xi)+1), \\ 0 & (\gamma \geq \mathrm{val}(\xi)+2) \end{cases}$$

$$= p^{\gamma}\Omega(p^{-\gamma}\xi) - p^{\gamma-1}\Omega(p^{-\gamma+1}\xi).$$

Then, its Fourier transform can be calculated as

$$\begin{aligned}
\hat{f}(\xi) &= \sum_{\gamma\in\mathbf{Z}} \int_{S_{-\gamma}} f(x)\chi_p(x\xi)dx \\
&= \sum_{\gamma\in\mathbf{Z}} f(p^{-\gamma}) \int_{S_{-\gamma}} \chi_p(x\xi)dx \\
&= \sum_{N\le\gamma\le l} f(p^{\gamma}) \int_{S_{\gamma}} \chi_p(x\xi)dx \\
&= \sum_{N\le\gamma\le l} a_{\gamma}\left(p^{-\gamma}\Omega(p^{\gamma}\xi) - p^{-\gamma-1}\Omega(p^{\gamma+1}\xi)\right).
\end{aligned}$$

In summary, we obtain the following result.

$$\hat{f}(\xi) = \begin{cases} 0 & (\mathrm{val}(\xi) < -l-1), \\ -a_l p^{-l-1} & (\mathrm{val}(\xi) = -l-1), \\ -a_{-\mathrm{val}(\xi)-1}p^{\mathrm{val}(\xi)} + \displaystyle\sum_{-\mathrm{val}(\xi)\le\gamma\le l} a_{\gamma}(p-1)p^{-\gamma-1} & (-l-1 < \mathrm{val}(\xi) < -N-1), \\ -a_N p^{-N-1} + \displaystyle\sum_{N+1\le\gamma\le l} a_{\gamma}(p-1)p^{-\gamma-1} & (-N-1 \le \mathrm{val}(\xi)). \end{cases}$$

This $\hat{f}(\xi)$ is also the function which depends only on the norm. The support of $\hat{f}(\xi)$ is $B(p^{l+1})$, and parameter of constancy of $\hat{f}(\xi)$ is $N+1$. That is, $\hat{f} \in \mathcal{D}^{N+1}_{l+1}(\mathbf{Q}_p) \subset \mathcal{D}^{N}_{l+1}(\mathbf{Q}_p)$. For k satisfying $-l-1 \le k \le -N-1$, putting $\hat{a}_k = \hat{f}(p^k)$, then we can express the Fourier transform of $f \in \mathcal{D}^l_N$ as the matrix calculation like

$$\begin{pmatrix} \hat{a}_{-N-1} \\ \hat{a}_{-N-2} \\ \hat{a}_{-N-3} \\ \vdots \\ \hat{a}_{-l+1} \\ \hat{a}_{-l} \\ \hat{a}_{-l-1} \end{pmatrix} = \begin{pmatrix} -p^{-N-1} & (p-1)p^{-N-2} & (p-1)p^{-N-3} & \dots & (p-1)p^{-l+1} & (p-1)p^{-l} & (p-1)p^{-l-1} \\ 0 & -p^{-N-2} & (p-1)p^{-N-3} & \dots & (p-1)p^{-l+1} & (p-1)p^{-l} & (p-1)p^{-l-1} \\ 0 & 0 & -p^{-N-3} & \dots & (p-1)p^{-l+1} & (p-1)p^{-l} & (p-1)p^{-l-1} \\ \vdots & \vdots & \vdots & \ddots & \vdots & \vdots & \vdots \\ 0 & 0 & 0 & \dots & -p^{-l+1} & (p-1)p^{-l} & (p-1)p^{-l-1} \\ 0 & 0 & 0 & \dots & 0 & -p^{-l} & (p-1)p^{-l-1} \\ 0 & 0 & 0 & \dots & 0 & 0 & -p^{-l-1} \end{pmatrix} \begin{pmatrix} a_N \\ a_{N+1} \\ a_{N+2} \\ \vdots \\ a_{l-2} \\ a_{l-1} \\ a_l \end{pmatrix}.$$

References

[1] S. Y. Park, P. U. Chung, An Application of p-adic Analysis to Windowed Fourier Transform, *Kangweon-Kyungki Math. Jour.* 12:2 (2004), 193-200

[2] T. Suzuki, The Construction of p-Adic Stockwell Transform and its Spectra. *p-Adic Numbers, Ultrametric Analysis and Applications* 13:2 (2021): 166-173.

[3] V.S. Vladimirov, I.V. Volovich, E.I. Zelenov, p-Adic Analysis and Mathematical Physics, *World Scientific* (1994).

A new pre-coding approach for MPROT based image compression

Keita Ashizawa[1,*] and Katsu Yamatani[2]

[1]Faculty of Informatics, Shizuoka Institute of Science and Technology
[2]Faculty of Urban Science, Meijo University

`*ashizawa.keita@sist.ac.jp`

Abstract. The Multi-neighbor Predictors and Residual Orthogonal Transformations (MPROT) method, previously proposed by the authors, which was a Haar transform-based lossy image compression method, was able to avoid mosquito noise but introduced a new artifact named ”isolated island noise”. In this paper, we propose a new coding approach for MPROT coefficients. This approach includes two new ideas: isolated frequency component removal and encode the decomposed distribution map obtained by slicing the frequency space into energy bands. Through numerical experiments, we demonstrate that the compressibility improves compared to the case of adapting conventional coding.

Keywords: Image compression, Coding, Haar transform, Wavelet transform

1. Introduction

Discrete cosine transform (DCT) encoding is widely used in image compression due to its compression ratio and reproducibility. It has been adopted as an international standard, such as in JPEG, and widely employed. In the JPEG standard, the image is divided into blocks of 8×8 pixels, and the DCT is performed on each block[1]. The information within the blocks is aggregated into low-frequency components, and the transformation coefficients are quantized to achieve compression. However, at high compression levels, the quantization of the low-frequency components leads to block artifacts due to the loss of correlation among individual blocks. Additionally, quantization of high-frequency components is known to introduce mosquito noise and blur the edge areas. Therefore, wavelet transform coding has been researched as an encoding method to reduce these distortions[2]. We previously proposed MPROT, which incorporates alternating current component prediction into the simplest wavelet transform, the Haar transform. The MPROT has been shown to theoretically suppress block artifacts and mosquito noise, but it has been reported to introduce noise resembling isolated islands with different resolutions from the surroundings[3]. Thus, in this paper, we propose an encoding scheme for MPROT to mitigate isolated island noise and improve compression efficiency. Fig.1 illustrates the overview of the image compres-

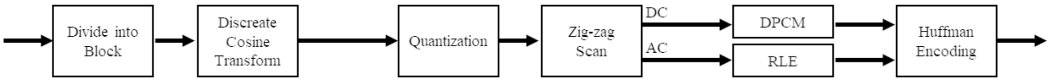

a) JPEG Baseline

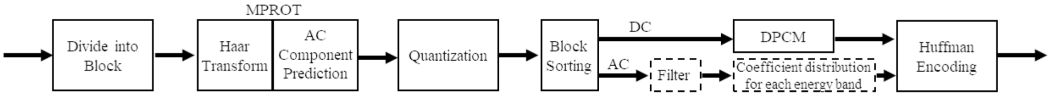

b) Proposed Scheme

Figure 1: Configuration comparison between the proposed scheme and the JPEG baseline.

sion method using MPROT proposed in this paper. The blocks enclosed by dashed lines in Fig.1b) represent a new approach in this study, which will be described in the next section.

2. Proposed pre-coding approach

Considering the computational cost and assuming the use of Huffman coding instead of arithmetic coding, we propose the following two ideas:

2.1. Isolated AC component removal filter

In the image compression using MPROT that was previously proposed, it has been reported that blocks with different resolutions from the surroundings result in visual flickering, resembling isolated islands. Therefore, we attempt to improve this issue by removing isolated frequency components in the frequency domain under certain conditions.

2.2. Slicing the frequency space into energy bands

MPROT is based on the simplest wavelet transform, the Haar transform, which results in transformation coefficients that possess spatial correlation and biased energy distribution. Hence, instead of directly coding them in the frequency domain like DCT coefficients, we propose dividing them into energy bands and performing an appropriate scan.

3. Numerical experiments

We compare the compression efficiency of the new pre-coding approach by evaluating it on the test image that consists of four images shown in Fig.2. The comparative subjects were the JPEG standard, DCT using 16×16 pixel block size, and MPROT based on hierarchical Haar Transform with a depth level of 4. Furthermore, the pre-coding was performed with a unit size of 256×256 pixels. The approach using pre-coding is referred to as ”proposed HMPROT,” while the conventional method that performs zero run-length encoding on AC components similar to the JPEG standard is referred to as ”previous HMPROT.” For objective evaluation, we used the Peak Signal-to-Noise Ratio (PSNR) value, which is obtained by normalizing the mean squared error with the peak value of the input signal. A higher PSNR

Figure 2: Test image (512 × 512 pixels, 8 bits/pixel grayscale).

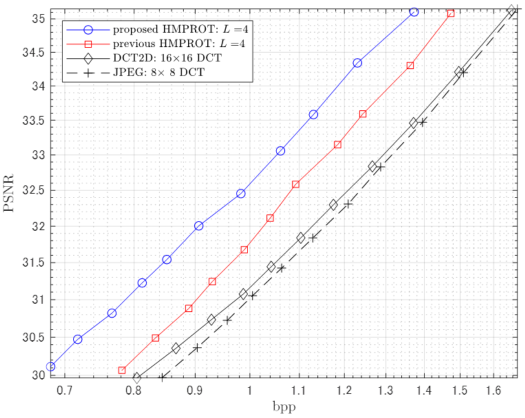

Figure 3: Comparison of the compression performance with PSNR values.

value indicates less error compared to the original image. From Fig.3, it can be confirmed that the PSNR value of the proposed method is improved by more than 1 dB compared to JPEG and about 0.7 dB compared to the conventional method at all tested compression ratios. This clearly shows that the proposed precoding greatly contributes to the improvement of compression efficiency.

4. Conclusions

This paper demonstrated that significant improvement in compression efficiency can be achieved by refining the encoding of coefficients obtained from the previously proposed MPROT. The newly devised method of ”Slicing the frequency space into energy bands” is believed to be applicable to other transform coefficients when there is a regular distribution of coefficients. In the presentation, we will also report on the effect of reducing image flicker, which was another target of the presentation, using compressed images as an example.

References

[1] G.K.Wallace: The JPEG still picture compression standard, *IEEE Trans. Consumer Electronics*, 38 (1992), xviii–xxxiv.

[2] A.S.Lewis, G. Knowles: Image compression using the 2-D wavelet transform, *IEEE Transactions on Image Processing*, 1:2(1992), 244–250.

[3] K. Ashizawa, K.Yamatani, N.Saito: The method of hierarchical multi-neighbor predictors and residual orthogonal transforms and its application to image compression, *Transactions of the Japan Society for Industrial and Applied Mathematics*, 17:3 (2007), 239–257.

Application of Modified ICCGH to Linear System Appearing in Shielding Current Analysis of HTS Film

Ayumu Saitoh[1,*]

[1]Graduate School of Science and Engineering, Yamagata University

*`saitoh@yz.yamagata-u.ac.jp`

Abstract. The $\mathcal{H}$-matrix-based preconditioning has been improved for accelerating a solver of the linear system which appears in the shielding current analysis of the HTS film. The result of computations shows that the modified ICCGH is faster than the conventional one.

Keywords: Finite element analysis, Iterative methods, Linear systems, $\mathcal{H}$-matrix method.

1. Introduction

In order to analyze the shielding current density in the high-temperature superconductor (HTS), the time evolution problem of the shielding current density must be solved numerically [1–3]. After discretizing with respect to space and time, the time evolution problem can be reduced to the linear system. Since the resulting linear system has a symmetric dense coefficient matrix, a direct method has been so far adopted as the linear-system solver.

To resolve the above difficulty, the $\mathcal{H}$-matrix-based acceleration technique has been proposed [4]. By using the acceleration technique, an execution speed of the shielding current analysis becomes fast. However, this acceleration technique has some disadvantages. First, the appropriate number of skips cannot be determined previously. Second, the skip interval is always constant. Therefore, it is difficult to give the appropriate preconditioner previously.

The purpose of the present study is to improve the $\mathcal{H}$-matrix-based acceleration technique for overcoming the above difficulties.

2. Shielding Current Analysis

In this study, the shielding current analysis in an uncracked HTS film is applied to the scanning permanent magnet method [4]. We assume that an uncracked HTS film which has a rectangle cross section Ω over the thickness is exposed to a time-varying magnetic field. Furthermore, $\boldsymbol{n}$ and $\boldsymbol{e}_z$ denote an outward normal unit vector on the boundary $\partial\Omega$ of Ω and a unit vector along the thickness direction, respectively.

Under the thin-plate approximation, the time evolution of the shielding current density is governed by the following integro-differential equation:

$$\mu_0 \frac{\partial}{\partial t}(\hat{W}T) + (\nabla \times \boldsymbol{E}) \cdot \boldsymbol{e}_z = -\frac{\partial}{\partial t}\langle \boldsymbol{B} \cdot \boldsymbol{e}_z \rangle, \tag{1}$$

where $\boldsymbol{E}$, $\boldsymbol{B}$, μ_0 and b are the electric field, the applied magnetic flux density, the permeability of vacuum and the film thickness, respectively. Furthermore, a scalar function T is z-component of the current vector potential. Moreover, $\langle\ \rangle$ is an average operator over the thickness of the HTS film. In addition, $\hat{W}$ is the operator corresponding to the magnetic flux density that is generated by shielding current density $\boldsymbol{j}$.

As the J-E constitutive relation, the power law is assumed [1–3]. The initial and boundary conditions are given by $T = 0$ at $t = 0$ and $\boldsymbol{j} \cdot \boldsymbol{n} = 0$ on $\partial\Omega$, respectively.

By discretizing both time and space, and applying of Newton method, the initial-boundary-value problem of the (1) can be reduced to the problem for solving the following linear system:

$$A(\boldsymbol{T})\, \delta\boldsymbol{T} = \boldsymbol{b}, \tag{2}$$

where, $\boldsymbol{T}$ denotes a nodal vector originating from T. Moreover, $\delta\boldsymbol{T}$ and $\boldsymbol{b}$ are N-dimensional unknown and given vectors, respectively. In addition, the coefficient matrix $A(\boldsymbol{T})$ is given by $A(\boldsymbol{T}) = U^T\,[W + J(\boldsymbol{T})]\,U + F$. Here, U is defined by $U \equiv I - F$, where I and F denote an identity matrix and a matrix derived from the boundary condition, respectively. Moreover, $W \in \mathbb{R}^{M\times M}$ and $J(\boldsymbol{T}) \in \mathbb{R}^{M\times M}$ are given matrices. Note that W denotes the symmetric dense matrix obtained by discretizing with respect to space, whereas $J(\boldsymbol{T})$ indicates the symmetric sparse matrix that changes depending both the iteration cycle of the Newton method and the time step.

3. $\mathcal{H}$-Matrix-Based Acceleration Technique

3.1. Conventional Method

In order to solve (2) fast, the $\mathcal{H}$-matrix-based acceleration technique has been proposed. The technique consists of the following two operations: the $\mathcal{H}$-matrix arithmetic and the $\mathcal{H}$-matrix-based preconditioning. By using the $\mathcal{H}$-matrix arithmetic, (2) is transformed to

$$A_{\mathrm{H}}\, \delta\boldsymbol{T} = \boldsymbol{b}, \tag{3}$$

where $A_{\mathrm{H}} \equiv U^T\,[H + J(\boldsymbol{T})]\,U + F$. In addition, H is the matrix obtained by applying the $\mathcal{H}$-matrix method [5] to W.

For the purpose of further accelerating the solver, the $\mathcal{H}$-matrix-based preconditioning is applied to (3). By using the preconditioner C, (3) is equivalently transformed to

$$\left(C^{-1} A_{\mathrm{H}} C^{-T}\right)\left(C^T \delta\boldsymbol{T}\right) = C^{-1}\boldsymbol{b}. \tag{4}$$

In this study, C is determined by using the following steps:

Step 1 H_{F} is generated by extracting all full-rank submatrices from H.

Step 2 If and only if $\left|(H_\mathrm{F})_{ij}\right| / |H_\mathrm{max}| < \epsilon_\mathrm{H}$ is satisfied, zero is substituted into $(H_\mathrm{F})_{ij}$. Here, ϵ_H is a constant and H_max indicates the maximum absolute value of H_F.

Step 3 The Jacobian matrix $J(\boldsymbol{T})$ is updated at every k time step. Otherwise, $J(\boldsymbol{T})$ is not changed.

Step 4 M is determined by $M = U^T\,[H_\mathrm{F} + J(\boldsymbol{T})]\,U + F$.

Step 5 M is approximated as LDL^T by means of the incomplete Cholesky factorization. Here, L and D are a lower triangular matrix and a diagonal matrix, respectively.

Step 6 $LD^{1/2}$ is adopted as C. Here, $D^{1/2}$ denotes the square root of the elements of D.

By solving (4) instead of (2), we get the numerical solution with the high speed. In the following, the CG method with $\mathcal{H}$-matrix-based acceleration technique is called the ICCGH.

3.2. Proposed Method

As mentioned in the introduction, $\mathcal{H}$-matrix-based preconditioning has some disadvantages. Therefore, $\mathcal{H}$-matrix-based preconditioning is enhanced. Specifically, the Step 3 in the $\mathcal{H}$-matrix-based preconditioning is replaced with the following process:

- $J(\boldsymbol{T}_\mathrm{new})$ is adopted as $J(\boldsymbol{T})$ only when $\|J(\boldsymbol{T}_\mathrm{new}) - J(\boldsymbol{T}_\mathrm{old})\|_\mathrm{F}/\|J(\boldsymbol{T}_\mathrm{new})\|_\mathrm{F} \geq \varepsilon$ is satisfied. Otherwise, $J(T)$ is not changed.

Here, $\boldsymbol{T}_\mathrm{new}$ and $\boldsymbol{T}_\mathrm{old}$ are nodal vectors for T obtained for the current and one previous cycles of Newton method, respectively. In addition, ε is a judgment parameter.

In this way, the appropriate k need not to be investigated by modifying the $\mathcal{H}$-matrix-based preconditioning. Throughout the present study, the ICCGH incorporated with the above procedure is called the modified ICCGH.

4. Performance Evaluation

In this section, we investigate the influence of the modified $\mathcal{H}$-matrix-based acceleration technique on the speed of the linear-system solver. As parameters for the solver, the judgment of convergence ϵ_CG and the initial guess $\delta\boldsymbol{T}_0$ are given by $\epsilon_\mathrm{CG} = 10^{-9}$ and $\delta\boldsymbol{T}_0 = \boldsymbol{0}$, respectively. Moreover, parameters for $\mathcal{H}$-matrix-based acceleration technique are fixed as follows: $k = 2$ and $\varepsilon_\mathrm{H} = 0.5$. In addition, the number N of unknowns is employed as $N = 11264$. The values of physical and geometric parameters are described in [3].

Let us evaluate the speed performance of the modified ICCGH. As the measure of the speed of the linear-system solver, the speedup ratios, $R_1 = \tau_\mathrm{c}/\tau_\mathrm{m}$ and $R_2 = \tau/\tau_\mathrm{m}$, are adopted. Here, τ_c, τ_m and τ denote CPU times for the conventional ICCGH, the modified ICCGH and the solver without any acceleration technique, respectively. R_1 and R_2 are calculated as a function of the judgment parameter ε and are depicted in Fig. 1. We see from this figure that the modified ICCGH is about 1.44 times faster than the conventional one. In addition, the speed of the modified ICCGH is about 46.3 times faster than that of the CG method without any acceleration technique.

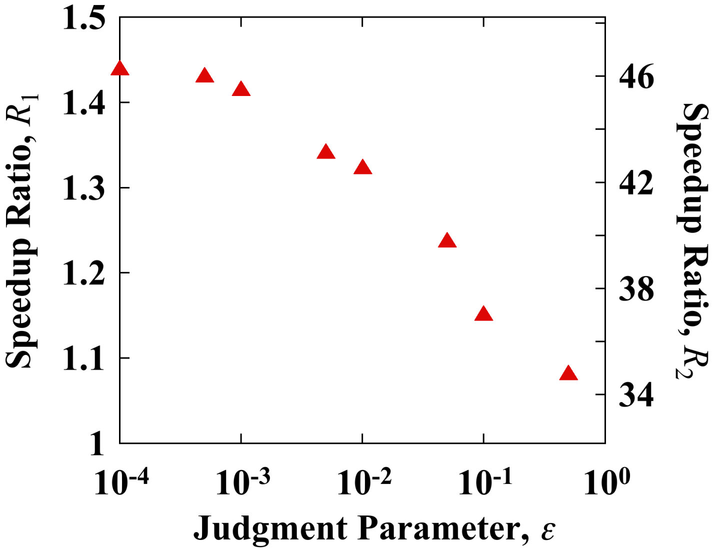

Figure 1: Dependence of speedup ratio R_1 and R_2 on the judgement parameter ε.

From the above results, the modified ICCGH might be a useful solver for the shielding current analysis.

References

[1] A. Kamitani, T. Takayama, and S. Ikuno: High-speed method for analyzing shielding current density in high-temperature superconductor *IEEE Trans. Magn.*, 47:5 (2011), 1138-1141.

[2] A. Kamitani, T. Takayama, S. Ikuno and H. Nakamura, "Numerical Investigations on Crack Identification in High-Temperature Superconducting Film" *Plasma Fusion Res.*, vol. 9, 3405085, Apr. 2014.

[3] A. Kamitani, T. Takayama, A. Saitoh and H. Nakamura, "Acceleration Techniques for Linear-System Solver in Shielding Current Analysis of Cracked HTS Film" *Plasma Fusion Res.*, vol. 16, 2405005, Dec. 2021.

[4] A. Saitoh "Performance Improvement of Symmetric Linear System Solver in Shielding Current Analysis of HTS Thin Film: Application of $\mathcal{H}$-Matrix-Based Preconditioner" *Plasma Fusion Res.*, vol. 17, 2401089, May. 2022.

[5] M. Bebendorf, *Hierarchical Matrices*, Springer-Verlag, Berlin, 2008, pp.49-98.

Development and performance evaluation of the Block GPBiCGrQ method with variable grouping strategy

Hiroto Tadano[1,*]

[1]Center for Computational Sciences, University of Tsukuba

*`tadano@cs.tsukuba.ac.jp`

The full paper of this paper has been published in Journal of Advanced Simulation in Science and Engineering (JASSE).

DOI: `https://doi.org/10.15748/jasse.11.32`

JSST 2023

Linear System Solvers for Large-Scale Asymmetric EFG-Type Saddle-Point Problem: Are There Any Variants of AiVRM?

Atsushi Kamitani[1,*] and Teruou Takayama[1]

[1]Department of Informatics and Electronics, Graduate School of Science and Engineering,
Yamagata University

*kamitani@yz.yamagata-u.ac.jp

Abstract. Discretization of a boundary-value problem with the eXtended Element-Free Galerkin (X-EFG) method yields an asymmetric EFG-type Saddle-Point (EFG-SP) problem that is difficult to solve numerically. As a high-performance solver for the problem, the Asymmetric-version improved Variable-Reduction Method (AiVRM) and its variant AiVRM2 were developed. However, it is not clear whether AiVRM2 is the only variant of AiVRM. In the present study, two other variants of AiVRM are successfully proposed by generalizing the derivation process of AiVRM and AiVRM2. A numerical code is developed for solving asymmetric EFG-SP problems with four types of AiVRMs and, by means of the code, performances of the four methods are investigated numerically. Consequently, it is found that, especially for a large-scale asymmetric EFG-SP problem, four types of AiVRMs are even superior to the preconditioned Krylov subspace method.

Keywords: Krylov subspace method, Meshless approach, Saddle-point problem

1. Introduction

As meshless approaches for solving a boundary-value problem, the Element-Free Galerkin (EFG) method [1] and the eXtended Element-Free Galerkin (X-EFG) method [2] were developed. If the X-EFG method is applied to a boundary-value problem of an elliptic partial differential equation, we obtain the following linear system [2–4]:

$$\begin{bmatrix} B & C \\ D^T & O \end{bmatrix} \begin{bmatrix} \boldsymbol{u} \\ \boldsymbol{\lambda} \end{bmatrix} = \begin{bmatrix} \boldsymbol{c} \\ \boldsymbol{d} \end{bmatrix}, \tag{1}$$

where $B \in \mathbb{R}^{N\times N}$ and $C, D \in \mathbb{R}^{N\times K}$ are given matrices. Also, $\boldsymbol{c} \in \mathbb{R}^N$ and $\boldsymbol{d} \in \mathbb{R}^K$ are both given vectors, whereas $\boldsymbol{u} \in \mathbb{R}^N$ and $\boldsymbol{\lambda} \in \mathbb{R}^K$ are both unknown vectors. Here, N and K are two natural numbers satisfying $K < N$. If submatrices, B, C and D, fulfill the 6 conditions described in [4], (1) is called an asymmetric EFG-type Saddle-Point (EFG-SP) problem.

As is well known, an asymmetric EFG-SP problem is difficult to solve numerically [5,6]. In order to resolve this difficulty, the authors developed the Asymmetric-version improved Variable-Reduction Method (AiVRM) and its variant AiVRM2 [4]. Furthermore, they found that both two methods can be a powerful tool for solving a large-scale asymmetric EFG-SP problem. However, do any other variants of AiVRM exist?

The purpose of the present study is to investigate whether other variants of AiVRM exist or not. Moreover, if they exist, we evaluate their performances numerically.

2. $\boldsymbol{\lambda}$-Eliminator and Boundary-Condition Descriptor

In AiVRM and AiVRM2 [4], after eliminating $\boldsymbol{\lambda}$ from (1), the resulting linear system is iteratively solved for $\boldsymbol{u}$. In this section, the linear system is called a reduced system and the method for deriving it is briefly explained. In the following, we assume that $\mathbb{R}^N$ is decomposed as the direct sum of $\mathrm{Im}\, C$ and its complementary space W: $\mathbb{R}^N = \mathrm{Im}\, C \oplus W$.

A reduced linear system is obtained by means of the following three steps. First, after multiplying $B\boldsymbol{u} + C\boldsymbol{\lambda} = \boldsymbol{c}$ by a projection matrix $\mathcal{U}_\lambda$ along $\mathrm{Im}\, C$ onto W, we get

$$\mathcal{U}_\lambda B \boldsymbol{u} = \mathcal{U}_\lambda \boldsymbol{c}. \tag{2}$$

Next, we multiply the discretized boundary condition $D^T\boldsymbol{u} = \boldsymbol{d}$ by a $N \times K$ matrix G with a full-column rank and, as a result, we have

$$\mathcal{F}_\mathrm{B}\, \boldsymbol{u} = G\, \boldsymbol{d}, \tag{3}$$

where $\mathcal{F}_\mathrm{B}$ is given by

$$\mathcal{F}_\mathrm{B} = GD^T. \tag{4}$$

Finally, the following reduced system:

$$B^\dagger \boldsymbol{u} = \boldsymbol{c}^\dagger, \tag{5}$$

is obtained as a single linear system equivalent to (2) and (3). Here, matrix $B^\dagger$ and vector $\boldsymbol{c}^\dagger$ are defined by $B^\dagger \equiv \mathcal{U}_\lambda B \mathcal{U}_\mathrm{B} + \mathcal{F}_\mathrm{B}$ and $\boldsymbol{c}^\dagger \equiv \mathcal{U}_\lambda(\boldsymbol{c} - BG\boldsymbol{d}) + G\boldsymbol{d}$. In addition, $\mathcal{U}_\mathrm{B}$ is given by $\mathcal{U}_\mathrm{B} = I - \mathcal{F}_\mathrm{B}$, where I denotes an identity matrix. Throughout the present study, $\mathcal{U}_\lambda$ and $\mathcal{F}_\mathrm{B}$ are called a $\boldsymbol{\lambda}$-eliminator and a boundary-condition descriptor, respectively.

As mentioned above, an arbitrary $N \times N$ matrix cannot be always chosen as either a $\boldsymbol{\lambda}$-eliminator or a boundary-condition descriptor. Indeed, two matrices can play a role as a $\boldsymbol{\lambda}$-eliminator and a boundary-condition descriptor if the following three conditions are satisfied:

C$_1$: The one matrix is a projection matrix along $\mathrm{Im}\, C$ onto W.

C$_2$: The other matrix is written as (4).

C$_3$: $\mathrm{Im}\, \mathcal{U}_\lambda \cap \mathrm{Im}\, \mathcal{F}_\mathrm{B} = \{\boldsymbol{0}\}$.

In other words, C$_1$, C$_2$, and C$_3$ are the sufficient conditions for a $\boldsymbol{\lambda}$-eliminator and a boundary-condition descriptor. Incidentally, if C$_3$ is fulfilled, we can ensure that (5) is equivalent to (2) and (3).

Table 1: Inner linear systems and inner solvers for AiVRMs

Solver	Inner Linear System	Inner Solver
AiVRM-NN	$(D^T C)z = v$	BiCGSTAB
AiVRM-OO	$(C^T C)z = v$	CG
	$(D^T D)z = v$	
AiVRM-NO	$(D^T C)z = v$	BiCGSTAB
	$(D^T D)z = v$	CG
AiVRM-ON	$(D^T C)z = v$	BiCGSTAB
	$(C^T C)z = v$	CG

3. Asymmetric-version iVRM

Let us search for matrices which satisfy the sufficient conditions for a λ-eliminator or a boundary-condition descriptor. As candidates for such matrices, the following six projection matrices are introduced: $F \equiv C(D^T C)^{-1} D^T$, $U \equiv I - F$, $F_C \equiv C(C^T C)^{-1} C^T$, $U_C \equiv I - F_C$, $F_D \equiv D(D^T D)^{-1} D^T$ and $U_D \equiv I - F_D$.

After a straightforward algebra, we can show that the following four combinations of $(\mathcal{U}_\lambda, \mathcal{F}_\mathrm{B})$ fulfill the conditions for a λ-eliminator or a boundary-condition descriptor:

$$(\mathcal{U}_\lambda, \mathcal{F}_\mathrm{B}) = (U, F), (U, F_D), (U_C, F), (U_C, F_D).$$

Throughout the present study, AiVRMs with $(\mathcal{U}_\lambda, \mathcal{F}_\mathrm{B}) = (U, F)$, (U, F_D), (U_C, F) and (U_C, F_D) are called AiVRM-NN, AiVRM-NO, AiVRM-ON and AiVRM-OO, respectively.

In solving (5) with AiVRMs, multiplications of projection matrices and vectors are calculated. The matrix-vector multiplications require the solution of a linear system with K unknowns. For example, for the purpose of evaluating a multiplication of a projection matrix U and a vector in AiVRM-NN, a linear system $(D^T C)z = v$ has to be solved for $z \in \mathbb{R}^K$. Such a linear system is called an inner linear system, whereas (5) is called an outer linear system. Moreover, Krylov subspace methods for solving inner and outer linear systems are called inner and outer solvers, respectively.

In the actual calculation, BiCGSTAB is always adopted as an outer solver in four types of AiVRMs. On the other hand, in solving inner linear systems with symmetric and asymmetric coefficient matrices, Conjugate Gradient method (CG) and BiCGSTAB are employed as inner solvers, respectively. In Table 1, inner linear systems and inner solvers are tabulated for four types of AiVRMs.

4. Performance Evaluation

As a test problem, we consider an asymmetric EFG-SP problem originating from the following 2D Poisson problem on the domain Ω bounded by a simple closed curve $\partial\Omega$: $-\nabla^2 u = p$ in Ω and $u = \bar{u}$ on $\partial\Omega$. Here, p and $\bar{u}$ are given functions in Ω and on $\partial\Omega$, respectively.

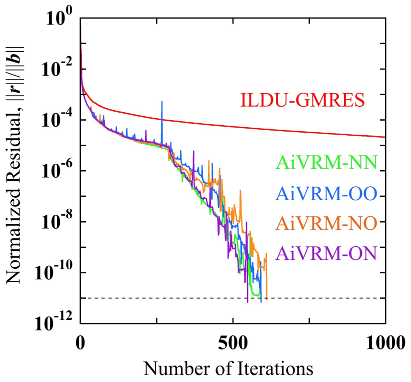

Figure 1: Residual histories of ILDU-GMRES and four types of AiVRMs for N = 1,050,625.

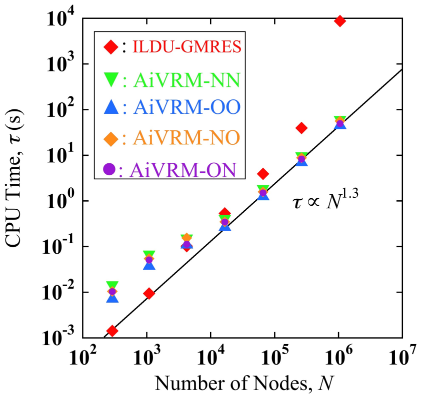

Figure 2: Dependence of the CPU time τ on the number N of nodes.

First of all, we compare a convergence property of four types of AiVRMs with that of ILDU-GMRES. To this end, residual histories for the five methods are shown in Figure 1. We see from this figure that, from the standpoint of a convergence property, four types of AiVRMs are even superior to ILDU-GMRES.

Next, we investigate the computational cost for the five methods. For this purpose, CPU times for the five methods are determined as functions of the number N of nodes and they are depicted in Figure 2. This figure indicates that ILDU-GMRES and AiVRM-OO become the fastest for $N \lesssim 10^4$ and for $N \gtrsim 10^4$, respectively. Moreover, the CPU times for AiVRMs are roughly proportional to $N^{1.3}$.

From the above results, we can conclude that four types of AiVRMs are suitable for solving large-scale asymmetric EFG-SP problems.

References

[1] T. Belytschko, Y.Y. Lu, L. Gu: *Int. J. Numer. Meth. Eng.*, 37:2 (1994), 229–256.

[2] A. Kamitani, T. Takayama, T. Itoh, H. Nakamura: *Plasma Fusion Res.*, 6 (2011), Art. No. 2401074.

[3] T. Itoh, A. Saitoh, S. Ikuno, A. Kamitani: *J. Adv. Simulat. Sci. Eng.*, 3:2 (2017), 188–205.

[4] A. Kamitani, T. Takayama, H. Nakamura: *Plasma Fusion Res.* 18 (2023), Art. No. 2403039.

[5] M. Benzi, G. H. Golub, J. Liesen: *Acta Numer.*, 14 (2005), 1–137.

[6] M. Rozložník: *Saddle-Point Problems and Their Iterative Solution*, Switzerland: Birkhäuser, 2018, Chaps. 1 and 4.

MoM analysis of scattered fields from nano-size spiral structure in UV vortex

Hideki Kawaguchi[1*], Masahiro Katoh[2], Koichi Matsuo[2]

[1]Dept. of Information and Electronic Eng., Muroran Institute of Technology
[2]Hiroshima Synchrotron Radiation Center, Hiroshima University
*kawa@mmm.muroran-it.ac.jp

Abstract. It is pointed out that a fundamental process of the circular dichroism (CD) spectroscopy strongly depends on interaction between angular momentum of the circularly polarized light and chiral materials. To effectively improve the CD spectroscopy, it is considered to use the optical vortex instead of the circularly polarized light, since the optical vortex carries much larger angular momentum. In this work, we discuss evaluation of the interaction between the angular momentum of the UV vortex and spiral structure materials quantitatively by using numerical simulations of the method of moment (MoM).

Keywords: method of moment (MoM), chiral molecule, circular dichroism (CD) spectroscopy, Ultra-violet light, circularly polarized light, optical vortex, angular momentum.

1. Introduction

Since property of orbital angular momentum of the optical vortex was pointed out in 1992, the optical vortex has been investigated actively from viewpoints of not only scientific but also industry applications. And investigations of optical vortex are now spreading out from optical frequency to other frequency ranges such as X-ray, UV, millimeter wave and microwave. One of most attractive phenomena related on the optical vortex is interaction of any spiral structure biomolecules (chiral molecules) such as DNA, protein and polysaccharide with the spiral wavefront structure of the optical vortex. It was already found that scattering phenomena of the right circularly polarized UV light from the spiral structure biomolecules has different characteristics from those of the left circularly polarized UV light [1],[2], which gives us effective method of circular dichroism (CD) spectroscopy. Then it is known that fundamental process of CD is related with interaction between angular momentum of circularly polarized light and the spiral structure of the chiral molecules. To aim to investigate such angular momentum interaction between the UV light and spiral structure materials quantitatively, we present a method of moment (MoM) analysis [3] of scattered fields from nano spiral structure in UV fields in this work.

2. MoM analysis of scattered phenomena from spiral structure

We here assume to simulate scattering phenomena from nano-size thin wire conductor in 190nm UV radiation fields. Then, the size of scatterer of the spiral conductor is about 20 times smaller than that of wavelength of the UV light and thickness of the spiral conductor is much smaller than its length. To effectively simulate such the numerical model, we here employ the MoM frequency domain analysis [3]. In the MoM for thin wire conductor, induced surface current K_l along a thin wire conductor is calculated by the following integral equation of EFIE,

$$\boldsymbol{E}(\omega,\boldsymbol{x}) = \boldsymbol{E}_{ext}(\omega,\boldsymbol{x}) + \frac{1}{4\pi}\int_S e^{-i\frac{\omega}{c}|\boldsymbol{x}-\boldsymbol{x}'|}\left\{ i\omega\mu\frac{K_l\boldsymbol{l}}{|\boldsymbol{x}-\boldsymbol{x}'|} - i\frac{1}{\varepsilon\omega}(\boldsymbol{x}-\boldsymbol{x}')\frac{\partial K_l}{\partial l}\right\} dS' \tag{1}$$

3. Numerical examples

Examples of numerical models of the spiral thin wire conductor and surface current distributions induced by the left circularly polarized UV light with 190 nm wavelength are depicted in Fig.1(a) and Fig.2(a) for the spiral pitch sizes of 190 nm and 5 nm respectively. In Fig.1(b) and Fig.2(b), radiation patterns corresponding to Fig.1(a) and Fig.2(a) are shown. It is confirmed that the radiation pattern has un-symmetric shape even if the size of the scatterer is much smaller that that of wavelength of the incident fields. We will process to detail investigations of the scattering phenomena from the nano-size spiral structures in the UV vortex in near future.

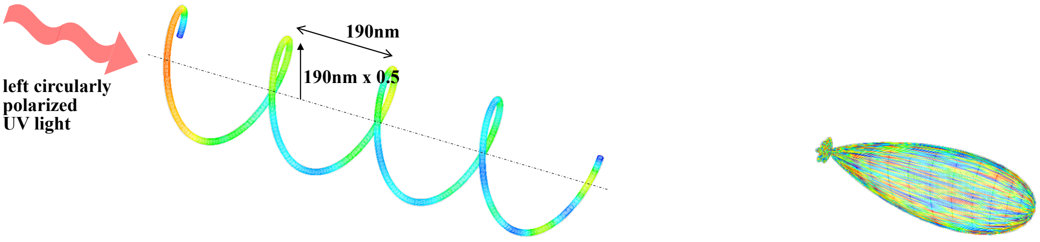

(a) induced surface current (b) radiation pattern

Fig.1 Scattering field simulation of 190 nm pitch spiral wire in 190 nm wavelength UV

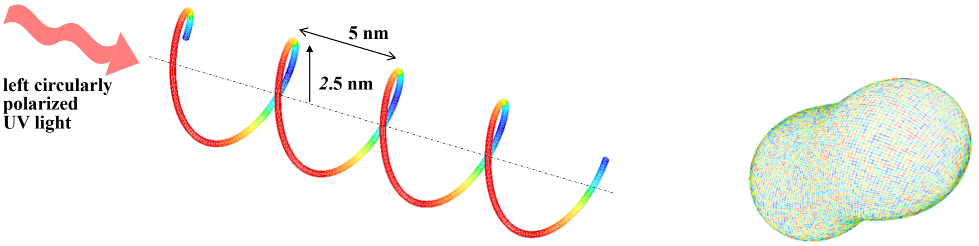

(a) induced surface current (b) radiation pattern

Fig.2 Scattering field simulation of 5 nm pitch spiral wire in 190 nm wavelength UV

References

[1] K. Matsuo, K. Gekko, Methods Mol. Biol., 2003, 253–279 (2019).

[2] K. Matsuo, K. Gekko, Bull. Chem. Soc. Jpn. 6, 675–689 (2013).

[3] J.J.H.Wang, "Generalized Moment Method in Electromagnetics", Wiley, 1991.

Acknowledgement

This work was supported by JSPS KAKENHI Grant Number 23H04597.

Numerical analysis of electric field surrounding a live-line worker climbing a 330kV transmission tower

Atsuki Takayama[1*], Shoji Hamada[1]

[1]Graduate School of Science and Engineering, Kansai University

*k943915@kansai-u.ac.jp

Abstract. Numerical analyses of the electric field experienced by a live-line worker climbing a transmission tower from the ground to the vicinity of a 330 kV high voltage conductor were conducted. This study focuses on calculating the induced charge, induced current, and body surface electric field strength of the worker to investigate the electrical environment of the worker. The calculated results were compared between a worker model grounded to a transmission tower and a worker model with a floating potential. Additionally, the calculated values were also compared to various regulatory limits.

Keywords: Transmission tower, Electric field, Induced current, Induced charge, Human body

1. Introduction

Live working is a crucial task for maintaining high-voltage transmission lines while ensuring uninterrupted power supply. It is essential to protect live-line workers from electrical accidents such as discharge and electric shock. Additionally, to improve the working environment, it is desirable to understand and reduce the levels of induced charge, induced current, and electric field strength ($|\boldsymbol{E}|$) on the body surface. To contribute to this goal, numerical analyses have been conducted to study the electric fields around high-voltage transmission lines, towers, and live-line workers [1]-[4]. In this study, we performed an electric field analysis assuming a live-line worker climbing a transmission tower from the ground to the vicinity of a 330kV high voltage conductor. We investigated the maximum $|\boldsymbol{E}|$, the amount of induced charge, and the induced current on the body surface. Both a worker model grounded with a steel tower and a worker model insulated from the tower with air were used. The shape of the steel tower model was created to resemble the tower illustrated in Ref. [1].

2. Calculation model

The voxel model created is depicted in Fig. 1, where the x and y directions are perpendicular to and along the transmission line, respectively. The voxel size is 1 cm, the height of the human body is 1.71 m, and the height of the transmission tower is 33.5 m. The peak value (V) of the phase voltage for the three-phase transmission line was set to 330 $\left(\sqrt{2}/\sqrt{3}\right)$ kV, with a frequency (f) of 50 Hz. The conductor consists of 6 subconductors with a diameter of 3 cm, and the maximum distance between the subconductors is 30 cm. The conductors are arranged in the x direction, following the order of A, B, and C phases. The holding heights of the conductors for each phase are 24.5 m, 30.4 m, and 24.5 m, respectively, and their respective voltages are V, $-V/2$, and $-V/2$. Although the calculated values represent instantaneous values at this voltage phase, they are expected to approximate the crest values for the worker near or below the phase-A conductor. The overhead ground wires have a diameter of 3 cm and a holding height of 33.5 m. The distance between steel towers is 120 m, the line sag is 8 m, and the lines are modeled within ±60 m in the y direction from the tower. Each steel frame is approximated as a cylinder with two hemispherical ends, and the diameter of the cylinder is set to 30 cm. Reference 1 does not list the dimensions of the steel members, so we assume that all steel members have the same diameter. However, this makes the cross-section of the brace member a little too thick. Fig. 2 illustrates a worker model in contact with a steel tower, and another worker model insulated from the tower by an air gap of 8 cm. The former is referred to as the grounded model, while the latter is referred to as the floating model, which has an unknown floating potential and zero total charge. Fig. 3 displays a live-line worker climbing a steel tower. The worker models are placed at 25 locations from h = 0 m to 24 m, where h is the vertical distance from the ground to the sole of the foot. The tower, lines, and the human body model are all approximated as perfect conductors, and eddy currents are not considered. The voxel-based fast multipole surface charge simulation method [5] was utilized for the electric field calculation, and a lossless compression format of voxel models [6] was employed to reduce memory usage and computational time for handling the model.

3. Calculation results

Fig. 4 illustrates the relationship between the maximum $|\boldsymbol{E}|$ on the body surface and h. The

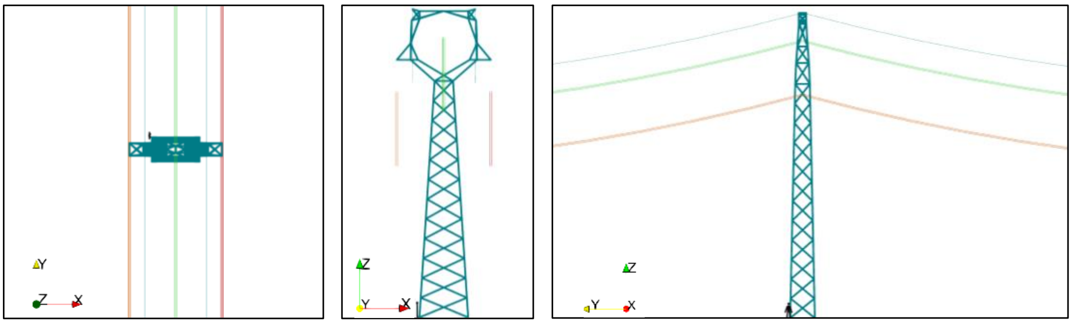

Fig. 1. A voxel model composed of a transmission tower, lines, and a worker.

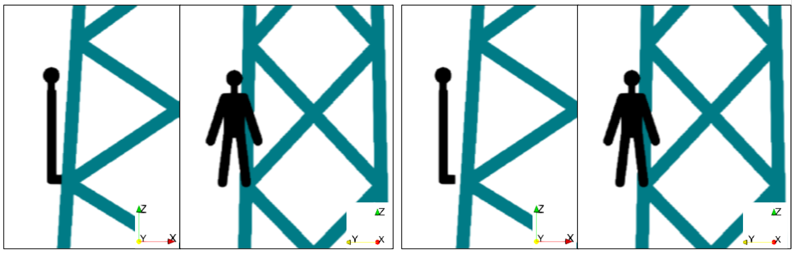

Fig. 2. Grounded (left) and floating (right) workers (h = 15 m).

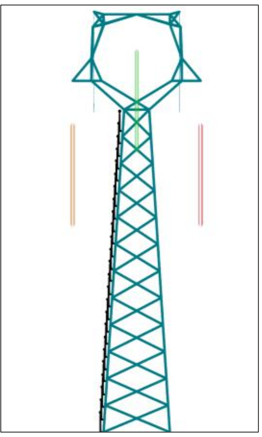

Fig. 3. A climbing worker.

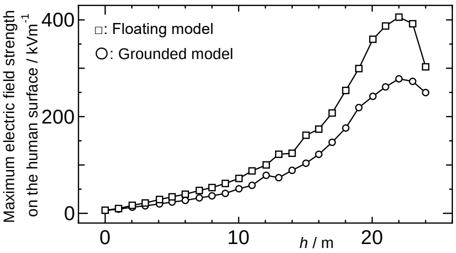

Fig. 4. Maximum |***E***| on the worker.

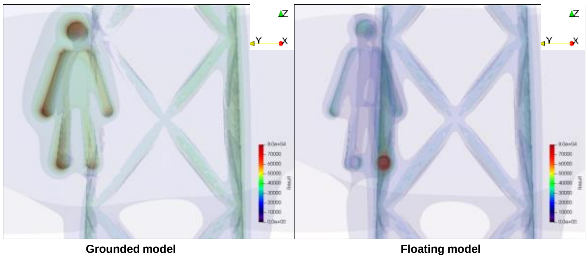

Fig. 5. Iso-|***E***| surfaces around the worker (h = 22 m).

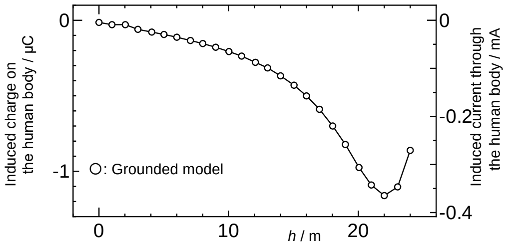

Fig. 6. Induced charge and current on the grounded model.

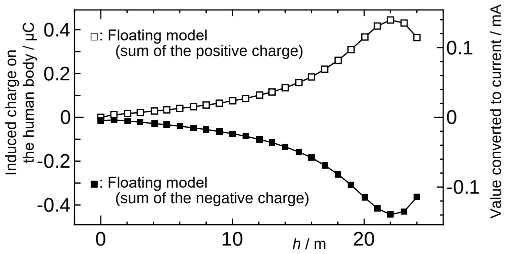

Fig.7. Positive and negative induced charge on the floating model.

maximum |***E***| increases with increase in h and reaches its peak value at h = 22 m. The peak values for the grounded and floating models are 278.2 kV/m and 405.7 kV/m, respectively. Fig. 5 displays the iso-|***E***| surfaces surrounding the worker at h = 22 m. In China, the electric field regulation value for exposed body parts of live-line workers wearing shielding clothing is specified as $\sqrt{2}\times240$ kV/m [3]. The calculated peak values for the grounded and floating models are lower and higher than this value, respectively. According to the ICNIRP guideline, the reference level for occupational exposure to 50 Hz electric field is $\sqrt{2}\times10$ kV/m [7]. The calculated maximum |***E***| values on the models exceed $\sqrt{2}\times10$ kV/m around h = 2 m. When comparing the maximum |***E***| values of the grounded and floating models, the latter is always greater than the former at any height. As shown in Fig. 5, the maximum |***E***| on the grounded model is seen at the head, while the maximum |***E***| on the floating model is observed at the toe, which is closest to the tower. In the floating model, a strong electric field is generated due to the floating potential applied to the narrow gap between the toe and the tower. Fig. 6 presents the induced charge and induced current on the surface of the grounded model. The induced current is obtained by multiplying the amount of induced charge by $2\pi f$. Fig. 7 illustrates the amount of positive and negative charges induced on the surface of the floating model, and the right vertical axis represents the value converted to current. The maximum absolute current in Fig. 6 is 0.365 mA at h = 22 m, which is approximately one-third of the contact current reference level of 1 mA specified in [7]. The maximum amount of charge induced on the grounded and floating models was -1.16 μC and ±0.444 μC, respectively, at h = 22 m. It is known that electric shock occurs when the amount of electric charge during discharge exceeds 0.2 to 0.3 μC [8]. Therefore, if a discharge occurs at the moment the floating model is grounded, it is necessary to prevent the discharge current from flowing through the human body.

4. Conclusion

A numerical analysis was conducted to analyze the electric field surrounding a live-line worker climbing a 330kV transmission tower, from the ground to the proximity of a high voltage conductor. To investigate the electrical environment of the worker, the induced charge, current, and electric field strength |***E***| on the worker were calculated. Two worker models were utilized: one grounded to the tower and another with floating potential. The peak |***E***| value of 405.7 kV/m on the toe of the floating model exceeds the regulation value in China; however, it is important to note that the toe can be protected by wearing shielding socks and shoes. On the other hand, the peak |***E***| value of 278.2 kV/m on the head of the grounded model is below the regulation value, indicating that wearing shielding clothing without a mask would meet the requirements. The maximum induced current for the grounded model was 0.365 mA, approximately one-third of the contact current reference level in Ref. [7]. The grounded model also exhibited a maximum induced charge of -1.16 μC. It is worth noting that if a discharge current flows through the exposed body part when the floating model is grounded to the tower, it may lead to an electric shock. In the future, we will adjust the cross-sectional shape and dimensions of the steel members to create a more precise tower model.

References

[1] B. Zhang, J. He, X. Cui, S. Han, and J. Zou: Electric field calculation for HV insulators on the head of transmission tower by coupling CSM with BEM, *IEEE Trans. on Magnetics*, 42:4 (2006), 543-546.

[2] C. Zhuang, R. Zeng, B. Zhang, P. Zhu, L. Wang, and J. He: The optimization of entering route for live working on 750 kV transmission towers by space electric-field analysis, *IEEE Trans. on Power Delivery*, 25:2 (2010), 987-994.

[3] X. Liu, Q. Yang, H. Li, J. Chen, J. Li, and L. Xu: The analysis of body surface electric field during live working on 500kV double-circuit lines on same tower, *2016 IEEE international Conf. on High Voltage Engineering and Application*, (2016. 9).

[4] Y. Peng, B. Xiao, K. Liu, X. Zhu, K. Han, and T. Wu: Calculation method for initial discharge formation parts of live line worker based on leader discharge theory, *IEEJ Trans. on Electrical and Electronic Engineering*, 18 (2023), 849-855.

[5] S. Hamada: Calculation of electrostatically induced electric fields in human models using a two-step process method of voxel-based fast multipole surface charge simulation method, *IEEJ Trans. on FM*, 140:10 (2020), 481-490 (in Japanese).

[6] S. Hamada: Surface charge simulation method based on lossless compression voxel models, *Proc. of the 2021 Annual Meeting IEE of Japan*, 1-024 (2021), 34 (in Japanese).

[7] International commission on non-ionizing radiation protection: ICNIRP guidelines for limiting exposure to time-varying electric and magnetic fields (1Hz – 100kHz), *Health Physics*, 99:6 (2010), 818-836.

[8] Recommendations for requirements for avoiding electrostatic hazards in industry 2007, Technical recommendations of the national institute of occupational safety and health, JNIOSH-TR-NO. 42 (2007) (in Japanese).

Calculation of electrostatically induced steady-state current through human body near a tree under power transmission lines

Hiroki Tanaka[1,*] and Shoji Hamada[1]

[1]Graduate School of Science and Engineering, Kansai University

*`k584765@kansai-u.ac.jp`

The full paper of this paper has been published in Journal of Advanced Simulation in Science and Engineering (JASSE).

DOI: `https://doi.org/10.15748/jasse.11.166`

On Graph Coloring and Its Appearance Probability for Wireless Communication

Hiroshi Tamura[1*], Keisuke Nakano[2]

[1]Faculty of Science and Engineering, Chuo University, Japan
[2]Graduate School of Science and Technology, Niigata University, Japan
[*]**tamura@elect.chuo-u.ac.jp**

Abstract. The relation of channel assignment problems in wireless communications and coloring problems of graph theory is well-known. A channel in the wireless communication is corresponding to a color assigned to a vertex (an edge) in a graph. It is popular to minimize the number of colors assigned to vertices of the graph. However, the maximum number of colors called Grundy Number is also important. In the previous study, we show the upper bounds of colors assigned to some graphs. The coloring with the maximum number of colors is thought to occur very rarely, but its probability has not been considered. This probability is important because it is directly related to the required number of channels. In this paper, we consider the probability of maximizing the number of colors in graphs using a model close to real wireless communication trees.

Keywords: Wireless communication, Channel assignment, Graph coloring, Grundy coloring, Appearance probability

Introduction

Relationship between graph coloring and channel assignment in wireless communication is well known. However, almost studies are about the minimum number of colors. This number is called the chromatic number of the graph and the problem of finding the chromatic number is NP hard. In the previous study [1], we paid attention to graph coloring assigned maximum number of colors called Grundy coloring. Because, it is important to find the required number of channels. The coloring with the maximum number of colors is thought to occur very rarely, but its probability has not been considered. This probability is important because it is directly related to the required number of channels.

1. Assumptions and definitions

First of all, we define greedy coloring[2]. A ***greedy coloring*** is a coloring of the elements (vertices or edges) of a graph formed by a greedy algorithm that considers the elements of the graph in sequence and assigns each element its first available color. Colors are assigned in order 1,2,3,…. The number of colors produced by the greedy coloring for the worst ordering of a given graph G is called its ***Grundy number***[3] and its coloring is called ***Grundy coloring***. The vertex Grundy coloring is popular. The conventional edge coloring version called ***edge Grundy number*** and ***edge Grundy coloring*** is discussed in [4].

In [1], we showed the graphs assigned many colors theoretically and vertex/edge ordering of coloring.

[Theorem 1][1]

Let G be a graph. For a greedy coloring, the number of colors is not greater than

max {deg(u) +1 | u is a vertex of G}, in case of vertex coloring,

max{deg(u)+deg(v) -1| (u,v) is an edge of G}, in case of edge colorings,

where deg(u) is the degree of vertex u.

In the above definition, a color is assigned to a vertex/edge once, the color remains on the vertex/edge. In this paper, we add an operation to delete a color once assigned. Because, in communication networks, when communication is terminated, the corresponding color is decolored. Therefore, in a graph coloring, we assume the deleting operation of color on a vertex/edge. For example, in vertex coloring, Grundy number is 2 in Fig.1. However, in the following ordering, the number of colors is 3. The bottom row represents the assigned or deleted colors.

v2, v3, v2(x), v1, v2
1 2 1(x) 1 3

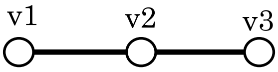

Fig.1 A graph G.

Here, v2(x) represents deletion of the color of v2. Namely, the worst case occurs in 5 steps at the minimum. This coloring is called ***Grundy coloring with decoloring***. Since Grundy coloring with decoloring is a generalized Grundy coloring, the number of colors may increase. ***Edge Grundy coloring with decoloring*** is defined similarly. In case of Grundy coloring with decoloring, Theorem 1 also holds.

2. Results

In this section, we calculate the probability that the worst cases occur in ***Grundy coloring with decoloring***. In case of ***Grundy coloring,*** we discussed in [5]. In calculating, we assume that at every vertex, we assign or remove colors with equal probability. For example, in graph G in Fig.1, we assign color 1 to v1or v2 or v3 with equal probability at first. Here, we assume that color 1 is assigned to v1. Next, we assign color 2 to v2 or assign color 1 to v3 or remove color 1 from v1 with equal probability. We repeat this operation to obtain the probability that color 3 is assigned to a vertex in 5 steps.

The color 3 is assigned to a vertex in 5 steps with the following 2-cases.

v2, v3, v2(x), v1, v2 or v2, v1, v2(x), v3, v2.

Since the number of cases is 3^5, the probability where color 3 is assigned to a vertex in 5 steps is $\frac{2}{3^5} = 0.0082$. This is the probability of obtaining the Grundy number with the minimum steps.

In general, in the case that

the number of vertices/edges is n,

a color is assigned to or removed from a vertex/edge with equal probability,

the minimum step that obtain a Grundy coloring is m, the number of cases is n^m. In this case, not all vertices/edges have been assigned a color after m steps.

Next we consider edge coloring. In Fig.2, we assign colors to edges to G. From Theorem 1, the Grundy number is not greater than max{deg(u)+deg(v) -1| (u,v) is an edge of G}. In e4, the value is 3+2-1=4. This value is the maximum.

Using the following 6 steps, the color 4 is assigned to e4. The bottom rows represent the assigned or deleted colors respectively.

e4, e2, e3, e4(x), e1, e4	or	e4, e3, e2, e4(x), e1, e4.
1 2 3 1(x) 1 4		1 2 3 1(x) 1 4

Since 6 is the minimum steps and the number of edges is 4, the probability is $\frac{2}{4^6} = 0.00048$. This value is also low.

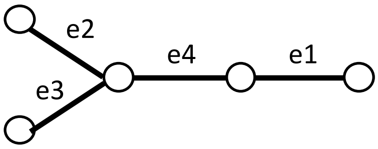

Fig.2 Graph G.

3. Conclusion

In this paper, we discussed the probability occurring Grundy coloring of graphs. We show that the probability is very low under minimum steps. In actual channel assignment of wireless communication, it may not be necessary to assume the worst case. Since the graphs dealt with in this paper are small, we can calculate the probabilities. We need to find methods to compute probabilities on larger graphs. Based on the results, we would like to calculate the appearance probability of the worst case by computer simulation in a situation close to reality.

In actual service, the blocking probability is required to be below a certain value. If the maximum number of channels is prepared, the blocking probability is 0%, but it has not reality. In the future we would like to focus on probability calculations that consider the blocking probability.

References

[1] H. Tamura, S. Matsumoto, K. Nakano, M. Sengoku, On Graph Coloring with Relation to Channel Assignment in Wireless Networks, IEICE Trans. Fundamentals, Vol.J102-A,No.7,pp.214-223,Jul. 2019.

[2] Tommy R. Jensen, Bjarne Toft, Graph Coloring Problem, John Wiley & Sons,1994.

[3] P. M. Grundy, Mathematics and games, Eureka, 2: 6–8, 1939.

[4] Leizhen Cai and Xuding Zhu, Game Chromatic Index of k-Degenerate Graphs, J. Graph Theory, Vol.36, 3, pp.144-155, 2001.

[5] H. Tamura and K. Nakano, On the probability of coloring with the maximum number of colors in graphs, IEICE Technical Report, ICTSSL2023-12, 2023-5.

Simulation of Sub-terahertz Leaky Wave Antenna for Beyond 5G

Hiroshi Hashiguchi[1,*] and Naobumi Michishita[1]

[1]Department of Electrical and Electronic Engineering, National Defense Academy

*`hhiroshi@nda.ac.jp`

The full paper of this paper has been published in Journal of Advanced Simulation in Science and Engineering (JASSE).

DOI: `https://doi.org/10.15748/jasse.11.83`

JSST2023

On Closeness Centrality Functions

Masakazu SENGOKU* and Hiroshi TAMURA**
*Graduate Institute for Entrepreneurial Studies
** Chuo University
* `masakazu.sengoku@gmail.com`

Abstract. There are various networks such as communication, social, biological, geographic, or contact networks under different disciplines. In these complex networks, centrality metrics have been used in order to study and analyze their effect on network resilience or to identify highly influential nodes. In this paper, we study closeness centrality. There are several ways of expressing closeness centrality mathematically which are called closeness centrality functions. We will investigate the characterization of closeness centrality functions.

Keywords: Complex networks, Closeness centrality functions, Graph theory

1. Introduction

There are various networks such as communication (World Wide Web , Internet, Mobile, etc.), social, biological, geographic, or contact networks under different disciplines. In these complex networks, centrality metrics have been used in order to study and analyze their effect on network resilience or to identify highly influential nodes in which the analytical method is used in big data analysis. As centrality metrics, degree centrality, neighbor centrality, eccentricity centrality, closeness centrality, betweenness centrality, eigenvector centrality etc. are known. In this paper, we study closeness centrality. There are several ways of expressing closeness centrality mathematically which are called closeness centrality functions. We will investigate the characterization of closeness centrality functions.

2. Closeness Centrality

The advantage of being central in this way comes from the possibility of sending or broadcasting information, being sure the time needed to reach the whole network is as short as possible. Closeness centrality is based on this idea: for each node, you calculate the distance to all the other vertices in the network, and define a centrality in which shorter distances imply higher closeness centrality, and vice versa. There are several ways of expressing closeness centrality mathematically. In a connected graph $G=(V, E)$, where V is the set of vertices and E is the set of edges, let the length(the number of edges) of a shortest path between vertices v_i and v_j be $d(v_i, v_j)$.Then, the following closeness centrality indices are known as the main ones.[1]-[5]

$$C(v_i) = \frac{1}{\sum_{v_j \in V} d(v_i, v_j)} \tag{1}$$

$$C_A(v_i) = \left(\frac{\sum_{v_j \in V} d(v_i, v_j)}{|V|-1}\right)^{-1} = \frac{|V|-1}{\sum_{v_j \in V} d(v_i, v_j)} \tag{2}$$

which is the formula where $C(v_i)$ is normalized by ($|V| - 1$).

$$C_{A'}(v_i) = \left(\frac{\sum_{v_j \in V} d(v_i,v_j)}{|V|} \right)^{-1} = \frac{|V|}{\sum_{v_j \in V} d(v_i,v_j)} \tag{3}$$

which is the formula where $C(v_i)$ is normalized by ($|V|$).

$$C_H(v_i) = \frac{1}{|V|-1} \sum_{v_j \in (V-v_i)} \frac{1}{d(v_i,v_j)}$$

$$= \frac{1}{|V|-1} \sum_{v_j \in V, d(v_i,v_j)>0} \frac{1}{d(v_i,v_j)} \tag{4}$$

which is the harmonic mean of the distances.

$$C_E(v_i) = 2^{-\sum_{v_j \in V} d(v_i,v_j)} \tag{5}$$

$$C_T(v_i) = \sum_{v_j \in V, d(v_i,v_j)<\infty} \{(|V|-1) - d(v_i,v_j)\ \} \tag{6}$$

Let us consider $G=(V, E)$ of Fig.1 as an example.

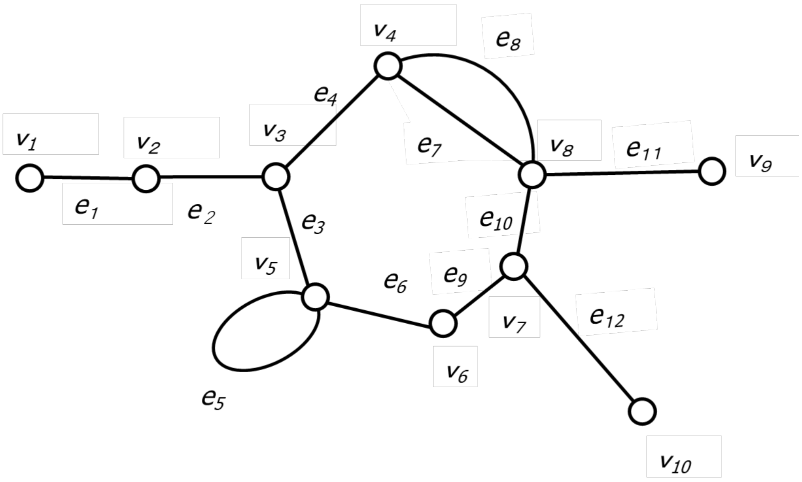

Fig.1 A graph $G=(V, E)$.

$d(v_1, v_2)=1$, $d(v_1, v_{10})=6$, ...

$\sum_{v_j \in V} d(v_1,v_j) = 33$, $\sum_{v_j \in V} d(v_2,v_j) = 25$, $\sum_{v_j \in V} d(v_3,v_j) = 19$, $\sum_{v_j \in V} d(v_4,v_j) = 17$, …

$C(v_1) = 1/33 = 0.03$, $C(v_2) = 1/25 = 0.04$, $C(v_3) = 1/19 = 0.05$, $C(v_4) = 1/17 = 0.059$...
$C_A(v_1) = 9/33 = 0.27$, $C_A(v_2) = 0.36$, $C_A(v_3) = 0.47$, $C_A(v_4) = 0.53$...
$C_{A'}(v_1) = 10/33 = 0.30$, $C_{A'}(v_2) = 0.4$, $C_{A'}(v_3) = 0.53$, $C_{A'}(v_4) = 0.59$...
$C_H(v_1) = (1/9)(1/1 + 1/2 + 1/3 + 1/3 + ... + 1/6) = (1/9)(97/60) = 0.18$, $C_H(v_2) = 0.49$,
$C_H(v_3) = 0.60$, $C_H(v_4) = 0.50$...
$C_E(v_1) = 2^{-33} = 1.16 \times 10^{-10}$, $C_E(v_2) = 2.98 \times 10^{-8}$, $C_E(v_3) = 1.91 \times 10^{-6}$,
$C_E(v_4) = 7.63 \times 10^{-6}$. . . .
$C_T(v_1) = (9-0)+(9-1)+(9-2)+…+(9-6) = 90-33 = 57$, $C_T(v_2) = 65$,
$C_T(v_3) = 71$, $C_T(v_4) = 73$…

In the above example, the maximum value calculated by $C(v_i)$, $C_A(v_i)$, $C_{A'}(v_i)$, $C_E(v_i)$ and $C_T(v_i)$ is at vertex v_4. On the other hand, the maximum value calculated by $C_H(v_i)$ is at vertex v_3. Although the maximum value calculated by $C(v_i)$, $C_A(v_i)$, $C_{A'}(v_i)$, $C_E(v_i)$ and $C_T(v_i)$ is at same vertex v_4, the difference between the values of vertices by the indices is different. The difference depends on the nature and environment etc. of the network. That is, the optimum closeness centrality indices will be selected according to the nature and environment of the network.

3. A Generalization of Closeness Centrality Functions

Let us considers that a high degree of centrality dues to the following two properties and let us call a function that satisfies (i) and (ii) a closeness centrality function.

(i) The degree of centrality of the vertices v_i and v_j in which the length between v_i and v_j has decreased, increases.

(ii)For an increase in the degree of centrality of a vertex, the increment of the vertices v_i and v_j is greater than the increment of the vertex in their vicinity.

Let us consider the following forms of the positive real function as a generalization of the closeness centrality functions, where $F(v_i)$: the greater the value of the function, greater the degree of centrality of a vertex, $T(v_i)$: the smaller the value of the function, greater the degree of centrality of a vertex.

$$F(v_i) = \sum_{v_j \in V} g\left(d(v_i, v_j)\right) = \sum_{v_j \in V, d(v_i, v_j) = x_k} g(x_k) \tag{7}$$

$$T(v_i) = \sum_{v_j \in V} s\left(d(v_i, v_j)\right) = \sum_{v_j \in V, d(v_i, v_j) = x_k} s(x_k) \tag{8}$$

where x_k takes discrete values 0, 1, 2, 3, . . . and let $x_k = k$.

The necessary and sufficient conditions for $F(v_i)$ and $T(v_i)$ to be closeness centrality functions for any G are as follows. [6]

$$g(x_0) > g(x_1) \geqq g(x_2) \geqq \ldots\ldots,\quad s(x_0) < s(x_1) \leqq s(x_2) \leqq \ldots\ldots \tag{9}$$

$$2g(x_k) \leqq g(x_{k-1}) + g(x_{k+1}) \quad (\forall k \geqq 1),\ 2s(x_k) \geqq s(x_{k-1}) + s(x_{k+1}) \quad (\forall k \geqq 1) \tag{10}$$

4. A Characterization of Closeness Centrality functions

Let $Q(v_i)$ be a closeness centrality function and consider the contribution $\Delta(Q, x_k)$ of a vertex v_j to $Q(v_i)$, where $d(v_i, v_j) = x_k$.

$$\Delta(Q, x_k) = \{ Q(v_i) \boxplus x_k \} - Q(v_i) \tag{11}$$

where $\{ Q(v_i) \boxplus x_k \}$ is obtained by adding x_k to the term consisting of the distance $d(\cdot, \cdot)$ in $Q(v_i)$. Let us show an example of $\{ Q(v_i) \boxplus x_k \}$ on $C(v_i)$ in (1). $\{ C(v_i) \boxplus x_k \} = 1/\{\left(\sum_{v_j \in V} d(v_i, v_j)\right) + x_k\}$.

Theorem 1

Closeness centrality functions $C(v_i)$, $C_A(v_i)$, $C_{A'}(v_i)$, $C_H(v_i)$, $C_E(v_i)$ and $C_T(v_i)$ are decreasing function with respect to the distance and the contribution $\Delta(Q, x_k)$ of distance x_k to a closeness centrality function Q satisfies the following inequality.

$$2\Delta(Q, x_k) \leqq \Delta(Q, x_{k-1}) + \Delta(Q, x_{k+1}) \ . \tag{12}$$

□

Let us consider the generalization of $C(v_i)$, $C_A(v_i)$, $C_{A'}(v_i)$, $C_E(v_i)$ and $C_T(v_i)$ using $T(v_i)$ as follows.

$$C_\gamma(v_i) = \frac{1}{T(v_i)} \tag{13}$$

$$C_{A\gamma}(v_i) = \frac{|V|-1}{T(v_i)} \tag{14}$$

$$C_{A'\gamma}(v_i) = \frac{|V|}{T(v_i)} \tag{15}$$

$$C_{H\gamma}(v_i) = \frac{1}{|V|-1}\sum_{v_j \in V, d(v_i,v_j)>0} 1/s(d(v_i,v_j)) \tag{16}$$

$$C_{E\gamma}(v_i) = 2^{-T(v_i)} \tag{17}$$

$$C_{T\gamma}(v_i) = |V|(|V|-1) - T(v_i) \tag{18}$$

We obtain the following theorem.

Theorem 2

Closeness generalized centrality functions $C_\gamma(v_i), C_{A\gamma}(v_i), C_{A'\gamma}(v_i), C_{H\gamma}(v_i), C_{E\gamma}(v_i)$ and $C_{T\gamma}(v_i)$ are decreasing function with respect to the distance and the contribution $\Delta(Q_\gamma, x_k)$ of distance x_k to a closeness generalized centrality function Q_γ satisfies the following inequality.

$$2\Delta\left(Q_\gamma, x_k\right) \leqq \Delta\left(Q_\gamma, x_{k-1}\right) + \Delta\left(Q_\gamma, x_{k+1}\right) . \tag{19}$$

□

Note that $F(v_i)$ also satisfy Theorem 2.

Let us show an example. Let $s(x_0)=0$, $s(x_1)=1$, $s(x_2)=1.5$, $s(x_3)=1.8$, $s(x_4)=1.8$, $s(x_5)=1.8$ ...where $2s(x_k) \geqq s(x_{k-1}) + s(x_{k+1})$ $(\forall k \geqq 1)$. Then , formula (19) is confirmed for $C_\gamma(v_i), C_{A\gamma}(v_i), C_{A'\gamma}(v_i), C_{H\gamma}(v_i), C_{E\gamma}(v_i)$ and $C_{T\gamma}(v_i)$.

In Fig.1, $C_\gamma(v_1)=0.066$, $C_\gamma(v_2)=0.071$, $C_\gamma(v_3)=0.078$, $C_\gamma(v_4)=0.075$,... and $C_{H\gamma}(v_1)=0.62$, $C_{H\gamma}(v_2)=0.68$, $C_{H\gamma}(v_3)=0.74$ and $C_{H\gamma}(v_1)=0.70$... .

The maximum value calculated by $C_\gamma(v_i)$ and $C_{H\gamma}(v_i)$ is at vertex v_3. In this example, since the value of $s(x_i)$ above x_3 is constant, the value of the centrality function is determined by the nearest and next nearest neighbors. That is, although closeness generalized centrality functions are derived for the closeness centrality, they are also applicable to neighbor centrality. This means that the generalization of centrality functions leads to the extension of applications.

5. Conclusions

We studied the characterization of the closeness centrality functions and their generalizations, and showed that they have common characteristics. This result contributes to the investigation of the nature of closeness centrality functions as well as to the extension of their applications.

References

[1] H. Tamura, K. Nakano and M. Sengoku, *Network Engineering,* IEICE, Corona Pub. 2020.

[2] Matjaž Krnc a and Riste Škrekovski b,c, “Centralization of transmission in networks”, Discrete Mathematics 338 (2015) 2412–2420, Elsevier B.V. 2015

[3] Sergio Gómez, *Centrality in Networks: Finding the Most Important Nodes*, Springer Nature Switzerland AG 2019

[4] Duanbing Chena, Linyuan Lüb, Ming-Sheng Shanga, Yi-Cheng Zhanga,b and Tao Zhoua,c, “Identifying influential nodes in complex networks”, Physica A: Statistical Mechanics and its Applications, 39(4), 1777-1787, 2011

[5] Z. Wan, Y. Mahajan, B.W. Kang, T.J. Moore, and J.H. Cho, “A survey on centrality metrics and their network resilience analysis,” IEEE Access, vol.9, pp.104773–104819, July 2021.

[6] M. Sengoku, *Graph Theory and Mobile Communications,* Advanced Series in Electrical and Computer Engineering, 23, World Scientific Pub Co Inc, 2023

Social network structures that achieve both infection control and knowledge discovery efficiency

Tetsuo Imai[1,*] and Ryo Yashiki[2]

[1]Graduate school of Information Sciences, Hiroshima City University
[2]Faculty of Information Sciences, Hiroshima City University

*`imai@hiroshima-cu.ac.jp`

The full paper of this paper has been published in Journal of Advanced Simulation in Science and Engineering (JASSE).

DOI: `https://doi.org/10.15748/jasse.11.102`

A Classification Algorithm for Facial Expression by Face Landmark Detection and Deep Neural Network

Siu Kang* and Kohei Otomo

Graduate School of Science and Engineering, Yamagata University

*`siu@yz.yamagata-u.ac.jp`

Abstract. We proposed a classification algorithm for facial expression recognition. The algorithm presents a classification of facial expressions by the deep convolutional neural network after automatic facial landmark detection. After the training by a large open dataset, the accuracy of the algorithm showed 66.2% in classification of seven categories.

Keywords: Facial expression recognition, Convolutional neural network, Deep learning, Feature value engineering, Sentimental analysis

1. Introduction

Recent progress in artificial intelligence affected automatic facial image detection and classification. Since facial parts detection is one of the core targets of facial image recognition, classical box-shape detection by rectangle has been implemented in standard image processing libraries such as OpenCV for a long time. Nowadays, more advanced detection methods including the shape of the facial parts expressed as dots, and their application which can provide real-time facial filtering, were implemented.

Facial expression recognition has been studied in various research fields such as psychology, psychiatry, etc. The algorithm is very useful in marketing and entertainment because facial expressions could capture emotional information from actors or actresses and the extracted facial expression could be overlayed onto virtual characters or avatars in real-time. Continuous monitoring and automatic detection of facial expressions were also applied to improving customer service in marketing, and predictive detection of signs of potential dangers in the security field.

In the classification of facial expression, "Action Unit" (AU)[1] defined as the combinations of facial parts transformation was well known as the basis of facial expression. However, facial expression recognition based on the AU requires annotation data for facial parts and is limited to frontal face recognition. Here, we proposed a novel facial expression recognition algorithm by the combination of automatic facial landmark detection and a deep neural network. The present method might lead to high-accurate and orientation-free facial recognition.

2. Method

2.1 Dataset

Small-scale and lab-controlled datasets were frequently used in facial expression recognition. However, they were insufficient in real-world and large-scale public data was standard in recent machine learning. We analyzed the Face Expression Recognition 2013 (FER2013) dataset which was once the subject of Prediction Competition on a machine learning platform, Kaggle[2]. The FER2013 consists of 48 x 48-pixel face images labeled with seven categories of facial expressions by various ethnicities, genders, and ages (Figure 1). The dataset also includes not only real humans but also illustrations. In particular, the orientations of the image are not orthogonally facing but diverse.

In the present study, we proposed a classification algorithm that is effective not only on frontal face images but also on natural raw images by a combination of facial landmark detection and deep neural network.

Fig 1. Example images in the FER2013 dataset

2.2 Image processing

All the images were upsampled for facial landmark detection. Since the face images have various angles and ranges, all landmarks may not fit within the image area for each face image. Therefore, all the images were enlarged by zero-padding with a margin of a few pixels width. The 68 landmarks from individual images were obtained by applying automatic landmark detection proposed by Kazemi and Sullivan[3]. We prepared three types of images, RAW (the original image itself), DOTs (landmark points), and LINEs (landmark points connected with lines). As training data for the deep neural network described in the next section, we created three-channel data by combination of these three image types.

2.3 Classification by deep neural network

In order to classify facial expressions, we employed a deep neural network based on a convolutional neural network (CNN)[4] (Figure 2).

In the present study, we were trying to discriminate seven categories of facial expressions, “Angry”, “Disgust”, “Fear”, “Happy”, “Sad”, “Surprise” and “Neutral” (see also Figure1).

Training data was augmented by image rotation from -45 to +45 degrees. The training epoch was 200 and classification accuracy was estimated by the average of the last 10 epochs in inference after the training.

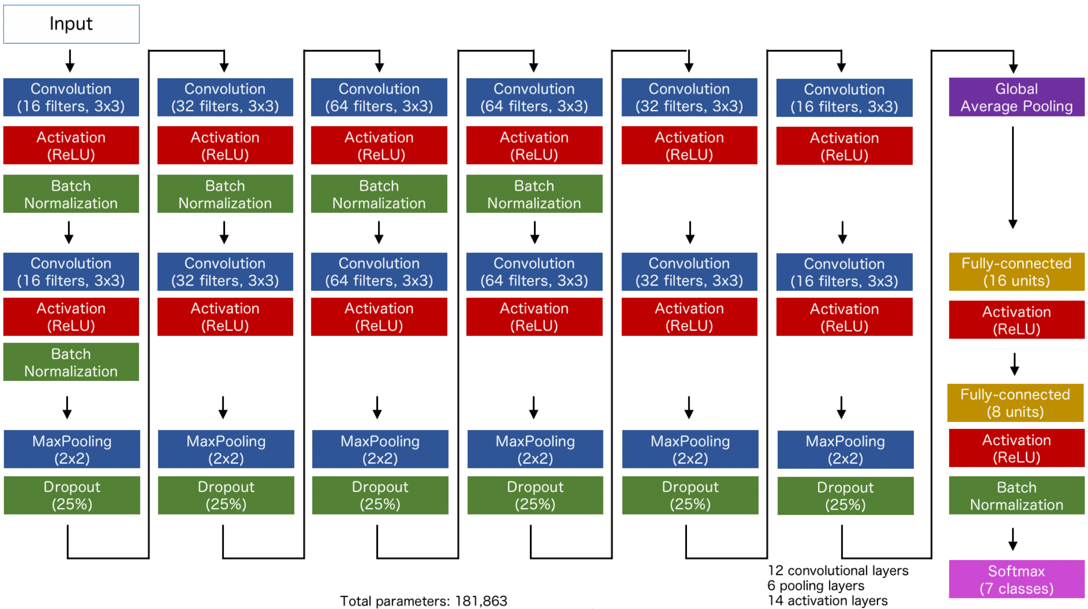

Total parameters: 181,863
Trainable parameters: 181,463
Non-trainable parameters: 400

Optimizer: Adadelta
Batch size: 128

12 convolutional layers
6 pooling layers
14 activation layers
2 fully-connected layers
1 output layer (softmax)

Fig 2. Network organization designed for the facial expression recognition

3. Result

The time course of the accuracy and loss function was shown in Figure 3. We can see that both accuracy and loss led to stational values during training and the inference of test data after the training (Figure 3). The confusion matrix of actual and predicted labels during inference after training was shown in Figure 4. Examples of classification were also shown in Figure 5. The accuracy of the seven-class classification for the inference after the training was 66.2% (chance level was 14.3%).

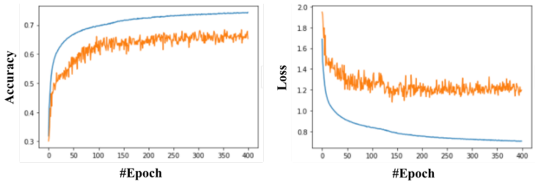

Fig 3. Time course of accuracy and loss for training data (blue) and test data (orange).

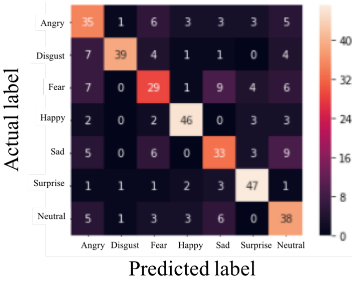

	Angry	Disgust	Fear	Happy	Sad	Surprise	Neutral
Angry	35	1	6	3	3	3	5
Disgust	7	39	4	1	1	0	4
Fear	7	0	29	1	9	4	6
Happy	2	0	2	46	0	3	3
Sad	5	0	6	0	33	3	9
Surprise	1	1	1	2	3	47	1
Neutral	5	1	3	3	6	0	38

Fig 4. Confusion matrix of actual- and predicted-classes

Fig 5. Examples of correctly-classified images

4. Conclusions

In the present study, we proposed a facial expression recognition algorithm based on the facial landmark. The images in the FER2013 dataset were collected by web search from 184 words for the six fundamental expressions such as “Angry”, “Happy” and an additional one “Neutral”. The class labels of training data were assigned based on the search word, so the validity of the labels was not guaranteed. Although there still were some classification errors due to such label ambiguity, the present method showed high accuracy in facial expression recognition for raw big data independent of facial orientation. In order to improve classification accuracy, data augmentation and network organization should be modified in future study.

Author information

The current affiliation of K. O. is FUJITSU CLOUD TECHNOLOGIES LIMITED.

References

[1] J. F. Cohn, Z. Ambadar, and P. Ekman (2007) “Observer-based measurement of facial expression with the facial action coding system”. *The Handbook of Emotion Elicitation and Assessment*, pp.203-221

[2] “Kaggle”, https://www.kaggle.com

[3] V. Kazemi and J Sullivan (2014) “One Millisecond Face Alignment with an Ensemble of Regression Trees”, *2014 IEEE Conference on Computer Vision and Pattern Recognition,* Columbus, OH, USA, 2014, pp. 1867-1874, doi: 10.1109/CVPR.2014.241.

[4] K. Fukushima. Neocognitron: a self-organizing neural network model for a mechanism of pattern recognition unaffected by shift in position. Biological Cybernetics, 36(4):93–202, 1980.

Triple Neural Network

Zhongda Liu[1,*], Hitoaki Yoshida[2], Satoshi Kawamura[3]

[1]Faculty of Science and Engineering, Ishinomaki Senshu University, Japan
[2]Faculty of Education, Iwate University, Japan
[3]Super-Computing and Information Sciences Center, Iwate University, Japan

[*]`liuzd@isenshu-u.ac.jp`

Abstract. The pseudo-random number generator is essential to a symmetric-key cipher. In this paper, we propose a new chaotic and random neural network consisting of three neurons to generate pseudo-random numbers. Compared to the previous neural network, the determinism of the time series is lower, and the rate of pseudo-random number generation is about 86% faster, and 69 times faster than AES.

Keywords: Neural Network, Pseudo-Random Number, Symmetric-Key Cipher

1. Introduction

Symmetric-key ciphers are widely used to protect communication data in IoT devices and embedded systems. The pseudo-random number (PRN) generator is essential to a symmetric-key cipher. We have been studying PRN generation by a chaotic and random neural network (CNN) [1][2] for symmetric-key encryption systems. Recently, we applied a CNN to an in-vehicle network that requires a low computation cost and high level of security[3].

In the present study, a new type of neural network that is also chaotic and random is proposed to generate PRNs. In order to provide high performance, the network consists of only 3 neurons, and a new efficient active function is applied to each neuron.

2. Triple Neural Network

Unlike the standard CNN of 4 neurons, a triple neural network(TNN) is composed of only 3 neurons to generate PRNs (Fig. 1). Specifically, those three neurons generate chaotic and random time series. Each neuron is computed with 32-bit fixed-point arithmetic (Q5.26) in a discrete time system.

The output of the *i*th neuron at time t is defined in Eq. (1), where the total value of inputs u_i at previous time $(t-1)$ is defined in Eq. (2) and new activation-function f is defined in Eq. (3) to reduce computing cost.

$$x_i^t = f(u_i^{t-1}) \tag{1}$$

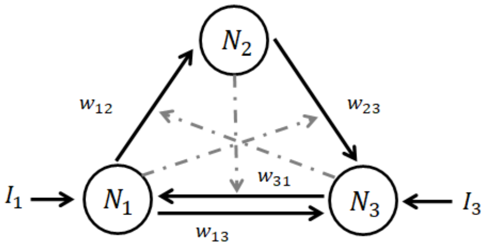

Figure 1: TNN has only three neurons in a discrete time system

$$u_i^{t-1} = \sum_{j=1}^{n} w_{ij} x_j^{t-1} + I_i \tag{2}$$

$$f(u_i^t) = u_i^t + x_j^{t-1} mod\, M \tag{3}$$

In Eq. (2), I_i is an external input of the ith neuron, x_j is an input from the jth neuron at the previous time (see the arrows with solid lines in Fig. 1) and w_{ij} is a synaptic weight. In Eq. (3), x_j^{t-1} is the output of the jth neuron (see the arrows with broken lines in Fig. 1) at the previous time, M is a constant.

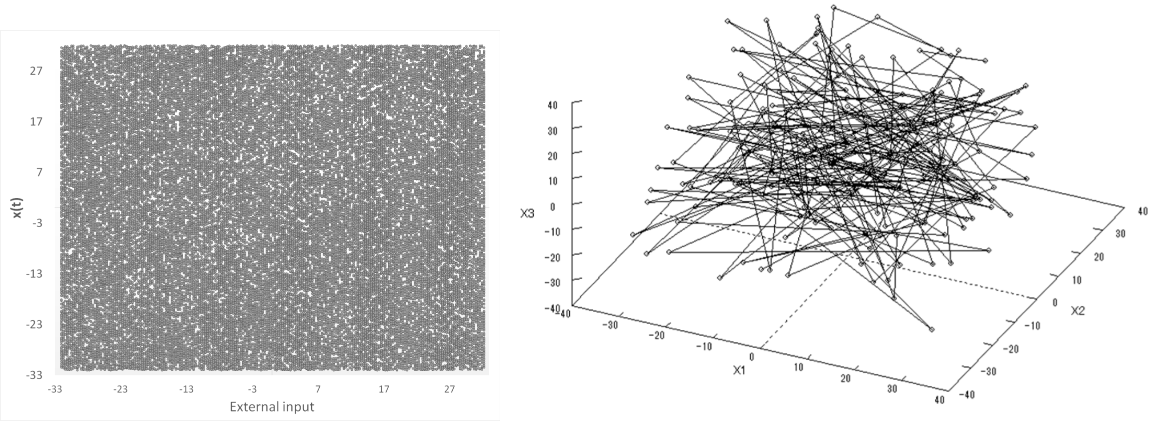

(a) Time series from a neuron

(b) Time series from the 3 neurons (200 points)

Figure 2: Input-output characteristics of a TNN

The time series from one neuron are shown in Figure 2(a). Figure 2(b) shows the time series from all 3 neurons. In order to observe the trajectory, we only plot 200 points in Figure 2(b). The trajectory is extended to three-dimensional space, whereas that of a CNN can be extended to only two dimensions. The time series of the TNN has no bifurcation but has chaotic characteristics; furthermore, all of the maximum Lyapunov exponents satisfy $\lambda > 3.6$. Those results demonstrate that the time series of a TNN are not only chaotic but also sensitively random.

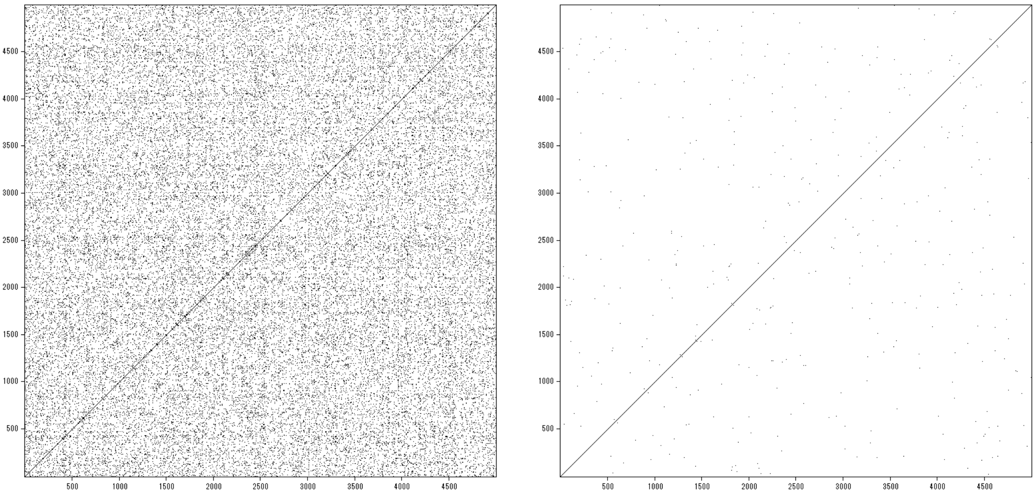

(a) CNN

(b) TNN

Figure 3: Iso-Directional Neighbors Plot

In Figure 3, the determinism of a time series is analyzed as an iso-directional neighbors plot (IDNP). An IDNP shows the set of points which maintain neighbors and move in similar directions[4]. The IDNP of the TNN has fewer points than the CNN, which suggests that the time series of the TNN has a lower degree of determinism and so is harder to predict than the CNN.

3. PRNs for Cipher

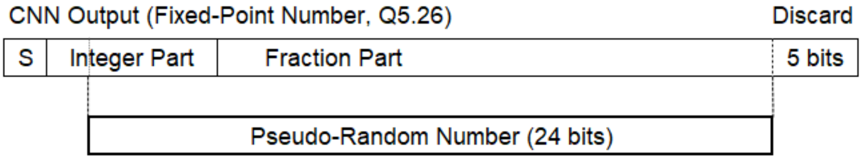

Figure 4: The extraction of PRNs from a neuron output of TNN

Figure 4 shows how to extract PRNs for a cipher in this study. For each fraction corresponding to a neuron output of a TNN, the lowest 5 bits are discarded and then the next lowest 24 bits are extracted as a PRN. Such PRNs from a TNN are applied to a symmetric-key cipher.

3.1. Randomness

NIST Special Publication 800-22 is widely used for a cipher as a statistical test suite for randomness. We performed the NIST test, generating $10^6 \times 1{,}000$ bits of PRNs. The PRNs from the TNN passed the NIST test.

3.2. Performance

The rate of PRN generation is an essential issue for a cipher. Here, we confirm the rate of the TNN and compare it to the CNN and the AES in the counter mode that turns the AES into a PRN generator. We performed three measurements with an Intel Xeon Silver 4208 2.1 GHz CPU and calculated the mean as the rate. As a result, the rate of the TNN was found to be about 2.10 Gbps, whereas the rate of the CNN was about 1.13 Gbps and that of the AES was only about 0.03 Gbps. The TNN has the best performance. It is about 86% faster than the CNN and 69 times faster than the AES.

4. Conclusions

In this study, we proposed a new neural network, TNN, as the PNG generator for a cipher. A TNN has lower determinism and higher performance as a PRN generator. Further, the PRNs from a TNN passed the NIST test.

As future work, we will analyze the characteristics of a TNN in detail. Especially, we are going to determine all transient trajectories and closed trajectories.

References

[1] H. Yoshida, H. Fukuchi, and T. Murakami, "Implementation of high-speed pseudo-random-number generator with chaotic and random neural networks," in *Proceedings of the 53rd Hawaii International Conference on System Sciences*, 2020.

[2] H. Yoshida, T. Murakami, and Z. Liu, "High-speed and highly secure pseudo-random number generator based on chaos neural network," *New Trends on System Science and Engineering: Proceedings of ICSSE*, vol. 276, pp. 224–237, 2015.

[3] Z. Liu, T. Murakami, S. Kawamura, and H. Yoshida, "Chaotic and random neural network cipher for in-vehicle network security," *IEICE Communications Express*, vol. 10, no. 12, pp. 1026–1031, 2021.

[4] S. HORAI, T. YAMADA, and K. AIHARA, "Determinism analysis with iso-directional recurrence plots," *IEEJ Transactions on Electronics, Information and Systems*, vol. 122, no. 1, pp. 141–147, 2002.

Influence of the MR-HMD system on the gait motion for the elderly people

Shigeho Noda[1*], Daigo Ikeno[2,3], Hideo Miyachi[2]

[1]RIKEN Center for Advanced Photonics
[2] Tokyo City University
[3]Hitachi Ltd.
*`shigeho@riken.jp`

Abstract. The use of physical obstacles in the measurement of the gait of elderly people entails risks such as the subjects fallin over. Therfore, the risks can negrect by displaying virtual obstacles to the subjects. However, it is known that differences occur in the perception of reality and virtuality. It is essential to evaluate the effects of these differences in order to construct a correct measurement method. In this study, we ecaluated the effects on the gait using a video-through MR-HMD system.

Keywords: Mixed Reality, Gait Measurement, Elderly people, Vision

1. Introduction

We are developing a system to evaluate motor function and reflex ability by measuring daily movements such as walking, and to establish prediction and prevention techniques for physical weakness. In order to measure not only normal walking but also avoidance movements in the obstacles such as steps and thresholds, we have constructed a measurement environment using a video-through MR-HMD system [1]. However, when this environment was compared with the real environment, it was found that there was a difference in the highest point reached by the leg, and that there was a difference between the two [2]. Therefore, with the aim of obtaining further indicators to simulate the same situation as in reality, we evaluated and examined the differences in walking behavior in normal walking with and without the MR device in a state with no obstacles. In this paper, we will report the results our study.

2. Methods

The video-through MR HMD system worn by the subject was created by attaching the OvrvisonPro which the stereo camera for HMD, to the OculusRift. Motive which an optical motion capture system, was used for gait measurement. Fig. 1 shows a photograph of the measurement environment. The measurement section is 4 m long, with an 80-cm walking distance before the measurement. Sixteen optical sensors for optical motion capture were placed around the measurement section on a tripod, and calibration was performed for each measurement. Subjects walked with motion capture markers on their legs and HMD. (Fig. 2)

Fig. 1 The measurement environment.

Fig. 2 Subject with HMD and Marker.

The subjects were 33 volunteers ranging in age from 55 to 80 years old. Fluorescent lights were not turned on during the measurement to suppress flicker generated in the video-through images. For the gait measurement, optical motion capture markers were attached to the subjects' feet at three points (heel, thumb toe, and base of pinky toe) for a total of six points, The three-dimensional positions of the each markers were measured at 1/100 second intervals.

The measurement protocol is shown in Table 1. As a validation of displaying obstacles in MR, the height of the virtual obstacles presented to the subject were estimated by matching it with the real obstacles. The equivalence of MR obstacle and real obstacle perception was suggested, and the feasibility of application in this field was confirmed.[3]

Table 1 Measurement protocol.

Name	Protocol
Task1	Walking without HMD
Task2	Walking with HMD
Pro Task	Walking with HMD and displaying obstacles
Task3	Walking with HMD
Task4	Walking without HMD

3. Results

As a sample of the measurement data, Fig. 3 shows the trajectory of the right heel marker. The direction of forward is the X-axis and the vertical direction is the Y-axis. Fig. 3 shows the trajectory for four steps, and the distance between the minima of the four points was defined as the stride length. The stride length calculated from each marker was calculated and discussed. Three subjects were excluded from the study due to incomplete measurement data, and a total of 120 tasks, four tasks for each of the 30 subjects, were tabulated.

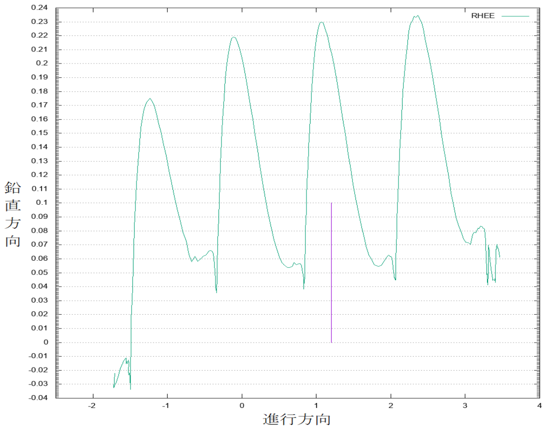

Fig. 3 The measurement result of the right heel marker.

For most subjects, the average value of stride length was smaller when wearing the HMD than when not wearing the HMD. The average value of walking speed was also smaller. This suggests that wearing the HMD restricted the walking motion of the subjects. Fig. 4 shows the change in stride length calculated from the right heel marker for each subject in Task 1 and Task 2. Fig. 5 shows the stride length change calculated from the right heel marker for each subject in Task 3 and Task 4. In Fig. 4, it can be seen that there are many differences in stride length between subjects with and without HMDs, but in Fig. 5, the differences are small. This indicates that the subjects were sufficiently accustomed to wearing the HMD, and the questionnaire we obtained separately showed the same impression. This indicates that it is important for subjects to become accustomed to the environment before measuring walking movements using a video-through MR-HMD.

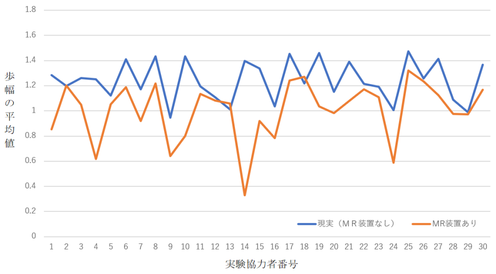

Fig. 4 Stride length for Task1 and Taks2.

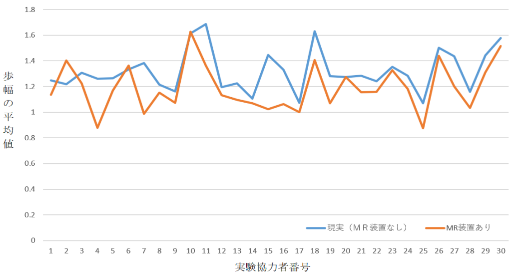

Fig. 5 Stride length for Task3 and Taks4.

4. Discuccion and Conclusion

We evaluated the effects of a video-through MR device on the measurement of walking behavior in elderly subjects. We measured simple gait in a realistic environment and when wearing the MR device, and confirmed that there were differences in stride length and walking speed between the two environments. We also found that the differences between the real environment and the MR environment decreased as the subjects repeated the walking motions in the MR environment. It is suggested that the number of trials should be taken into consideration when conducting measurement in the MR environment in the future.

References

[1] Hideo Miyachi, Shigeho Noda, Shintaro Kawahara, Yurika Kawazoe, A study on acquisition of oedestrian motion information using the simple MR system, The 22nd annual conference of the virtual reality society of Japan, Sept. 2017 (in Japanese)

[2] Tomoyasu Ishii, Hideo Miyachi, Shigeho Noda, Shintaro Kawahara, Evaluation of the effect of wearing the video-through MR system on walking motion, The 23rd annual conference of the virtual reality society of Japan, Sept. 2018 (in Japanese)

[3] Hiroshige Takeichi, Tomoyasu Ishii, Shigeho Noda, Ryutaro Himeno, Development of fall prediction and prevention technology using the mixed reality technology, The 23rd annual conference of cirtual reality society of Japan, Sept. 2018 (in Japanese)

JSST 2023

Three-Dimensional Ion Crescent-Shaped Velocity Distribution in Magnetic Reconnection

Shunsuke Usami[1,2,*] and Seiji Zeniani[3]

[1]National Institute for Fusion Science, National Institutes of Natural Sciences
[2]The University of Tokyo
[3]Kobe University

*`usami.shunsuke@nifs.ac.jp`

Abstract. By means of theory and particle simulations, we investigate crescent-shaped velocity distributions. Particle simulations demonstrate that ion crescent-shaped velocity distributions are formed in the outflow region of magnetic reconnection, and the ion crescents have a three-dimensional structure. We construct the theory explaining the three-dimensional crescent shape of ion velocity distributions, on the basis of three kinds of conservation laws of the canonical momentum, the energy, and the magnetic moment, assuming a spatial 1D electromagnetic field. Comparing the theory and our simulation result, we can see that the theory accounts for ion velocity distributions found in the simulation.

Keywords: Particle simulation, Crescent-shaped distribution, Magnetic reconnection

1. Introduction

Magnetic reconnection is a fundamental process in plasmas which contains various kinetic physics such as acceleration, heating, and chaotic motions. In order to clarify the kinetic physics related to magnetic reconnection, particle velocity distributions are analyzed in computer simulations and satellite observations. In 2016, electron crescent-shaped distributions have been observed by the MMS satellite [1], and have been investigated by particle simulations and theory [2, 3, 4]. In contrast, we deal with ion cases. We find ion crescent-shaped velocity distributions by means of particle simulations of magnetic reconnection and realize the difference from the electron crescent. Electron crescents are formed in asymmetric reconnection with no or a weak guide magnetic field, while ion crescents are created in symmetric reconnection with a strong guide field, where the guide field means the out-of-plane component of the magnetic field. Furthermore, we show that ion crescents have a three-dimensional structure in the velocity space, unlikely the electron crescents.

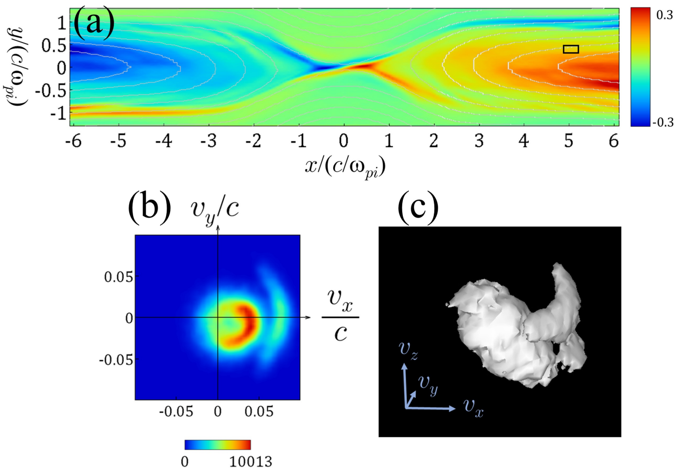

Figure 1: Simulation results of magnetic reconnection. (a) The magnetic field lines and electric field E_y (color contours), (b) the ion velocity distribution in the (v_x, v_y) plane at the boxed area, and (c) an isosurface of the ion density in the (v_x, v_y, v_z) space at the boxed area.

2. Particle simulation

We carry out particle-in-cell simulations of magnetic reconnection in the presence of a guide magnetic field. Figure 1(a) shows the magnetic field lines and the electric field E_y (color contours). Magnetic reconnection takes place at the center of the simulation domain. Figure 1 (b) displays an ion velocity distribution at the boxed area designated in Fig. 1(a) in the outflow region. We can find that a ring-shaped distribution [5, 6] exists near the central part and a crescent-shaped distribution coexists on the right side of it. In Fig. 1(c), we depict an isosurface of the ion density at the same boxed area in the (v_x, v_y, v_z) space. We can intuitively understand a three-dimensional crescent-shaped structure.

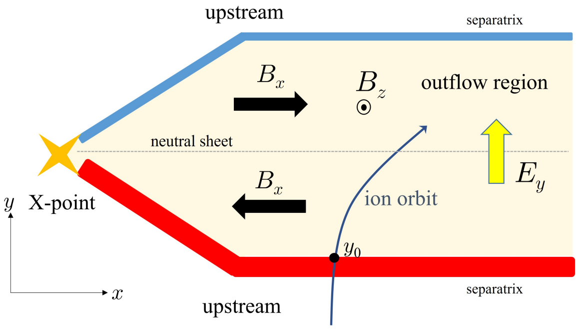

Figure 2: Schematic diagram of the electromagnetic fields and the orbit of a typical ion which makes up a crescent-shaped velocity distribution.

3. Theory for the crescent distribution

We construct a theory which explains the three-dimensional shape of ion crescent velocity distributions. Figure 2 shows the schematic diagram of the electromagnetic field and a typical ion orbit responsible for a crescent-shaped velocity distribution. The theory is based on the following two points. (A) Ions start from the lower-side of the upstream, cross the lower-side of the separatrix, and enter the outflow region. (B) The spatial 1D electromagnetic fields $E_y(y)$, $B_x(y)$, and $B_z(y)$ only exist in the outflow region under quasi-steady state. Integrating the equations of motion in the x and z directions from $t = 0$, when the ion position is $y = y_0$ as shown in Fig. 2, to a later time t, we obtain

$$v_x - v_{x0} = -\frac{q}{mc}A_x(y), \tag{1}$$

$$v_z - v_{z0} = -\frac{q}{mc}A_z(y), \tag{2}$$

where $A_x(y) = -\int_{y_0}^{y} B_z dy$ and $A_z(y) = \int_{y_0}^{y} B_x dy$. These mean the conservation of the canonical momentum. Next, the energy conservation is expressed as

$$\frac{1}{2}(v_{x0}^2 + v_{y0}^2 + v_{z0}^2) = \frac{1}{2}(v_x^2 + v_y^2 + v_z^2) + \frac{q}{m}\phi(y), \tag{3}$$

where $\phi(y) = -\int_{y_0}^{y} E_y dy$. The substitution of Eqs. (1) and (2) into Eq. (3) and the use of $v_{y0}^2 > 0$ lead to the following inequality,

$$\frac{q}{mc}\left(A_x v_x + A_z v_z\right) < \frac{1}{2}v_y^2 + \frac{q}{m}\phi - \frac{1}{2}\left(\frac{q}{mc}\right)^2\left(A_x^2 + A_z^2\right). \tag{4}$$

On the other hand, if we substitute the maximum velocity at $y = y_0$, $v_{0,\mathrm{max}}^2$ into $v_{x0}^2 + v_{y0}^2 + v_{z0}^2$ of Eq. (3), the equation becomes the following inequality,

$$v_x^2 + v_y^2 + v_z^2 < v_{0,\mathrm{max}}^2 - 2\frac{q}{m}\phi. \tag{5}$$

The inequalities (4) and (5) always hold for any cases, whereas the inequality derived below is satisfied when the magnetic moment is conserved in the moving frame with the outflow speed u_{out}, i.e., the downstream frame. (This will be satisfied when the guide field B_z [nearly uniform] is greater than the antiparallel reconnection field B_x.) The conservation of the magnetic moment and the kinetic energy in the downstream frame ($v_{dx} = v_x - u_{\mathrm{out}}$, $v_{dy} = v_y$, and $v_{dz} = v_z$, where d means the downstream frame.) are written as follows.

$$v_{d\perp}^2/B = v_{d\perp 0}^2/B_0, \tag{6}$$

$$v_{d\perp}^2 + v_{d\|}^2 = v_{d\perp 0}^2 + v_{d\| 0}^2 = v_{d0}^2, \tag{7}$$

where the subscriptions $\|$ and $\perp$ denote parallel and perpendicular to the magnetic field, respectively. Omitting $v_{d\perp}$ and $v_{d\perp 0}$ in Eqs. (6) and (7), and substituting maximum values into v_{d0}^2 and $v_{d\|0}^2$, respectively,

$$-Bv_\alpha + B_x u_{\mathrm{out}} < B_x v_x + B_z v_z < Bv_\alpha + B_x u_{\mathrm{out}}, \tag{8}$$

is derived in the laboratory frame, where

$$v_\alpha^2 = \left(1 - \frac{B}{B_0}\right)v_{d0,\mathrm{max}}^2 + \frac{B}{B_0}v_{d\|0,\mathrm{max}}^2. \tag{9}$$

4. Comparison between the theory and the simulation result

Lastly, we compare the theory with the ion velocity distribution at the boxed area in Fig. 1(a). Figure 3(a) illustrates the shape designated by the three inequalities (4), (5), and (8), and Fig. 3 (b) plots the velocities (v_x, v_y, v_z) of only the ions constituting the crescent part of Figs. 1(b)(c). Three-dimensional structures are projected to the (v_x, v_y) plane (red color) and to the (v_y, v_z) plane (blue color). In both the theory and the simulation, the projections in the (v_x, v_y) plane are convex upward and the projections in the (v_y, v_z) plane are convex downward. As a whole, 3D characteristic shapes are consistent between theory and simulation.

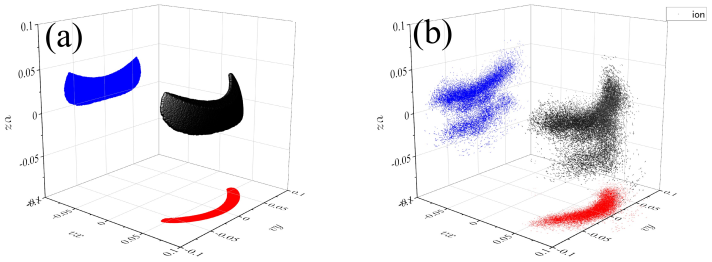

Figure 3: (a) Region derived by the theory and (b) velocity plots of the ions constituting the crescent part of Figs. 1(b)(c). In the panel (b), the crescent has two-layer structure. This issue is beyond the theory of Sec. 3, and will be briefly discussed in the presentation.

References

[1] J. L. Burch et al.: Electron-scale measurements of magnetic reconnection in space, *Science*, 352 (2016) aaf2939.

[2] N. Bessho et at.: Electron distribution functions in the diffusion region of asymmetric magnetic reconnection, *Geophys. Res. Lett.*, 43 (2016) 1828-1836.

[3] S. Zenitani et al.: Electron dynamics surrounding the X line in asymmetric magnetic reconnection, *J. Geophys. Res. Space Physics*, 122 (2017) 7396-7413.

[4] N. Bessho et al.: Effects of the guide field on electron distribution functions in the diffusion region of asymmetric reconnection, *Phys. Plasmas*, 26 (2019) 082310.

[5] S. Usami, R. Horiuchi, H. Ohtani: Effective heating of nonadiabatic protons in magnetic reconnection with a guide field, *Phys. Plasmas*, 24 (2017) 092101.

[6] S. Usami et al.: Dependence of the pickup-like ion effective heating on the poloidal and toroidal magnetic fields during magnetic reconnection, *Phys. Plasmas*, 26 (2019) 102103.

Analysis of plasma particle orbits in boundary layers with the efficient electrostatic particle-in-cell simulation code

Hiroki Hasegawa[1,2*] and Seiji Ishiguro[1,2]

[1]National Institute for Fusion Science, National Institutes of Natural Sciences

[2]Fusion Science Program, The Graduate University for Advanced Studies, SOKENDAI

*`hasegawa.hiroki@nifs.ac.jp`

Abstract. A sophisticated procedure to observe plasma particle orbits has been installed into the "up3bd" code which is a three-dimensional (3D) electrostatic particle-in-cell (PIC) simulation code for investigations of transport phenomena in fusion boundary layer plasmas or other plasmas in nature. In this procedure, particle-orbit data is collected into additional processes which are prepared for recording this data. In order to launch these additional processes, an MPI communicator is separated into a communicator for the main calculation and that for recording particle-orbit data. That is, communications among the additional processes are performed with the latter communicator. On the NEC SX-Aurora TSUBASA, an extra computer resource for the procedure is not necessary since the additional processes can be launched on Vector Hosts (VH). Using this procedure, we have observed phase-space orbits of ion particles thought to be accelerated with a collisionless drift wave.

Keywords: particle-in-cell, fusion boundary layer, phase-space orbit, stochastic ion heating

1. Introduction

The "up3bd" code is an efficient three-dimensional (3D) electrostatic particle-in-cell (PIC) simulation code which has been developed to study kinetic properties of transport phenomena in fusion boundary layer plasmas or other plasmas in nature. In the up3bd code, a one- or two-dimensional domain decomposition has been applied for large-scale simulations [1]. Although our previous 3D-PIC code, called "p3bd" [2], proved various microscopic dynamics in transports of a blob and a hole, which are filamentary coherent plasma structures generated in fusion boundary layers, e.g., Ref. [3]; it is difficult for the p3bd code to perform the blob generation process simulation which needs a large-scale system, since only particle data are parallelized in the code. However, the up3bd code is applicable to the large-scale simulation.

In large-scale simulations for the study of blob generations, the plasma density gradient perpendicular to the magnetic field is initially provided. This will induce some instabilities, that is, interchange or drift wave ones, which are related to the formation of coherent structures. On the other hand, it has been theoretically proposed that drift waves will cause stochastic ion heating and that it may bring coronal heating [4]. Thus, such a large-scale 3D-PIC simulation is considered to be a powerful method to kinetically study not only the blob generation but also the stochastic ion heating. In order to investigate such a heating with PIC simulations, phase-space orbits of accelerated particles should be recorded. Also, particle-orbit data is necessary to research details of cross-field plasma dynamics in a detachment state [5]. However, it is complicated for the up3bd code to save time variations of phase-space positions for designated particles, because the data of particles which move out to domains assigned to neighbor processes is transferred to these. Therefore, in this work, we have developed a sophisticated procedure to record particle-orbit data, which avoids the above difficulty and also keeps a computation speed of the main routine. Furthermore, using the procedure, we have observed the phase-space orbits of ion particles thought to be accelerated with a collisionless drift wave.

2. Procedure to record particle orbits

Since time variation data of all particles cannot be recorded, tracked particles should be extracted by designation with a flag. The up3bd code retains the particle data in a four-dimensional array during computation. Each dimension size of the particle data array corresponds to numbers of components in the phase space, particles per a thread on OpenMP parallelization, threads, and particle species, in order from the inner dimension. The size of the first dimension is six, i.e., three dimensions in space and three components for velocity, in the original up3bd code. In the installation of the procedure to record particle orbits, we have changed the size of the first dimension into seven. In this additional component, the flag for recording the data is saved. That is, if the data of a certain particle is recorded, an individual number is stored in the component. Also, the particles of which the flag is not zero can be visualized with an in-situ visualization library “VISMO” [6].

In the procedure, additional MPI processes which belong to an MPI communicator different from that for the main routines are prepared for recording the data. During the simulation, the data of designated particles is copied to these additional processes at intervals of arbitrary time steps. After that, the data is collected into a root process in the additional communicator and sorted with an individual flag number. Finally, the sorted data is written in a file. The procedure has been optimized for the NEC SX-Aurora TSUBASA in which each node called a “Vector Host” (VH) is composed of one scalar processor for controlling the system and eight “Vector

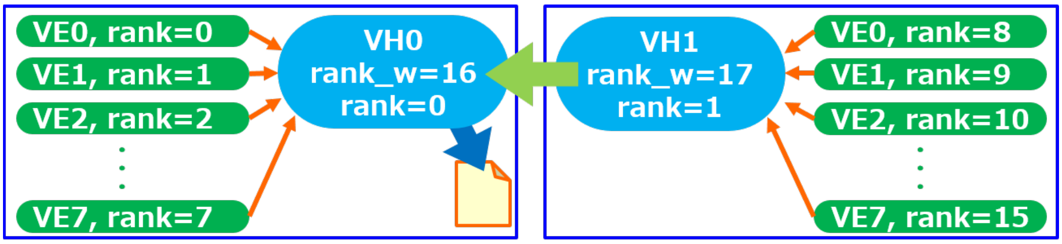

Figure 1: Schematic diagram of the procedure to record particle orbits on the NEC SX-Aurora TSUBASA. The green and light blue colors represent the MPI communicators for the main routines and for recording orbit data, respectively. The data of designated particles on Vector Engines (VEs) are copied to a scalar processor on the Vector Host (VH) which includes the VEs (orange arrows). After that, the data is collected into a root process in the light blue communicator (yellow green arrow) and the sorted data is written in a file (blue arrow).

Engine" (VE) accelerators for high-speed computing [7]. Although the main role of VH scalar processors is the control of the system, light computations can be performed with them. That is, heterogeneous computation is available. In the optimized procedure, the additional processes are launched on VH scalar processors using a Multiple Program Multiple Data (MPMD) model, as shown in Fig. 1. Thus, on the SX-Aurora TSUBASA, extra nodes for the recording are not necessary and the computation for the recording can be hidden under the main calculation on VEs. On other high performance computing systems, we should prepare extra nodes for the additional processes.

The updated up3bd code in which the procedure is applied has been run on the SX-Aurora TSUBASA of the Plasma Simulator at NIFS in order to evaluate the computation performance. In the simulations, the system size is 64×64×256 cells, the average number of particles per cell is 144, and two VHs including 16 VEs are used in which 16 MPI processes for the main computation and two MPI ones for the recording are launched. The number of tracked particles is ~ 1.5×10^5. The particle data is recorded every 100 time-steps. As a result, the elapsed time of the calculation for 600 time-steps is 38.574 s, while that without the procedure is 38.153 s. That is, the computation speed with the procedure becomes only 1.1% slower.

3. Preliminary result of observation

Next, we have actually observed orbits of ion particles thought to be accelerated with a collisionless drift wave using the updated up3bd code. The generation of drift waves requires not only a density gradient but also a long system length in the direction parallel to the magnetic field. Thus, the system size is set as 64×64×2048 cells, in which the *z* direction is parallel to the magnetic field. The initial plasma density is given by $n(x) = n_0\{\tanh[(x - L_x/2)/\Delta] + 1\}$, that is, the gradient is in the *x* direction, in which L_x is the system size in the *x* direction. The transition width Δ is set as $\Delta = 8.0\Delta_\mathrm{g}$. Here, Δ_g is the grid size given by $\Delta_\mathrm{g} = 0.2\,\rho_\mathrm{s}$, $\rho_\mathrm{s} = c_\mathrm{s}/\Omega_\mathrm{i}$; c_s is the ion acoustic speed presented by $c_\mathrm{s} = \sqrt{T_\mathrm{e}/m_\mathrm{i}}$; Ω_i is the ion-cyclotron frequency, and the mass and temperature ratios between ions and electrons are $m_\mathrm{i}/m_\mathrm{e} = 100$ and $T_\mathrm{i}/T_\mathrm{e} = 0.01$, respectively. The magnetic field strength is given by $\Omega_\mathrm{i}/\omega_\mathrm{pi} = 0.2$ and the time-step width is $\Delta t = 5\times10^{-4}\ \Omega_\mathrm{i}^{-1}$. In the *y* and *z* directions, a periodic boundary condition is applied. The simulation has been performed on eight VHs, including 64 VEs, in which 64 MPI processes for the main computation and eight MPI processes for the recording were launched. The number of tracked particles is ~ 1.2×10^5.

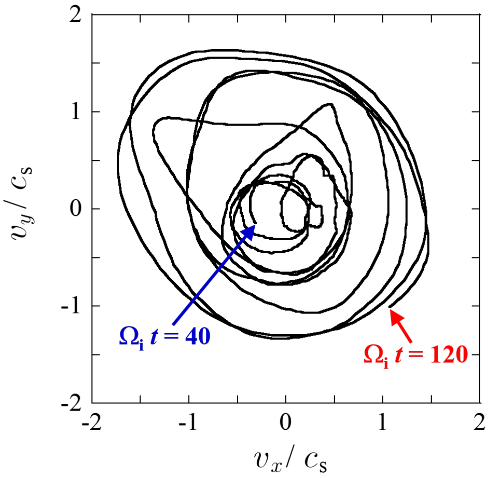

Figure 2: Orbit of an accelerated ion in v_x-v_y phase-space from $\Omega_\mathrm{i}t = 40$ to 120.

Figure 2 shows the orbit of an accelerated ion in v_x-v_y phase-space from $\Omega_\mathrm{i}t = 40$ to 120, in which v_x and v_y are the velocities in the *x* and *y* directions. This figure indicates that the particle is accelerated for a few gyro periods on the plane perpendicular to the magnetic field. Furthermore, from Fig. 3, in which scatter plots of ions in $v_\parallel$-$v_\perp$ phase-space at $\Omega_\mathrm{i}t =$

0 and 112 are drawn, it is found that the ion velocity distribution at $\Omega_{\mathrm{i}}t = 112$ becomes broader than that at $\Omega_{\mathrm{i}}t = 0$, not only in perpendicular, but also parallel directions. Here, $v_{\parallel}$ and $v_{\perp}$ are the velocities parallel and perpendicular to the magnetic field. Both Figs. 2 and 3 have been obtained from the orbit data recorded by the developed procedure.

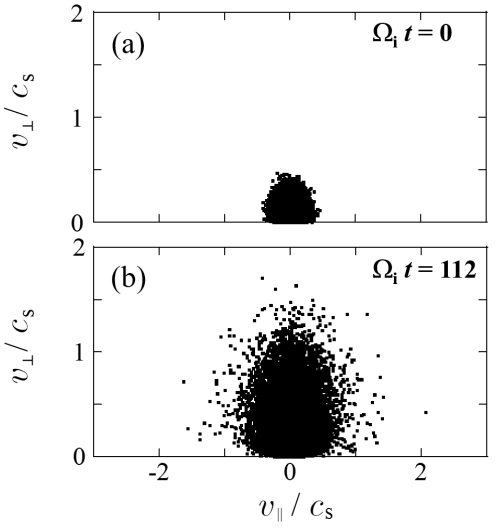

Figure 3: Scatter plots of ions in $v_{\parallel}$-$v_{\perp}$ phase-space at $\Omega_{\mathrm{i}}t = 0$ (a) and 112 (b).

Acknowledgments

This work was performed on the “Plasma Simulator (PS)” (NEC SX-Aurora TSUBASA) of NIFS with the support and under the auspices of the NIFS Collaboration Research programs (NIFS22KISS004) and supported by JSPS KAKENHI Grant Number JP19K03787. Also, some simulations were carried out on the supercomputer “Flow” at the Information Technology Center, Nagoya University with the “Joint Usage/Research Center for Interdisciplinary Large-scale Information Infrastructures (JHPCN)” and the “High Performance Computing Infrastructure (HPCI)” in Japan (Project ID: jh220004 and jh230006).

References

[1] Hiroki Hasegawa, Seiji Ishiguro: Improvement of the efficient electrostatic plasma particle simulation code for the investigation of boundary layer plasmas, *Proceedings of the 41st JSST Annual International Conference on Simulation Technology* (2022), 248-251.

[2] Hiroki Hasegawa, Seiji Ishiguro: Development and Verification of the Three-dimensional Electrostatic Particle Simulation Code for the Study of Blob and Hole Propagation Dynamics, *Plasma and Fusion Research*, volume:12 (2017), 1401044-1-1401044-9.

[3] Hiroki Hasegawa, Seiji Ishiguro: Three-dimensional effect of particle motion on plasma filament dynamics, *Physics of Plasmas*, volume:26 (2019), 062104-1-062104-5.

[4] J. Vranjes, S. Poedts: Features of coronal heating by drift waves, *Journal of Physics: Conference Series*, volume:511 (2014), 012054-1-012054-5.

[5] Hiroki Hasegawa, Hirohiko Tanaka, Seiji Ishiguro: Linear analysis of cross-field dynamics with feedback instability on detached divertor plasmas, *Nuclear Fusion*, volume 61 (2021), 126005-1-126005-8.

[6] Nobuaki Ohno, Hiroaki Ohtani: Development of In-Situ Visualization Tool for PIC Simulation, *Plasma and Fusion Research*, volume:9 (2014), 3401071-1-3401071-4.

[7] NEC SX Vector Supercomputer:
https://www.nec.com/en/global/solutions/hpc/sx/index.html?

Effects of lung model specifications on calculated electric field around the heart when using AED

Shoji Hamada[1*]

[1]Department of Electrical Electronic and Information Engineering, Kansai University

*shamada@kansai-u.ac.jp

Abstract. Conduction currents generated around the heart when an automated external defibrillator is used are calculated using anatomically realistic voxel models. As the lungs are adjacent to the heart, the lung conditions affect the currents around the heart. To investigate the effects of lung model specifications, we create a TARO-B model numerically by generating bronchi and bronchioles in the lung region of TARO-A, which is a TARO model with a voxel side length of 1 mm. By changing the lung interstitium conductivity from 0.0684 $\mathrm{Sm^{-1}}$ (= σ_I) to 0.205 $\mathrm{Sm^{-1}}$ (= σ_D), the inter-electrode resistance and the electric field around the heart are calculated. The values calculated using TARO-B with a lung interstitial conductivity of σ_D are similar to those of TARO-A with a lung conductivity of σ_{ave} = 0.14 $\mathrm{Sm^{-1}}$ $\cong (\sigma_I + \sigma_D)/2$.

Keywords: Contact current, Electric field calculation, Voxel model, Lung, Heart, Defibrillator

1. Introduction

Numerical analyses of electric currents and electric fields in the human body are widely performed using anatomically realistic voxel models such as TARO [1][2], which consider multiple biological tissues. To set the conductivity and permittivity of each tissue, the values in Ref. [3] are widely used at frequencies below 1 MHz. In this study, we numerically calculate the conduction current generated around the heart when an automated external defibrillator (AED) is used [4]. Because the lungs are adjacent to the heart, they affect the calculated current around the heart. However, the specifications of the lung model present the following problems: First, Ref. [3] contains both conductivity values for deflated and inflated lungs (σ_D and σ_I, respectively); however, whether the lungs of the TARO are deflated or inflated remains ambiguous. For example, an average conductivity $\sigma_{ave} \cong 0.5(\sigma_D + \sigma_I)$ was used in Ref. [2]. Second, the lungs of TARO contain only a few bronchi and no bronchioles. However, because the bronchi and bronchioles are filled with air with a conductivity of 0 S/m, these structures significantly affect the conductivity of the entire lung. The validity of applying σ_D or σ_I to such a simplified lung model of TARO remains unclear. Therefore, in this study, we investigated the effects of lung conductivity settings on the current distribution around the heart by the following procedure: (i) A numerical lung model including bronchi and bronchioles was generated partially adopting the method described in Ref. [5] and implanted to TARO [6], (ii) we investigated the inter-electrode resistance and the electric field around the heart when the conductivity of the lung interstitium was changed from σ_I to σ_D.

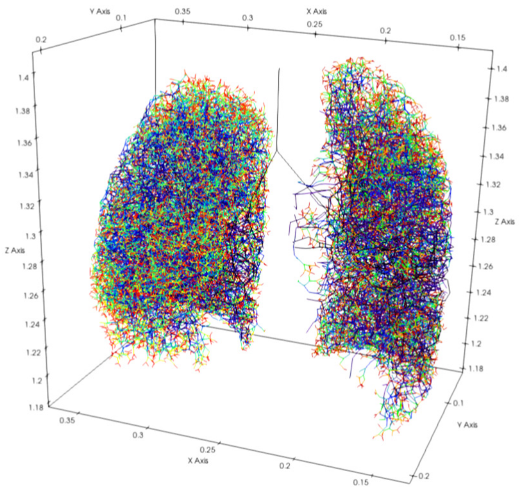

Fig. 1. Line model of bronchi and bronchioles.

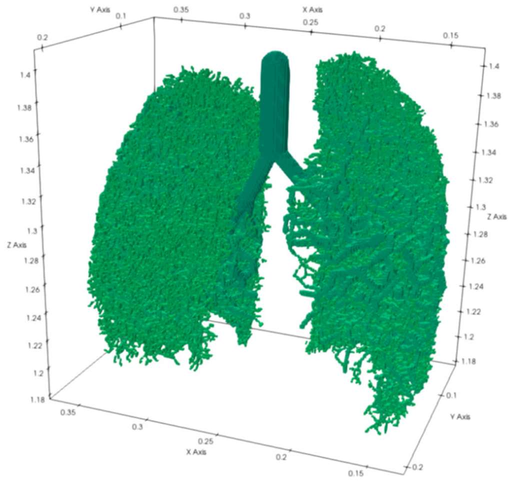

Fig. 2. Voxel model of bronchi and bronchioles.

2. Calculation model, method, and conditions

A TARO model with a voxel side length of 1 mm, named TARO-A, was used. Two closed subregions of TARO-A containing lungs, the main bronchi, and blood inside the lungs were extracted and referred to as the lung frame. Bifurcated tubules were grown inside this frame to generate a numerical model of the bronchi and bronchioles [6]. The positions of the trachea and main bronchi were the same as those of TARO-A, and smaller bronchi and bronchioles (referred to as branches) were grown by determining the rotating and branching angles using random numbers. The diameters and lengths of the branches were set based on the layer of branching (a maximum of 23 layers). Branch-to-branch collisions and branch-to-frame collisions were avoided; however, if that was not possible, only one branch was grown. If the latter was unsuccessful, the growth was halted. Fig. 1 shows the branches created as line segments, and Fig. 2 shows a voxel model created on the basis of Fig. 1. The total numbers of branches and terminal branches were 43,182 and 14,739, respectively. The inside of the branch was regarded as air, and the remaining region was regarded as the lung interstitium. This model was replaced with the lung frame of TARO-A, and the blood portion of the lung frame of TARO-A was overwritten. This model was named TARO-B and was adopted as an approximate model, although a voxel side length of 1 mm did not accurately represent the bronchiole shape with a diameter of less than 1 mm.

The AED electrodes were attached to TARO-A and TARO-B, and the internal electric fields were calculated. A voxel-based fast multipole surface charge simulation method was used for the calculations [7] and square voxel walls located at the boundaries between different media were utilized as surface elements. The frequency was assumed to be 50 Hz and the conductivities of the tissues, except for the lungs, were set to the values presented in Ref. [2]. Only the conductivity and conduction current were considered. The conductivity of the inflated lung, σ_I, was 0.0684 Sm^{-1}, that of the deflated lung, σ_D, was 0.205 Sm^{-1}, and the average of both, σ_{ave}, was approximately 0.14 Sm^{-1}. The inflated lungs contain a significant amount of air and therefore present a low conductivity. Fig. 3 shows the electrodes attached to TARO-B, heart, and lungs. The approximate location of the sinoatrial node, which is the source of the cardiac pacemaker signal, is shown as a sphere with a radius of 5 mm. The electrode was composed of body-surface elements inside a sphere with a radius of 6.5 cm. The internal electric field was obtained under a voltage of 2000 V [4] applied between the

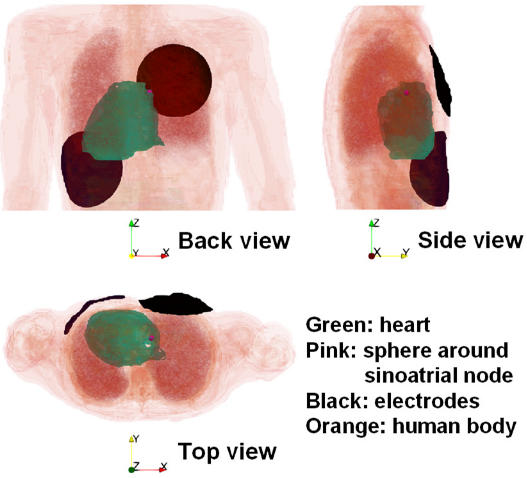

Fig. 3. Electrodes, heart, and sinoatrial node.

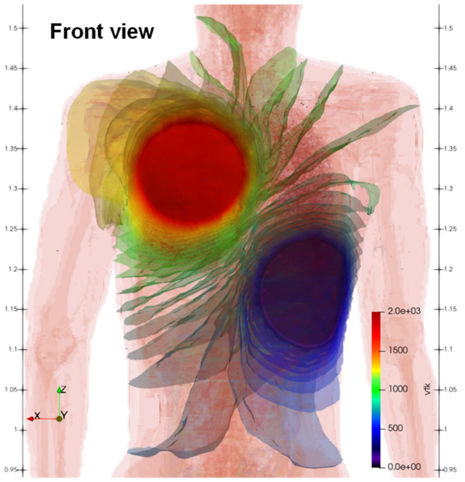

Fig. 4. Equipotential surfaces (50 surfaces).

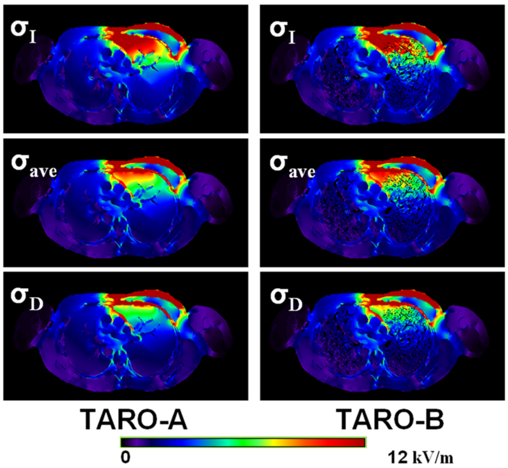

Fig. 5. |*E*| on horizontal plane crossing through sinoatrial node.

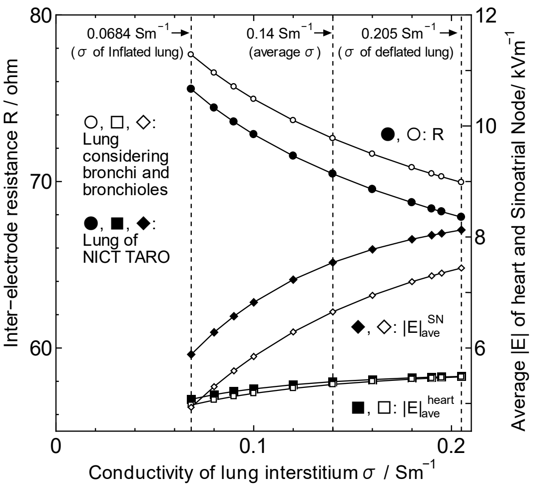

Fig. 6. Inter-electrode resistance and average |*E*| of heart and sinoatrial node vs. conductivity of lung interstitium.

electrodes.

3. Calculation result

Fig. 4 shows 50 equipotential surfaces between the electrodes in TARO-B with σ_{ave}. Fig. 5 shows the absolute electric field $|\boldsymbol{E}|$ in the horizontal plane through the sinoatrial node. TARO-B contained many cavities formed by the bronchi and bronchioles, where the electric fields were disturbed. Fig. 6 shows the inter-electrode resistance R, average electric field of the heart $|\boldsymbol{E}|_{\mathrm{ave}}{}^{\mathrm{heart}}$, and average electric field of the sinoatrial node $|\boldsymbol{E}|_{\mathrm{ave}}{}^{\mathrm{SN}}$ with respect to σ varying from σ_{I} to σ_{D}. The R ranges of TARO-A and TARO-B were 67.9–75.6 and 69.9–77.6 Ω, respectively. The R range for adults is 70–80 Ω [4], and the calculated results were approximately within this range. The $|\boldsymbol{E}|_{\mathrm{ave}}{}^{\mathrm{heart}}$ ranges of TARO-A and TARO-B were 5.08–5.49 and 4.97–5.48 kVm^{-1}, respectively, and their $|\boldsymbol{E}|_{\mathrm{ave}}{}^{\mathrm{SN}}$ ranges were 5.88–8.13 and 4.93–7.44 kVm^{-1}, respectively. Therefore, the local electric field fluctuations were significant in the heart but less so throughout the heart. This suggests that the positions of the attached electrodes were appropriate. The R, $|\boldsymbol{E}|_{\mathrm{ave}}{}^{\mathrm{heart}}$, and $|\boldsymbol{E}|_{\mathrm{ave}}{}^{\mathrm{SN}}$ calculated using TARO-B with σ_{D} were 69.9 Ω, 5.48 kVm^{-1}, and 7.44 kVm^{-1}, respectively, and those calculated using TARO-

A with σ_{ave} were 70.5 Ω, 5.39 kVm^{-1}, and 7.54 kVm^{-1}, respectively, which corresponded to ratios of 0.993, 1.016, and 0.987, respectively. Therefore, assuming that the conductivity of the lung interstitium of TARO-B is similar to σ_D, the setting used in Ref. [2], where the lung conductivity of TARO-A is σ_{ave}, is considered acceptable.

4. Summary

A numerical model, TARO-B, was created by generating bronchi and bronchioles in the lung region of TARO-A, which is a TARO model with a voxel side length of 1 mm. Based on an applied voltage of 2000 V, the conduction currents around the heart, which simulated the use of an AED, were calculated. The inter-electrode resistance and average electric field of the heart and sinoatrial nodes were calculated by changing the conductivity of the lungs. The values calculated using TARO-B with a lung interstitial conductivity of σ_D were similar to those calculated using TARO-A with a lung conductivity of σ_{ave}.

Acknowledgments

We would like to thank Mr. Ryo Sakamoto, a master's degree graduate at Kansai University, for his effort in creating the bronchi and bronchiole models used in this study.

References

[1] T. Nagaoka, S. Watanabe, K. Sakurai, E. Kunieda, S. Watanabe, M. Taki, Y. Yamanaka: Development of realistic high-resolution whole-body voxel models of Japanese adult males and females of average height and weight, *Phys. Med. & Biol.*, 49 (2004), 1-15.

[2] A. Hirata, K. Yamazaki, S. Hamada, Y. Kamimura, H. Tarao, K. Wake, Y. Suzuki, N. Hayashi, and O. Fujiwara: Intercomparison of induced fields in Japanese male model for ELF magnetic field exposures: effect of different computational methods and codes, *Radiation Protection Dosimetry*, 138:3 (2010), 237–244.

[3] C. Gabriel, A. Peyman, and E. H. Grant: Electrical conductivity of tissue at frequencies below 1MHz, *Phys. Med. Biol.*, 54 (2009), 4863-4878.

[4] Y. Tamura, and N. Akiyama: AED: Measurement of cardiac electrical activity and control technique by electric shock, Journal of the society of instrument and control engineers, 57:8 (2018), 582-587 (in Japanese).

[5] H. Kitaoka, R. Takaki, and B. Suki: A three-dimensional model of the human airway tree, *J. Appl. Physiol.*, 87:6 (1999), 2207-2217.

[6] R. Sakamoto, S. Hamada: Numerical analysis of contact current in the human body using automatically generated bifurcated tubule model of lung bronchioles, *Kansai-section Joint Convention of institutes of Electrical Engineering*, G1-18 (2022), 19-20 (in Japanese).

[7] S. Hamada: GPU-accelerated indirect boundary element method for voxel model analyses with fast multipole method, *Computer Physics Communications*, 182 (2011), 1162-1168.

FE Analysis of Numerical Human Body Model with 270 Million DOFs in Electromagnetic Field – Heat Conduction Coupled Problem

Shin-ichiro Sugimoto[1*], Amane Takei[2], Masao Ogino[3]

[1]Department of Mechanical Engineering, Faculty of Engineering,
Hachinohe Institute of Technology

[2]Department of Electrical and System Engineering, Faculty of Engineering,
University of Miyazaki

[3]Department of Information Systems, Faculty of Informatics, Daido University

*`sugimoto@hi-tech.ac.jp`

Abstract. This paper deals with a high-frequency electromagnetic field - heat conduction coupled analysis of a numerical human body model in a parallel environment. The iterative substructuring method has been considered to be an efficient parallel computing method.

Keywords: High-Frequency Electromagnetic Field - Heat Conduction Coupled Analysis, Parallel Computing, Finite Element Method, Hierarchical Domain Decomposition Method, Numerical Human Body Model

1. Introduction

In order to evaluate an effect of cancer treatment by hyperthermia quantitatively, we have been studying its high-frequency electromagnetic field – heat conduction coupled analysis in a parallel environment. In our study, the NICT numerical human body model [1] is analyzed. This model uses a binary data format wherein types of organs are encoded using voxels with a size of 2 mm. However, the boundaries of its different materials are not smooth; thus, unwanted reflection and scattering of electric fields has been observed in numerical simulator results. To reduce this numerical noise, some mesh smoothing techniques with tetrahedral elements have been developed [2]. Furthermore, the diameters of cancers treated with hyperthermia are several millimeters. Therefore, elements must be refined to obtain sufficient accuracy. However, there are approximately 130 billion degrees of freedom (DOFs) provided that the element sizes are 0.25 mm. In addition, smoothing techniques increase the DOFs further.

The efficient parallel computing method for large-scale finite element analysis (FEA) that we have been studying is the iterative substructuring method in the form known as the domain decomposition method (DDM) based on the iterative method [3]. It is expected to obtain scalable parallel efficiency on distributed memory parallel computers with the implementation of a Hierarchical Domain Decomposition Method (HDDM) [4].

The HDDM has been applied to the large-scale FEA of structural mechanics [5], and heat transfer [6]. In structural analysis, the problem with 100 billion DOFs has been analyzed [7]. In addition, the HDDM has been applied to the large-scale FEA of electromagnetics [8]-[9], too. In recent years, it has been clarified that the conjugate orthogonal conjugate residual (COCR) method [10] is very effective for problems that involve symmetric systems with complex numbers and ill-conditioned systems [11]-[12]. Thus, in the electromagnetic field analysis, high-frequency electromagnetic field problems have been solved with 30 billion DOFs [11] and 130 billion DOFs [13]. These achievements have been implemented as a parallel electromagnetic field analysis module called ADVENTURE_Magnetic [14].

In order to analyze large-scale problems, the parallel analysis of the electromagnetic field problem has been mainly studied. As the next step, a parallel coupled analysis of the high-frequency electromagnetic field and the heat conduction problems was considered. Then, the numerical human body model involving 270 million DOFs was analyzed in the parallel environment. However, a non-parallelized coupler took a long time, and the computational time increased as the number of nodes increases. In this paper, to reduce the computational time, parallelization of the coupler is considered.

2. High-Frequency Electromagnetic field – heat conduction coupled problem

Since the hyperthermia heats the human body from normal body temperature (36-37 degrees Celsius) to the temperature at which the cancer dies (42-43 degrees Celsius), the temperature change is only about 5 degrees; thus, changes in physical quantities related to the electromagnetic field analysis due to temperature are negligible. Therefore, in this paper, a one-way coupled analysis using the results of the electromagnetic field analysis for the heat conduction analysis is performed.

The numerical human body model is composed of voxels generated from tomographic images obtained by CT or MRI. Therefore, the boundaries of its different materials are not smooth; thus, unwanted reflection and scattering of electric fields has been observed in numerical simulator results. To reduce this numerical noise, some mesh smoothing techniques with tetrahedral elements will be used in the future; thus, the HDDM based on the finite element method is used for the numerical analysis, in this paper. Since the one-way coupled problem is considered, separate solvers are used for the electromagnetic field and heat conduction analyses. In this paper, ADVENTURE_Magnetic is used for the electromagnetic field analysis, and a parallel heat conduction analysis module called ADVENTURE_Thermal [14] is used for the heat conduction analysis.

3. Hierarchical Domain Decomposition Method (HDDM)

In the HDDM, an original domain Ω is divided without overlapping elements. Furthermore, the original domain is hierarchically divided into parts, which are further decomposed into smaller domains called subdomains.

$$\Omega = \bigcup_{i=0}^{N_p-1} \bigcup_{j=0}^{N_s-1} \Omega^{(i,j)}, \tag{1}$$

where $\Omega^{(i,j)}$ denotes the subdomain j in the part i, the superscript (i,j) corresponds to the subdomain $\Omega^{(i,j)}$. N_p and N_s are the number of parts and that of subdomains in each part, respectively. N_s is equal for all parts. In Fig. 1, the original domain is first divided into two parts, and then further decomposed into two subdomains within each part ($N_P = N_s = 2$). The solid circles in the figure are the DOFs shared between parts and subdomains, which are called interface DOFs.

In the HDDM, the interface problem which is obtained by statically reducing DOFs to the interface DOFs is solved by the parallel iterative methods such as the Conjugate Gradient method and COCR method.

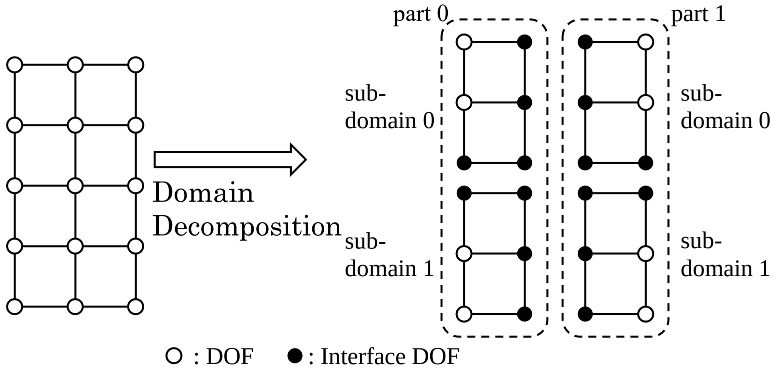

Fig. 1. Hierarchical domain decomposition.

4. Parallelization of coupler

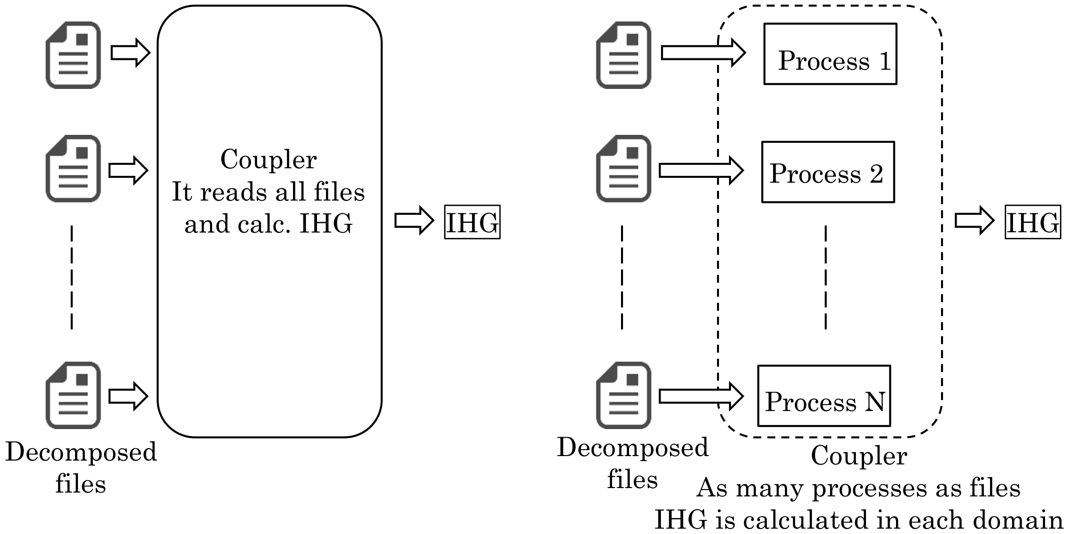

(a) Non-parallelized coupler (b) Parallelized coupler

Fig. 2. Parallelization of coupler.
* IHG: Internal Heat Generation.

The coupler reads files that are output by the simulation module of electromagnetic field analysis, and calculates the internal heat generation (IHG) in each element (Fig. 2). Files are decomposed into the same number as the number of Message Passing Interface (MPI) processes that are used by the simulation module. Previously, the coupler was not parallelized; thus, it reads all files, synthesizes data, and calculates IHG in whole domain. The parallelized coupler starts as many MPI processes as files. Each process reads one file, and calculates IHG in each domain. Then, the parallelized coupler synthesizes IHG, and outputs it.

5. Numerical example

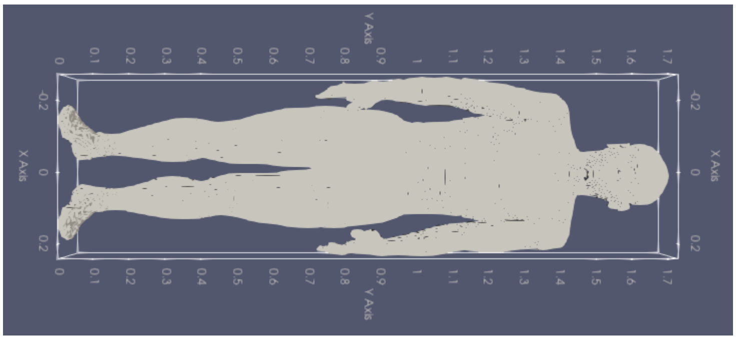

Fig. 3. Numerical human body model with 270 million DOFs.

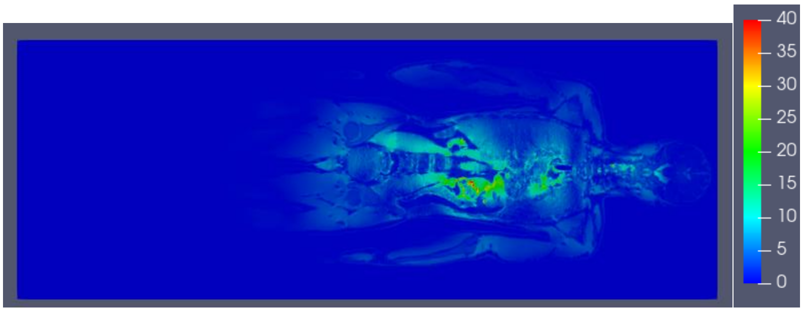

Fig. 4. Result of the electromagnetic field analysis. Eddy current density (real part) [A/m^2]

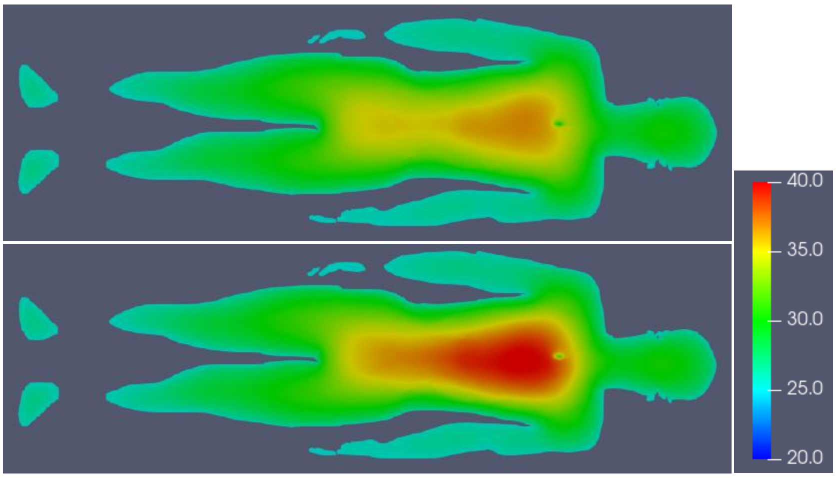

Fig. 5. Results of the heat conduction analysis (body temperature (degrees Celsius)).
Upper: without heating, Lower with heating.

The NICT numerical human body model involving 270 million DOFs provided that the element sizes are 2 mm (Fig. 3) is analyzed in parallel environment. Assumption of the treatment of the chest, the electromagnetic waves are emitted from the antenna in front of the chest. The physical quantities of each organ are quoted from [15] and [16]. The numerical simulation is performed by Oakbridge-CX supercomputer of Supercomputing Division, Information

Technology Center, The University of Tokyo [17]. It consists of Fujitsu PRIMERGY CX2550 M5 computers (Intel Xeon Platinum 8280 (2.7GHz, 28+28 cores), 192 GB memory) with 1,280 nodes. Nodes are connected by Intel Omni-Path.

Fig. 4 and Fig. 5 show the eddy current density and temperature distribution, respectively. It can be confirmed that the eddy current density around the heart near the antenna is strong, and temperature around the heart is rising.

Table 1 shows the computational times of coupler. They were reduced more than 96 % by parallelization.

Table 1. Computational times of coupler.

Nodes (Cores)	Non-parallelized [s]	Parallelized [s]	Reduction rate
8 (448)	288	11	96.2 %
16 (896)	326	10	96.9 %
32 (1,792)	390	11	97.2 %
64 (3,584)	529	14	97.4 %

6. Conclusions

In this paper, the high-frequency electromagnetic field – heat conduction coupled analysis of the numerical human body model involving 270 million DOFs provided that the element sizes are 2 mm has been attempted in the parallel environment. The computational times of coupler were reduced more than 96 % by parallelization.

In the future, the analysis of larger models and the analysis considering the influence of blood flow will be tried.

Acknowledgment

This work is partially supported by Takahashi Industrial and Economic Research Foundation, and JSPS KAKENHI Grant Number 22H03605 and 22K19779.

References

[1] Electromagnetic Compatibility Laboratory, Applied Electromagnetic Research Institute, National Institute of Information and Communications Technology HP: http://emc.nict.go.jp/index_e.html

[2] A. Takei, K. Murotani, S. Sugimoto, M. Ogino, H. Kawai: High-Accuracy Electromagnetic Field Simulation using Numerical Human Body Models, *IEEE Transaction on Magnetics*, Vol.52, Issue 3, 7402704 (2016), 4p.

[3] A. Quarteroni, A. Valli: Domain Decomposition Methods for Partial Differential Equations, *Clarendon Press, Oxford* (1999).

[4] R. Shioya, G. Yagawa: Iterative domain decomposition FEM with preconditioning technique for large scale problem, *ECM'99 Progress in Experimental and Computational Mechanics in Engineering and Material Behaviour* (1999), pp.255-260.

[5] S. Yoshimura, R. Shioya, H. Noguchi, T. Miyamura: Advanced general-purpose

computational mechanics system for large-scale analysis and design, *Journal of Computational and Applied Mathematics*, Vol.149, Issue 1 (2002), pp.279-296.

[6] A.M.M. Mukaddes, M. Ogino, M, H. Kanayama, R. Shioya: A scalable balancing domain decomposition based preconditioner for large scale heat transfer problems, *JSME International Journal Series B Fluids and Thermal Engineering*, Vol,49, No.2 (2006), pp.533-540.

[7] M. Ogino, R. Shioya: Scalable non-overlapping domain decomposition method for finite element simulations with 100 billion degrees of freedom model, *Proceedings of the 1st International Conference on Computational Engineering and Science for Safety and Environmental problems* (2014), pp.96-99.

[8] H. Kanayama, S. Sugimoto: Effectiveness of A-ϕ method in a parallel computing with an iterative domain decomposition method, *IEEE Transactions on Magnetics*, Vol.42, Issue 4 (2006), pp.539-542.

[9] A. Takei, S. Yoshimura, H. Kanayama: Large-scale parallel finite element analyses of high frequency electromagnetic field in commuter trains, *Computer Modeling in Engineering & Sciences*, Vol.31, No.1 (2008), pp.13-24.

[10] T. Sogabe, S.L. Zhang: A COCR method for solving complex symmetric linear systems, *Journal of Computational and Applied Mechanics*, Vol.199, No.2 (2007), pp.297-303.

[11] S. Sugimoto, A. Takei, M. Ogino: Finite Element Analysis with Tens of Billions of Degrees of Freedom in A High-Frequency Electromagnetic Field, *Mechanical Engineering Letters*, Vol.3, p.16-0067 (2017), 10p.

[12] M. Ogino, A. Takei, H. Notsu, S. Sugimoto, S. Yoshimura: Finite element analysis of high frequency electromagnetic fields using a domain decomposition method based on the COCR method, *Theoretical and Applied Mechanics Japan*, Vol.61 (2013), pp.173-181.

[13] S. Sugimoto, A. Takei, M. Ogino: High-Frequency Electromagnetic Field Analysis with 130 Billion of Degrees of Freedom, *The 38th JSST Annual Conference, International Conference on Simulation Technology*, (2019), pp.290-295.

[14] ADVENTURE Project HP: https://adventure.sys.t.u-tokyo.ac.jp/

[15] Human organs property Database for Computer simulation, RIKEN:
http://cfd-duo.riken.go.jp/cbms-mp/index.htm

[16] Tissue Properties Database V4.0:
https://itis.swiss/virtual-population/tissue-properties/downloads/database-v4-0/

[17] Supercomputing Division, Information Technology Center, The University of Tokyo:
https://www.cc.u-tokyo.ac.jp/

Simulation of a Beam Dechirper using Dispersionless FDTD Scheme

Kazuhiro Fujita[1,*]

[1]Department of Information Systems, Faculty of Engineering, Saitama Institute of Technology

*`kfujita@sit.ac.jp`

The full paper of this paper has been published in Journal of Advanced Simulation in Science and Engineering (JASSE).

DOI: `https://doi.org/10.15748/jasse.11.136`

An estimation of produced oxygen in the track of heavy-ion using Geant4-DNA

Yoshiyuki Hirano[1,*], Tsukasa Aso[2], Yoshuya Horii[1]

[1]Nagoya University, Graduate School of Medicine, Biomedical Imaging Sciences, Japan
[2]National Institute of Technology, Toyama College, Computer Engineering, Japan

[*]`hirano@met.nagoya-u.ac.jp`

The full paper of this paper has been published in Journal of Advanced Simulation in Science and Engineering (JASSE).

DOI: `https://doi.org/10.15748/jasse.11.207`

Droplet autonomous motion induced by laser irradiation

Shoichiro Handa[1*], Satoshi Takatori[1], Takahiro Kenmotsu[1]

[1]Faculty of Life and Medical Sciences, Doshisha University

*ctuj0004@mail4.doshisha.ac.jp

Abstract. We have constructed experiments to manipulate an oil droplet of paraffin floating aqueous solution using laser with wavelength of 532 nm. The experiment results show that the droplets of paraffin exhibit both elastic and reciprocating motions by the laser irradiation. We have confirmed the formation of the temperature gradient caused by the laser irradiation, adopting the infrared thermal camera. Based on the experimental results, we found that the temperature gradient takes an essential role for the behavior of the oil droplet. We have succeeded to generate the spontaneous motions of the oil droplets, adopting the methodology based on laser technic.

Keywords: laser irradiation, oil droplet

1. Introduction

Laser have been applied to manipulate objects including cell and oil droplet floating on aqueous solution and some researchers have reported the translational, circle and reciprocating motions of paraffin droplet made of paraffin are caused by laser irradiation [1,2]. We have performed to experiments based on laser technic to investigate more efficient method to generate motion of paraffin droplet in the present work. We have found that the paraffin droplet with lower viscosity of 3.07 and 8.71 Pa·s tend to take the reciprocating motion. Meanwhile, the paraffin droplet with higher viscosity of 75.9 Pa·s shows the elastic motion. Based on the experimental results, we have revealed the motion of paraffin droplet depend on its amount and viscosities, and we can control the motion of paraffin droplet adjusting suitable amount and viscosity of paraffin droplet.

2. Experimental

Figure 1 show the experimental setup, which are used in the present work. Continuous wave laser with wavelength of 532 nm and power of 1.05 kW is adopted in the present work. We have used paraffin droplets with different viscosities of 3.07, 8.71 and 75.9 Pa·s, which are colored red by Sudan stain to efficiently absorb the laser energy. The laser was set to irradiate the paraffin droplet vertically from above. The container contains the purified water of 7 mL and ethanol of 2 μl, which is 100 mm in length, 10 mm in height and 10 mm in width.

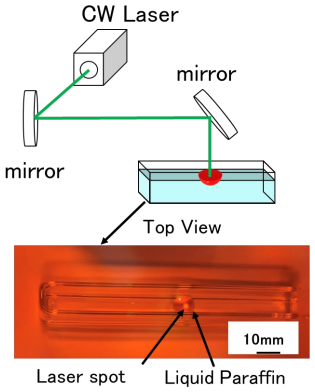

Fig. 1. Experimental setup

3. Results and discussion

Figure 2 shows the spatial-temporal plot on the elastic and reciprocating motions caused by the laser irradiation of paraffin droplets of 10 μL with viscosity of 3.07 Pa·s. The experimental results indicated that the laser irradiation leads to cause the elastic and reciprocating motions spontaneously. We have also performed the observation of temperature around laser focus and conformed the formation of temperature gradient around laser spot due to laser irradiation. Based on experimental results, we have considered that the temperature gradient result in the spontaneous motion of paraffin droplets and tale an essential role for the motion of paraffin droplet, which leads to the gradient of surface tension around laser focus.

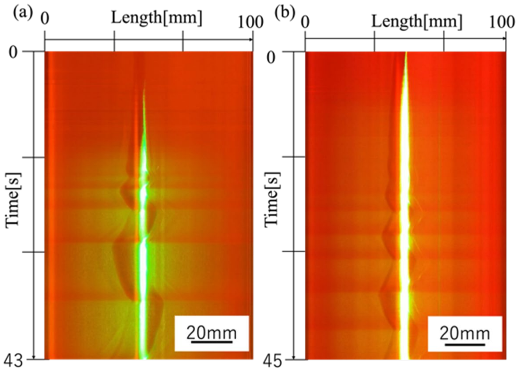

Fig. 2. spatial-temporal plot of paraffin droplet. (a) droplet with density of around 0.80 g/mL. (b) droplet with density of around 0.83 g/mL.

4. Summary

We have succeeded to induce both the elastic and reciprocating motions of paraffin droplet by laser irradiation and control these motions by choosing suitable viscosity of paraffin droplet. We expect that our findings provide a novel methodology for the manipulation of oil droplet based on laser technic.

References

[1] K. H. Nagai, F. Takabatake, Y. Sumino, H. Kitahara, M. Ichikawa, N.Yoshinaga: *Physical Review Letters*, 94 (2005), 013009/1-5.

[2] F. Takabatake, K. Yoshikawa, M. Ichikawa: *The Journal of Chemical Physics*, 141 (2014), 051103/1-7.

Vibrational motion of cm-size object induced by CW laser irradiation

Kosuke Imanaka[1*], Satoshi Takatori, Takahiro Kenmotsu

[1]Faculty of Life and Medical Sciences, Doshisha University

*ctuj0011@mail4.doshisha.ac.jp

Abstract. We have proposed a novel methodology to manipulate a cm-sized object using laser technique and revealed the laser irradiation with wavelength of 532 nm leads to cause oscillation and one direction motions of a cm-sized plastic plate floating on liquid solution. Based on the experiment results, we found that the temperature gradient around the focus of laser leads to generate force gradient on interface tension, which cause the motion of the plastic plate.

Keywords: Laser manipulation, cm-sized object

1. Introduction

The laser tweezer technic can manipulate μm-sized objects including cell and have been adopted in the entire research filed including life and medical sciences using highly focused laser beam, which based on the strong gradient of electric field around laser focus and scattering force as laser beam pass through an object [1,2]. However, the laser tweezer has an upper limit in size that can be handled, which cannot be handled objects more than several tens μm. Thus, we focus on the extension for application field of laser in size and propose a novel methodology to manipulate a cm-sized material, applying a temperature gradient dur to laser irradiation, which differ from the mechanism of laser tweezer. Based on the experimental results, we have succeeded to make oscillation and one direction motions of cm-sized plate floating on a aqueous solution, adopting the methodology proposed in the present work.

2. Experimental

Figure 1 and 2 show a cm-sized U-shaped sheets made of plastic with red and experimental setup, which are used in the present work, respectively. We have adopted continuous wave laser with wavelength of 532 nm and we vary laser power from 0.04 to 0.88 W. The laser was set to irradiate the sheets vertically from above. The plastic sheets are floating on the aqueous solution containing purified water of 7 μl and ethanol of 2 μl in the container, which is 100 mm in length, 10 mm in height and 8 mm in width.

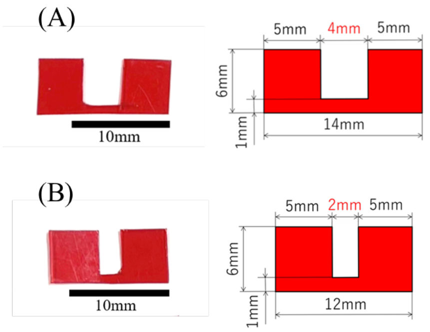

Fig. 1 U-shaped plastic sheet (a) gap of 4 mm (b) gap of 2 mm

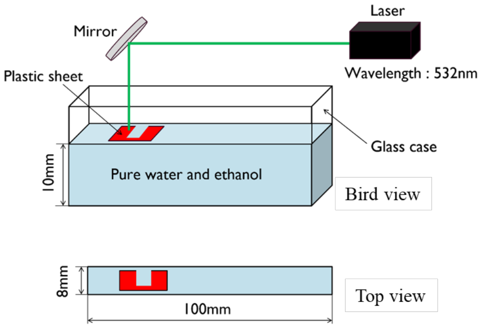

Fig. 2 Experimental setup

3. Results and discussion

Figure 3 shows the oscillatory and one direction motions of the cm-sized plastic sheets caused by laser irradiation with power of 0.42 W, together with spatial-temporal plot. The experimental results indicated that the period of the oscillation is around 5.9 sec. We have also performed the measurement on temperature around laser focus. Based on the experimental results, the laser irradiation leads to the formation of the temperature gradient around the laser focus of around 10 °C. Considering surface tension around the laser point, the surface tension in low temperature area is larger than that in high temperature. Thus, the sheets move to outside of the laser focus due to the difference of surface tension caused by the temperature gradient.

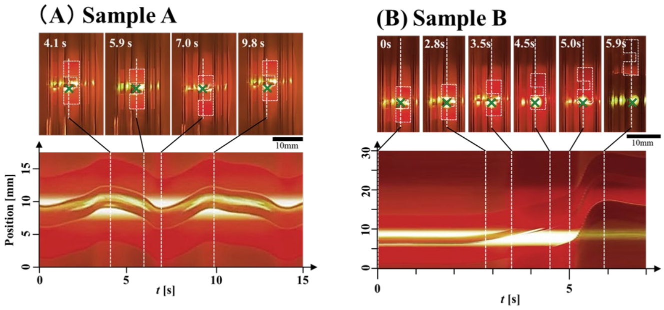

Fig. 3 Behavior of the plastic sheet (A) Oscillation of Sample A, (B) One direction motion of Sample (B)

4. Summary

We have succeeded to manipulate the cm-sized objects due to laser irradiation. Our findings provide the fundamental understanding to manipulate cm-sized object.

References

[1] A. Ashkin: *Proc. Natl. Acad. Sci. USA*, 94 (1997), 4853–4860.

[2] S. Hashimoto, A. Yoshida, T. Ohta, H. Taniguchi, K. Sadakane, K. Yoshikawa: *Chemical Physics Letters*, 655–656 (2016), 11–16.

JSST 2023

Cellular Automaton Traffic Simulation Considering Drivers' Characteristics

Atsushi Tanaka[1,*] and Ayumu Hashimi[2]

[1]Graduate School of Science and Engineering, Yamagata University
[2]Faculty of Engineering, Yamagata University

*`tanaka@yamagata-u.ac.jp`

Abstract. In this study, in order to analyze traffic jam on urban roads, individual differences among drivers into a regular CA model is introduced. We varied the ratio of vehicles with different stopping/starting characteristics at intersection signals and the effects of these differences are investigated. The results are as expected as the mixing ratio increases. However, the results differed significantly depending on the synchronization of the signals. The simulation would be more realistic if opposing lanes and intersections were taken into account.

Keywords: Traffic Jam, Cellular Automaton Model, Traffic Signal

1. Introduction

Traffic jam is becoming more and more intense every year, especially in emerging countries. This has given rise to new problems, such as noise and air pollution. Various policies are being considered to solve these problems, but no effective solution has yet been reached. On the other hand, studies on traffic jam have been very active since the establishment of simulation methods using CA models, and many results have been obtained[1]. However, CA is based on local rules that consider each car as a single particle, and it is difficult to reflect the characteristics of individual cells.

In this study, we focused on straight roads with multiple traffic signals to analyze traffic jam on urban roads in a more realistic manner. We focused on a straight road with multiple traffic signals, using CA simulation as a basis. The stopping and starting behavior at traffic signals were varied in order to include individual differences among drivers. That is, most drivers obey signals strictly though, some tend to intrude intersections even in the yellow signal. And some make snap decisions, others are slow to react because of some reasons. In addition the effect of multiple traffic signals was also investigated by turning the timing of signal change.

2. Experimental method

In this study, the following two models were introduced into the regular CA to take into account individual differences among drivers.

- ASEP model[2]
- Slow start rule[3]

The former is a stochastic model in which the car moves with probability p when it can move, and the latter is a model in which the car starts after a certain step delay when it starts, and we varied the proportion of the ratio of these two models was varied. The common parameters in the simulations are as follows.

- Number of cells 200
- Number of cars 120
- Cycle of signals 200 steps
    - Blue signal 95 steps
    - Yellow signal 10 steps
    - Red signal 95 steps
- Boundary condition Periodic
- Car velocity Constant

In each experiment, the signals were equally spaced and the number of signals varied from 1 to 3. The periodic boundary condition means that all the distances between successive two signals are equal during all the process of our simulation. When there were multiple signals, we considered the case where successive signals were changed simultaneously(synchronized phase) or inverted blue and red(opposite phase). The average flow rate for 2000 steps after 1000 steps was measured in the simulation.

3. Simulation results

3.1. Reaction to the yellow signal

The change in flow rate when the percentage of vehicles passing through a yellow light at an intersection is varied from 0 to 1 in increments of 0.1 is shown in Fig.1. This is correspond to change the drivers' characteristics to the yellow signal.

3.2. Effect of slow start cars

Figure 2 shows the change in flow rate when cars with a slow start standby step count of 3 are mixed and the ratio is varied in increments of 0.1 from 0 to 1 as well. Varying the rate of very slow start cars is practically correspond to change the probability p in the ASEP model.

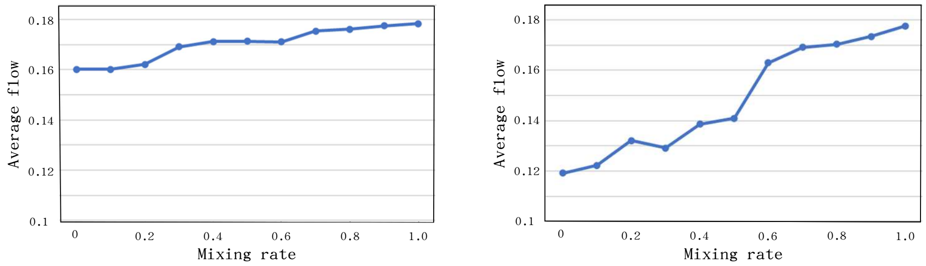

(a) 2 signals with synchronized phase (b) 2 signals with opposite phase

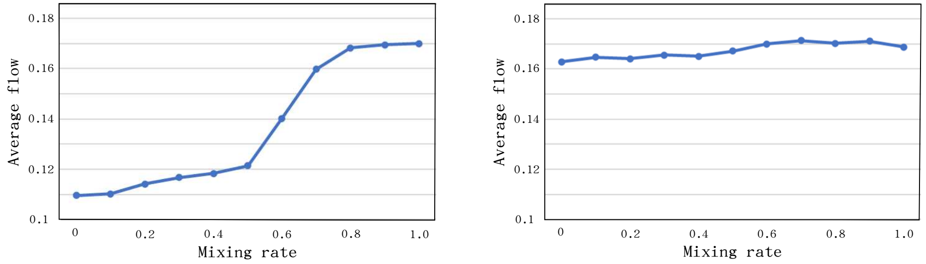

(c) 3 signals with synchronized phase (d) 3 signals with opposite phase

Figure 1: Simulation results of the reaction to the yellow signal.

4. Discussion

In the first experiment, the average flow rate tended to increase in all cases. This is because going straight through a yellow light is equivalent to increasing the number of steps through a green light by the number of steps through a yellow light. In the second experiment, there was a trend toward a decreasing average flow rate in all cases. This is due to the fact that vehicles sometimes stop at red lights or in traffic jam. In both Experiments, the slope of the graph differed when the period of the second traffic light was opposite. This difference was caused by conditions around the traffic signals that were not taken into account in this study, such as the period of the traffic signals and the distance between traffic signals.

5. Summary

In this study, in order to analyze traffic jam on urban roads, individual differences among drivers into a regular CA model is introduced. We varied the ratio of vehicles with different stopping/starting characteristics at intersection signals and the effects of these differences are investigated. The results are as expected as the mixing ratio increases. However, the results differed significantly depending on the synchronization of the signals.

In our simulations, we focused on driver characteristics and did not consider traffic signals in detail. The traffic volume of opposing lanes and roads to be intersected at the intersection were also not taken into account. Therefore, a better simulation would be to investigate the traffic flow on the entire road using a model and traffic signal settings that are similar to those of the actual road.

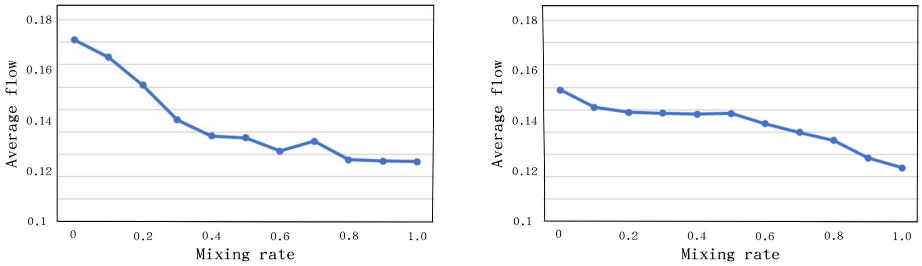

(a) 2 signals with synchronized phase (b) 2 signals with opposite phase

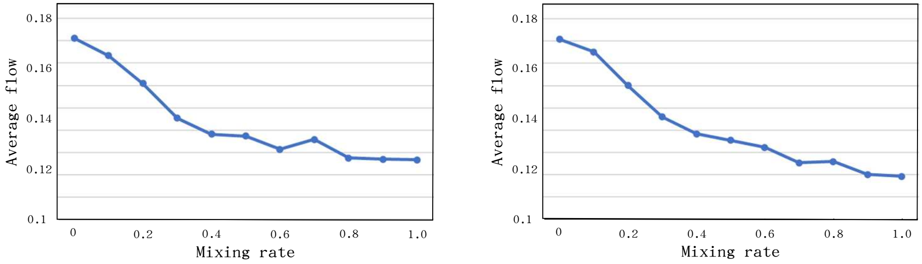

(c) 3 signals with synchronized phase (d) 3 signals with opposite phase

Figure 2: Simulation results of the effect of slow start cars.

References

[1] Schadschneider A., Chowdhury D. and Nishinari K.: Stochastic Transport in Complex Systems, *ELSEVIER, Amsterdam*, (2010).

[2] MacDonald C. T., Gibbs J. H. and Pipkin A. C.: Kinetics of biopolymerization on nucleic acid templates, *Biopolymers*, 6, 1 (1968), 1–25.

[3] Bejamin S. C., Johnson, N. F. and Hui P. M.: Cellular automata models of traffic flow along a highway containing a junction, *J. Phys.*, A, 29, 12 (1996) 3119–3127.

Proposal of Extension of Ant System Algorithm for Traveling Salesman Problem

Atsushi Tanaka[1,*] and Shota Miyazaki[2]

[1]Graduate School of Science and Engineering, Yamagata University
[2]Graduate School of Informatics, Nagoya University

*`tanaka@yamagata-u.ac.jp`

Abstract. In this paper, we improve the Ant System, one of the metaheuristic methods for solving the traveling salesman problem. The results showed that changing the selection probability in path selection according to the number of encounters sometimes produced better results than not changing it. It is also clarified that the combination of extension parameters that can obtain the shortest tour route is determined by the number of cities and the arrangement of the cities. Our promising future works include gathering all initial ant agents in one city and increasing the number of cities.

Keywords: Traveling Salesman Problem, Ant System, Multiagent Simulation

1. Introduction

The traveling salesman problem is one of the NP-hardest problems. The number of possible combinations of traveling paths increases on an exponential order with the number of cities, making it difficult to solve the problem in a tight time frame. The solution is also important in the real world, for example, to improve the efficiency of delivery routes. An algorithm to find a solution close to the exact solution in polynomial time is required. In this context, Ant Colony Optimization (ACO)[1] is the general name of an optimization method that uses pheromones when ants collect food and optimize it. Combinatorial optimization is the main target problem. It is characterized by swarm intelligence based on feedback, stochastic action selection by pheromone value and pheromone evaporation to search for optimization. It is one of the meta-heuristics methods for combinatorial optimization problems, and has also been applied to the traveling salesman problem. In this study, we use ACO meta-heuristics for solving the traveling salesman problem. The Ant System(AS), one of the ACO meta-heuristics methods for solving the traveling salesman problem, we propose a partially extended version of the algorithm and evaluate its performance.

2. AS and its problems

The AS is an ACO meta-heuristic for solving the traveling salesman problem. It was proposed by M. Dorigo et al. in 1991[2]. Multiple artificial ant Pheromones are placed on the edges connecting cities by multiple artificial ant agents. The pheromone influences the choice of city by the ant agents, thereby realizing pheromone feedback. The pheromone plays a role in the probability of path selection when ants generate a traveling path, and the value of the pheromone plays an important role in the selection of a city. The higher the pheromone value, the more likely the selection will be made. In the AS, the probability of selecting the next city j for the ant that is at the city i is given as follows.

$$p^k(i, j) = \frac{\{\tau(i, j)\}^\alpha \{\eta(i, j)\}^\beta}{\sum_{l \in N^k} \{\tau(i, l)\}^\alpha \{\eta(i, l)\}^\beta} \tag{1}$$

where $\tau(i, j)$ and $\eta(i, j)$ are the pheromone value between i and j and the inverse of the distance of i and j, respectively. And the pheromone is evaporated with the rate ρ.

The AS has two major problems. First, it is prone to local optima, and second, it tends to generate crossed paths. We propose improvements to overcome these problems.

3. Extension algorithm

The required conditions for extending the algorithm to overcome these problems while taking advantage of the strengths of the AS are to maintain diversity of ant-generated traveling paths and consider pathways that include long edges while taking advantage of heuristics information. Specifically, the pheromone values are determined based on the traveling paths generated by the ant agents. After determining the value of the pheromone based on the patrol paths generated by the ant agents, we propose changing the pheromone value of the edges in the traveling paths of ant agents that satisfy certain conditions. In changing the value of the pheromone, the following is an extended algorithm that introduces three values: the number of encounters(NE), the enhance rate(ER), and the characteristic index(CI). The concrete algorithm is as follows.

- Place all ant agents one by one in all initial cities.
- Initialize the number of ant agent encounters(NE) to 0.
- Repeated pheromone path selection to generate cyclic paths.
- Count the number of encounters for each ant agent.
- Update pheromone values based on traveling paths.
- Based on the number of encounters and the characteristic index(CI), multiply the probability of selecting the route edge that meets the condition by the enhance rate(ER).
- Repeat above a specified number of times.
- The traveling path with the shortest total distance among the generated paths is selected to the solution.

Table 1: Comparison of the path lengths and their parameters.ER and CI means Enhance Rate and Characteristic Index, respectively.

No. of cities	51	76	101
Optimal	426	538	629
AS	438.23	560.96	686.00
Extended AS	434.70	554.59	665.41
ER	0.3	0.7	4.7
CI	1.7	2.0	1.4

4. Simulation method and results

For comparison, programs were created and carried out on the AS without and with extensions. The input city data were eil51, eil76, and eil101 from the TSP benchmark library TSPLIB[3]. We set AS parameters $\alpha = 1, \beta = 5, \rho = 0.5$, and number of steps to 2000. We make the path length by the nearest neighbor method starting and ending at the first city in the city data $\tau_o = \frac{m}{C^{nn}}$ where m and C^{nn} are the number of cities and the path length obtained by this method, respectively. For the extended algorithm with three new values, we varied the parameters ER and CI from 0.1 to 5.0, respectively. The changes in the solutions for the combinations were observed. The solution with the shortest total distance among these 2,500 combinations was compared with the solution with the longest total distance. The total distance obtained without extension was compared with the solution with the shortest total distance among those 2,500 combinations. The result of comparing the shortest value of the total distance of the traveling path calculated with or without extension algorithm. The results and parameters of the comparison of the shortest value of the total length of the path calculated by the extended algorithm are shown in Table 1.

5. Discussion

For cities 51 and 76, ER was less than 1. For city 101, ER was 4.7, which is a very large value. The shortest circuits were obtained with very large values. CI were all greater than or equal to 1. The situation for the number of cities 51 is shown in Fig.1. As can be seen from the figure, the shortest paths are concentrated in areas where ER is less than 1 and CI is greater than 1.4. In other words, the shortest paths are those of ants that have fewer NE with other ants than the average. This means that it is better to reduce the pheromone values of the edges in the paths of ants that have fewer than average NE with other ants.

If the diversity of ant pathways is not important, then short circuits should be concentrated even in regions where CI is between 1 and 1.4. The fact that this is not the case suggests that the existence of slightly outlying paths improves the performance of the solution search, and that the diversity of the solution is important. This suggests the importance of solution diversity.

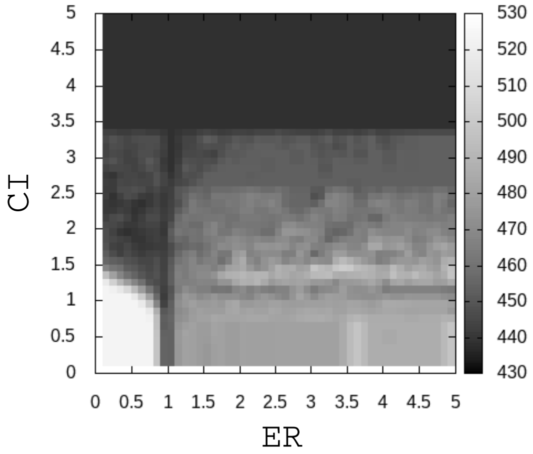

Figure 1: The heat map of path lengths with the parameters ER and CI(eil51). Each pixel density means the shortest path length.

In all cities, when CI exceeded a certain value, the change in solution was small even when the combination changed. The reason for this is that CI is too large. This may be due to the fact that the number of ants that reflect ER became extremely small because CI was too large. The reason for the shortened paths in the expanded algorithm is that the extreme pheromone bias was suppressed by evaluating the paths of ants that encountered fewer than average other ants. As the result, it brought us a diversity, and may have a positive effect on the search for a solution.

6. Summary

In this paper, we improve the Ant System, one of the metaheuristic methods for solving the traveling salesman problem. The results showed that changing the selection probability in path selection according to the number of encounters sometimes produced better results than not changing it. It is also clarified that the combination of extension parameters that can obtain the shortest tour route is determined by the number of cities and the arrangement of the cities. Our promising future works include gathering all initial ant agents in one city and increasing the number of cities.

References

[1] Marco Dorigo and Thomas Stützle: *Ant Colony Optimization*, The MIT Press (2004).

[2] Dorigo M., Maniezzo V. and Colorni A.: *Positive feedback as a search strategy*, Technical report 91-016, Dípartímento di Elettronica, Politecnico di Milano, Milan (1991).

[3] TSPLIB: *http://comopt.ifi.uni-heidelberg.de/software/TSPLIB95/*.

Simulation of Hydrogen Atoms in Tungsten Material

Shingo Sato[1], Miyuki Yajima[2,3], Hiroaki Nakamura[2,4] ,Chako Takahasi[1,5],

Keisuke Takeuchi[6], Seiki Saito[1*]

[1]Department of Information and Electoronics
, Graduate School of Science and Engineering , Yamagata University
[2]Department of Research, National Institute for Fusion Science
[3]Department of Fusion Science, Graduate School of Physical Sciences
, The Graduate University for Advanced Studies
[4]Department of Electrical Engineering, Graduate School of Engineering, Nagoya University
[5]AI Design Education and Research Promotion Center, Yamagata University
[6]Department of Information and Electoronics, Faculty of Engineering, Yamagata University
*saitos@yz.yamagata-u.ac.jp

Abstract.

In this study, we conduct molecular dynamics simulations to analyze the interaction between a vacancy and hydrogen bubbles in fusion reactor walls. A vacancy is created in the center of the tungsten material, and hydrogen atoms are placed within the vacancy. The experimental conditions are temperature and the number of hydrogen atoms on tungsten with the vacancy. Results of the simulation, hydrogen atoms ooze from the vacancy under certain conditions.

Keywords: Molecular dynamics simulation, Hydrogen bubble, Nuclear fusion, Tungsten

1. Introduction

Tungsten is a promising material for plasma-facing components in fusion reactor walls due to its high melting point. However, exposure to neutrons can create vacancies in fusion reactor walls. Hydrogen atoms colliding with fusion reactor walls can be captured in these vacancies, leading to the formation of hydrogen bubbles. This phenomenon can cause embrittlement of fusion reactor walls. To solve this problem, it is crucial to understand the interaction between vacancies and hydrogen atoms in fusion reactor walls.

Previous studies have utilized positron annihilation measurements [1] to investigate the interaction between vacancies and hydrogen. In this experiment, a neutron-irradiated tungsten sample is irradiated with deuterium plasma, revealing changes in the size of vacancies depending on the temperature and the amount of deuterium retained during irradiation.

In this study, we conduct molecular dynamics simulation to analyze the effects of temperature and the number of hydrogen atoms on tungsten containing vacancy.

2. Simulation method and Analysis method

Figure 1 shows the simulation model of this study.First, we create a vacancy in the center of a body-centered cubic (bcc) arrangement of tungsten. A vacancy is created by removing one tungsten atom in the center of the model and eight tungsten atoms close to it.Subsequently, an arbitrary number of hydrogen atoms are placed within the vacancy, and molecular dynamics simulation is performed. For the experimental conditions, place 0,2,4,6 hydrogen atoms near the position of the removed tungsten atom. Therefore, the experimental conditions for hydrogen atoms are 0,18,36,54. Also, from the experimental conditions of previous research, the temperature experimental conditions are 573 K, 773 K, and 1073 K.

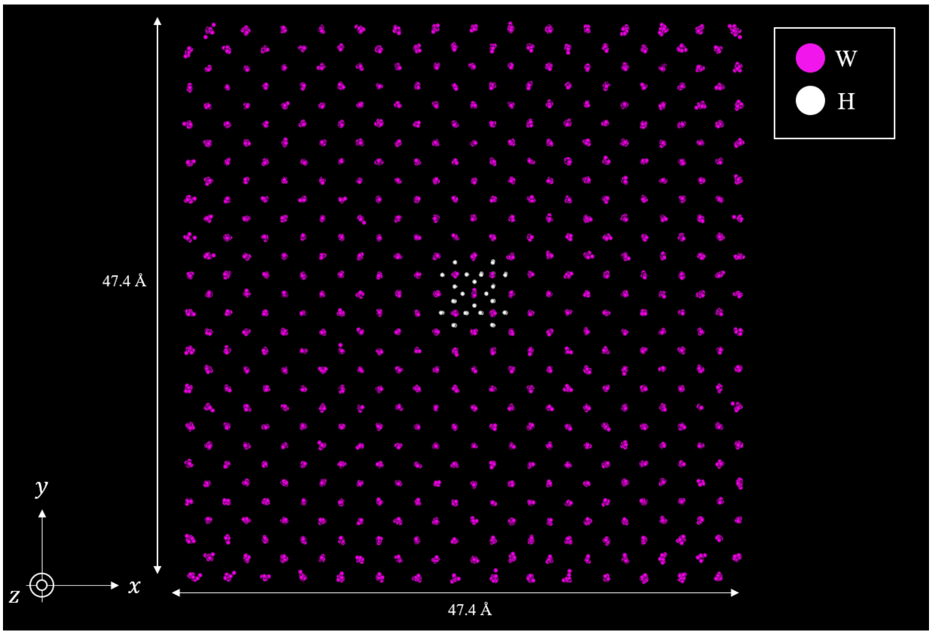

Fig 1: Simulation model.

To calculate the volume occupied by hydrogen atoms, the volume occupied by hydrogen atoms is defined Voronoi polyhedron. The volume occupied by the defined hydrogen atoms is obtained using the Monte Carlo method. It can be expressed as

$$\frac{N_\mathrm{H}}{N} \simeq \frac{V_\mathrm{H}}{V} \tag{1}$$

where N is the number of times we generated random three-dimensional coordinates, N_H is the number of times the particle closest to the most generated three-dimensional coordinates was hydrogen, V [Å^3] is the total volume of the tungsten structure, V_H [Å^3] is the volume occupied by hydrogen atoms.

We generate three million random coordinates for the simulation model and approximate the ratio of the number of times the nearest particle is the hydrogen atom to the total number of coordinates as the ratio of the volume occupied by the hydrogen atoms to the total volume of the simulation model.

3. Simulation results

Figure 2 shows the time evolution of the volume occupied by hydrogen atoms. The vertical axis represents the volume occupied by hydrogen atoms, while the horizontal axis represents simulation time. When the simulation was performed under each experimental condition, it was found that the volume occupied by hydrogen atoms increased at 54, which is the maximum among the experimental conditions for hydrogen atoms.This result indicates that the increase of hydrogen atoms in the vacancy leads to oozing of hydrogen atoms from the vacancy. Furthermore, the oozing of the hydrogen atoms in the vacancy means that the pressure exerted by the hydrogen atoms on the tungsten increases.

These findings suggest that as the number of hydrogen atoms in the vacancy increases, the pressure exerted by the hydrogen atoms on tungsten increases, and the size of the vacancy increases.

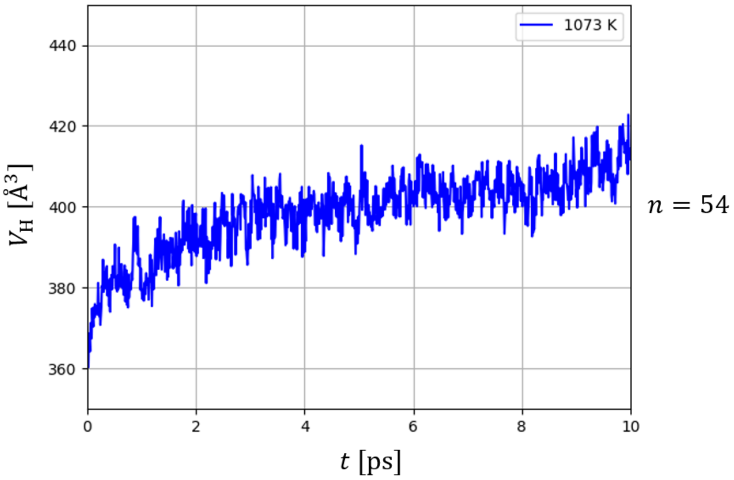

Fig. 2: Graph of the time evolution of the volume occupied by hydrogen atoms.

4. Current Research

Our ongoing research focuses on analyzing the hydrogen recycling process when the tungsten structure dynamically changes due to the irradiation of hydrogen atoms. However, the time scale between consecutive hydrogen atom interactions is too long to be calculated using the molecular dynamics (MD) method [2] alone. Additionally, the kinetic Monte Carlo (kMC) method [3] cannot be employed since the tungsten structure undergoes dynamic changes.

To address these challenges, we are developing a hybrid calculation method that combines molecular dynamics and the kinetic Monte Carlo (kMC) method with the assistance of deep learning.

Our approach involves developing a deep learning model to predict the potential distribution of hydrogen atoms based on their atomic configurations. This information is essential for the kMC method to accurately calculate the hydrogen atom behavior.

By integrating the strengths of molecular dynamics, which captures the atomistic dynamics at short time scales, and the kMC method, which effectively simulates long-time processes, we aim to gain a comprehensive understanding of the hydrogen recycling process in tungsten under dynamic structural changes.

Acknowledgment

The research was partially supported by Grant-in-Aid for Scientific Research, No.19K14692, No21K17804, No.22K03572 and No.23K03362 from the Japan Society for the Promotion of

Science, and by the NIFS Collaborative Research Program NIFS22KIGS002 and NIFS22KISS021.The ExCELLS Special Collaboration Program of Exploratory Research Center on Life and Living Systems.The NINS program of Promoting Research by Networking among Institutions.The GIMRT Program of the Institute for Materials Research, Tohoku University (Proposal No. 202212-IRKMA-0510). The computations were performed using the JFRS-1 supercomputer system at Computational Simulation Centre of International Fusion Energy Research Centre (IFERC-CSC) in Rokkasho Fusion Institute of QST (Aomori, Japan), Research Center for Computational Science (Okazaki, Aichi, Japan) and Plasma Simulator of NIFS (Toki, Gifu, Japan) .

References

[1] M. Yajima, Y. Hatano, V. K. Alimov, T. Toyama, T. Kuwabara, T. Schwarz-Selinger, Y. Oya, A. V. Spitsyn, and N. Ohno, *Penetration of deuterium into neutron-irradiated tungsten under plasma exposure,* Phys. Scr. **96**, (2021) 124042.

[2] S. Saito, H. Nakamura, K. Sawada, G. Kawamura, M. Kobayashi, M. Hasuo. *Molecular dynamics simulation model of hydrogen recycling on carbon divertor for neutral transport analysis in large helical device,* Contrib Plasma Phys. (2020) e201900152.

[3] A. M. Ito, A. Takayama, Y. Oda, T. Tamura, R. Kobayashi, T. Hattori, S. Ogata, N. Ohno, S. Kajita, M. Yajima, Y. Noiri, Y. Yoshimoto, S. Saito, S. Takamura, T. Murashima, M. Miyamoto, and H. Nakamura, *Molecular dynamics and Monte Carlo hybrid simulation for fuzzy tungsten nanostructure formation*, Nuclear Fusion vol.55 (2015) 073013.

Comparison of Locomotion Methods for VR Experience of Borobudur Temple

Yasuaki Suzuki[1*], Fadjar I. Thufail[2], Brahmantara[3], Hiroshi Yamaguchi[4],
Kyoko Hasegawa[5], Liang Li[5], Satoshi Tanaka[5]

[1]Graduate School of Information Science and Engineering, Ritsumeikan University, Japan
[2]Research Center for Area Studies, National Research and Innovation Agency, Indonesia
[3]Borobudur Conservation Office, Indonesia
[4]Nara National Research Institute for Cultural Properties, Japan
[5]College of Information Science and Engineering, Ritsumeikan University, Japan
*`is0462se@ed.ritsumei.ac.jp`

Abstract. This paper presents a virtual reality (VR) system that utilizes three-dimensional scanned point cloud data of Borobudur Temple, a World Cultural Heritage site in Indonesia, to provide a virtual experience of the temple as a digital archive. We implemented and compared three locomotion methods: walking, teleportation, and touchpad. Through three experimental tasks evaluating completion time, Simulator Sickness Questionnaire (SSQ), and Igroup Presence Questionnaire (IPQ), we assessed the performance of these locomotion methods. The experimental results indicated that a combination of walking and teleportation proved to be the most suitable locomotion method for navigating the VR space of Borobudur Temple.

Keywords: Borobudur Temple, Point cloud, Locomotion, Virtual reality

1. Introduction

In order to preserve historical cultural properties for future generations, efforts of digital archives are being made to digitize, store, and share data. With advancements in three-dimensional (3D) measurement technology, these digital archives can now accurately capture and store large-scale tangible cultural properties as point clouds [1]. In this study, we utilize the 3D scanned point cloud of Borobudur Temple to create an immersive virtual reality (VR) experience. In a VR environment, locomotion-based navigation is a crucial aspect that significantly impacts user comfort and performance. Different locomotion methods, such as walking, teleportation, and joystick/touchpad, have their own advantages and disadvantages depending on the specific tasks. In addition to the conventional teleportation and touchpad methods enabled by the head-mounted display (HMD)'s controller, we also implemented a walking experience utilizing an omni-directional VR treadmill. To evaluate and compare these three locomotion methods, we conducted three tasks commonly performed in the VR Borobudur environment. The assessment included the measurement of VR sickness and the sense of presence experienced by the participants [2, 3].

2. Creation of VR Borobudur Temple environment

Two point clouds of Borobudur Temple obtained by photogrammetry were used to create the overall representation and detailed sections of the temple (Fig. 1).

(a) Entire Borobudur Temple (b) A detailed section of Borobudur Temple

Figure 1: 3D scanned point clouds of Borobudur Temple

HTC VIVE Pro Eye and KAT Walk C were used as the VR interfaces (Fig. 2). KAT Walk C is an omni-directional VR treadmill that enables natural walking movement in a VR environment.

Figure 2: The experimental setup

In this research, Unity was employed as the development platform. Two viewpoint functions were implemented: a subjective perspective and a bird's-eye perspective. In the subjective perspective shown in Fig. 3(a), users can navigate through teleportation, walking, and touchpad interactions. Additionally, the eye-tracking function of VIVE Pro Eye allows users to trigger text description pop-ups of the relief panel. On the other hand, in the bird's-eye perspective shown in Fig. 3(b), users can freely move in all directions using the controller. The touchpad facilitates movements in the forward, backward, left, and right directions.

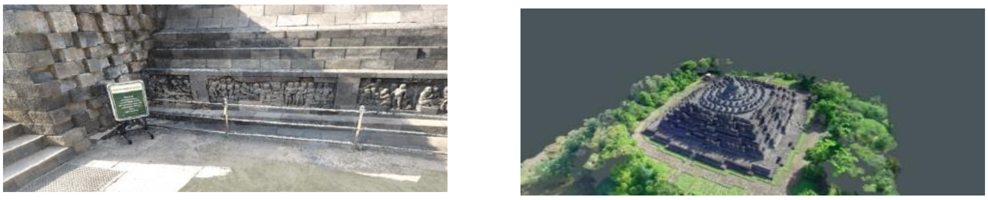

(a) Subjective perspective (b) Bird's-eye perspective

Figure 3: VR Borobudur Temple with two viewpoint functions

3. Comparison of locomotion methods

A comparative experiment was conducted to assess the suitability of three locomotion methods (teleportation, walking, and touchpad) for navigation within the subjective perspective of the VR Borobudur Temple. Ten participants underwent a 5-minute training session before performing three tasks. These tasks were designed to simulate typical movements within the VR environment of Borobudur Temple: (a) Displaying text descriptions by observing relief panels to evaluate the ability to approach targets and perform eye-tracking-based operations, (b) Ascending and descending stairs to assess fine movements, and (c) Walking around the temple to evaluate performance in long-distance movements (see Fig. 4). The time taken by participants to complete each task was recorded. After completing each task, participants were required to fill out a questionnaire. The questionnaire consisted of five items from the Simulator Sickness Questionnaire (SSQ), which measures VR sickness, and 14 items from the Igroup Presence Questionnaire (IPQ), which measures immersion levels.

Shows the stark difference between a happy family and a drunk family.
Due to self-forgetfulness, the drunkards commit forbidden crimes, such as lewd acts and dancing irregularly.

(a) Observing relief panels (b) Stair movements (c) Long-distance movements

Figure 4: Three tasks in the experiment

4. Experimental results

Table. 1 shows the average task completion time for the participants. Five SSQ items (discomfort, fatigue, headache, nausea, and dizziness) were assessed using a 3-point Likert scale (1 = slightly, 2 = moderately, and 3 = very). Figure 5 shows the average SSQ scores for each locomotion method. The IPQ was evaluated in terms of General Presence (GP), Spatial Presence (SP), Involvement (INV), and Realism (REAL). GP had 1 item, SP had 5 items, INV had 4 items, and REAL had 4 items. Figure 6 shows the average IPQ scores for each locomotion method.

Table 1: Average task completion time (in seconds)

	Walking	Teleportation	Touchpad
Observing relief panels	17.1 s	13.1 s	13.2 s
Stair movements	21.6 s	32.0 s	N/A
Long-distance movements	38.2 s	12.0 s	25.0 s

The findings of our study revealed differences among the locomotion methods in terms of task completion times and subjective experiences. In the context of long-distance movements, walking was slower compared to teleportation (Table 1). However, when it came to ascending and descending stairs, walking showed faster completion times. The SSQ scores in Fig. 5 illustrate that teleportation was associated with lower levels of discomfort compared to touchpad and walking. However, regarding the IPQ scores shown in Fig. 6, walking and teleportation yielded comparable scores, suggesting similar levels of immersion and presence. Notably, walking received higher scores in the REAL items, indicating an increased sense of perceived realism. This may be attributed to the fact that walking mimics a more natural movement compared to teleportation or touchpad interactions, aligning more closely with real-life experiences.

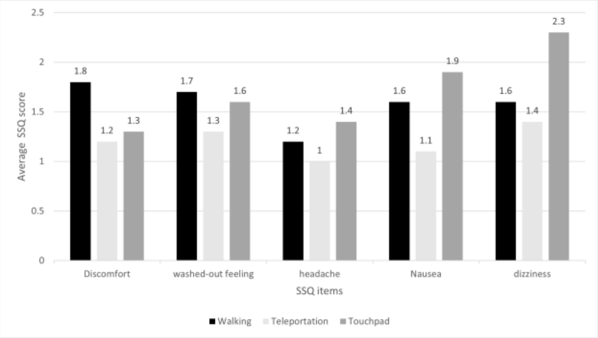

Figure 5: SSQ scores for each locomotion method

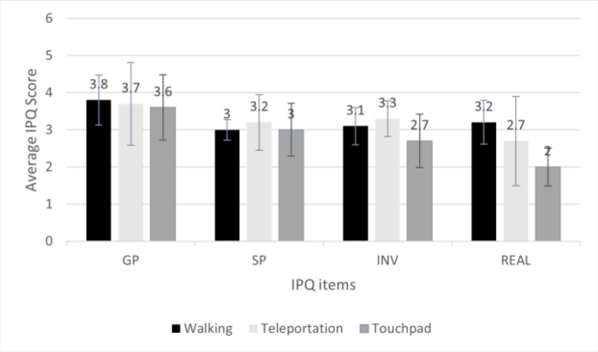

Figure 6: IPQ scores for each locomotion method (Error bars: Standard deviation)

5. Conclusion

In this study, we developed a VR environment based on the 3D scanned point cloud data of Borobudur Temple. We compared three locomotion methods, and the results show that teleportation is more suitable for long-distance movements, while walking is more effective for fine movements. Moreover, the experimental results suggest that both teleportation and walking contribute to a higher level of immersion. The current study is based on the point cloud data of Borobudur Temple, and in the future, we aim to generalize the findings to other VR systems for large-scale cultural heritage.

References

[1] D. Zorich: A Survey of Digital Cultural Heritage Initiatives and Their Sustainability Concerns, *Council on Library and Information Resources*, (2003), pp. 56.

[2] H. Kim, J. Park, Y. Choi, M. Choe: Virtual reality sickness questionnaire (VRSQ): Motion sickness measurement index in a virtual reality environment, *Applied Ergonomics*, Vol. 69 (2018), pp. 66-73.

[3] "igroup presence questionnaire (IPQ) overview", http://www.igroup.org/pq/ipq/index.php, 30 May 2023.

Object shape dependence of size perception in binocular parallax virtual reality devices

Yuichi Tamura[1,*], Hiroyuki Makino[2], Nobuaki Ohno[2]

[1]Department of Information and Informatics, Konan University
[2]Graduate School of Information Science, University of Hyogo

*`tamura@konan-u.ac.jp`

The full paper of this paper has been published in Journal of Advanced Simulation in Science and Engineering (JASSE).

DOI: `https://doi.org/10.15748/jasse.11.93`

JSST 2023

Tilted Gaussian beam coupling with vortex beam mode in cylindrical waveguide

Yoshihisa Fujita[1,*], Hiroaki Nakamura[2], Hideki Kawaguchi[3]

[1]College of Industrial Technology, Nihon University
[2]National Institute for Fusion Science, National Institute of Natural Science
[3]Division of Information and Electronic Engineering, Muroran Institute of Technology

*`fujita.yoshihisa@nihon-u.ac.jp`

Abstract. An efficient method for excitation of high-power millimeter-wave optical vortices has not yet been established. As a first step for proposing a new excitation method, this study clarified the relationship between the angle of incidence and vorticity by calculating the coupling with the vortex modes of the waveguide by injecting a Gaussian beam at an oblique angle. It was found to couple to various modes and vorticity depending on the angle of incidence. Detailed results will be presented at the conference.

Keywords: Computer simulation, Numerical methods

1. Introduction

Since optical vortices have more degrees of freedom than plane waves, they have potential applications in measurement and heating technology [1, 2]. Various methods of excitation of optical vortices have already been proposed [3, 4]. The application of optical vortices to plasma heating is also expected, but Joule losses cannot be ignored at high power millimeter waves. Therefore, this study aims to propose a new method of excitation of optical vortices.

Cylindrical waveguides are suitable for long-distance transmission of electromagnetic waves. It is known that vortex modes can be represented by the superposition of two waveguide modes with different phases and polarizations [5]. Corrugated waveguides have a proven track record in transmitting high-power millimeter waves. Hybrid modes, which are modes of propagation in corrugated waveguides, can also be expressed as vortex modes. However, in any case, it is difficult to excite multiple arbitrary modes simultaneously. Therefore, we focused on the fact that higher-order modes are generated by axial misalignment when a Gaussian beam is used to excite the fundamental mode of a waveguide. The relationship between the degree of misalignment and higher-order modes will be clarified, which will enable control of the excitation modes. The influence of the incident angle of the Gaussian beam on the excitation mode has already been clarified. [6]. Unfortunately, the angular momentum is not taken into account, which is not sufficient to evaluate the excitation of optical vortices.

In previous studies, excitation modes were investigated by calculating the coupling between the Gaussian beam and waveguide modes. This research makes it possible to evaluate vorticity by calculating not only the directional component, as in the conventional method, but also the azimuthal component. As a first step for proposing a new excitation method for optical vortices, the purpose of this study is to clarify the relationship between the angle of incidence and the vorticity.

2. Coupling theory for angular momentum

The energy associated with beam propagation can be expressed by using the pointing vectors: $\boldsymbol{S} = \frac{1}{2}(\boldsymbol{E} \times \boldsymbol{H}^* + \boldsymbol{E}^* \times \boldsymbol{H})$. In a previous study, mode coupling was evaluated at the waveguide mouth as follows:

$$\boldsymbol{C} = \int_0^{2\pi} \int_0^a r(\boldsymbol{E}_\mathrm{G} \times \boldsymbol{H}_\mathrm{W}^*)\,\mathrm{d}r\,\mathrm{d}\phi \tag{1}$$

where the subscripts G and W denote the Gaussian beam and waveguide modes, respectively. Until now, only the directional component of the equation has been calculated, so it has not been possible to evaluate the vorticity.

We now consider the angular momentum of light. The total momentum density is given by $\boldsymbol{p} = \frac{1}{c^2}\boldsymbol{S}$. From the equation, it is possible to evaluate the vorticity by calculating the azimuthal coupling, since the angular momentum density $\boldsymbol{j}$ is given by $\boldsymbol{j} = \boldsymbol{r} \times \boldsymbol{p}$. where $\boldsymbol{r}$ is the displacement. In this study, we use the rotation matrix $R(\theta)$ to calculate the relationship between incidence angle θ and the coupling coefficient as follow:

$$\boldsymbol{C} = \int_0^{2\pi} \int_0^a r(R(\theta)\boldsymbol{E}_\mathrm{G} \times \boldsymbol{H}_\mathrm{W}^*)\,\mathrm{d}r\,\mathrm{d}\phi\,. \tag{2}$$

Note that in the case of the Laguerre Gaussian beam, the angular momentum in the z-axis direction is $j_z = rp_\phi$, which means that not only S_ϕ but also C_ϕ is proportional to the angular momentum.

References

[1] H. Minagawa et al., *Plasma Fusion Res.*, 17 (2022).

[2] S. Zhang et al., *Phys. Plasmas*, 29:123504 (2022).

[3] H. Chung et al., *Sci. Rep.*, 10:8289 (2020).

[4] B. He et al., *J. Opt. Soc. Am. B*, 38 (2021), 1518–1524.

[5] D. Mao et al., *APL Photonics*, 4:060801 (2019).

[6] K. Ohkubo et al., *Int. J. Infrared Milli. Waves*, 18 (1997), 23–41.

JSST2023

Analysis of Magnetic Device Using Homogenized Finite Element Method and Cauer Circuit

Qiao Liu[1*], Hajime Igarashi[1]

[1] Graduate School of Information science and technology, Hokkaido university, Sapporo, Japan

[*]liuqiao@em.ist.hokudai.ac.jp

Abstract. In the realm of magnetic devices, such as inductors and wireless power transfer systems, it is often necessary to account for the impact of eddy currents, particularly when operating at high frequencies. Conventional finite element method can be applied to solve the problem, however, with long computational time. Moreover, for the complicated model, the consumed time in building model is extremely long. In this paper, a semi-analytical homogenization method is used to calculate the impedance of device based on magnetostatic analysis. Subsequently, Cauer circuit can be built based on the calculated impedance to consider the instantaneous copper loss.

Keywords: Magnetic device, Eddy current, Homogenization method, Cauer circuit

1. Introduction

To reduce the size of device, the driving frequency of power electronics circuits has been increased, sometimes up to MHz. The impedance of magnetic devices working at high frequency would be frequency dependent owing to the skin effect and proximity effect [1]. Although the devices can be analyzed using Finite Element Method (FEM), it needs large computing time at high frequencies because of the discretized elements which must be much smaller than skin depth. To accelerate the simulation process, the semi-analytical homogenization method is used for the round conducting wire [2]. The impedance of devices can be calculated using complex permeability based on magnetostatic analysis. The identification method using adjoint variable method is applied to build the Cauer equivalent circuit [3]. The improved objective function is applied to upgrade the performance in low frequency domain [4].

This paper presents a comprehensive and efficient approach for analyzing magnetic devices operating at high frequencies. Based on the result from semi-analytical homogenization method, Cauer circuit is built using the improved identification method [4]. We achieve accurate results while significantly reducing computational time and simplifying the model construction process. Based on the Cauer circuit, instantaneous copper can be simulated, and it will be compared with the formula in [1].

2. Semi-Analytical Homogenization Method

We consider the case of a round wire carrying a uniform current in whole region and immersed in a uniform time-harmonic magnetic field $Be^{j\omega t}$ [2]. The magnetic field is perpendicular to the wire axis. The coordinate system is shown in Fig. 1.

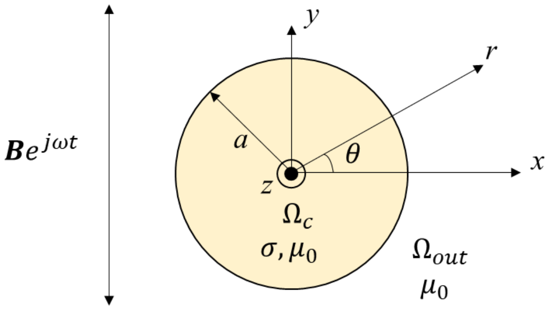

Fig. 1 Cross section of a round wire immersed in ***B***

We consider the electric field only in z direction as the current flows. The conductivity σ is 0 in Ω_{out}. The Maxwell equations under the quasi-static approximation are shown as below.

$$\nabla \times \boldsymbol{H} = \sigma \boldsymbol{E} \tag{1}$$

$$\nabla \times \boldsymbol{E} = -jw\mu \boldsymbol{H} \tag{2}$$

The complex permeability of a solid round wire is derived as below. It is under the condition of (1) and (2).

$$\dot{\mu}_r = \mu_r \frac{J_1(z)}{zJ_1'(z)} \tag{4}$$

In (4), $z = a * \sqrt{-j\omega\sigma\mu} = (1-j)/\delta$ is relevant to the skin depth δ. The complex permeability gives the complex power, which is consistent with that obtained from the energy conservation law. The complex power supplied by the external source equals the increase in the magnetic energy and copper loss in the wire. For further simplicity, Ollendorff formula is adopted to turn several turns into one single solid area shown in (5).

$$< \dot{\mu}_r >= 1 + \frac{\eta(\dot{\mu}_r - 1)}{1 + N(1-\eta)(\dot{\mu}_r - 1)} \tag{5}$$

$\dot{\mu}_r$ is calculated from (4). η and N denote the volume fraction and diamagnetic constant which is 0.5 for round wire. The real part and imaginary part of $< \dot{\mu}_r >$ versus normalized wire radius a/δ are plotted in Fig. 2.

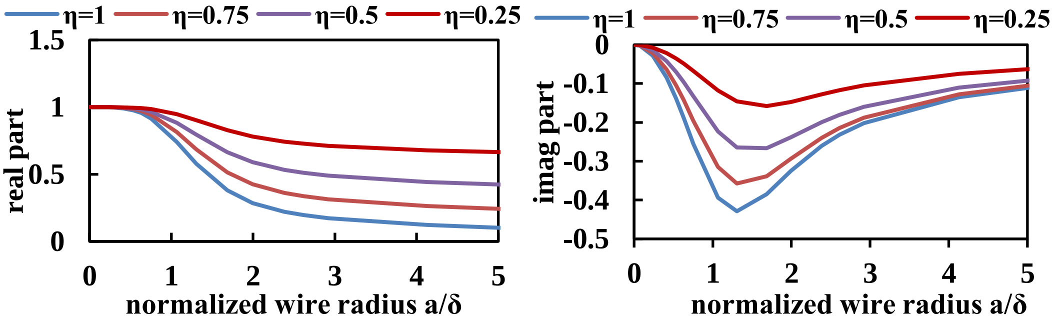

(a) Real part of $< \dot{\mu}_r >$ (b) Imaginary part of $< \dot{\mu}_r >$

Fig. 2 Complex permeability versus normalized wire radius

3. Cauer circuit

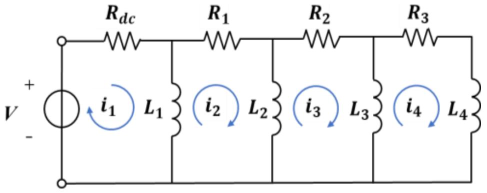

Fig. 3 Construction of Cauer circuit

Fig. 3 exemplifies a 4-stage Cauer circuit, where R_{dc} and L_1 denote the DC resistance and inductance of the device. When frequency is sufficiently low, most current flows through R_{dc} and L_1. As frequency increases, the eddy current loss and demagnetizing effect come to emerge, which are represented by R_1, R_2 ... L_2, L_3 ...

Identification method is applied to calculate the parameters of Cauer circuit based on the input impedance calculated from homogenization method in Section.2, which was not applied in [4]. The objective function is shown as below. The complex adjoint method and argument Lagrangian method are applied to the algorithm [4].

$$\min F(\boldsymbol{x}) = \sum_{q=1}^{N_s} \frac{\left|R(\boldsymbol{x},\omega_q) - R_s(\omega_q)\right|^2}{\left|R_s(\omega_q)\right|^2} + \frac{\left|X(\boldsymbol{x},\omega_q) - X_s(\omega_q)\right|^2}{\left|X_s(\omega_q)\right|^2} \tag{6}$$

4. Numerical result

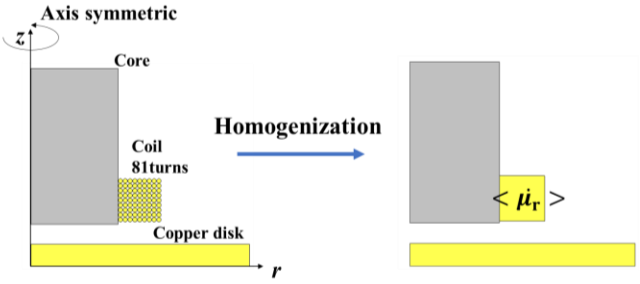

Fig. 4 Inductor model

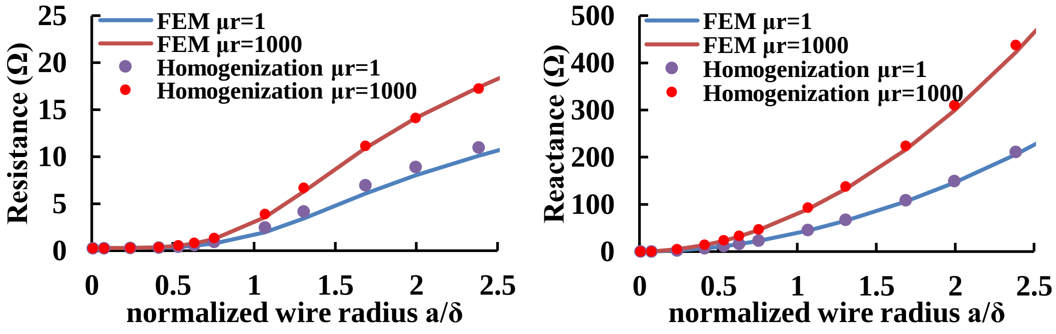

(a) Resistance (b) Reactance

Fig. 5 Impedance versus normalized wire radius

We consider the inductor model shown in Fig. 4. It locates in an axis-symmetric coordination and the relative permeability μ_r of the core is set as 1 and 1000. For the impedance calculated from homogenization FEM (JMAG^{TM}), we find it fits well with conventional FEM shown in Fig. 5 and is much faster.

We build the 4-stage Cauer circuit based on the impedance calculated from homogenization method when the relative permeability of core is set as 1000. The parameters of Cauer circuit are shown in Table 1. Moreover, we find that the impedance of Cauer circuit is consistent with that calculated from FEM in frequency domain in Fig. 6.

Table 1 Parameters of Cauer circuit.

R_{dc} [Ω]	R_1 [Ω]	R_2 [Ω]	R_3 [Ω]	L_1 [μH]	L_2 [μH]	L_3 [μH]	L_4 [μH]
0.279	991.24	20092.87	69993.52	356.922	3144.08	21416.37	79974.75

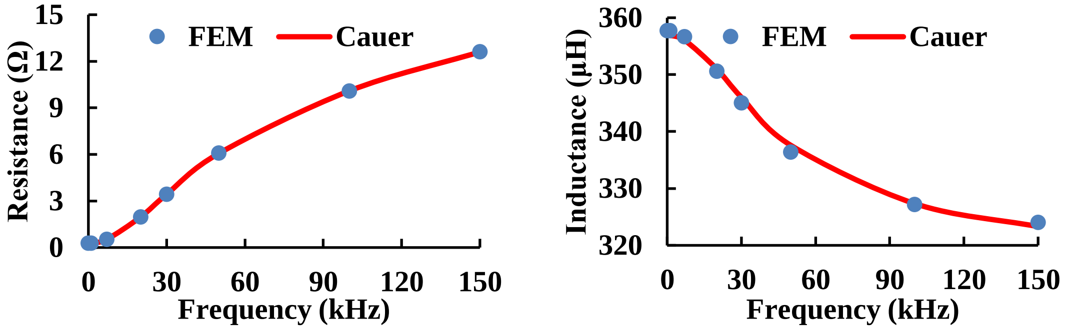

(a) Resistance (b) Inductance

Fig. 6 Resultant impedance in frequency domain

5. Conclusion

In this abstract the homogenization is applied to calculate the impedance of magnetic device in which round wire is used. It is feasible and much efficient. Based on the result calculated from homogenization method, parameters of Cauer circuit are identified by adjoint variable method. The Cauer circuit is consistent with input impedance in frequency domain.

In the presentation, we will compare the instantaneous copper loss of devices computed using Cauer circuit with that computed by the conventional formula in [1].

References

[1] C. R. Sullivan, "Computationally efficient winding loss calculation with multiple windings, arbitrary waveforms, and two-dimensional or three-dimensional field geometry," in IEEE Transactions on Power Electronics, vol. 16, no. 1, pp. 142-150, Jan. 2001

[2] H. Igarashi, "Semi-Analytical Approach for Finite-Element Analysis of Multi-Turn Coil Considering Skin and Proximity Effects," in IEEE Transactions on Magnetics, vol. 53, no. 1, pp. 1-7, Jan. 2017, 7400107

[3] Y. Otomo and H. Igarashi, "Synthesis of a Cauer Equivalent Circuit for Electric Devices from Computed and Measured Data," in IEEE Transactions on Power Electronics, vol. 36, no. 4, pp. 4513-4521, April 2021

[4] Q.Liu, Y. Uehara, N. Terauchi, H. Igarashi, "Loss Evaluation of Magnetic Devices using Cauer Equivalent Circuit Identified from Input Impedance" Compumag 2023, PB-A1, Apr. 2023

A Generalized SIR Model with Chaos Dynamics

Masahiro Nakagawa

TOFFEE Inc.

Nagacho 1-2-6-402
Nagaoka, Niigata 940-0053, JAPAN

mnext@toffee.jp

Abstract. In the present work, we shall extend the conventional SIR model to involve a chaos dynamics in a certain analogy with the predator-prey model. From the numerical simulation results, it will be elucidated that our model implies a chaos dynamics in the state variables, *i.e.* the susceptible population, the infectious population, the recovered population, the immune vector animals and the viral load. Moreover the corresponding Lyapunov spectra for the above state variables will be derived so as to confirm the presence of chaotic dynamics by means of the Lyapunov analysis method.

Keywords: SIR MODEL , CHAOS DYNAMICS, LYAPUNOV ANALYSES, NUMERICAL SIMULATIONS

1. Introduction

Since the pioneering work founded by Kermack and McKendrick[1], a variety of infection disease models have been proposed extensively up to date[2-5] . Especially, in recent years the COVID viruses spreading over the world since 2020 have been found to crucially affect not only on the human health-ware but also on the global economy[5]. In order to suppress the induced economic blow under the lock down of the specified areas as well as medical facilities crises, it has been appreciated to be significant to accurately predict a trend of chaotic divergence of the virus infection disease [6] in advance, whereas it has not been clarified yet to date because the conventional SIR (susceptible-infectious- recovered) model does not produce such a chaotic behavior according to the mathematical framework [1]. Recently, to accomplish the above-noted suppression of the infection disease, the present author challenged to realize an optimal control of the contact rate [1-5] in the SIR [7] and SEIR (susceptible-exposed-infectious-recovered) models [8] on the basis of the maximum principle theory established by Pontryagin[9]. Therein optimal control schemes of both the duration of the state of emergency declaration and the degree of the suppression of the effective reproduction number in the infectious disease models have been conducted under the maximum principle control strategy [7,8,9].

From another aspect, a chaotic behavior in the predator-prey model has been found in the discrete-time model not in the continuous-time one under a certain set of model parameters[10]. In addition some chaotic SIR models have been proposed even in the continuous-time approaches [11,12] not in the above-mentioned discrete-time model. They reported that such a chaotic behavior may be induced with the periodically time-dependent parameter concerned with the effective contact rate according to the seasonality in outbreak. Nevertheless the validity of such a periodic oscillation of the above-mentioned model parameter has not been substantially clarified yet as the meteorological phenomena reads intrinsically a chaotic behavior but not periodic one[13].

From the above-noted viewpoints we shall put forward herewith an extended SIR model introducing the immune vector animals and the viral loads as additional state variables[10] into the conventional SIR model[1] in order to involve chaotic dynamics.

2. Theory

In the followings, the present theoretical frame work will be described in brief. The dynamics of the presently proposed SIR model is to be defined as follows,

$$\frac{dx_1}{dt} = -\beta x_1 x_2 + \gamma \alpha_x x_1 - \gamma \varepsilon_x x_1 x_5 + \gamma \xi x_3, \tag{1}$$

$$\frac{dx_2}{dt} = +\beta x_1 x_2 - \gamma x_2 - \gamma \varepsilon_x x_2 x_5, \tag{2}$$

$$\frac{dx_3}{dt} = +\gamma x_2 - \gamma \left\{ \left(\alpha_x - \varepsilon_x x_5 \right) x_1 \right\} + \gamma \varepsilon_x x_2 x_5 - \gamma \xi x_3, \tag{3}$$

$$\frac{dx_4}{dt} = \gamma \alpha_y x_4 - \gamma \varepsilon_y x_4 x_5, \tag{4}$$

$$\frac{dx_5}{dt} = \gamma \eta_x \left(x_1 + x_2 \right) x_5 + \gamma \eta_y x_4 x_5 - \gamma \sigma x_5, \tag{5}$$

where x_1, x_2 and x_3 are for the susceptible population, the infectious population and the recovered population after the infection, respectively as in the conventional SIR model[1]. Then x_4 and x_5 correspond to the immune vector animal population and the viral loads, *e.g.* COVID-19 viruses, respectively[10]. In addition β denotes the effective contact rate between the susceptible and the infectious populations[1], γ is the recovery rate after the infection[1-11], ε_x represents a contact rate of the susceptible (also infectious) population to the viruses, ξ denotes the transfer rate from the recovered population to the susceptible population in accordance with the depression of the immune effect through the elapsed days after the acquisition of immunity, α_x may be regarded as the birthrate which is assumed to be equal to the mortality rate for simplicity in the present framework, α_y is related to the Malthusian coefficient[5] for the immune vector animals, ε_y is the contact rate between the immense animals and the viruses, η_x corresponds to the Malthusian coefficient for the virus proliferate concerned with the susceptible and the infectious populations, η_y is concerned with the contact rate between the immune animals, *i.e.* bats, and the virus, and σ represents a parameter for the life-span of the virus. We have to note here that x_4 and x_5

correspond to additionally introduced variables into the present extended SIR model[1]. Especially, one has to note that our model presented by eqs.(1)-(5) is to be reduced to the conventional SIR model[1] if $\alpha_x = \varepsilon_x = \xi = 0$, in which SIR dynamics[1] defined by eqs.(1)-(3) and the predator-prey dynamics[10] by eqs.(4) and (5) are to be decoupled each other. Since the present model is based on the continuous-time framework different from the previous model[10], it has to be noted that the predator-prey model defined by eqs.(4) and (5) with $\alpha_x = \varepsilon_x = \xi = 0$ does not involve any chaotic behavior [1-8].

Then we are at the position to introduce the following normalized state variables as

$$s_1 = \frac{\eta_x}{\sigma} x_1 \equiv S, s_2 = \frac{\eta_x}{\sigma} x_2 \equiv I, s_3 = \frac{\eta_x}{\sigma} x_3 \equiv R, s_4 = \frac{\eta_y}{\sigma} x_4 \equiv P, s_5 = \frac{\varepsilon_x}{\alpha_x} x_5 \equiv V, \tag{6}$$

where S, I, R, P and V denote here the normalized state variables corresponding to the susceptible population, the infectious population, the recovered population, the immune animals, and the viral loads, respectively.

3. Simulation Examples and Concluding Remarks

Setting $\gamma R_0 = \beta(\sigma / \eta_x)$ (R_0 :the basic reproduction number), $\nu = \alpha_y, \rho = \nu / (\alpha_x \mu)$, $\alpha = \alpha_x, \mu = \varepsilon_y / \varepsilon_x$ and as $R_0 = 2, \alpha = 0.01, \gamma = 0.2, \mu = 2, \rho = 0.5, \sigma = 0.5, \xi = 0$, as a set of model parameters to involve a chaotic dynamics as found in the computer simulations, and $S(0) = 1 - I(0) - R(0), I(0) = 10^{-4}$, $R(0) = 0, P(0) = 1 - (1+\alpha)/R_0, V(0) = \rho$ assuming an epidemic process, we present examples of the time dependence of the state variables, the chaos attractor and the Lyapunov spectrum derived from eqs.(1)-(5)[14,15] in Figs.1-3, respectively. Therein one may obviously confirm chaotic behaviors of all state variables, S, I, R, P, V. Moreover an enhancement of the maximum Lyapunov exponents, *i.e.* $\lambda_{\max}$, on R_0 is found over $R_0 \sim 1.5 \sim 3.5$ in Fig.4.

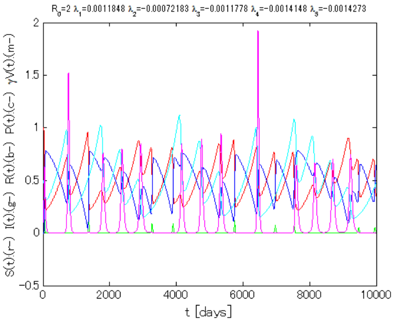

Fig.1 An example of the state variables

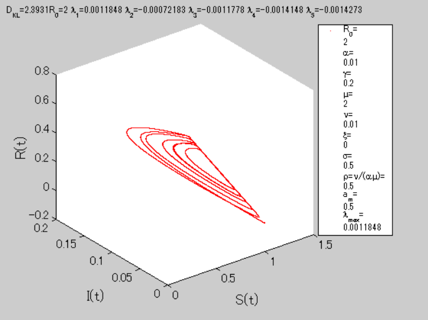

Fig.2 An example of the chaos attractor

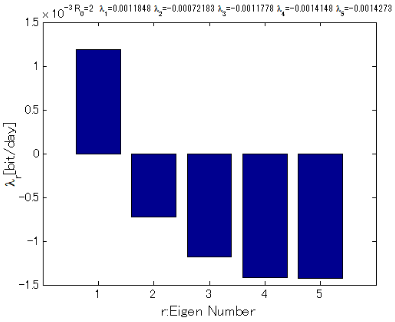

Fig.3 An example of the Lyapunov spectrum

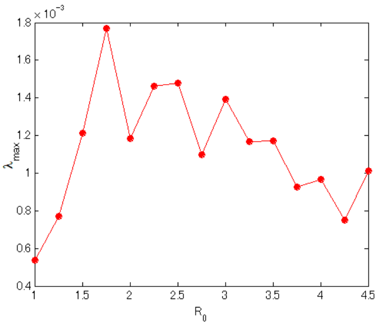

Fig.4 The dependence of the maximum Lyapunov exponents $\lambda_{\max}$ on the basic reproduction number R_0

It has to be noted from this finding that the chaotic strength *i.e.* $\lambda_{\max}$ may be emphasized with an appropriate infection capability, *i.e.* R_0 of the concerned viruses.

References

[1] W. O. Kermack and A. G. McKendrick: “Contributions to the mathematical theory of epidemics I”, *Proceedings of the Royal Society,* 115A(1927) pp.700-721.

[2] H. Inaba: “The variable susceptibility model for infectious diseases”, *Japan J. Indust. Appl. Math*., 18(2)(2001) pp.273-292.

[3] H. Inaba and H. Sekine: “A mathematical model for Chagas disease with infection-agedependent infectivity”, *Math. Biosci.* ,190(2004) pp.39-69.

[4] H. Inaba, “Endemic threshold results for age-duration-structured population model for HIV infection”, *Math. Biosci.* ,201(2006) pp.15-47.

[5] R. M. Anderson and R. M. May:“Infectious Diseases of Humans”, Dynamics and Control, *Oxford Univ. Press*, Oxford, (1991).

[6] Nabin Sapkota, Atsuo Murata , Waldemar Karwowski , Mohammad Reza Davahli, Krzysztof Fiok ,Awad M. Aljuaid , Tadeusz Marek and Tareq Ahram: “The Chaotic Behavior of the Spread of Infection during the COVID-19 Pandemic in Japan”, I*nt. J. Environ. Res. Public Health*, 19, (2022) 12804-1-16.

[7] M. Nakagawa:“A Consideration on an Optimal Control Strategy of SIR Model on the Basis of the Maximum Principle”, *Japan Society for Simulation Technology*, Vol.14, No.2(2022) pp. 85–95.

[8] M. Nakagawa:“A Consideration on a Control Method of the Injection Rate to Suppress the Infected Population on the basis of SIR Model by means of Numerical Simulations”, *Japan Sosciety for Fuzzy Theory and Intellignent Informatics*, Vol.34, No.4(2022) pp.501 – 513.

[9] L. S. Pontryagin V.G. Boltyanskii, R.V. Gamkrelidze, E.F. Mishchenko: “The Mathematical Theory of Optimal Processes”, *New York, NY, USA, Wiley*, 1962.

[10] Gary C.W. Sabin, Danny Summers:” Chaos in a periodically forced predator-prey ecosystem model”, *Mathematical Biosciences*, Vol. 113, No. 1, (1993) ,pp. 91-113.

[11] Q. Zhang, F. Zhang and F. Bai:“Chaos Analysis and Control for A Class of SIR Epidemic Model with Seasonal Fluctuation”, *International Journal of Biomathematics*, Vol. 6, No. 1(2013) ,pp.1250063-1-1250063-11.

[12] N. Stollenwerk , S. Spaziani , J. Mar, I. E. Arrizabalaga,D. Knopoff , N. Cusimano , V. Anam , A. Shrivastava , and M. Aguiar:“Seasonally Forced SIR Systems Applied to Respiratory Infectious Diseases, Bifurcations, and Chaos”, *Computational and Mathematical Methods*(2022)pp.3556043-1-3556043-2.

[13] E. N. Lorenz: “Deterministic Nonperiodic Flow”, *J. of the Astronomic Sciences*,Vo.20,No.3(1963)pp.130-141.

[14] M. Nakagawa:“Chaos and Fractals in Engineering”, *World Scientific, Inc*.,(1999).

[15] S. N. Rasband: “Chaotic Dynamics of Nonlinear Systems”,*John Wiley & Sons*(1989).

Sound field evaluation with nonsteady state for experimental environment with ADVENTURE_Sound

Akihiro Kudo[1*], Amane Takei[2]

[1] Department of Engineering for Innovation, Tomakomai Collage, Japan
[2] Faculty of Engineering, University of Miyazaki, Japan

*kudo@tomakomai-ct.ac.jp

Abstract. Identifying the acoustic effects of sound sources on listeners is important for understanding the acoustic phenomena that occur to listeners. We have focused on loudspeaker-snowman model including a chair as more practical acoustical simulation model at JSST2022. The acoustical impact of the chairs on the sound field around the snowman was evaluated. In this presentation, we will try to compute the same model by nonsteady state with the sinc function as a sound source, because the function enables to obtain frequency characteristics.

Keywords: wave-sound analysis, Parallelized finite element method, Domain decomposition method, ADVENTURE_Sound., experimental environment, nonsteady state

1. Introduction

A wave-sound analysis based on a numerical analysis method, such as the finite element method, has become widespread due to recent improvements in computer performance and numerical calculation technology. In the case of accurately reproducing an analysis model of complicated shape, it is necessary to use many small the elements. In the case of analyzing the state of wave-sound propagation in a wide range, a wide analysis domain is examined. Furthermore, to perform a high-accuracy analysis, it is necessary to model the analysis domain with a sufficiently small element for the wavelength, and, in this case, the number of elements also increases. Increasing the number of elements increases the scale of the problem. Therefore, a method that can calculate large-scale problems has come to be demanded. Moreover, large-scale problems must be solved with high accuracy.

We have focused on loudspeaker-snowman model including a chair as more practical acoustical simulation model at JSST2022. Our conclusion of previous presentation was even the presence of a chair was found to have the possibility to trigger changes in sound localization. On the other hand, since the results of the previous presentation were obtained under steady-state conditions, it was not possible to evaluate the temporal variation of sound waves around the snowman's ears. While our acoustic target remains the same in this presentation, the simulation conditions are non-stationary in order to calculate the time evolution of sound waves.

2. Basic target model

Fig.1 shows the target model used for a simulation. This model states more practical because this includes a loudspeaker, listener with a chair. These enable us to reproduce a situation at the psychoacoustical experiments.

The listener is a snowman that consists of two spheres. The diameters of the listener head and torso are 0.177[m] and 0.3[m], respectively. The distance from the loudspeaker to the listener is set to 1.5[m]. This distance assumes that ordinary psychoacoustical experiment. A chair was placed at the bottom and back of the snowman. This was to hold the listener in place.

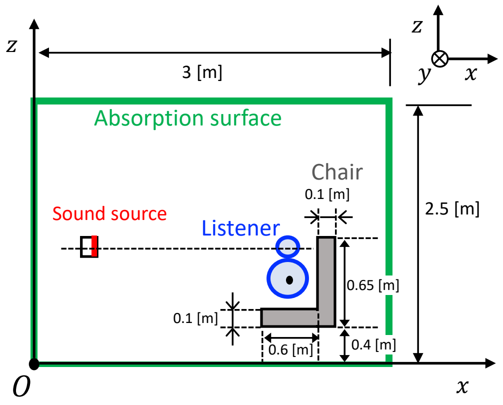

Fig.1 Dimensions of the side view in the loudspeaker-snowman model

We will try to evaluate the impact on sound localization of the obstacles like a chair by analyzing sound field around the both ears with non-stationary.

3. Numerical example

For examining ADVENTURE_Sound on a real-world problem, we model the environment of acoustic experiments. The computations are performed on a 8-node (128-core) PC cluster (Intel® Xeon E5-2650L,1.8GHz with 16 cores L2 20480[KB]) with 32 GB RAM per node. The simulation statistics are shown in Table 1. More detail thins will be shown at the conference.

Table 1 Simulation Statistic

Frequency	2000 [Hz]
No. of Elements	1.0×10^8
No. of DOF	1.0×10^8
Platform	8-node workstation cluster with Intel Xeon, 1.8 GHz
No. of cores	16
Main memory per node	32 [GB/node]

References

[1] A. Takei, A. Kudo: Over 100 million degrees of freedom scale wave sound analysis based on parallel finite element method, JSST, 12:2 (2020), 76-84.

[2] A. Takei, S. Sugimoto, M. Ogino, S. Yoshimura, H. Kanayama: Full wave analyses of electromagnetic fields with an iterative domain decomposition method, *IEEE Trans. on Magn.*, 46:8 (2010), 2860-2863.

[3] A. Kudo, A. Takei: Performance evaluation of wave-sound analysis code: ADVENTURE_Sound, JSST, 17:1 (2021).

[4] A. Kudo, A. Takei: Sound field evaluation of experimental environment with ADVENTURE_Sound, JSST, 36:2 (2022).

Numerical Analysis of Insect Flight Maneuverability Using Feedback Control Model

Kaede Sugikawa[1,*], Minato Onishi[1], Daisuke Ishihara[2]

[1]Department of Computer Science and Systems Engineering, Kyushu Institute of Technology
[2]Department of Intelligent and Control Systems, Kyushu Institute of Technology

*sugikawa.kaede544@mail.kyutech.jp

The full paper of this paper has been published in Journal of Advanced Simulation in Science and Engineering (JASSE).

DOI: https://doi.org/10.15748/jasse.11.201

Highlighting the color boundary of 3D scanned point clouds by PCA in color space

Keigo Furuya[1*], Kyoko Hasegawa[2], Liang Li[2], Satoshi Tanaka[2]

[1]Graduate School of Information Science and Engineering, Ritsumeikan University
[2]College of Information Science and Engineering, Ritsumeikan University
*`is0473ff@ed.ritsumei.ac.jp`

Abstract. There are efforts to preserve traditional techniques and use them in academic research by digitizing historical cultural properties as 3D scanned point clouds, which may become impossible to survey and analyze due to deterioration over time. Highlighting the shape of feature areas in 3D scanned point clouds is effective in accurately understanding the structure of cultural properties. In this study, we propose to improve the visibility of cultural properties by using the color information contained in 3D point clouds to highlight color boundaries.

Keywords: Principal component analysis, Color boundary-highlighting, Color space

1. Introduction

In recent years, *digital archives*, in which tangible cultural properties are converted into digital data and passed on to future generations, have developed and spread. Three-dimensional (3D) measurement is widely used as an effective technology for digitizing the current state of tangible cultural properties. This has made it possible to record the entire 3D structure of tangible cultural property by combining the exterior and interior 3D measured point clouds. Stochastic point-based rendering point rendering [1] has been developed as a visualization method for the obtained point clouds, and its visibility has been improved by noise tranparentization of the point clouds [2]. Furthermore, a method to improve visibility by extracting and highlighting characteristic geometrical regions of visualization targets has been proposed [3]. Similarly, in the case of 3D point clouds with multiple color regions on a surface, highlighting and visualizing the boundaries of color information in the point clouds are considered to be useful for understanding the structure [4].In this study, we propose a method for extracting and highlighting color boundaries by applying a feature-enhancement visualization method for shapes based on principal component analysis (PCA) in the RGB color space.

2. Proposed method

2.1. Stochastic point-based rendering: SPBR

This study uses Stochastic point-based rendering (SPBR) as a visualization method for 3D point clouds. SPBR enables fast transparent visualization because it does not require depth sorting. SPBR visualizes 3D point clouds using the following procedure.

Step 1: Generate an ensemble of point clouds

Generate an ensemble of point clouds with a uniform point density distribution on a plane or planar surface from an input 3D point cloud.

Step 2: Point projection for ensemble point clouds

For each of the L ensemble point clouds obtained in Step 1, each point is independently projected onto the image plane to produce L intermediate images. The points are assumed to be opaque during the projection, and the hidden-point removal is executed at each pixel.

Step 3: Averaging of intermediate images

The final transparent image is created by averaging the corresponding pixel intensities of the L intermediate images generated in Step 2.

2.2. PCA in color space

It is known that we can extract 3D-edge regions from 3D point data based on PCA (principal component analysis) [5]. In this study, we propose a conversion of the conventional PCA-based feature area extraction method, which detects local shape change in real space, into a method that detects the degree of local color change on the RGB color surface. The same definitions of feature values, such as *change of curvature*, *linearity*, and *aplanarity*, used in the real space are applied to the RGB color space. These feature values can also be utilized to extract color boundaries instead of the conventional extraction of 3D edges. Figure 1 shows a model consisting of point cloud data of a cube with different colors at the center, and principal component analysis is performed on the point cloud around the point of interest $P^{(i)}$. The steps of the proposed method are summarized as follows.

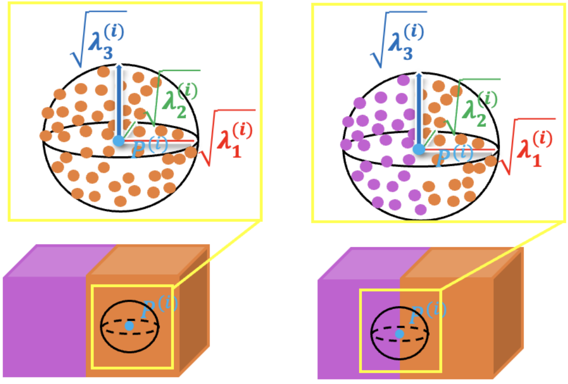

Figure 1. Concept of color boundary extraction using PCA

Step 1:
Compute the covariance matrix from the color information of the points in the sphere centered at the point of interest $P^{(i)}$.
Step 2:
Calculate the feature $F^{(i)}$ after obtaining the eigenvalues $(\lambda_1^{(i)} \geq \lambda_2^{(i)} \geq \lambda_3^{(i)})$ from the covariance matrix.
Step 3:
A threshold value f_{th} is set for the feature value $F^{(i)}$, and the point $P^{(i)}$ with a feature value f greater than the threshold value is visualized as a color boundary.

3. Proposed feature values for color boundary extraction in RGB color space

Here we demonstrate the effectiveness of our method by applying it to 3D scanned data shown in Figure 2. We found that *linearity* is the best feature value among the conventional feature values. However, we also found that color boundaries disappear in some areas (see the right-bottom area in the image of Figure 3). This problem occurs when the first principal component value is extremely large compared to the second and third principal components. Therefore, we propose a new feature value of Eq.(1), where $\overline{\lambda_1^{(i)}}$, $\overline{\lambda_2^{(i)}}$, and $\overline{\lambda_3^{(i)}}$ are the average values of the eigenvalues at the time of calculation. This feature formula enables the extraction of parts that cannot be extracted by the conventional feature using $\lambda_1^{(i)}$by adding weights to $\lambda_2^{(i)}$ and $\lambda_3^{(i)}$. The result of extracting the color boundary is shown in Figure 4. We can clearly observe improvement in the area where *linearity* does not work well.

$$F^{(i)} = \begin{cases} \dfrac{\overline{\lambda_1^{(i)}}}{\overline{\lambda_2^{(i)}}}\lambda_2^{(i)} + \dfrac{\overline{\lambda_1^{(i)}}}{\overline{\lambda_3^{(i)}}}\lambda_3^{(i)} \quad . & (\lambda_1^{(i)} < f_{\lambda_1}) \\ \lambda_1^{(i)} \quad . & (\lambda_1^{(i)} \geq f_{\lambda_1}) \end{cases} \qquad (1)$$

Figure 2. Input point cloud data

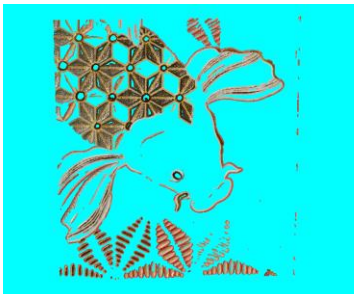

Figure 3. Color boundary extraction using *linearity*

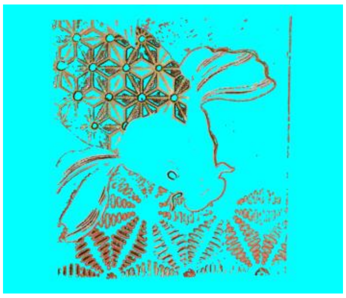

Figure 4. Color boundary extraction using the proposed feature value

4. Conclusion

In this study, to understand the detailed structure of 3D point clouds with multiple color regions on a surface, we proposed an enhanced visualization of color boundaries of 3D point clouds using PCA in color space. Comprehensible observation is realized based on the transparent fused visualization of the extracted edge data and the original-colored 3D point data. We also proposed a new feature value appropriate for extracting color boundaries. As for future studies, we will improve the accuracy of color boundary ex-traction by using color distance in HSV or L*a*b color spaces.

References

[1] S. Tanaka, K. Hasegawa, N. Okamoto, R. Umegaki, S. Wang, M. Uemura, A. Okamoto, K. Koyamada: *See-Through Imaging of Laser-scanned 3D Cultural Heritage Ob- jects based on Stochastic Rendering of Large-Scale Point Clouds*, ISPRS Ann. Photo- gramm. Remote Sens. Spatial Inf. Sci., III-5, (2016), pp. 73-80.

[2] T. Uchida, K. Hasegawa, L. Li, M. Adachi, H. Yamaguchi, F. I. Thufail, S. Riyanto, A. Okamoto, S. Tanaka: *Noise-robust transparent visualization of large-scale point clouds acquired by laser scanning*, ISPRS Journal of Photogrammetry and Remote Sensing, Vol.161, (2020), pp.124-134.

[3] K. Kawakami, K. Hasegawa, L. Li, H. Nagata, , M. Adachi, H. Yamaguchi, F. I. Thufail, S. Riyanto, Brahmantara, S. Tanaka: *Opacity-based edge highlighting for transparent visualization of 3D scanned point clouds*, ISPRS Ann. Photogramm. Remote Sens. Spatial Inf. Sci. (Proc. XXIV ISPRS Congress), Vol.V-2-2020, (2020), pp.373-380.

[4] D. Fujimoto, T. Ito, S. Nakata, T. Kitagawa, M. Oka, S. Tanaka: *Implicit Surface Reconstruction with Color Distribution Using MPU Implicits*, The IEICE transactions on information and systems, Vol.89, No.6, (2006), pp.1391-1402.

[5] M. Weinmann, B. Jutzi, C. Mallet: *Semantic 3D sceneinterpretation: A framework combining optimal neighborhood size selection with relevant features*, ISPRS Annals of Photogrammetry, Remote Sensing and Spatial Information Sciences, Vol.II- 3, (2014), pp.181-188.

High-precision rendering of 3D scanned point cloud based on noise transparency method

Qingyu Mao[1], Liang Li[2], Kyoko Hasegawa[2], Tomomasa Uchida[3], Satoshi Tanaka[2]

[1] Graduate School of Information Science and Engineering, Ritsumeikan University

[2] College of Information Science and Engineering, Ritsumeikan University

[3] FUJIFILM Business Innovation Corp

*is0597rs@ed.ritsumei.ac.jp

Abstract. This paper proposes a method called “point-based depth peeling” to reduce the measurement noise of 3D scanned point clouds. The method extracts visible portions of the point cloud near the viewpoint and makes noise points of the portions transparent, i.e., invisible. The method realizes high-precision visualization of 3D scanned point clouds with noises. We demonstrate its effectiveness by applying it to various real 3D scanned point clouds.

Keywords: 3D scanned point cloud, depth peeling, measurement noise

1. Introduction

3D scanned point clouds have been widely used in cultural heritage preservation and various fields according to technological advancements in laser scanning and photogrammetry [1,2]. However, 3D scanned data often include measurement noise due to environmental and weather conditions, resulting in poor-quality visualization. This paper proposes a method we call “point-based depth peeling” to process visible regions of a given 3D scanned point cloud and make noise points of the regions transparent, i.e., invisible.

2. Noises in 3D scanned point clouds

There are two typical types of measurement noise found in 3D scanned point clouds, the outlier noise and the Gaussian noise [3]. First, outlier noise refers to noise points that deviate significantly from the region where they should exist. It arises due to the effects of shiny objects such as glass windows and tree leaves. Such noise points result in messy visualization. Second, Gaussian noise refers to the noise points that are distributed around the 3D scanned surface of the object. They often arise due to measurement errors or vibrations of the target object. This type of noise introduces ambiguity in the visualization of the scanned surface, making it difficult to use for visual analysis.

3. Polygon-based depth peeling

Polygon-based depth-peeling is a technique that has been used in polygon rendering where layers of polygons are peeled off one by one, starting from the layer closest to the viewpoint to the furthest layer. This method can process each layer with hidden surface removal and alpha blending (Fig.1).

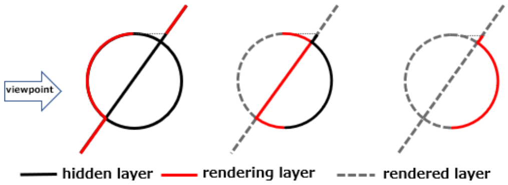

Fig.1 Depth peeling method

In the depth peeling, a depth buffer is used to determine the depth values (Z-values) from the viewpoint. Using hidden surface removal to extract the nearest surface from the viewpoint, which is referred to as the "first layer". Then, the contents of the depth buffer are preserved and rendered again. The preserved depth values are referenced to extract the surfaces that are behind them, and this will be the "second layer." This process is repeated iteratively to extract surfaces until the deepest layer of the object is rendered.

4. Noise transparency method

Point-based depth peeling uses points as the rendering units. Each pixel generates layers in the order of points closest to the viewpoint. The closest point to the viewpoint will be the first layer of each pixel (Fig.2). Each pixel has different layer counts, but the group of layers closest to the viewpoint always represents the visible surface of the shape. It is important to extract an appropriate number of layers for each pixel. Having too many or too few layers results in a deterioration of the smoothing effect.

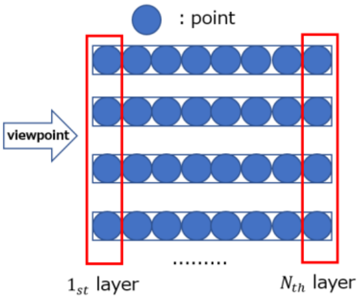

Fig.2 Layer in the point-based depth peeling

As explained in Section 2, outlier or Gaussian noise are points that deviate from the scanned surface, resulting in unstable pixel colors. However, Large-scale 3D point clouds have a very high point density and quantity, with repeated sampling occurring at the same location. Consequently, nearby points record the position and color of the same part of the objects in the 3D point clouds. Therefore, the points of the objects will be far more than the noise points, and they exhibit good color stability. Our idea is to execute pixel-by-pixel smoothing without deterioration of the image resolution by averaging the colors of points projected onto the same pixel.

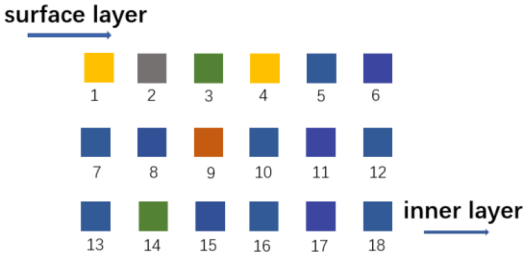

Fig.3 Color distribution of points within a pixel

Figure 3 shows 18 points within the same pixel that are closer to the viewpoint. In this example, the majority of points are blue and exhibit better stability. So we can consider the true color to be blue. The following steps show the process of getting the true color of a pixel.

Step 1. Determine the maximum layer count $N_{\max}$, as a parameter to extract a portion of the point cloud for the object surface.

Step 2. Determine the number of layers N to evaluate the color stability for every point.

Step 3. Evaluate the color stability using the variance of the colors of the N layers nearest from the viewpoint layers. To evaluate the variance, we use the sum of variances of red, green, and blue colors.

Step 4. Remove the layer closest to the viewpoint from the N layers in the calculation of Step 3. Starting from the second closest layer, perform the same calculation as in Step 3.

Step 5. Repeat Step 4 until $N_{\max}$ layers are calculated.

Step 6. Determine the pixel color as the median value of the N layers with the lowest value.

5. Visualization Experiments

We demonstrate the effectiveness of the proposed method by applying it to real 3D scanned points of the festival float of the Gion Festival (Kyoto, Japan). Generally, outlier noise points have a wide distribution in the point clouds and low point density, while Gaussian noise points are distributed around objects with higher noise density. We use the point cloud with 1% outlier noise points (Fig.4) and the point cloud with 10% Gaussian noise points (Fig.5) to verify the feasibility of the proposed method.

Fig.4 Left: 3D scanned point with outlier noise added. Right: Result of the proposed method.

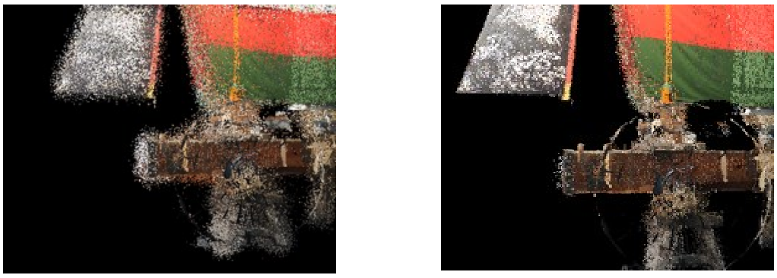

Fig.5 Left: 3D scanned point with Gaussian noise added. Right: Result of the proposed method.

When processing the point cloud with outlier noise points (Fig.4), almost all the noise points are effectively removed. This is because the density of outlier noise points is much lower than that of the object itself, and generally, they have no significant color correlation with the nearby points of the object. Therefore, they will have a larger variance value during computation and are unlikely to be selected as the final output color.

When dealing with Gaussian noise points (Fig.5), most are removed, but a few persist. These points arise from nearby point movement and similar colors. Object points generally exhibit better color stability. However, Gaussian noise points are usually caused by the movement of nearby points and have similar colors. In large-scale 3D point clouds, there will still be a small number of noise points that are mistakenly considered as correct color outputs due to their good color stability. Moreover, pixels with points below a threshold are treated as noise and made transparent. But high-density Gaussian noise pixels are retained if their point count exceeds the threshold.

6. Conclusions

This paper has proposed the point-based depth peeling method, a high-quality point rendering method suitable for noisy 3D scanned point clouds. The method makes measurement noise invisible without deteriorating the image resolution based on pixel-by-pixel smoothing. The pixel-by-pixel smoothing is possible because of the redundancy of points in 3D scanned point clouds. We have also demonstrated the effectiveness of the method by applying it to real 3D scanned points to which heavy noise points are added.

References

[1] H. Masuda: Challenges and Technological Trends in Large-scale Point Cloud Processing Based on 3D Measurement, *Journal of the Japan Society for Precision Engineering*, 79:5 (2013), 384-387.

[2] S. Tanaka: Visualization of Cultural Heritage and Interdisciplinary Research in the ICT Era, *Trends in the sciences*, 24:4 (2019), 4_62-4_69.

[3] T. Uchida, K. Hasegawa, L. Li, M. Adachi, H. Yamaguchi, F. Thufail, S. Riyanto, A. Okamoto, S. Tanaka: Noise-robust transparent visualization of large-scale point clouds acquired by laser scanning, *ISPRS Journal of Photogrammetry and Remote Sensing*, 161 (2020), 124-134

Natural Biocomputing and Brain- like Computer

Osamu ONO*1 *2

1LLP- IPTI Lab. and 2Meiji University
tmocompany@gmail.com and ono@meiji.ac.jp
http://tmocompany-ipti.la.coocan.jp/index.html

Abstract: In this paper, we show that W. R. Ashby's electronic device is the beginning of today's artificial intelligence and that it is a hybrid storage device of analog and digital information. We discuss the anatomical prediction of the dielectric constant of water as a solution in the electron- dense layer similar to this hybrid device. It is considered that there is room for reconsideration as a simulation model that introduces human mind and consciousness into the artificial neural networks**.** This paper emphasizes these designs of artificial intelligence as a hybrid of analog and digital circuits.

Keywords: Biocomputing, Brain chip, Artificial mind

1. Ashby's Neural Circuit

A homeostat proposed by W. R. Ashby in 1954 is a vacuum tube electronic circuit device with the property of homeostasis [1]. It can be recognized that W. R. Ashby, who was involved in clinical research in neuromedicine for a long time, wanted to realize an artificial neural network corresponding to this principle with a network of electronic circuits. He named this circuit device "electronic brain" and used a unique name even at that time to describe it in its entirety. In this paper we show that this electronic device is the beginning of today's artificial intelligence and that it is a hybrid storage device of analog and digital information. According to G. -Th. Guilbaud's recognition suggests that even at the time Ashby's bold ideas were not accepted well [2]. As a recent medical knowledge, it is estimated that there are 11 th powers of 10 neurons in the human brain and they are also divided into several types, each of which is thought to have its own characteristics. By a particular main classification, it is into the cerebrum and the cerebellum according to the size of the shape. The characteristics of this significant difference have been explained by a brain clinical researcher T. Nakada [3]. The classical model is useful currently as AI that is based on the McCulloch and Pitts model, which is believed to correspond to the structure of the cerebellum. A model corresponding to the cerebrum has not yet been seriously considered, however, classical Kohonen's network model [4], [5] seems to correspond to one of them that have been considered so far, but it is still not sufficient and further structural development is needed more. A crucial point of the structure of this network is that some disturbances spread the influence of the parameters according to the motion of the fluid in three dimensions in an artificial neural network. In the cerebrum, nerve cells are thought to be connected to each other about 10 quadruple times, so this effect is a principal factor. As a result, the cerebrum finally has connections of the order of 15th power of 10 neurons.

However, this connection of neural circuits in the brain is obviously not infinite, even complex but finite.

If we assume that there are only four neurons in the brain here, imaginably, this connection corresponds to the device designed by W. R. Ashby and implemented in a network of vacuum tube electronics circuits (Fig. 1.). Although this network is obviously finite and does not match the scale of neural circuits in the brain, it is thought to have at least basic equivalent properties. The structure of AI , which is currently attracting the attention of many researchers, is structurally similar to this vacuum tube electronic circuit, although there are differences in order and there are no major differences, rather, Ashby's circuit is not made of logic circuits with only binary bits, but uses analog values with a device that incorporates electronic physical phenomena by vacuum tubes. Depending on the way of thinking, it has elements that lead to quantum bits. This paper emphasizes this point and considers the design of artificial intelligence as a hybrid of analog and digital circuits.

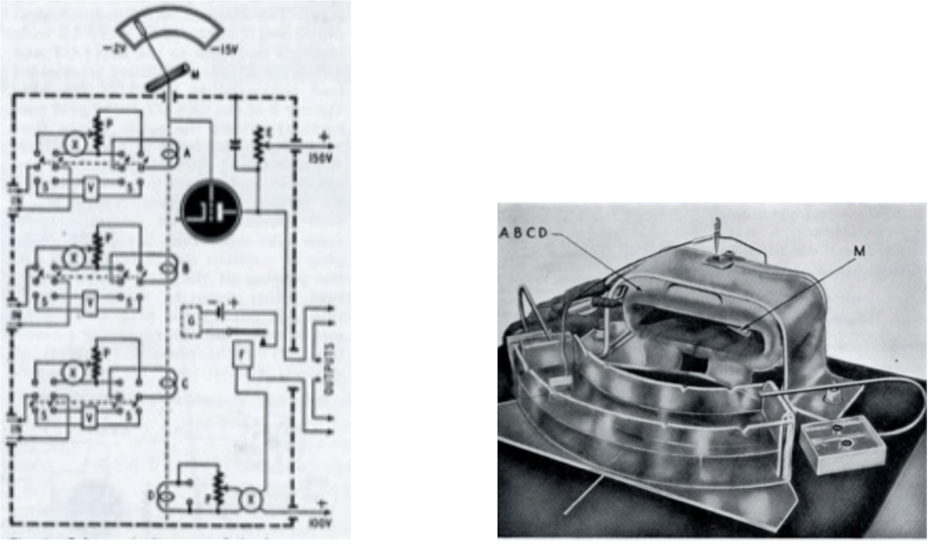

Fig. 1. “The Electronic Brain” by W. R. Ashby, MD. In Radioelectronics No.3, 1949 pp.77-80

2. Analog Computer and LISP Language

It is said that the beginning of artificial intelligence lies in language abstraction. Therefore, programs were first proposed and designed that could handle the languages that humans use today. This is the LISP language and now extremely near to the generative pretraining network. Human language is made up of symbols and associated sounds. The LISP language was developed as a program that could handle symbols directly. Bits and qubits are currently used as a means of distinguishing between symbols in a set of symbols, so symbols are still important. Therefore, artificial intelligence can be treated as a dynamic change of this combination of symbols. The critical point here is that there is an analog value as a parameter in this transformation of dynamics. Here lies an important new mission for analog computers. Although it is possible to digitally approximate the variation of the parameters, it is only an approximation and not a true analog value. It is believed that continuous analog values excite dynamics in the brain to perform all activities, including consciousness. This is the reason this paper still emphasizes analog computers. This point will be explained again in Section 4. This point will be discussed in relation to the cerebral computer proposed by T. Nakada, who is a brain researcher and brain clinician, and its realization will be discussed there.

3. Neural Network as Natural Biocomputing

The brain-like network conceived by W. R. Ashby is considered only as a homeostat device, but it is still important in terms of making use of it in the current structure of artificial intelligence as natural biocomputing. This device relies on thermoelectric physical phenomena in the vacuum tube as analog parameters, while the input and output signals are logic circuits with relays on and off, but the output is the movement in the viscous aqueous solution. It depends on the movement of the board. According to Ashby's research at the time, it settled into a stable state according to various environments, and this is homeostatic hyperstability. This can also be understood as memorizing stability according to the environment. Such an idea would be a new and important point to incorporate into current AI devices with analog and digital information memory. They are recorded as temporary memories of this ultra- stable network shape and become artificial mind and consciousness. In addition, the dynamic mechanism in an aqueous solution has similarities to the effect on neural circuits due to the high- density electron layer described by T. Nakada [3].

4. Brain- like Computer: Brain Chip

The ideas corresponding to the considerations so far can also be seen in the brain- type computer: Brain Chip derived by T. Nakada, a world authority on brain clinical medicine who has studied brain function by image analysis of functional nuclear magnetic resonance MRI. On the other hand, based on a novel hypothesis, he is proposing a brain- type computer: a brain chip. It is a neural network computer system with a structure like that of the brain from an anatomical point of view. It is not based on special structures specialized for multi- layered deep learning applications such as convolutional neural networks and back propagation that are commonly used today. There are 6 layers, and the network between the layers is not important, and the structure is designed considering the increase of the curved surface in the 3 dimensional structure of the nerve cells. It is thought that they are aiming for an optimal configuration comparable to the current human brain that can be considered by clinicians. Also, as an important analogue element of the gradient heat flow by glial cells is considered as a control parameter. The heat flow considered in current supercomputers is only a safety device for heat diffusion of digital LSI devices, however T. Nakada regards this heat flow as one of the important control elements for computation. This is the Nakada's unique point of view, because even in quantum computers the heat flow is only concerned with maintaining the coldness of quantum physical phenomena and is not considered as an important functional computing element involved in computational operations. The structure in which network operations are performed by thermal diffusion through hierarchical and three-dimensional diffusion centered on the cylinder axis is neither a normal deep learning nor a neuromorphic network, but an artificial brain that corresponds to biological optimization obtained from clinical knowledge. It has an intelligent structure that is very interesting [6].

5. Evolution on A Generative AI with AM

Backpropagation, which is currently used on a large scale, sequentially calculates the weighting coefficients along each layer into the input side. No differentiation takes place. Clearly, the actual cerebrum has functional area differentiation of neuronal groups as seen in functional MRI image measurement. Based on this fact T. Nakada proposed a cerebral computer brain chip. Among the neural networks that correspond to the discussion so far, Kohonen's neural network corresponds to this. Artificial neurons distributed on a two-dimensional plane have a structure that affects neighboring cells. The influence of a neuron r and its neighboring cell s is modeled by the following variance equation.

$$h_{rs} = e^{-\frac{\|r-s\|^2}{\sigma}}$$

The weight coefficients of the McCulloch-Pitts artificial neuron model are given by the following equation.

$$w_r^{t+1} = w_r^t + \varepsilon h_{rs}(x - w_r^t)$$

where x is the stimulus. This structure that has been simply called unsupervised learning until now, however, it should be more basic of the structure that leads to any innovative ideas and consciousness. The position- dependent function of h_{rs} forms the control parameter of the neural network, which is different from the weighting factor. It will be assumed there is a speculate point related to advanced ideas. It is considered that there is room for reconsideration as a simulation model that introduces human mind and consciousness into the artificial neural networks.

Anatomically predicts the dielectric constant of water as a solution in the electron- dense layer. This can be seen in analogy to the electric field layer device, in which electrode plates are floated in an aqueous solution so that they can be placed in the number of vacuum tube electric circuits that W. R. Ashby assumed four nerve cells already in 1945 (Fig. 1.). In the future brain chip this similar structure is necessary when considering a generative AI with artificial mind (AM).

References

[1] W. R. Ashby: *"The Electronic Brain"*, Radio Science, 1949, pp.77-80

[2] G.- Th. Guilbaud : *"La Cybernétique"*, Presses Universitaires de France, Paris, 1954

[3] T. Nakada: *"Brain Chip: A Hypothesis"*, Magnetic Resonance in Medical Sciences, Vol. 3, pp. 51-63, 2004

[4] T. Kohonen: *"Self-Organizing Maps"*, 3rd ed. Berlin, Heidelberg, Springer 2001.

[5] Y. Tsuboi, S. Shimoda, Y. Ichihara, and H. Kimura: *"Vision System for Postural Control, Emergence of Functional Cooperation"*, Proc. of the 2007 JSME Conference on Robotics and Mechatronics, 2P1-C12 (1), 2007

[6] O. Ono: *"Simulation in the Brain"*, Journal of the Japan Society for Simulation Technology, Vol. 24, No.2, pp. 91-92, 2005

Implementation of Neural Network on FPGA with Algorithm of Logic Circuit Estimation

Yuya Adachi[1*], Yusei Tsuboi[2]

[1,2]Department of Market Product Management, SICK.K.K.

*`yuya.adachi@sick.jp`

Abstract. In this research, we proposed a system based on the development of the human brain to represent the acquisition of the human unconscious at the architectural level and implemented it in practical hardware. Specifically, we constructed an efficient neural network model using pruning process and implemented it in FPGA and confirm the improvement in processing speed. This approach has demonstrated its effectiveness in applications that require real-time processing, and it is possible to consider its potential as a means of automating human tasks.

Keywords: Pruning process, Real-time performance, Bioinspired

1. Introduction

In light of the declining working-age population, the automation of production lines has gained traction, necessitating high-speed operations. There are many recent research focusing on pruning processes[1][2]. By applying pruning processing to neural networks, it is possible to reduce the size of the model, build an efficient network, and achieve high-speed processing. This pruning process is thought to be related to human brain development. Figure 1 shows the development of the human brain and indicates that synaptic connections increase until the age of 6, after which pruning occurs and synaptic connections decrease[3]. This is supposed to allow the human brain to build an efficient network that allows for high-speed processing.

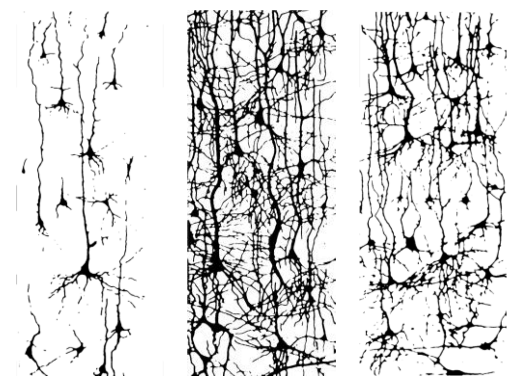

Figure 1: Human Brain Development

2. Human behavior and System proposal

There are two types of behavior: conscious and unconscious behavior. Conscious behavior involves thoughts, judgments, and actions that individuals are aware of, while unconscious behavior refers to actions performed without conscious awareness. Unconscious behavior is supposed to be acquired by optimizing the synaptic connections in the brain based on prior learning from conscious behavior, enabling fast decision-making and operations. In this research, this brain process is represented at the architectural level by utilizing training with pruning process on a fully-connected neural network and achieving high speed processing. To represent and construct this process, We propose a system performs the neural network training on a CPU, while the inference calculation is implemented on an FPGA to achieve high-speed operations through this hybridization (Fig.2).

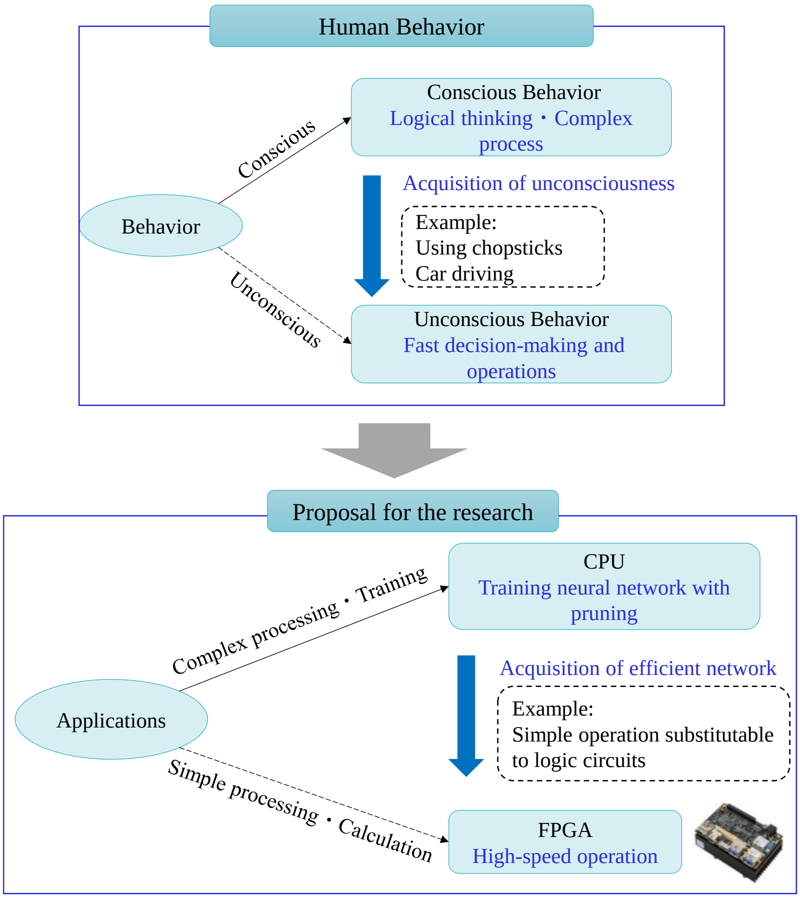

Figure 2 : Human Behavior & Proposal for the research

3. Logic Circuit Estimation Algorithm

The synaptic weight parameters are considered to reflect the degree of excitatory influence, and synapses with small absolute values of the parameters are considered to have lesser impact in the neural network. By performing a pruning process on nodes with the smallest absolute values of synaptic weights, it becomes possible to extract the characteristics of a logical circuit, retaining only the nodes with significant influence on transmission (Fig.3).

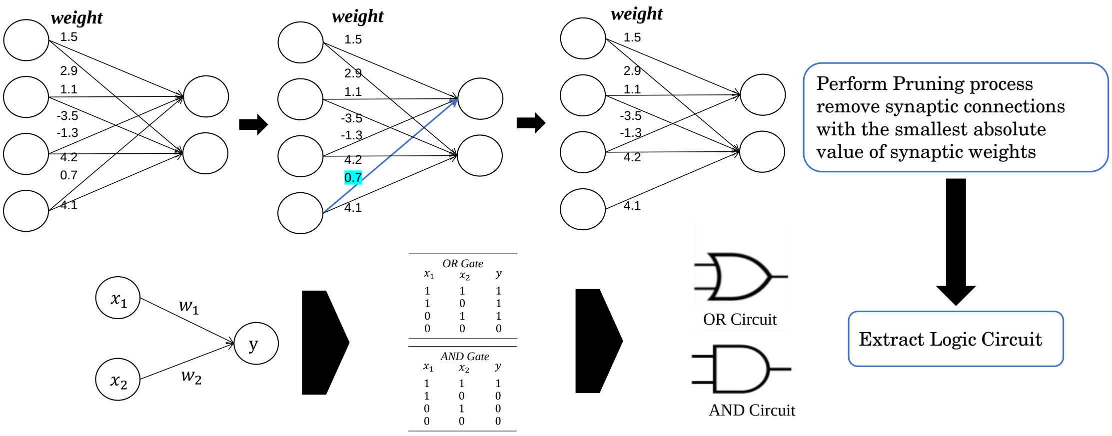

Figure 3 : Logic circuit estimation algorithm

Smallest absolute values of the synaptic wight in a neural network will be pruned (1) (2)

$$W_{min} = min\{W_1, W_2, W_3, \cdots W_i\} \tag{1}$$

$$W_i : synaptic\ weight\ (i = 1, \dots, i)$$

$$|W_{min}| \leftarrow 0 * W_{min} \tag{2}$$

The termination condition is set to when the number of synapses for each node is equal to or less than two (3).

$$SNP_N \leq 2 \tag{3}$$

$$SNP_N : Number\ of\ synaptic\ connections\ (N = 1, \dots, N)$$

4. Experimental Result

We created a neural network model that follows a truth table and trained it with the logic circuit estimation algorithm (Fig.4).

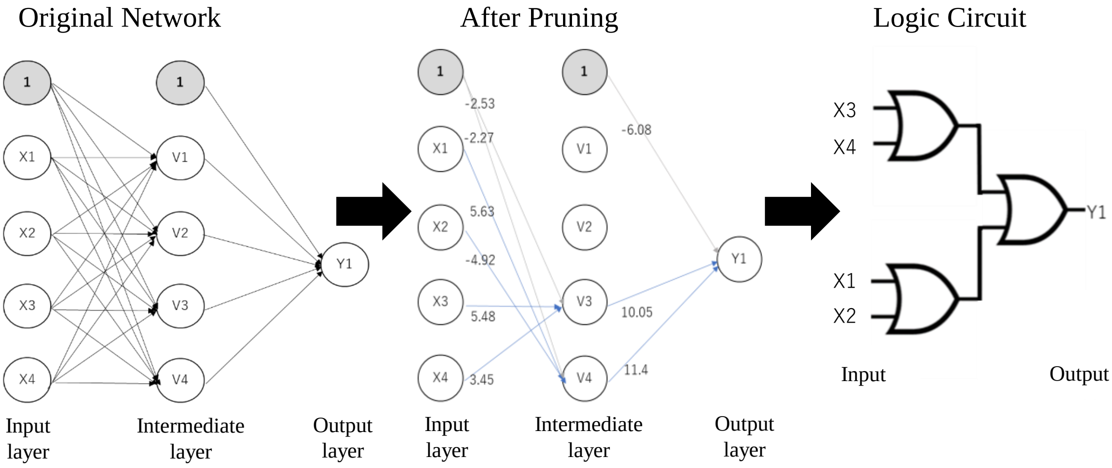

Figure 4 : The process of pruning and logic circuit estimation in a neural network with 4 inputs and 1 output.

The estimated logic circuit shown in Figure 4 was implemented on the Xilinx Ultra96 board. We conducted a comparison of the inference time using the CPU and the FPGA of the Ultra96board. The results showed that the FPGA processing was 2.96 times faster than the CPU processing. This result demonstrates the possibility of accelerating inference processing by replacing the massive matrix calculations performed on CPU with logical circuits. FPGA can directly implement logical circuits as hardware, enabling highly efficient processing specialized for specific computations. For reference, we implemented the same neural network on the Raspberry Pi, which is available at a similar price point and size as the Ultra96board, and measured the processing time (Fig.5).

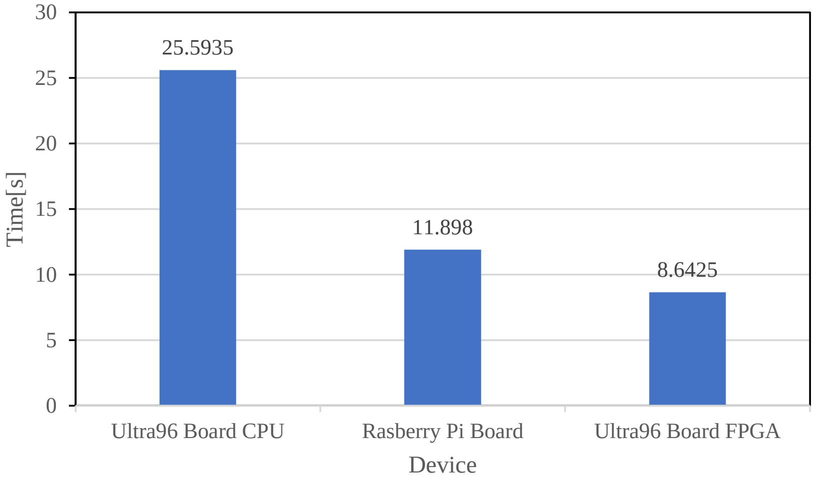

Figure 5 : Run time comparation
Number of Input : 512×512
Number of layer : 9

5. Conclusion

In this study, the processes of the human brain were configured at the architectural level.This configuration was implemented on hardware, and the processing speed was significantly enhanced by FPGA processing. The proposed system was represented based on human brain beheivor such as consciousness and unconsciousness, just as people working on production lines become skilled workers. It is expected that this system could be applied to automate human tasks in the future.

References

[1] Mirkes.E.M: Artificial Neural Network Pruning to Extract Knowledge, *2020 International Joint Conference on Neural Networks (IJCNN),* (2020), 1-8.

[2] Davis.B, Ortiz.G, Jose.J.G.O, Jonathan.F, John.G: What is the state of neural network pruning?, *Proceedings of machine learning and systems*, 2 (2020), 129-146.

[3] Rima.S: Rethinking the Brain New Insights into Early Development, *Families and Work Institute,* (1997), 20.

[4] Sohn.J, Suzuki.M, Youssef.M, Hatada.S, Larkum.M.E, Kawaguchi.Y, Kubota.Y: Presynaptis supervision of coritical spine dynamics in motor learning, *Sci Adv,* 8 (2022).

Validation of Novel Hand-eye Calibration Method for Laser-based Triangulation Camera by Simulation

Yusei Tsuboi[1*]

[1]Department of Market Product Management, SICK K.K.

*yusei.tsuboi@sick.jp

Abstract. In this paper, a novel hand-eye calibration method using a specially designed calibration target is proposed. Once the calibration is performed, our method does not need any 3D rotation of 3D data measured by a camera. The method is partly performed and evaluated by simulations. The simulation result proves feasibility of the proposed method and explains estimation of the calibration error.

Keywords: Robot vision, Laser-based triangulation camera, Hand-eye calibration, Simulation

1. Introduction

A laser-based triangulation camera is expected to cover a lot of kinds of applications in a wide range of industries [1]. It is striking that the recent camera contains a powerful microprocessor that is tailored for image analysis of 3D images. It measures 3D shape of objects, where 3D shape data is a set of collected profiles containing values for measured points along the laser cross-section as shown in Fig.1. One of the characters of the laser-based triangulation, either an object or a camera must be moved in the Y axis direction. An industrial robot and a camera mounted on it have different orthogonal coordinate systems. The hand-eye calibration which aligns a camera frame with a robot frame is one of the most important steps to integrate 3D-based robot vision with an industrial robot. Many methods that need 3D rotation of data measured by a camera after hand-eye calibration have been proposed and evaluated in related works [2, 3]. Their methods imply that high-performance hardware and excessive computational time for handling massive 3D data are vitally necessary.

In this paper, a novel hand-eye calibration method that does not need 3D rotation of 3D data is proposed, and then feasibility of the proposed method is validated by simulations.

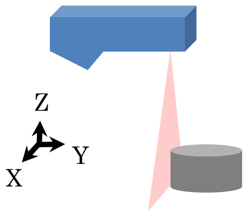

Fig.1. A laser-based triangulation camera and its coordinate system

2. Calibration target and modeling

A robot attached with a laser-based triangulation camera and newly proposed calibration target which is formed of simple parts such as a flat plate and a cubical block are shown in Fig.2. The cubical block is fixed along orthogonal lines of X axis and Y axis. Using this calibration target, a local coordinate system can be defined by an origin, X axis and Y axis drawn on the plate. The block will play a key role in a later calibration method.

In Fig.2 four coordinate systems: robot base coordinate system (RBCS), laser-based triangulation camera coordinate system (LCCS), end-effector coordinate system (EECS) and calibration target coordinate system (CTCS) are differently defined. The $^{CT}T_{LC}$ is a 4 × 4 homogeneous transformation matrix which transforms laser-based camera coordinates into calibration target coordinates. The EECS is located at the tip of the pin mounted on the robot. The tip of the pin, the origin of the end-effector, accesses and touches with the origin and any point on the X axis line and Y axis line drawn on the calibration target to create a reference frame. In this way a 4 ×4 homogeneous transformation matrix $^{CT}M_{RB}$ which transforms calibration target coordinates into robot base coordinates is internally calculated in a robot controller. Once the reference frame is created, any movements of the robot can be taught by using this frame. For measurement, the robot moves lineally from a start point until an end point along with Y axis with respect to the created CTCS.

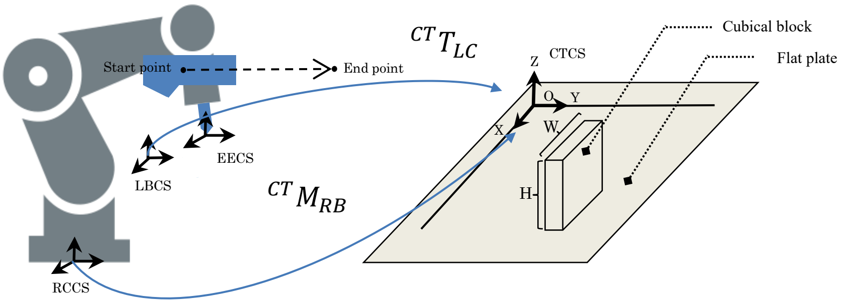

Fig.2. Component frames for hand-eye calibration

The purpose of the calibration is to transfer all the defined frames into the world coordinate system which provides a fixed frame of reference that serves as a common point of reference for various object. The RBCS in this work can be specified as the world coordinate system. The $^{CT}T_{LC}$ and $^{CT}M_{RB}$ are composed of 3×3 rotation matrix $^{CT}R_{LC}$ and $^{CT}R_{RB}$, and 3 × 1 translation vector $^{CT}P_{LC}$ and $^{CT}P_{RB}$ expressed by

$$^{CT}T_{LC} = \begin{bmatrix} ^{CT}R_{LC} & ^{CT}P_{LC} \\ 0^T & 1 \end{bmatrix} \tag{1}$$

$$^{CT}M_{RB} = \begin{bmatrix} ^{CT}R_{RB} & ^{CT}P_{RB} \\ 0^T & 1 \end{bmatrix} \tag{2}$$

The coordinates of a certain point $[x_{LC}, y_{LC}, z_{LC}]^T$ with respect to LCCS is transformed into robot base coordinates $[x_{RB}, y_{RB}, z_{RB}]^T$ by a following equation:

$$\begin{bmatrix} x_{RB} \\ y_{RB} \\ z_{RB} \\ 1 \end{bmatrix} = (^{CT}M_{RB})^{-1}\, {}^{CT}T_{LC} \begin{bmatrix} x_{LC} \\ y_{LC} \\ z_{LC} \\ 1 \end{bmatrix} \tag{3}$$

3. Calibration method

The camera is moved up to the calibration target to project a laser line onto the top surface of the block on the calibration target as shown in Fig.3. The camera can measure this surface to obtain height h and width w and gradient m, which is implemented every laser-based triangulation camera measures a profile. The actual values of the height H and width W are previously known. The angles $\alpha, \beta,$ and γ are respectively calculated by following equations:

$$\alpha = \arccos(H/h) \tag{4}$$

$$\beta = \arctan(|m|) \tag{5}$$

$$\gamma = \arccos(W/w) \tag{6}$$

Those values express rotation degrees different between the laser-based triangulation camera frame and the calibration target frame, which ideally means when

$$\alpha, \beta, \gamma = 0, \tag{7}$$

the rotation of laser triangulation camera frame is completely corresponded to that of calibration target. Practically, converging those values to 0 is quite challenging because of the manufacturing error with regards to H or W of the calibration target. Instead of the equations (4-6), $\alpha_{min}, \beta_{min}$ and γ_{min} are calculated by equations (8-10):

$$\underset{h \geq H}{\mathrm{Min}} \arccos(H/h) = \alpha_{min} \tag{8}$$

$$\mathrm{Min} \arctan(|m|) = \beta_{min} \tag{9}$$

$$\underset{w \geq W}{\mathrm{Min}} \arccos(W/w) = \gamma_{min} \tag{10}$$

The procedure of the proposed hand-eye calibration is divided into two steps. At the first step, by moving the camera, α, β and γ values are minimized to find out $\alpha_{min}, \beta_{min}$ and γ_{min}. Thus, the element ${}^{CT}R_{LC}$ of ${}^{CT}T_{LC}$ is given as

$${}^{CT}R_{LC} = I \tag{11}$$

A transformation matrix that transforms laser-based camera coordinates into target calibration coordinates is expressed by

$$\begin{bmatrix} x_{CT} \\ y_{CT} \\ z_{CT} \\ 1 \end{bmatrix} = \begin{bmatrix} I & {}^{CT}P_{LC} \\ 0^T & 1 \end{bmatrix} \begin{bmatrix} x_{LC} \\ y_{LC} \\ z_{LC} \\ 1 \end{bmatrix} \tag{12}$$

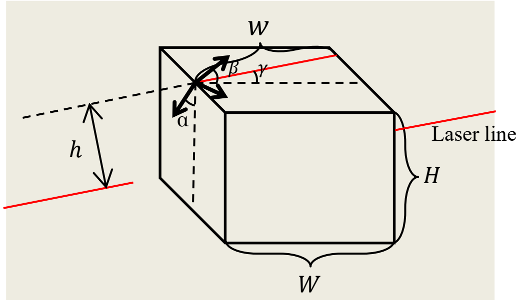

Fig.3. The cubic block in the calibration target with measured α, β and γ

At the second step, to calculate the transition vector ${}^{CT}P_{LC}$, by lineally moving the camera along with Y axis direction, the camera obtains 3D data of the top surface of the block on the calibration target. The center coordinates of the block's top surface $\hat{p}^c_{LC} = [\hat{x}^c_{LC}, \hat{y}^c_{LC}, \hat{z}^c_{LC}]^T$ with respect to LCCS is measured. The actual coordinates $p^c_{LC} = [x^c_{LC}, y^c_{LC}, z^c_{LC}]^T$ with respect to CTCS are specified as known values. Thus, it is possible to calculate ${}^{CT}P_{LC}$ expressed by a simple equation (13):

$${}^{CT}P_{LC} = p^c_{LC} - \hat{p}^c_{LC} \tag{13}$$

As a result, the elements composing the equation (3) are supposed to be all calculated.

4. Simulations

Firstly, by varying a robot posture in a simulation initial $\alpha = 2.5, \beta = 2.0$ and $\gamma = 1.4$ (deg) are optimized following by the equations (8-10). Fig.4 (a) illustrates the relationship between transitions of Rx (roll), Ry (pitch) and Rz (yaw) with respect to CTCS and the corresponding values of α, β and γ . The simulation result proves those values gradually became close to 0, and then the values are supposed to rise through minimum values $\alpha_{min}, \beta_{min}$, and γ_{min} respectively. Secondly, we varied Rx, Ry, and Rz in this order using α, β and γ values, namely $Rx = \alpha, Ry = \beta$ and $Rz = \gamma$ per measurement. All the values reached less than 0.05 (deg) in a mere 3 robot posture motion as shown in Fig.4 (b). And finally, we generated 4 different random initial rotation errors: $4 < E_1, E_2, E_3, E_4 < 6$ (deg) corresponded to α, β and γ. Fig.4 (c) shows the result of the error evaluation in 9 robot posture motion. The rotation errors achieved less than 2.3×10^{-5} (deg) on the 5th motion, and then eventually became almost 0.

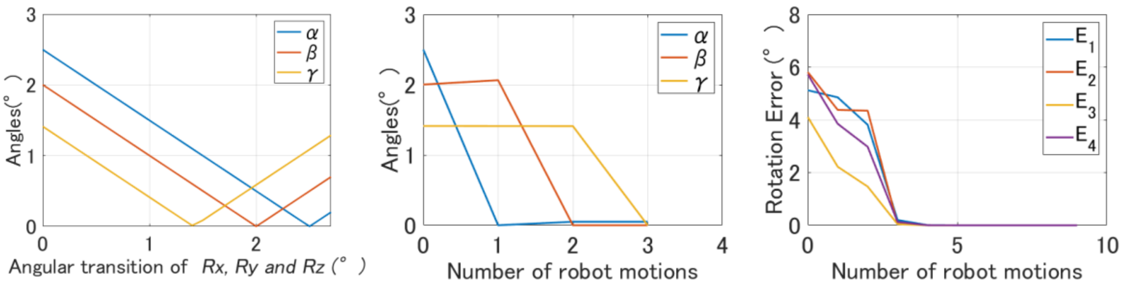

(a) (b) (c)

Fig.4. Simulation results of the proposed hand-eye calibration method. (a) Effect of the angular transitions of *Rx, Ry, Rz* on α, β, γ. (b) Convergence close to 0 in robot posture motions. (c) Effect on the number of robot motions on rotation errors.

5. Conclusion

This paper presented a novel hand-eye calibration method using a special calibration target for a laser-based triangulation camera. In addition, using computer simulation, our method was partly performed with regards to a relative frame of orientation between of LTCS and CTCS. The simulation result proved feasibility of the proposed method and explained the rotation errors to estimate calibration accuracy. It is expected that this method is a novel approach for hand-eye calibration which does not need to rotate 3D data after the calibration.

References

[1] G. Sansoni, M. Trebeschi, F. Docchio: State-of-the-art and applications of 3D imaging sensors in industry, cultural heritage, medicine, and criminal investigation, *Sensors 2009*, 9, 568-601.

[2] J. Santrolaria, D. Guillomia, C. Cajal, J.A. Albajez, J.J. Aguilar: Modelling and Calibration Technique of Laser Triangulation Sensors for Integration in Robot Arms And Articulated Arm Coordinate Measuring Machines, *Sensors 2009*, 9, 7374-7396.

[3] I. Enebuse, BKSMK, Ibrahim, M, Foo, RS, Matharu, A.Ahmed: Accuracy evaluation of hand-eye calibration tequniques forvision-guided robots, *PLoS ONE* 2022, 17(10).

Development of Supporting Tools for In-Situ Visualization Library VISMO

Nobuaki Ohno*

[1]Graduate School of Information Science, University of Hyogo

*`ohno@gsis.u-hyogo.ac.jp`

Abstract. In-situ visualization is becoming indispensable to researchers who perform large-scale computer simulations. We developed in-situ visualization tools VISMO and VISMO-YY. To perform in-situ visualization with VISMO, users have to write a configuration file written about how VISMO should visualize the data. It requires some basic knowledge of three-dimensional computer graphics, which can be burdensome for researchers. To solve this problem, two cross-platform tools have been developed. They help write a configuration file for VISMOs.

Keywords: scientific visualization, in-situ visualization, computational fluid dynamics

1. Introduction

As supercomputers have become powerful, the size of computer simulations has also become large. The sizes of some results of simulations are so large that they cannot be visualized in the traditional way. So, in-situ visualization, i.e. visualization performed with the simulation on the supercomputer using its rich memory and powerful CPUs, draws a lot of researchers' attention. There are several tools for carrying out in-situ visualization, for example, Catalyst [1] and Libsim [2]. They are interfaces for ParaView and VisIt respectively. Both of them are based on VisualizationToolkit (VTK)[3] and have various visualization methods. We developed in-situ visualization libraries called VISMO [4, 5]. Currently, two kinds of VISMOs, original VISMO and VISMO-YY, can be downloaded from [7]. The original VISMO is for simulations defined on Cartesian coordinates, and VISMO-YY is for Yin-Yang grid [6]. They can be used by calling some subroutines of VISMOs from researchers' simulation codes. They have been used for visualizing CFD simulations [8, 9]. To use the basic functions of VISMOs, no computer graphics (CG) related library, like VTK or Mesa, is needed but a little basic knowledge of three-dimensional CG is. The users are required to write a "configuration file" and provide VISMO with cameras, visualization methods, and other information in advance. This task can be burdensome for some users. To solve this problem, we have developed supporting tools for writing a configuration file of VISMOs.

2. Supporting tools

In general, executions of simulation programs are scheduled by job scheduling systems.

Subroutines of VISMOs are called from simulation codes so that visualization parameters have to be set in advance. And it is a configuration file of VISMOs in which that information is described. Figure 1 shows a result of Hall MHD turbulence simulation [8], and it is an example of visualization by VISMO. The enstrophy density and current density are visualized with green and gray isorufaces respectively. To obtain such visualization results, parameters of the camera such as viewing position and direction, the material properties of isosurfaces, and properties of lights have to be properly determined and described in a configuration file in advance. Trial and error must be needed to obtain good parameters. It can be very burdensome for researchers.

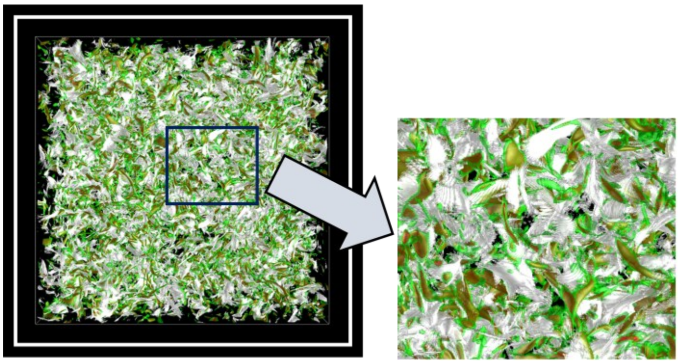

Figure 1: Isosurface visualization of Hall MHD turbulence simulation. The enstrophy density and current density are visualized with green and gray isosurfaces. This is a visualization result of the same simulation as in [8] but the data is from a different timestep. Image courtesy of Dr. Miura of National Institute for Fusion Science.

To solve this problem, we have developed two tools, Camera tool and Color Editor. They help users to write configuration files of VISMOs. To make tools multiplatform, we have written them in Python with Tkinter. Tkinter is a Python interface to Tcl/Tk and makes it possible to create GUI programs.

2.1. Camera Tool

VISMO needs information about "cameras" in its configuration file. This camera information is mandatory. It is necessary to describe not only its position and viewing direction but also the upward direction and field of view angle for the perspective projection. To determine the information intuitively, we have developed "Camera tool." Figure 2 shows the main screen and six panels of this tool.

This tool enables users to determine the camera position, viewing direction, and so on, looking at a semi-transparent box that shows the data boundary on the main screen (see Fig. 2(a)). For Yin-Yang grid, the boundary is spherical but the format of camera information is the same, so this tool can be also used. The users can move the position of the camera by their keyboard while checking what angle the boundary box is viewed. The camera parameters for VISMO are output as text in a panel (see Fig. 2(g)). The users can copy and paste it into their configuration files.

The camera tool can be used to set not only camera information but also isosurface, slice, and light information. The properties of lights, the material properties of isosurface, and the equation of slice can be determined while viewing a sphere that mimics the isosurface or slice plane

displayed on the main screen. The results are output as text in the same panel.
The sphere, box, and slice are drawn by the ray-casting method, and Namba is used to accelerate it.

(b) ☑ Isosurface ☑ Slice ☑ Frame
Min Corner -0.5 -0.5 -0.5
Max Corner 0.5 0.5 0.5

(c) NSCAL 1
LEVEL 0.0
ALPHA 1.0
Ambient: red 0.33, green 0.45, blue 0.65
Diffusion: red 0.20, green 0.50, blue 0.65
Specular: red 0.20, green 0.20, blue 0.20
Shininess: shininess 1

(d) NSCAL 1
ALPHA 1.0
ax+by+cz+d=0 a 0.5 b 0.0 c 1.0 d 0.0
Ambient 0.40
Difusion 0.50
Specular 0.20
Shininess 1

(e) Near 0.1
Far 10.0
Projection ● Pers ○ Ortho
Fovy(degree) 45.0
width 0.0
● X-Y-Z
Pos(x,y,z) 2.0 1.0 2.0
Front(x,y,z) -0.66776671 -0.32890002 -0.66776671
Up(x,y,z) -0.59528567 -0.30263348 0.744343962
○ R-Theta-Phi
Center 0.0 0.0 0.0
R-T(deg)-P(deg) 3.0 48.1896851C 26.56505117

(f) Light1 ☑ used Pos(x,y,z) 0.2 -1.0 1.0 Ambient 0.60 Difusion 0.60 Specular 0.00
Light2 ☐ used Pos(x,y,z) 0.0 0.0 0.0 Ambient 0.00 Difusion 0.00 Specular 0.00
Light3 ☐ used Pos(x,y,z) 0.0 0.0 0.0 Ambient 0.00 Difusion 0.00 Specular 0.00

(g)
```
CAMERA
POSITION 2.000 1.000 2.000
FRONT -0.668 -0.329 -0.668
UP -0.595 -0.303 0.744
FOVY 45.000
NEARFAR 0.1 10.000
END_CAMERA
```

Figure 2: The main screen and 6 panels of Camera editor: (a) main screen, (b) general setting panel, (c) isosurface panel, (d) slice panel, (e) camera panel, (f) light panel (g) result panel.

2.2. Color Editor

To visualize data by the visualization methods like slice, volume rendering, colored stream tubes, and colored particle visualization, VISMO requires transfer functions, and they have to be described in its configuration file. Transfer functions are relationships between data values and colors. They play an important role in visualization. For example, volume rendering needs a transfer function between scalar values and colors including opacities, and whether data is well visualized depends on it. To make this task easier, we have developed Color Editor with Tkinter and Matplotlib. Matplotlib is a visualization library that provides various visualization methods. Figure 3 shows the main screen and panel of this editor.
To define a transfer function with this tool, all the users have to do is select a scalar, vector, or particle data number, enter the minimum and maximum values, and select a color map from the several well-used color map provided by Matplotlib on the panel (Fig.3(b)). For scalar data, the users can also edit the opacity graph for volume rendering by moving control points with their mouse on the main screen (Fig.3(a)). The control points of the opacity graph can be increased by double clicks. For particle data, the graph of particle radii can be edited in the same way as the opacity graph of scalar data. The result can be output as a text file.

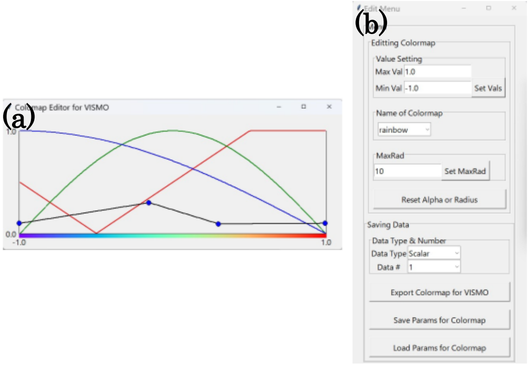

Max Val 1.0
Min Val -1.0
Name of Colormap: rainbow
MaxRad 10
Data Type Scalar
Data # 1

Figure 3: The main screen (a) and a panel (b) of Color editor. The blue points on the main screen are the control points. Users can increase and move them to edit the opacity graph.

Summary

We have developed supporting tools for VISMOs. The camera tool helps determine not information about the camera but also the parameters of light, isosurface, and slice. The color editor is for defining transfer functions for mainly scalar data visualization. These tools enable the users to determine the parameters of the camera and define a transfer function intuitively, which solves a big problem of using VISMOs, namely the difficulty in writing its configuration file. These tools can be downloaded from the same website as VISMO [7].

Acknowledgment

The author thanks Dr. Miura of National Institute for Fusion Science for kindly providing Figure 1. This work is supported by "Joint Usage/Research Center for Interdisciplinary Large - scale Information Infrastructures (JHPCN)" in Japan (Project ID:jh200003-NAH, jh220005).

References

[1] U. Ayachit, A. Bauer, B. Geveci, P. O'Leary, K. Moreland, N. Fabian, J. Mauldin: ParaView catalyst: enabling in situ data analysis and visualization, *Proceedings of the first workshop on in situ 485 infrastructures for enabling extreme-scale analysis and visualization—ISAV,* (2015), 25–29,

[2] B. Whitlock, M. J. Favre, S. J. Meredith: Parallel in situ coupling of simulation with a fully featured visualization system, *Eurographics Symposium on Parallel Graphics and Visualization*, (2011), 101–109,

[3] https://vtk.org/

[4] N. Ohno, H. Ohtani: Development of In-Situ Visualization Tool for PIC Simulation, *Plasma and Fusion Research*, volume:9 (2014), 3401071.

[5] N. Ohno, A. Kageyama: In-situ visualization library for Yin-Yang grid simulations, *Earth Planets Space*, volume:73 (2021), 158.

[6] A. Kageyama, T. Sato: “Yin-Yang grid”: an overset grid in spherical geometry. *Geochem Geophys Geosyst*, volume:5 (2004), Q09005

[7] https://vizlab.sakura.ne.jp/en/vismo.en.html

[8] H. Miura: Extended Magnetohydrodynamic Simulations of Decaying, Homogeneous, Approximately-Isotropic and Incompressible Turbulence, *Fluids*, volume:4 (2019), 3401030.

[9] A. Kageyama, N. Ohno: Chiral pattern in nonrotating spherical convection, *Physical Review Fluids*, volume: 7 (2022), 013502.

Reproduction of Braginskii solutions in anisotropic-ion-pressure fluid scheme using a viscous-flux approximation (VFA) modeling

Satoshi Togo[1,*], Tomonori Takizuka[2], Yuki Homma[3], Kenzo Ibano[2], Keishi Homma[1], Naomichi Ezumi[1], Mizuki Sakamoto[1]

[1]Plasma Research Center, University of Tsukuba
[2]Graduate School of Engineering, Osaka University
[3]National Institutes for Quantum Science and Technology

*`togo@prc.tsukuba.ac.jp`

Abstract. A viscous-flux approximation (VFA) modeling applicable to anisotropic-ion-pressure (AIP) fluid scheme has been developed [S. Togo *et al.*, Plasma Fusion Res. **18** (2023) 1203005.]. The AIP scheme is more suited to a self-consistent treatment of the sheath boundary condition concerning the ion parallel flow (i.e. the Bohm criterion) than the conventional Braginskii plasma fluid model. It has been demonstrated that the VFA model incorporated within AIP code reproduces the Braginskii solutions and thus makes it possible to perform a direct comparison in a single code.

Keywords: plasma fluid simulation, anisotropic ion pressure, parallel ion viscous flux, open magnetic field

1. Introduction

Controlling the divertor heat load is one of the most crucial issues in future fusion reactors. The divertor heat load as well as plasma profiles along the scrape-off layer (SOL)-divertor region is computed by kinds of integrated simulation codes such as SONIC [1, 2], SOLPS [3] and UEDGE [4]. These codes adopt the Braginskii plasma fluid model [5] for plasma modeling in which effects of the ion pressure anisotropy are approximated by a parallel-viscous flux term.

The anisotropic-ion-pressure (AIP) fluid scheme deals directly with AIP without the parallel-viscous flux approximation and thus describes the characteristics of plasmas in open-field systems more accurately [6]. Direct comparisons between the Braginskii model and AIP scheme have been recently performed in order to investigate the impact of introduction of AIP within the plasma fluid scheme on its solutions [7, 8, 9, 10]. However, due to differences in element models in both codes, it is not always easy to perform a fair comparison between them focusing only on the approximation validity of the parallel-viscous flux. For example, AIP fluid scheme is more suited to a kind of self-consistent treatment of the sheath boundary condition concerning the ion parallel flow (i.e. the Bohm criterion) because its parallel momentum equation becomes hyperbolic [11] while the Braginskii model requires an explicit imposition of the Bohm criterion. Therefore, it is practical to create a scheme to perform such a comparison by using a single code.

We have developed a viscous-flux approximation (VFA) modeling applicable to AIP fluid scheme [12]. It has been incorporated within our AIP code [8, 9, 10, 13] which self-consistently treats the sheath boundary conditions by using a virtual-divertor (VD) model [11]. In this study, we perform comparisons between AIP solutions and the Braginskii ones which are reproduced by the VFA modeling in various simulation conditions in simple mirror configurations.

2. Viscous-flux approximation (VFA) modeling

By incorporating the viscous-flux approximation (VFA) modeling [12] within our AIP code, the ion energy transport equations (Eqs. (3) and (4) in Ref. [13]) are modified as follows;

$$\begin{aligned}\frac{\partial}{\partial t}\left(\frac{1}{2}m_{\mathrm{i}}nV^2+\frac{1}{2}p_{\mathrm{i}\|}\right) &+ B\frac{\partial}{\partial s}\left[\frac{1}{B}\left(\frac{1}{2}m_{\mathrm{i}}nV^3+\frac{3}{2}p_{\mathrm{i}\|}V+q_{\mathrm{i}\|}\right)\right]+\frac{p_{\mathrm{i}\perp}V+q_{\mathrm{i}\perp}}{B}\frac{\partial B}{\partial s}\\ &= Q_{\mathrm{i}\|}+\frac{p_{\mathrm{i}\perp}-p_{\mathrm{i}\|}}{\tau_{\mathrm{rlx}}}+\frac{m_{\mathrm{e}}}{m_{\mathrm{i}}}\frac{p_{\mathrm{e}}-p_{\mathrm{i}\|}}{\tau_{\mathrm{e}}}-V\frac{\partial p_{\mathrm{e}}}{\partial s}-\alpha_{\mathrm{VFA}}\frac{\delta p_{\mathrm{i}}-\pi_{\mathrm{i}}}{L/c_{\mathrm{s}}},\end{aligned}\tag{1}$$

$$\begin{aligned}\frac{\partial p_{\mathrm{i}\perp}}{\partial t} &+ B\frac{\partial}{\partial s}\left(\frac{p_{\mathrm{i}\perp}V+q_{\mathrm{i}\perp}}{B}\right)-\frac{p_{\mathrm{i}\perp}V+q_{\mathrm{i}\perp}}{B}\frac{\partial B}{\partial s}\\ &= Q_{\mathrm{i}\perp}+\frac{p_{\mathrm{i}\|}-p_{\mathrm{i}\perp}}{\tau_{\mathrm{rlx}}}+\frac{2m_{\mathrm{e}}}{m_{\mathrm{i}}}\frac{p_{\mathrm{e}}-p_{\mathrm{i}\perp}}{\tau_{\mathrm{e}}}+\alpha_{\mathrm{VFA}}\frac{\delta p_{\mathrm{i}}-\pi_{\mathrm{i}}}{L/c_{\mathrm{s}}}.\end{aligned}\tag{2}$$

Here, the final terms in the right-hand-sides of Eqs. (1) and (2) are added. Notations $\delta p_{\mathrm{i}}(\equiv 2(p_{\mathrm{i}\|}-p_{\mathrm{i}\perp})/3)$ and $\pi_{\mathrm{i}}(\equiv -\eta B^{-1/2}\partial(B^{1/2}V)/\partial s)$ are the anisotropic component of the ion pressure and the parallel ion viscous flux, respectively. The parallel ion viscosity η is modified from its classical form $\eta_0 = 0.96p_{\mathrm{i}}\tau_{\mathrm{i}}$ [5] to $\eta = \eta_0/\left[1+\beta^{-1}\tau_{\mathrm{i}}\left|B^{-1/2}\partial(B^{1/2}V)/\partial s\right|\right]$, where the viscous-flux limiter β is set less than unity to keep $|\pi_{\mathrm{i}}|/p_{\mathrm{i}} < \beta < 1$. The parallel system length is denoted by L and α_{VFA} is an artifical enhancement factor of the VFA modeling. Note here that $\delta p_{\mathrm{i}} \approx \pi_{\mathrm{i}}$ is the VFA adopted in the Braginskii model. Note also that the total ion energy transport equation obtained by the summation of Eqs. (1) and (2) keeps its original form (i.e. Eq. (7) in Ref. [10]) even with this modification. Therefore, by setting $\alpha_{\mathrm{VFA}} \gg 1$, it is possible to force δp_{i} to asymptotically approach π_{i}, realizing solutions with the VFA.

3. Results

The VFA modeling has been demonstrated in a simple mirror configuration [12]. The configuration is the same one used in our previous study [8] in which solutions from our AIP code and the B2 code (the Braginskii model) are compared in a range of collisionality. The VFA modeling in our AIP code successfully reproduces B2 solutions for both rare-collisional and high-collisional cases, satisfying $\delta p_{\mathrm{i}} \approx \pi_{\mathrm{i}}$ with $\beta = 0.5$. Here, $\alpha_{\mathrm{VFA}} = 10^5$ is set. It is also recognized that the modification model of η in B2 ($\eta = \eta_0 / \left[1 + \beta^{-1} \tau_{\mathrm{i}} \left|\partial V / \partial s\right|\right]$) is not adequate to satisfy $|\pi_{\mathrm{i}}| / p_{\mathrm{i}} < \beta$. In the presentation, we will show results of comparisons in other simulation conditions concerning the mirror ratio, β and the ion heat flux limiting coefficients [10].

Acknowledgement

This work is performed on “Plasma Simulator” (NEC SX-Aurora TSUBASA) of NIFS with the support and under the auspices of the NIFS Collaboration Research program (NIFS23KIST050).

References

[1] H. Kawashima et al: Development of Integrated SOL/Divertor Code and Simulation Study in JAEA, *Plasma and Fusion Research*, volume:1 (2006), 031-1–13.

[2] K. Shimizu et al: Kinetic modelling of impurity transport in detached plasma for integrated divertor simulation with SONIC (SOLDOR/NEUT2D/IMPMC/EDDY), *Nuclear Fusion*, volume:49 (2009), 065028-1–9.

[3] R. Schneider et al: Plasma Edge Physics with B2-Eirene, *Contributions to Plasma Physics*, volume:46 (2006), 3–191.

[4] T.D. Rognlien et al: A fully implicit, time dependent 2-D fluid code for modeling tokamak edge plasmas, *Journal of Nuclear Materials*, volume:196-198 (1992), 347–351.

[5] S.I. Braginskii: Transport process in a plasma, *Review of Plasma Physics*, volume:1 (1965), 205.

[6] W. Fundamenski: Parallel heat flux limits in the tokamak scrape-off layer, *Plasma Physics and Controlled Fusion*, volume:47 (2005), R163–R208.

[7] M. Zhao et al: Impact of ion temperature anisotropy on 2D edge-plasma transport, *Nuclear Materials and Energy*, volume:26 (2021), 100881-1–6.

[8] S. Togo et al: Benchmarking of B2 Code with a One-Dimensional Plasma Fluid Model Incorporating Anisotropic Ion Pressures on Simple Mirror Configurations, *Plasma and Fusion Research*, volume:13 (2018), 3403022-1–4.

[9] S. Togo et al: Characteristics of plasma flow profiles in a super-X-divertor-like configuration, *Nuclear Materials and Energy*, volume:19 (2019), 149–154.

[10] S. Togo et al: Self-consistent simulation of supersonic plasma flows in advanced divertors, *Nuclear Fusion*, volume:59 (2019), 076041-1–11.

[11] S. Togo et al: Self-consistent treatment of the sheath boundary conditions by introducing anisotropic ion temperatures and virtual divertor model, *Journal of Computational Physics*, volume:310 (2016), 109–126.

[12] S. Togo et al: Viscous-Flux Approximation Modeling in Anisotropic-Ion-Pressure Fluid Scheme, *Plasma and Fusion Research*, volume:18 (2023), 1203005-1–2.

[13] S. Togo et al: Fluid simulation of plasmas with anisotropic ion pressure in an inhomogeneous magnetic field of a tandem mirror device GAMMA 10/PDX, *Journal of Advanced Simulation in Science and Engineering*, volume:9 (2022), 185–197.

Basic Study on Parallel Finite Element Method for Non-Liner Sound Field Analysis

Kentaro Koga[1], Amane Takei[2]

[1]Faculty of Engineering Graduate School of Engineering, University of Miyazaki, Japan
[2]Faculty of Engineering, University of Miyazaki, Japan

*hl19026@student.miyazaki-u.ac.jp

Abstract. We are investigating a large-scale non-liner and non-steady wave sound analysis method based on the parallel finite element method by developing ADVENTURE_Sound as an opensource software. The iterative domain decomposition method is employed in the analysis code as a parallel technique. As a basic study, firstly, we have confirmed that the non-steady wave sound analysis code: ADVENTURE_Sound is very high-accuracy with errors within the allowable range in a numerical analysis.

Keywords: Parallel Finite Element Method, Sound Field Analysis, Domain Decomposition Method, Non-Liner and Non-Steady Analysis

1. Introduction

There is growing demand for advanced sound design, such as noise reduction and high-quality indoor and outdoor acoustic environment. It is thus necessary to understand the sound pressure distribution with high accuracy. There is also a need to reduce the costs of designing acoustic spaces [1] and electrical equipment for noise-suppression equipment. Acoustic analysis techniques have been used for the acoustic design of concert halls and noise suppression equipment due to improvements in computer hardware and software performance.

2. Governing equations and algorithm for parallel computing

In ADVENTURE_Sound, the wave equation is employed as a governing equation that is expressed by the following weak form equation:

$$[A]\{\Phi\} - k^2[M]\{\Phi\} + j\rho\omega[C]\{\Phi\} = \{q\}, \tag{1}$$

where Φ is the velocity potential, q is the distribution function. k and ω are the wave number and angular frequency, ρ is the medium density, and Z_n is the specific acoustic impedance.

To derive a weak form, the Galerkin method is applied to the Helmholtz equation [1]. When the inverse Fourier transform is applied to convert Eq. (4) obtained by the finite element approximation to the time domain expression, the following expression is obtained.

$$[A]\{\Phi\}_t + \frac{1}{c^2}[M]\{\ddot{\Phi}\}_t + \rho[C]\{\dot{\Phi}\}_t = \{q\}. \tag{2}$$

Here, $\dot{}$, $\ddot{}$ are the first and second time derivatives, respectively. c is the speed of sound. To obtain the velocity potential {Φ} in the time domain problem, we apply the linear acceleration method in the time direction of Eq.(8). When velocity potential $\{\Phi\}_t$, $\{\dot{\Phi}\}_t$, $\{\ddot{\Phi}\}_t$ at time t are known, $\{\Phi\}_{t+\Delta t}$, $\{\dot{\Phi}\}_{t+\Delta t}$ are given by the Newmark β method, when $\beta = \frac{1}{6}$, $\gamma = \frac{1}{2}$, velocity potential $\{\Phi\}_t$ is approximated by following equations:

$$\{\Phi\}_{t+\Delta t} = \{\Phi\}_t + \{\dot{\Phi}\}_t \Delta t + \frac{1}{3}\{\ddot{\Phi}\}_t \Delta t^2 + \frac{1}{6}\{\ddot{\Phi}\}_{t+\Delta t} \Delta t^2, \tag{3}$$

$$\{\dot{\Phi}\}_{t+\Delta t} = \{\dot{\Phi}\}_t + \frac{1}{2}\left(\{\ddot{\Phi}\}_{t+\Delta t} + \{\ddot{\Phi}\}_t\right)\Delta t. \tag{4}$$

Next, substituting equations (9) and (10) into equation (8) and obtaining $\{\ddot{\Phi}\}_{t+\Delta t}$, we obtain the following simultaneous linear equations.

$$\{\ddot{\Phi}\}_{t+\Delta t} = (\{q\}_{t+\Delta t} - [A]\{Q\} - \rho[C]\{P\})[L]^{-1} \tag{5}$$

Also, {Q}, {P}, and [L] in equation (11) are as follows:

$$\{Q\} = \left(\{\Phi\}_t + \{\dot{\Phi}\}_t \Delta t + \frac{1}{3}\{\ddot{\Phi}\}_t \Delta t^2\right), \tag{6}$$

$$\{P\} = \left(\{\dot{\Phi}\}_t + \frac{1}{2}\{\ddot{\Phi}\}_t \Delta t\right), \tag{7}$$

$$[L] = \left(\frac{1}{6}[A]\Delta t^2 + \frac{1}{c^2}[M] + \frac{1}{2}\rho[C]\Delta t\right). \tag{8}$$

Here, the solutions of at time t+Δt can be obtained by substituting the solution obtained in Eq.(4) into Eq.(2) and Eq.(3).

The equation contains complex numbers and becomes a complex symmetric matrix. In the present study, the speed potential Φ is obtained using the conjugate orthogonal conjugate gradient (COCG) method. The finite element approximation (1) is rewritten as $Ku = f$ by the coefficient matrix K, the unknown vector u, and the right-hand side vector f. Next, Ω is divided into N subdomains (Eq. (9)). Eq. (10) and (11) are obtained from Eq. (9) [2].

$$\begin{bmatrix} K_{II}^{(1)} & 0 & 0 & K_{IB}^{(1)} R_B^{(1)\mathrm{T}} \\ 0 & \ddots & 0 & \vdots \\ 0 & 0 & K_{II}^{(N)} & K_{IB}^{(N)} R_B^{(N)\mathrm{T}} \\ R_B^{(1)} K_{IB}^{(1)\mathrm{T}} & \cdots & R_B^{(N)} K_{IB}^{(N)\mathrm{T}} & \sum_{i=1}^{\mathrm{N}} R_B^{(i)} K_{BB}^{(i)} R_B^{(i)\mathrm{T}} \end{bmatrix} \begin{bmatrix} u_I^{(1)} \\ \vdots \\ u_I^{(N)} \\ u_B \end{bmatrix} = \begin{bmatrix} f_I^{(1)} \\ \vdots \\ f_I^{(N)} \\ f_B \end{bmatrix} \tag{9}$$

$$K_{II}^{(i)} u_I^{(i)} = f_I^{(i)} - K_{IB}^{(i)} u_B^{(i)} \quad (i = 1, \dots, N) \tag{10}$$

$$\left\{ \sum_{i=1}^{\mathrm{N}} R_B^{(i)} \left\{ K_{BB}^{(i)} - K_{IB}^{(i)\mathrm{T}} \left(K_{II}^{(i)} \right)^{-1} K_{IB}^{(i)} \right\} R_B^{(i)T} \right\} u_B = \sum_{i=1}^{\mathrm{N}} R_B^{(i)} \left\{ f_B^{(i)} - K_{IB}^{(i)T} \left(K_{II}^{(i)} \right)^{-1} f_I^{(i)} \right\} \tag{11}$$

where ${f_B}^{(i)}$ is the right-hand vector for u_B, and $\left(K_{II}^{(i)} \right)^{-1}$ is the inverse matrix of $K_{II}^{(i)}$. Equation (11) is referred to as an interface problem and is an equation for satisfying the continuity between domains in the domain decomposition method. For simplicity, rewrite equation (12) as follows:

$$Su_B = g, \qquad S = \sum_{i=1}^{N} R_B^{(i)} S^{(i)} R_B^{(i)T}, \;\; S^{(i)} = K_{BB}^{(i)} - K_{IB}^{(i)T} \left(K_{II}^{(i)} \right)^{-1} K_{IB}^{(i)}. \tag{12}$$

3. Numerical Analysis

For examining ADVENTURE_Sound on a real-world problem, we model the environ-ment of acoustic experiments. The computations are performed on a 16-node (62-core) PC cluster (Intel(R) Xeon(R) CPU E5-2650L; 1.80 GHz; L2 20480 KB) with 32 GB RAM per node. The simulation statistics and the numerical are shown in Table 1 and 2, respectively. More detail thins will be shown at the conference.

Table 1 Simulation Statistic

Frequency	442[Hz]
No. of Elements	911,133
No. of DOF	1,249,959
Platform	10-node workstation cluster with Intel(R) Xeon(R) CPU E5-2650L, 1.8 GHz
No. of cores per node	16
No. of nodes	8
Main memory per node	32 [GB/node]

Table 2 Numerical result

Elapsed time	509.153 [s]
Memory requirements	0.26 [GB/node]

Acknowledgements

The present study was supported in part by a JSPS Grant-in-Aid for Scientific Research (Basic Research (B), 17H03256). The computer environment used in the present study was supported in part through a JST Adaptable and Seamless Technology transfer Program (A-STEP (Search Type), AS262Z02631H).

References

[1] A. Takei and A. Kudo: Over 100 Million Degrees of Freedom Scale Wave Sound Analysis Based on Parallel Finite Element Method, JSST, Vol.12, No.2, pp.76-84, 2020. (in Japanese)

[2] A. Takei, S. Sugimoto, M. Ogino, S. Yoshimura, H. Kanayama: Full Wave Analyses of Electromagnetic Fields with an Iterative Domain Decomposition Method, IEEE Transactions on Magnetics, Vol.46, No.8, pp.2860-2863, 2010.

Study on Parallel Finite Element Method for Electromagnetic Analysis of large space inside

Nanako Mizoguchi[1], Amane Takei[2]

[1]Faculty of Engineering Graduate School of Engineering, University of Miyazaki, Japan
[2]Faculty of Engineering, University of Miyazaki, Japan

*hl19045@student.miyazaki-u.ac.jp

Abstract. In high-frequency electromagnetic field analysis, it is necessary to divide the space into elements with a maximum side length of 1/10 to 1/20 of the wavelength so that the waveform can be expressed with a low error when dividing the space. Therefore, in many cases, it becomes a large-scale problem. In order to solve this difficulty, our research group is researching and developing a side element finite element full-wave electromagnetic field analysis method based on a domain decomposition type parallelization algorithm. In this research, we take TEAM Workshop Problem29, which is one of the benchmark to verify the accuracy of the analysis code and confirm the convergence judgment value, etc., in order to improve the speed and stability of the high-frequency electromagnetic field analysis. Then, we set up a research and development policy for improving the method.

Keywords: Parallel Finite Element Method, Full-Wave Electromagnetic Analysis, Domain Decomposition Method, TEAM Workshop Problem29

1. Introduction

High-frequency electromagnetic fields in the MHz to GHz band have become an object of analysis due to recent improvements in the performance of computers and computers, as well as advances in numerical calculation technology. In this study, for the execution of a high-frequency electromagnetic field analysis in large-space inside, we focus on the appropriate convergence judgment value of the iterative method applied to the interface problem [1] of the domain decomposition method, which is known as the parallelization method of the finite element method. By conducting a survey, we examine the conditions necessary for human body calculation.

2. Equations to be solved and parallelization method

Consider an analysis region Ω and let its boundary be $\partial\Omega$. The basic equation is the vector wave equation with the electric field **E** [V/m] derived from Maxwell's equation including the displacement current as an unknown [1]. Let us consider deriving a weak form of this equation using the Galerkin method. The electric field **E** is approximated by a Nedelec tetrahedral linear element, which is an edge element, and the current density **J** is approximated by a tetrahedral linear element. Where $\mathbf{E}_\mathbf{h}$ and $\mathbf{J}_\mathbf{h}$ are the finite element approximations of the electric field **E** and the current density **J**, respectively. $\mathbf{E}_\mathbf{h}^*$ represents an arbitrary test function [2].

$$\iiint_{\Omega} (1/\mu)\mathrm{rot}\mathbf{E}_\mathrm{h} \cdot rot\,\mathbf{E}_\mathrm{h}{}^{*} dv - \omega^2 \iiint_{\Omega} \varepsilon \mathbf{E}_\mathrm{h} \cdot \mathbf{E}_\mathrm{h}{}^{*} dv = j\omega \iiint_{\Omega} \mathbf{J}_h \cdot \mathbf{E}_h{}^{*} dv \quad (1)$$

Let equation (1) be the equation to be solved.

As a parallel computing method for large-scale analysis, this research applies the domain decomposition method [3]. The domain partitioning method divides the analysis domain into several subdomains and divides them into finite calculations on the internal degrees of freedom of the subdomains and iterative calculations of the interface problem that balances the degrees of freedom on the internal boundaries. and an iterative method to achieve contraction of degrees of freedom.

In this research, we apply the iterative domain decomposition method as a parallelization method based on the domain decomposition method. This method solves the interface problem by an iterative method such as the Conjugate Orthogonal Conjugate Gradient (=COCG) method, and the internal problem by a direct method. Furthermore, by introducing a hierarchical domain decomposition method, parallel computation with multiple computers was made possible.

3. Accuracy verification by TEAM Workshop Problem29

TEAM Workshop Problem29, a benchmark problem, is analyzed. TEAM29 is a reentrant cavity resonator, and frequency response analysis was performed to verify accuracy. Investigate the response in steps of 2[MHz] between 60[MHz] and 200[MHz] for three convergence criteria $\varepsilon = 1.0 \times 10^{-3}$, 1.0×10^{-5}, 1.0×10^{-7} was investigated, and the resonance frequency was detected from the analysis results and compared with the measured values. Figure 1 shows the frequency response of the magnetic field.

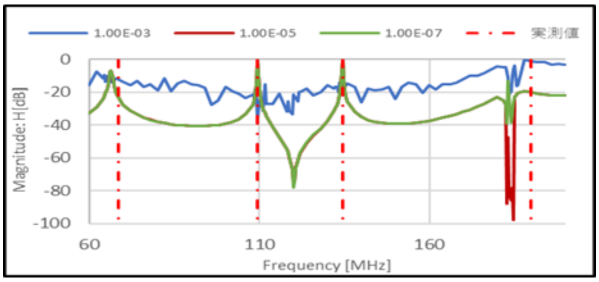

Figure 1: Comparison of frequency response analysis and actual measurements

At $\varepsilon = 1.0 \times 10^{-3}$ and 1.0×10^{-5}, there were cases where the analysis ended due to pseudo-convergence. On the other hand, with $\varepsilon = 1.0 \times 10^{-7}$, the analysis is completed up to the 4th mode, and each error rate satisfies less than 5[%], which is suitable for numerical analysis. We adopt $\varepsilon = 1.0 \times 10^{-7}$.

4. Numerical Analysis

Numerical analyses are performed using the model of large space inside. The numerical model becomes large-scale of over 100 million elements in the frequency of 2.45[GHz]. Numerical results and several considerations will be shown and discussed at JSST2023 Conference.

References

[1] A.Takei, M.Ogino, S.Sugimoto, “High-frequency electromagnetic field analysis by COCR method using anatomical human body models,” IEEE Transaction on Magnetics, Vol 54, No 3, DOI:10.1109/TMAG.2017.2756098, 2018.

[2] A. Takei, S. Sugimoto, M. Ogino, S. Yoshimura and H. Kanayama, “Full Wave Analyses of Electromagnetic Fields with an Iterative Domain Decomposition Method,” IEEE Transactions on Magnetics, Vol. 46, No. 8, pp.2860-2863, 2010.

[3] A.Takei, K.Murotani, S.Sugimoto, M.Ogino, T.Yamada, S.Yoshimura, “Performance evaluation of parallel finite element electromagnetic field analysis using numerical human models,” Journal of Advanced Simulation in Science and Engineering, Vol 1, No 1, pp.127-140,2014

Proposal of fast and robust technique to generate larege scale tetrahedral mesh

Hiroshi Kawai[1*]

[1]Faculty of Information Systems and Arts, Toyo University

*kawai063@toyo.jp

Abstract. Using modern HPC and supercomputing technology, huge scale finite element analysis using a very fine mesh can be realized. 3-D large-scale electro-magnetic analysis with more realistic complicated geometry and more detailed material modeling may be handled. However, its model preparation phase is now a clear bottleneck. A robust and fast mesh generation technique is desired. To overcome the situation, a simple tetrahedral mesh generator is developed. It is based on a voxel-based, with boundary fitting techniques. To generate a very fine mesh for a large scale analysis on HPC and supercomputing environment, it is also designed to be fully parallelizable.

Keywords: Numerical Simulation, Finite Element Method, Pre- and Post-processing, Mesh Generation, Tetrahedral Element

1. Introduction

ADVENTURE AutoMESH is a simple and handy library / toolkit fo mesh generation and pre-processing in general. Using this library, a researcher or a developer using numerical simulation methods can develop his or her own mesh generator or pre-processing tools, to generate and modify simulation model data. Currently, the library / toolkit is used among many researchers and simulation users, mainly in universities and national research centers. Its functionalities and supported platforms are explained. AutoMESH applications of various kinds of simulation meth-ods are demonstrated also.

Currently, through on-going mini-project, a more robust and efficient version of the automatic tetrahedral mesh generator is being implemented and tested for ADVENTURE AutoMESH. It is based on a voxel-based, with boundary fitting techniques. To generate a very fine mesh for a large scale analysis on HPC and supercomputing environment, it is also designed to be fully parallelizable. The prototype implementation of the mesh generator is demonstrated, and its performance evaluation is shown.

References

[1] ADVENTURE project HP: http://adventure.sys.t.u-tokyo.ac.jp/

[2] Hiroshi Kawai: ADVENTURE AutoGL: A Handy Graphics and GUI Library for Researchers and Developers of Numerical Simulations, CMES, Vol. 11, No. 3, pp.111-120, 2006.

[3] Hiroshi Kawai: How to make your own mesh generator using ADVENTURE AutoMESH ?, JSST, (online) 2022.

Nodal Discontinuous Galerkin schemes with Taylor-type Time Discretization for conservation law systems

ZHANG MENG[1*], Yamamoto Kyosuke [2],

[1] Graduate School of Systems and Information Engineering, University of Tsukuba
[2] Assistant Professor, Institution of Systems and Information Engineering, University of Tsukuba
[*]yamamoto_k@kz.tsukuba.ac.jp, phone: +81-29-853-5146

Abstract. This study presents a novel approach that combines a Taylor-type time discretization scheme with the Nodal DG (Discontinuous Galerkin) method for numerically solving a system of conservation laws, including mass, momentum, and thermodynamic energy. The proposed method offers advantages over the conventional Taylor-Galerkin methods, particularly in terms of its simpler integration process. Unlike the prevalent Runge-Kutta DG method, which requires significant computational costs due to the frequent application of limiters to control nonphysical oscillations, the proposed algorithm reduces the need for limiters, thereby mitigating computational burdens. This study provides a comprehensive examination on the theoretical foundation of the new algorithm and compare its computational efficiency with that of the Taylor-Galerkin method. Furthermore, the computational results are validated through two distinct continuous test cases.

Keywords: Discontinuous Galerkin method, Taylor expansion, high order accuracy

1. Introduction

This paper presents a study on the application of the Taylor time discretization to the Nodal Discontinuous Galerkin methods (Nodal-DG) for solving conservation laws. The DG method is a well-known finite element method that was initially proposed by Reed and Hill [1]. The hyperbolic system and its discretization have been discussed in previous studies [2][3]. The Runge-Kutta DG method has been utilized for solving one-dimensional problems in [4]. The Taylor-type time discretization scheme is derived from the Lax-Wendroff-type time discretization [5]. Unlike the prevalent Runge-Kutta time discretization, the Lax-Wendroff method directly constructs higher-order approximations using Taylor expansions of unknowns. The Taylor-Galerkin finite element approach has been presented in [5][6] for the hyperbolic equation by utilizing the third-order Taylor series expansion. In this research, a novel method that employs the Taylor time discretization and simplifies the complex weak integration process of the conventional Taylor-Galerkin method is proposed.

2. Methodology

In this novel method, the Nodal-DG method is directly applied to obtain the first-order time derivatives. Furthermore, the higher-order time derivatives are estimated using the matrix A and its time derivatives. Using Taylor expansion, the unknown variable can be expressed as follows:

$$u^{n+1} = u^n + \Delta t \frac{\partial u^n}{\partial t} + \frac{\Delta t^2}{2} \frac{\partial^2 u^n}{\partial t^2} + \frac{\Delta t^3}{6} \frac{\partial^3 u^n}{\partial t^3} \tag{1}$$

To estimate the higher-order time derivatives, the first-order time derivative, matrix A, and the time derivative of matrix A can be utilized:

$$\frac{\partial^2 u^n}{\partial t^2} = -\frac{\partial}{\partial x}(A \frac{\partial u^n}{\partial t}), \frac{\partial^3 u^n}{\partial t^3} = -\frac{\partial}{\partial x}(A \frac{\partial^2 u^n}{\partial t^2} + \frac{\partial A}{\partial t} \frac{\partial u^n}{\partial t}) \tag{2}$$

The procedure of the novel and the conventional algorithms can be demonstrated as follows:

<u>Procedure Of Novel TDG scheme</u>

Step 1. Employ the DG formulation to obtain the first order time derivative of *u*:

$$\int_{x^{k-1}}^{x^{k+1}} \left(\frac{u_h^n}{\partial t} + \frac{\partial f^n}{\partial x} \right) \Phi \, dx = 0 \tag{3}$$

Step 2. Estimate the higher-order time derivatives of *u* by first order derivative:

$$\frac{\partial^2 u_h^n}{\partial t^2} = -\frac{\partial}{\partial x}\left(A^n \frac{\partial u^n}{\partial t} \right) \tag{4}$$

$$\frac{\partial^3 u_h^n}{\partial t^3} = -\frac{\partial}{\partial x}\left(A^n \frac{\partial^2 u^n}{\partial t^2} + \frac{\partial A^n}{\partial t} \frac{\partial u^n}{\partial t} \right) \tag{5}$$

Step 3. Utilize Taylor expansion to estimate the value of *u* by Eqs. (4) and (5):

$$u_h^{n+1} = u_h^n + \Delta t \frac{\partial u_h^n}{\partial t} + \frac{\Delta t^2}{2} \frac{\partial^2 u_h^n}{\partial t^2} + \frac{\Delta t^3}{6} \frac{\partial^3 u_h^n}{\partial t^3} \tag{6}$$

Step 4. Obtain the value of *u* at next time using F_2 operator:

$$u^{n+1} = F_2(u^n, \frac{\partial u^n}{\partial t}, A^{n-1}, \frac{\partial A^{n-1}}{\partial u}) \tag{7}$$

<u>Procedure Of Conventional TDG scheme</u>

Step 1. Utilize Taylor expansion to express the first order time derivative of *u*:

$$\frac{\partial u_h^{n-1}}{\partial t} = \frac{u_h^n - u_h^{n-1}}{\Delta t} - \frac{\Delta t}{2} \frac{\partial^2 u_h^{n-1}}{\partial t^2} - \frac{\Delta t^2}{6} \frac{\partial^3 u_h^{n-1}}{\partial t^3} \tag{8}$$

Step 2. Estimate the higher-order time derivative of *u* by derivative of flux *f*:

$$\frac{\partial^2 u_h^n}{\partial t^2} = \frac{\partial}{\partial x}(A^n \frac{\partial f^n}{\partial x}) \tag{9}$$

$$\frac{\partial^3 u_h^n}{\partial t^3} = -\frac{\partial}{\partial x}\left(A^n \frac{\partial}{\partial x}\left(A^n \frac{\partial f^n}{\partial x} \right) + \frac{\partial A^n}{\partial u}\left(\frac{\partial f^n}{\partial x} \right)^2 \right) \tag{10}$$

Step 3. Replace the first-order time derivative of *u* by (8) in DG formulation:

$$\int_{x^{k-1}}^{x^{k+1}} (\frac{u_h^{n+1} - u_h^n}{\Delta t} - \frac{\Delta t}{2} \frac{\partial^2 u_h^n}{\partial t^2} - \frac{\Delta t^2}{6} \frac{\partial^3 u_h^n}{\partial t^3} + \frac{\partial f^n}{\partial x}) \Phi dx = 0 \tag{11}$$

Step 4. Obtain the value of *u* at next time using F_1 operator:

$$u^{n+1} = F_1(u^n, f^n, A^n, \frac{\partial A^n}{\partial u}) \tag{12}$$

Comparing the time iteration formulas of the last step reveals the differences between the two approaches:

1) Time Discretization of the Novel TDG Scheme:

$$u_h^{n+1} = u_h^n + \Delta t \int_{x^{k-1}}^{x^{k+1}} \frac{\partial \varphi_i}{\partial x} f^n \, dx - f^n \varphi_i |_{x^{k-1}}^{x^{k+1}} + \frac{\Delta t^2}{2} A^n \left(f^n \varphi_i |_{x^{k-1}}^{x^{k+1}} - \frac{\partial \varphi_i}{\partial x} f^n |_{x^{k-1}}^{x^{k+1}} \right) + \frac{\Delta t^3}{6} f(u^n, A^n, \frac{\partial A^n}{\partial t})$$

2) Time Discretization of Conventional TDG

$$u_h^{n+1} = u_h^n + \Delta t \int_{x^{k-1}}^{x^{k+1}} \frac{\partial \varphi_i}{\partial x} f^n \, dx - f^n \varphi_i |_{x^{k-1}}^{x^{k+1}} + \frac{\Delta t^2}{2} A^n \left(\frac{\partial f^n}{\partial x} \varphi_i |_{x^{k-1}}^{x^{k+1}} + \int_{x^{k-1}}^{x^{k+1}} \frac{\partial f^n}{\partial x} \frac{\partial \varphi_i}{\partial x} dx \right) + \frac{\Delta t^3}{6} f(u^n, A^n, \frac{\partial A^n}{\partial U})$$

The two approaches share the same form in the first-order temporal derivative term. However, they differ in the steps taken for the second-order temporal derivative term. The novel approach avoids the use of complicated three-dimensional matrices (tensors) in the third-order temporal derivative term by differently utilizing the Jacobi matrix A as shown in Fig. 1.

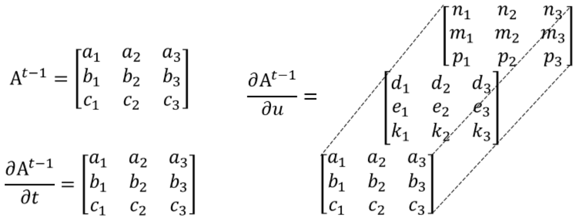

Fig.1 Jacobi matrix

In this study, the central difference method is employed to estimate the higher-order time derivatives. Two new variables, G and H, are defined as follows:

$$G = A \frac{\partial u^n}{\partial t}, H = A \frac{\partial^2 u^n}{\partial t^2} + \frac{\partial A}{\partial t} \frac{\partial u^n}{\partial t} \tag{13}$$

Therefore, the higher-order time derivatives can be expressed as:

$$\frac{\partial^2 u^n}{\partial t^2} = -\frac{(G_{i-2} - 8G_{i-1} + 8G_{i+1} - G_{i+2})}{12\Delta x}, \quad \frac{\partial^3 u^n}{\partial t^3} = -\frac{(H_{i-2} - 8H_{i-1} + 8H_{i+1} - H_{i+2})}{12\Delta x} \tag{14}$$

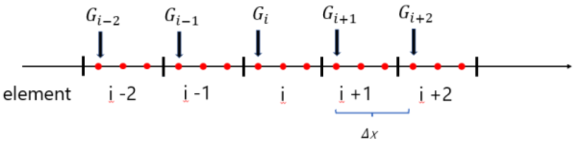

Fig.2 Position of G

The second-order time derivative for any discrete point in cell i is calculated using the G values of the points at the same positions in the four neighboring cells.

3. Numerical Results

This section demonstrates the results of two continuous conservation law examples using the new algorithm presented above. First, the simple linear wave equation is considered:

$$\frac{\partial u}{\partial t} + 2\pi \frac{\partial u}{\partial x} = 0, \quad x \in [0,2\pi]; \; u(x,0) = \sin(x); \; u(0,t) = \sin(2\pi t) \tag{15}$$

Fig.3 shows the results of this equation. As time progresses, nonphysical oscillations occur at the boundary and gradually expand.

Secondly, the viscous Burgers' equation is examined:

$$\frac{\partial u}{\partial t} + \frac{\partial}{\partial x}\left(\frac{u^2}{2}\right) = \varepsilon \frac{\partial^2 u}{\partial x^2}, \quad x \in [-1,1]; \; \varepsilon = 0.2 \tag{16}$$

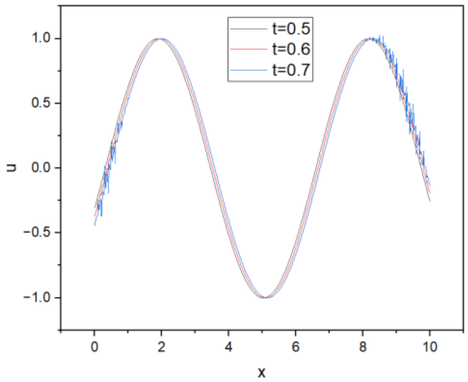

Fig.3 Result of wave equation

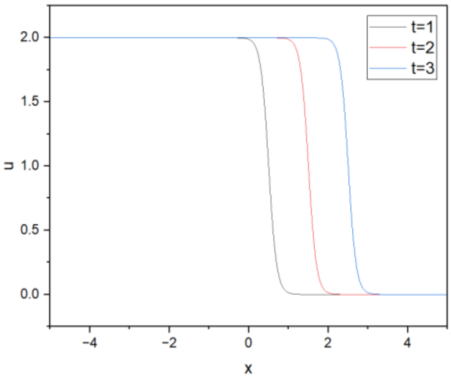

Fig.4 Result of Burgers' equation

Fig.4 illustrates the results of the Burgers' equation based on the new algorithm. The new algorithm performs well, particularly in the absence of input data at the boundary.

4. Discussion and Conclusion

Based on the results, several observations can be made. In the first case, the calculated results exhibit variations from the boundary to the center over time, and these variations tend to increase with time. On the other hand, the calculation outcomes of the second case demonstrate the good continuity. These cases demonstrate that the numerical results are significantly influenced by the boundary condition. Noted that these two cases never use limiter to control non-physical oscillation. This suggests that the new algorithm realizes accurate computational results within the continuous domain and at the unchanging boundary.

In conclusion, the novel algorithm combining the Taylor-type time discretization with the Nodal Discontinuous Galerkin method offers advantages over conventional approaches in terms of its simplified integration process and reduced need for limiters. The presented numerical results demonstrate its effectiveness in solving conservation law systems.

References

[1] W.H. Reed and T.R. Hill, Triangular mesh methods for the neutron transport equation, Los Alamos Scientific Laboratory Report, LA-UR-73-479, 1973. Cited on page(s) 10, 236

[2] F. Brezzi, L.D. Marini, and E. Suli, Discontinuous Galerkin methods for first-order hyperbolic problems, M3AS: Math. Models Methods Appl. Sci. 14(2004), pp. 1893–1903, 2004. Cited on page(s) 10

[3] A. Ern and J.-.L. Guermond, Discontinuous Galerkin methods for Friedrichs' systems. I. General theory, SIAM J. Numer. Anal. 44(2006) pp. 753–778. Cited on page(s) 10

[4] B. Cockburn, Lin SY, Shu CW. TVB Runge–Kutta local projection discontinuous Galerkin finite element method for conservation laws III: one dimensional systems. J Comput Phys 1989;84:90–113.

[5] J Qiu, CW Shu, LAX–WENDROFF-TYPE TIME DISCRETIZATIONS SIAM. Journal on Scientific Computing, 2003 - SIAM

[6] Donea, J. (1984) A Taylor-Galerkin method for convective transport problems, Int. J. Num. Meth. Erg. 20, 101-l 19

Current profile optimization for improving performance of superconducting linear acceleration system

Teruou Takayama[1,*], Ayumu Saitoh[1], Atsushi Kamitani[1]

[1]Graduate School of Science and Engineering, Yamagata University, Japan

*`takayama@yz.yamagata-u.ac.jp`

Abstract. The improving performance of a superconducting linear accelerator (SLA) system for pellet injection in nuclear fusion reactors was investigated numerically. For this purpose, a numerical code using FEM was developed to analyze the shielding current density and the dynamic motion of the high-temperature superconducting film. The computational results showed that by optimizing the current profile, the acceleration time to reach 5 km/s hardly changes compared with the homogenized profile. However, the filaments at both ends disappear and the length of the electromagnets is shortened.

Keywords: Computer simulation, Numerical methods

1. Introduction

A superconducting linear acceleration (SLA) system to fuel magnetic confinement fusion reactors has been proposed. To investigate the feasibility of the SLA system, we investigate the acceleration performance of the SLA system[1]. To this end, the FEM code was developed to analyze both the time evolution of a shielding current density in a high-temperature superconductor film and the dynamic motion of the film.

By using the code implementing a program to solve optimization problems, we optimized a current profile of the acceleration magnet [1]. The results of the computations show that the pellet speed for the magnet shape obtained using the normalized Gaussian network (NGnet) is significantly faster than that of the homogeneous current profile of the electromagnet. In another of our studies, we found that an exponentially increasing current with time was employed to accelerate a pellet drastically. The computational results indicate that an acceleration time to reach the target speed of 5 km/s is reduced by about 1/10. Although we have not yet performed optimization at exponentially increasing currents, the optimization of the current profile may improve acceleration performance of the SLA system.

The purpose of this study is to investigate the possibility of the improving performance of SLA system by using the topology optimization method for the exponentially increasing current profile in electromagnets.

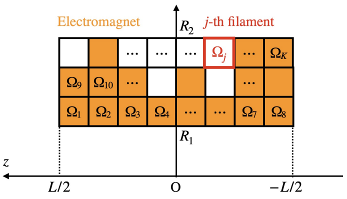

Figure 1: Schematic view of the electromagnet cross-section.

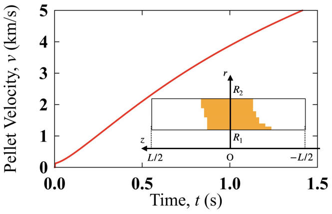

Figure 2: Time dependence of the velocity.

2. Current profile optimization

In this study, the rectangular cross-section of an electromagnet was optimized under the following assumptions (see Fig. 1). The length of the electromagnet is L, and the inner and outer diameters are R_1 and R_2, respectively. The first step in determining the electromagnet shape was to equally divide the electromagnet into filaments.

A current in jth filament Ω_j is expressed as $I_j(t, Z) = I(t, Z)x_j/K_{\mathrm{on}}$, where x_j represents the binary state of the filament as follows: $x_j = 1$ for on-state in Ω_j and $x_j = 0$ for off-state. K_{on} denotes the number of the filaments for on-state. Furthermore, the current I applied to electromagnets has been expressed as follows:

$$I(t, Z) \equiv \begin{cases} I_0[1 - \exp(-t/\tau)] & (0 \leq Z \leq Z_{\mathrm{L}}) \\ 0 & (\text{otherwise}) \end{cases} . \tag{1}$$

Here, I_0 is the maximum value of the current and τ is the time constant. Z and Z_{L} denote the HTS position and the left end of acceleration region.

Next, to determine a current profile, we employ the on-off method based on NGnet in the present study. The output of NGnet is determined by the gene of GA. A filament is in the on-state for the case where its value is positive, whereas a filament is in the off-state for the negative. In this abstract, the objective function is given by $v_{\mathrm{opt}}/v_{\mathrm{h}} \rightarrow \max$, where v_{opt} is the final velocity for the optimization, and v_{h} is that for the homogenized profile. In this study, the parameters are fixed as follows: $R_1 = 5$ cm, $R_2 = 7$ cm, $L = 10$ cm, $Z_{\mathrm{L}} = 20$ cm, $I_0 = 100$ kA, and $\tau = 1$ ms.

In Fig. 2, we show the time dependence of the pellet velocity v for the optimization. Moreover, the inset shows the current profile in the electromagnet. We found that the acceleration time to reach 5 km/s hardly changes compared with the homogenized current profile. In addition, the filaments at both ends are vanished, and the length of the electromagnets is shortened. This result suggests that the acceleration distance of the pellets can be shortened by reducing the distance between the magnets. In JSST2023, we will present that the results of the electromagnet topology optimization using multi-objective functions.

References

[1] T. Takayama, T. Yamaguchi, A. Saitoh, A. Kamitani, and H. Nakamura: *Plasma and Fusion Research*, 16 (2021), p. 2401025.

Fracture strength evaluation of multi-hole materials by improved linear notch mechanics

Wataru Fujisaki[1*]

[1]Department of Science and Technology, Kyushu Sangyo University

*fujisaki@ip.kyusan-u.ac.jp

Abstract. Conventional linear notch mechanics (LNM) was proposed to clarify the distinction between the fracture and non-fracture zones using a master-curve. It is effective for evaluating the fracture strength of notched materials with a single hole. When multiple notches are adjacent to each other, the conventional LNM is less accurate in predicting the fracture strength. In this study, the effectiveness of the improved linear notch mechanics, which uses the stress gradient χ at the bottom of the notch instead of the notch radius ρ, in evaluating the fracture strength of plates with multiple notches is verified.

Keywords: Fracture Strength, Linear Notch Mechanics, Multiple notches, Weight Reduction

1. Introduction

This paper is a study of a new prediction method for accurately evaluating the brittle fracture strength of notched materials of various shapes. The physical meaning of fracture mechanics for this notch problem is the same as that of fracture mechanics for cracked materials as shown in Figure 1. The conventional linear notch mechanics, proposed in the 1980s, clarifies the distinction between fracture and non-fracture zones in notched materials. This mechanics is effective for evaluating the fracture strength of brittle materials with a single hole except for the big one. While linear fracture mechanics, a method for evaluating the strength of cracked materials, requires only one measure of severity, the stress intensity factor K, this mechanics requires two measures. Namely, the maximum stress σ_{max} at the bottom of the notch and the notch radius ρ. In this study, the concept of improved linear notch mechanics (ILNM), which uses the stress gradient χ at the bottom of the notch instead of the notch radius ρ, is explained and its applicability and effectiveness are verified for notched materials with multiple holes.

2. Limitations of application of conventional linear notch mechanics

The author has proposed a new fracture criterion[1] that can predict the brittle fracture strength of notched materials. We will refer to this as improved linear notch mechanics. In general, notched products are useful for weight reduction of products that contribute to effective use of global resources and energy conservation. For smooth materials, there are failure criteria based on a single parameter, such as maximum shear stress or maximum von Mises stress. On the other hand, for notched materials, Nisitani proposed linear notch mechanics [2] using the maximum stress $\sigma_{\max}$ at the bottom of the notch and the notch radius ρ. The question is up to what value of L/ρ the conventional LNM is valid. Here, L is the half length of the minimum cross section.This question is not clear from past studies. Recently, we have systematically calculated the relative stress gradient [3] between the center notch and the side notch using the specimen as shown in Figure 2. To calculate accurate stress gradients, we used the finite element method (FEM, SolidWorks simulation) with a D.O.F. ranging from 0.3 to 1.4 millon as well as the method of fundamental solutions [4] .

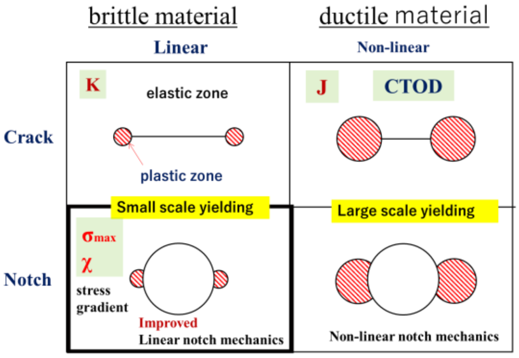

Fig. 1 Fracture criterions

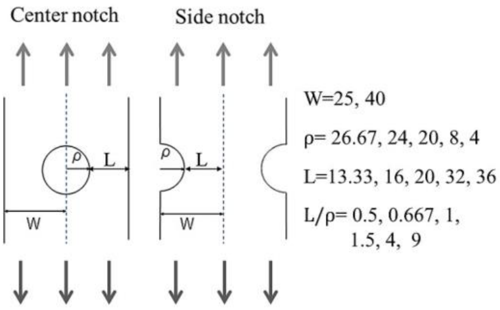

Fig. 2 Test pieces（Single holes）

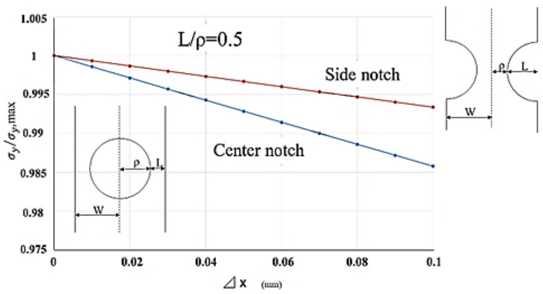

Fig. 3 Stress gradients of big notches

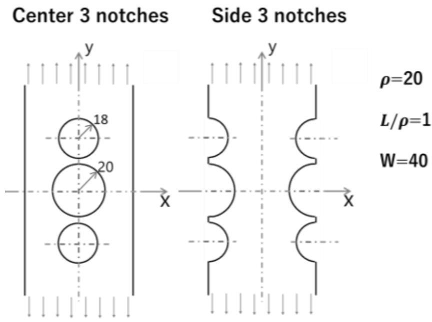

Fig. 4 Test pieces（3 holes）

Figure 3 shows the stress gradients of two big notches(L/ρ=0.5). When the notch radius ρ increases to this point, the correspondence between the notch radius and the stress gradient χ is lost. This means that conventional linear notch mechanics cannot be used. Another case is when other notches are adjacent as shown in Figure 4. At this distance, when notches are adjacent to each other, the force flow is significantly different from that of a single hole, reducing stress concentration. Thus, the breaking load can be expected to increase.

3. Usefulness of the improved LNM

Therefore, it is necessary to apply the improved LNM, which directly utilizes the stress gradient χ, to accurately predict the fracture strength. In this study, tensile tests of Cu notched plates (W=40mm, t=30μm) were conducted systematically. First, the master curves obtained from the experimental results using the conventional LNM are shown in Figure 5. Each condition of the tensile test was repeated six times, and the vertical bars in the figure represent 99% confidence intervals. The data for small circular notches ($L/\rho>1.0$) are on the master curve, but the data for large notches ($L/\rho=0.667$; cases A, B) are off the master curve[5]. Therefore, the conventional LNM cannot accurately estimate the fracture strength for large notch, lower than $L/\rho=1.0$. Furthermore, in the case of the 3 circle holes (cases C, D), the experimental data also depart from the master curve.

On the other hand, the new master curve based on the improved LNM is shown in Figure 6. The improved LNM can accurately estimate the fracture strength for cases A to D, where the stress gradient χ is $\Delta\sigma_y / \Delta x$ of the notched bottom element in the finite element method. It is clear that the data for cases A to D are on the master curve. Therefore, the modified LNM can be used to correctly evaluate the fracture strength of notched materials with multi-holes.

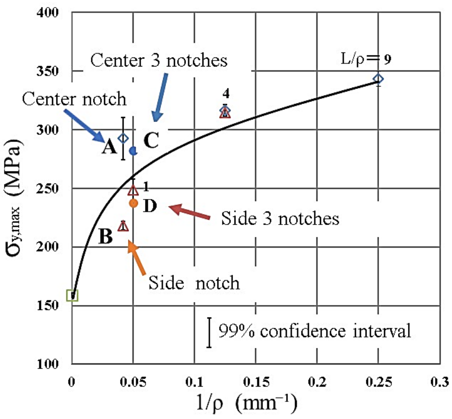

Fig.5 Conventional LNM

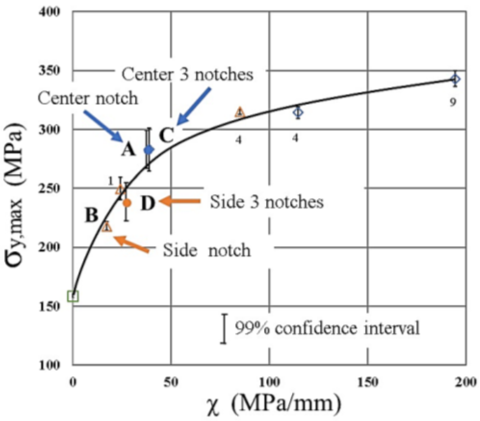

Fig. 6 Improved LNM

The range of application of conventional LNM and improved linear notch mechanics (ILNM) for a single hole is illustrated in Figure 7. The conventional LNM can be used only when $L/\rho>1.0$. On the other hand, experiments have shown that ILNM can be applied to very large notches up to $L/\rho=0.5$. This improved linear notch mechanics is effective for the rational design of products containing large notches. In the case of two-circle holes as well as three-circle holes as shown in Figure 8. The conventional linear notch mechanics has poor prediction accuracy when the notches change the force flow between each other as shown in (B) and (C).

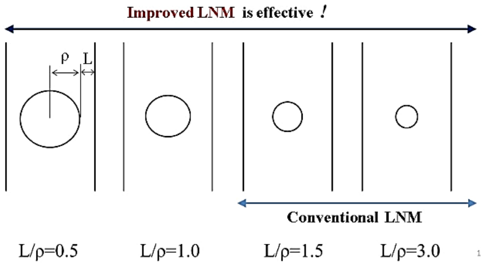

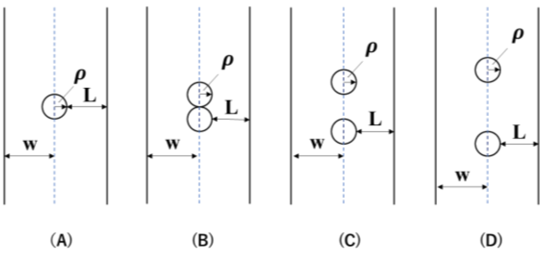

Fig.7 Comparison of application limit

Fig.8 Application for multple holes

If we apply the improved linear notch mechanics, we can obtain accurate predictions for all cases, whether single or multiple holes, because it uses the stress gradient χ directly.

4. Conclusion

Up to now, we have conducted systematic tensile tests and found this improved LNM can be applied to the very big single notch problem with $L/\rho=0.5$. Furthermore, we clarified that the improved LNM can be applied to the multi-hole materials. Improvements to the LNM will greatly expand its range of application and efficiently achieve both product weight reduction and mechanical safety.

References

[1] W.Fujisaki, Y.Takamiya,: Generalized Linear Notch Mechanics for Strength Evaluation, *Proc. Inter. Conf. Japan Society of Simulation and Technology, JSST2017*,pp.1-4,2017.

[2] H.Nisitani: Linear Notch Mechanics as an Extention of Linear Fracture Mechanics, *Proc. Inter. Conf. Role of Fracture Mechanics in Modern Technology*, (Eds; Sih,G.C. and Nisitani,H.), pp.23-37, Elsevier, 1987.

[3] W.Fujisaki, H.Iwatsubo, Y.Takamiya : Effectivness of Generalized Linear Notch Mechanics in View of Stress Gradient, *Proc. Inter. Conf. Japan Society of Simulation and Technology, JSST2018*, pp.1-4,2018.

[4] W.Fujisaki: Recent Studies in Meshless & Other Novel Computational Methods, pp.57-69, Tech Science Press, 2010.

[5] W.Fujisaki, R.Yamasaki : Estimation of fracture strength using improved linear notch mechanics for notched materials, *Proc. 3rd. Inter. Conf. on Comp. Engineering and Science for Safe and Environmental Problems, COMPSAFE 2020*, pp.1-4, 2020.

Overlay Analysis of Fruit Growing and Soil in Agricultural Heritage Systems

Yoichi Shimazaki[1*]

[1]Faculty of Life and Environmental Sciences, University of Yamanashi

*`simazaki@yamanashi.ac.jp`

Abstract. This study analyzed environmental factors related to suitable areas for fruit growing in one region of Yamanashi Prefecture. This work demonstrated a method of using geographical information systems for the quantitative assessment of climate, topographic, and soil data. Based on aerial photographs of 201,917 farmland blocks, growing areas were divided into eight categories. Grapes growing areas had high ratios of Brown Forest soils. Peaches growing areas had high ratios of Allophonic Andosols and Brown Lowland soils. The average slope angles were 4.5, 3.7, 4.7, and 7.3 degrees, respectively, for grapes, peaches, vegetables, and others. This method enables researchers to incorporate information about topographical conditions and weather conditions into area maps.

Keywords: Climate change adaptation, Environment factor, Geographical information system

1. Introduction

Since December 2018, the Climate Change Adaptation Act has been enforced in Japan. Rising temperatures cause product quality deterioration and shifts in the locations which are suitable for growing products. Fruits have a smaller range of adaptability to climate than other crops. Climate change adaptation to support fruit growing is a top agricultural priority from a long-term perspective because fruits are perennial crops.

Sugiura et al. [1] evaluated climate-change induced changes in the skin color of table grapes in Japan. Nemoto et al. [2] investigated shifts in climatic suitability for cultivating grapes in Hokkaido. Nevertheless, researchers must consider geographical conditions in addition to weather conditions. Particularly, the question remains of the manner in which and the degree to which suitable areas for fruit growing change with rising temperatures, based on their soil conditions. Shimazaki [3] conducted to quantify environmental factors affecting fruit growing. However, this study must expand the analysis area.

This study analyzed environmental factors related to suitable areas for fruit growing in the Kyoto Region of Yamanashi Prefecture: The Globally Important Agricultural Heritage Systems since 2022 [4]. This work demonstrated a method of using geographical information systems for the quantitative assessment of climate, topographic, and soil data. These results are expected to contribute to the development of sustainable agriculture and are expected to be helpful as science-based criteria for future examinations when suitable land areas are altered by rising temperatures.

2. Methods

This study area included the three cities of Yamanashi, Fuefuki, and Koshu. Based on aerial photographs of 201,917 farmland blocks, growing areas were divided into eight categories: grapes, peaches, cherries, persimmons, apples, paddies, vegetables, and others. Figure 1 shows a fruit growing map of farmland blocks. Others examples are abandoned farmlands and converted farmlands. The author used Google Maps to conduct a complementary check. Soil data were referred from the Comprehensive Soil Classification System of Japan [5]. Figure 2 shows a soil classification map of farmland blocks. Overlay analysis was subsequently applied for investigation to assess the eight growing areas with six soil classifications using intersect tool in ArcGIS.

Data related to environmental factors cannot be extracted from farmland blocks because the area is an irregular polygon. Currently, data related to environmental factors such as weather, topography, and population are available in grid units [6][7]. The author used numerical programming to distribute the growing area of the farmland blocks to satisfy the conditions of the overlay analysis to the grid. Weighted averages of environmental factors other than soil were calculated the respective growing areas by creating a program to split irregular polygon data into regular grid data.

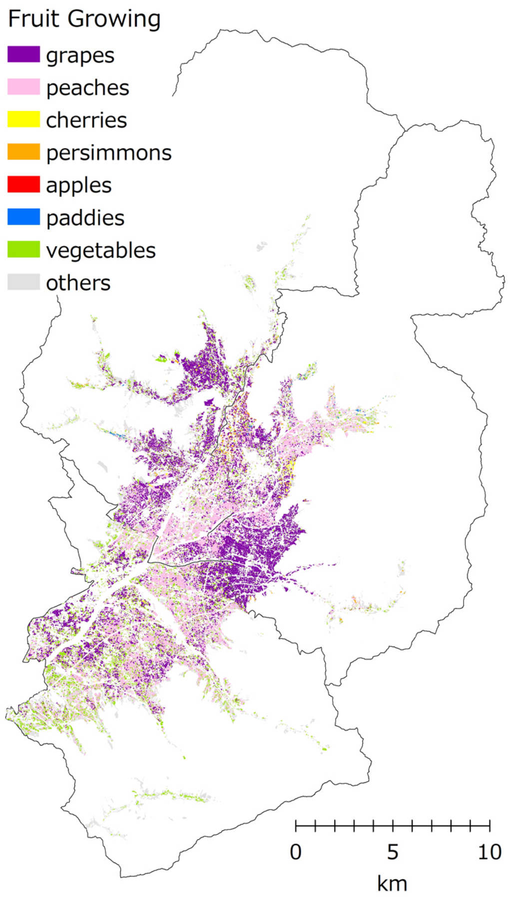

Figure1 Fruit growing map of farmland blocks

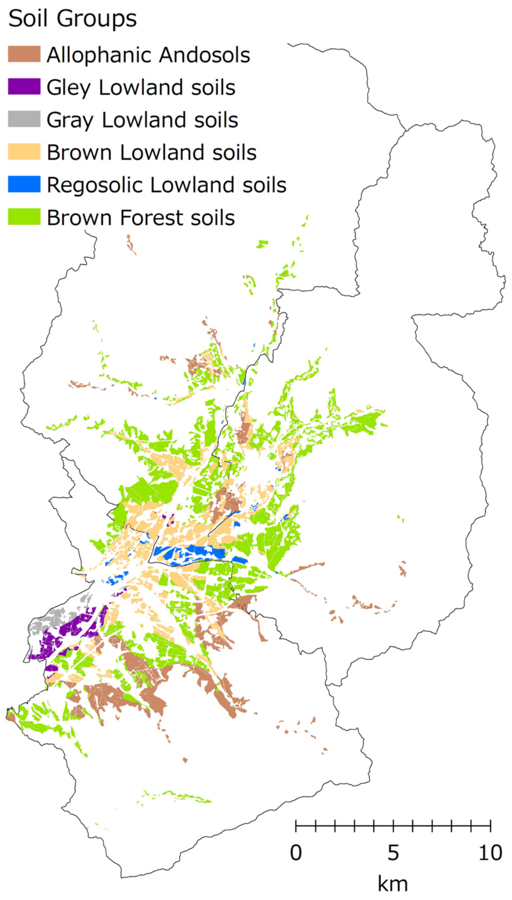

Figure 2 Soil groups map of farmland blocks

3. Results

Results show that peaches accounted for 35.6%, grapes were 32.8%, others were 18.2%, and vegetables were 11.8% of the total area. The proportion of just these four growing areas to the total subject area was therefore 98.4%. Although survey years and crop area definitions differed, estimates and statistics were compared for growing areas according to the fruit type. Statistical data were obtained from the Census of Agriculture and Forestry [8]. The relative errors of the estimates and statistics were found to be 17.0% for grapes and 6.8% for peaches. The author judged that the error was small and continued the analysis. The study specifically addressed these four growing areas because cherries, persimmons, apples, and paddies fields each accounted for less than 0.9% of the total subject area.

Figure 3 presents the overlay analysis results. The findings indicated the respective proportions of soil groups to the total fruit growing as 18.0% for Andosols, 32.9% for Lowland soils, and 49.0% for Brown Forest soils. Grapes growing areas had high ratios of Brown Forest soils. The typical grape-growing areas presented a wide distribution among hillocks. Peaches growing areas had high ratios of Allophonic Andosols and Brown Lowland soils. Peaches had a similar vegetable composition ratio to that found for grape. Peaches growing areas had small percentages of poorly drained Grey Lowland soils. These results suggest poorly drained areas as the worst soil environment for peaches.

Table 1 shows the weighted averages of environmental factors. The average slope angles were 4.5, 3.7, 4.7, and 7.3 degrees, respectively, for grapes, peaches, vegetables, and others compared to 4.8 degrees for all farmland in the region. Other had the highest inclination angle and the smallest population. Findings obtained from this study indicate that farmers in this region assign priority to peach growing in preference to either paddies or vegetables cultivation.

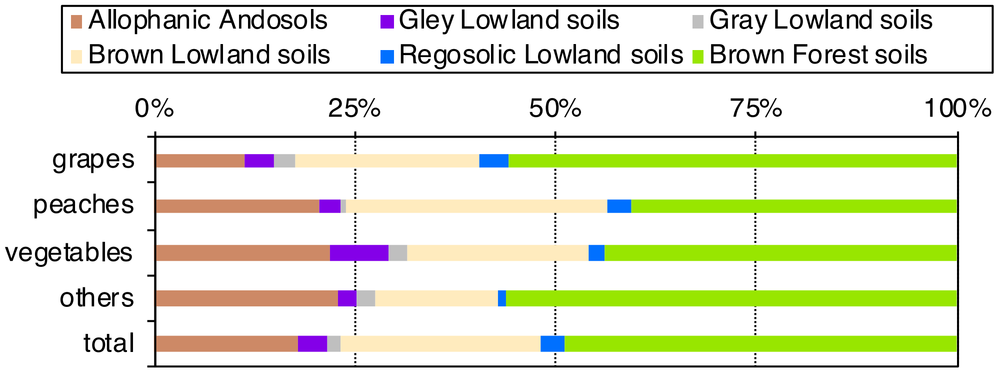

Figure 3 Overlay analysis results

Table 1 Weighted averages of environmental factors

	grapes	peaches	vegetables	others	total
average temperature (degree)	13.4	13.5	13.3	12.7	13.3
annual precipitation (mm)	1128.2	1157.9	1196.6	1188.2	1158.1
average elevation (meter)	418.4	390.3	422.0	516.7	428.3
average inclination angle (degree)	4.5	3.7	4.7	7.3	4.8
population (people)	738.5	793.2	746.3	491.6	710.6
offices number (place)	28.8	29.9	28.1	19.6	27.3

4. Discussion

The author simulated the replanting of fruit growing areas in the future because of rising temperatures. Current cultivation in the basin might be replaced by planting in mountainous areas at higher elevations and lower average temperatures refer to Table 1. These findings indicate that mountainous areas have Brown Forest soils. Simulation results indicate that the soil compatibility enables grape to be suitable. Grapes are more tolerant of humidity than peaches are. For that reason, they have high potential for cultivation, even on strong clay. However, the steep slope angle of such areas is likely to make fruit growing inconvenient.

5. Conclusion

This study developed a fruit growing map based on aerial photographs. This method enables researchers to incorporate information about topographical conditions and weather conditions into area maps. Its accuracy is attributed to the fruit types. The abandoned farmland had high average elevation, a large average slope angle, and a small total population.

The accuracy of fruit growing identification using aerial photographs can be improved. The method should be developed based on regional characteristics of fruit growing.

Acknowledgement

The author is very grateful to the members of Council for the Promotion of the Kyoto Region as a GIAHS, Yamanashi Prefectural Agriculture Department, and Yamanashi Prefectural Land Improvement Projects Federation. The author would like to thank Ms. Yuki Shirinashihama, Ms. Mona Nakajima, Ms. Ayumi Nakaya, and Mr. Taisei Yamamoto for their assistance during fruit cropping map construction. This work was supported by JSPS KAKENHI Grant Number JP20K12297.

References

[1] T. Sugiura, M. Shiraishi, S. Konno and A. Sato: *Journal of Agricultural Meteorology*, 75:2, (2019), 67-75.

[2] M. Nemoto, T. Hirota and T. Sato: *Journal of Agricultural Meteorology*, 72:3-4, (2016), 167-172.

[3] Y. Shimazaki: *Environmental Science*, 36:2 (2023), 42-52.

[4] Council for the Promotion of the Kyoto Region as a GIAHS: The Fruit Farming System, https://kyoutou-giahs.jp/en/ (Last access: 2023.5.24)

[5] National Agriculture and Food Research Organization: Japanese Soil Inventory, https://soil-inventory.rad.naro.go.jp/ (Last access: 2023.5.24)

[6] Ministry of Land, Infrastructure, Transport and Tourism: National Land Numerical Information, https://nlftp.mlit.go.jp/ksj/ (Last access: 2023.5.24)

[7] Ministry of Internal Affairs and Communications: Grid Square Statistics Compiled by Statistics Bureau, https://www.stat.go.jp/data/mesh/ (Last access: 2023.5.24)

[8] Ministry of Agriculture, Forestry and Fisheries: Census of Agriculture and Forestry, https://www.maff.go.jp/j/tokei/census/afc/ (Last access: 2023.5.24)

Research on improving the accuracy of super-resolution techniques using GANs by sharpening target images and optimizing discriminator learning

Akihiro Abe[1*] and Hiroyuki Kamata[2]

[1]Graduate School of Science and Technology, Meiji University, Japan

[2]School of Science and Technology, Meiji University, Japan

*`ce221002@meiji.ac.jp`

Abstract. The objective of this study is to improve the accuracy of image generation without changing the learning mechanism of GAN-based super-resolution techniques. The U-net discriminator used in this method learns the truth of the parts of high-resolution and super-resolution images that do not need to be discriminated. In addition, blurred images tend to have reduced visual clarity and contrast. In this study, we propose the use of a filter that removes low-frequency portions of the image to make the U-net discriminator learn appropriately. In addition, the target image for learning is processed to be sharper using wavelet transform to produce a visually superior image. Wavelet transform can decompose the image into high-frequency and low-frequency components, which makes it possible to sharpen only the high-frequency component, which has a substantial impact on learning. By modifying the above two points, we succeeded in generating a visually superior image compared to the image without modification. These results suggest a favorable learning outcome by setting the discriminator input appropriately and the effectiveness of processing the target image.

Keywords: Super Resolution, Deep Learning, GAN, Wavelet Transformation

1. Introduction

This study aims to improve the accuracy of image generation without changing the learning mechanism of GAN-based super-resolution techniques. Specifically, to improve the learning of the U-net discriminator used in Real-ESR GAN [1] and several other GANs. To improve the problem that blurred images reduce visual clarity and contrast. In conventional U-net discriminators, the training model also feeds back the truth of low-resolution portions where there is minor difference between high-resolution and super-resolution images. Therefore, we propose to reduce the influence of low-frequency components on learning by using a filter that removes them. Furthermore, we propose a method to target images that emphasize only the high-frequency component by using the property of the wavelet transform [2] that can separate the image into high-frequency and low-frequency components. These two modifications are expected to improve the accuracy of the generator by making the discriminator more appropriate and to generate sharper images.

2. GAN for Super Resolution

The GAN-based super-resolution technique is trained using two networks: a generator and a discriminator. The generator takes a low-resolution image as input and produces a super-resolution image as output. The discriminator takes the super-resolution image and the target image as input and determines whether the image is true or false. By mutually training these two networks, the target image is brought closer to the discriminator. In this verification, RRDN is used as the generator and U-net as the discriminator, based on Real-ESR GAN.

In addition, Blind Super Resolution [1] enables more realistic super resolution by performing preprocessing that is close to real-world image degradation. In this study, we will verify two types of super resolution: normal super resolution and Blind Super Resolution.

3. Experiments

3.1. proposal_1

The method of generating sharpened images is as follows.

(1) Apply a sharpening filter to the target image.
(2) Subtract 0.5 times the target image multiplied by the Laplacian filter from the image in (1).
(3) Wavelet transform (decomposition level 3, db3) the target image and the sharpened image in (2).
(4) The HL, LH, and HH components of the sharpened image and the LL component of the target image are used to generate an image by inverse wavelet transform.

Sharpened images are used as target images other than for discriminator training.

3.2. proposal_2

The method of creating a filter is as follows.

(1) Apply a Laplacian filter to the target image and take absolute values.
(2) Convert to a black and white image and determine the average value of the pixels.
(3) The average value obtained in (2) is used as the threshold value and binarized to 0 and 1.
(4) The image is generated by extracting the outline of the image and making it a line of thickness 2.

The filter is applied as follows.

When training the discriminator, the filter is multiplied on the discriminator output and the correct image (false images are not applied since they are 0-filled images). The discriminator losses are multiplied by (sum of the number of pixels in the image/pixel value 1), which scales up to a number of losses equivalent to that of normal discriminator learning. The same is also applied and scaled up for generator training.

3.3. Study Details

Learning is done according to Real-ESR GAN. Changes include a patch size of 128, batch size of 10, and reduced preprocessing.

3.4. Datasets and Evaluation Indicators

DIV2K_train_HR, Flickr2K, and OutdoorSceneTrainig are used for the training dataset. Note that they are not used for training images below the patch size. Set14, Urban100, and DIV2K_test_HR are used for the evaluation dataset. Manga109 [3] is used as the result image, although numerical evaluation is not performed. PSNR, LPIPS Alex, and LPIPS VGG [4] are used as evaluation metrics.

4. Results

The training results are shown in the following table. Comparison images are also shown in the following figures. It can be seen that LPIPS values have improved in many cases compared to the conventional method. In particular, the improvement in accuracy by proposal_1, which uses edge-enhanced images, is significant.

Table1. Quantitative comparison between HR and SR (x4 Normal SR)

		Normal	Proposal_1	Proposal_2	Proposal_1+2	bicubic
Set14	LPIPS VGG	0.2439	0.2347	0.2428	0.2427	0.3544
	LPIPS Alex	0.1638	0.1442	0.1627	0.1538	0.3861
	PSNR [dB]	25.8179	24.4635	25.8336	23.7633	24.2323
Urban100	LPIPS VGG	0.2161	0.2209	0.2163	0.2232	0.3617
	LPIPS Alex	0.1348	0.1266	0.1347	0.1285	0.4205
	PSNR [dB]	24.0761	22.3834	24.1204	21.8332	21.6991
DIV2K	LPIPS VGG	0.2277	0.2200	0.2247	0.2182	0.3389
	LPIPS Alex	0.1469	0.1222	0.1448	0.1224	0.3407
	PSNR [dB]	28.1079	26.7047	28.1390	26.1729	26.6942

Table2. Quantitative comparison between HR and SR (x4 Blind SR)

		Normal	Proposal_1	Proposal_2	Proposal_1+2	bicubic
Set14	LPIPS VGG	0.3046	0.3026	0.3041	0.3021	0.3544
	LPIPS Alex	0.2187	0.2004	0.2206	0.1989	0.3861
	PSNR [dB]	24.8076	23.5733	24.8953	23.6579	24.2323
Urban100	LPIPS VGG	0.2873	0.2885	0.2863	0.2877	0.3617
	LPIPS Alex	0.2000	0.1800	0.2039	0.1792	0.4205
	PSNR [dB]	22.7061	21.3052	22.7834	21.4547	21.6991
DIV2K	LPIPS VGG	0.2910	0.2945	0.2892	0.2916	0.3389
	LPIPS Alex	0.1948	0.1852	0.1972	0.1830	0.3407
	PSNR [dB]	26.7726	25.2057	26.8588	25.2910	26.6942

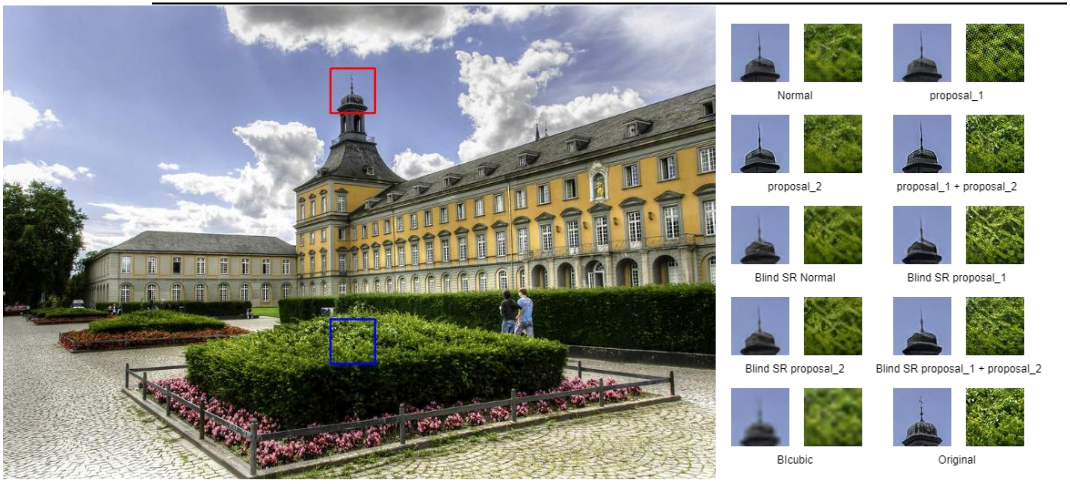

Fig1. Urban100 img077 x4 (Enlargement after reduction)

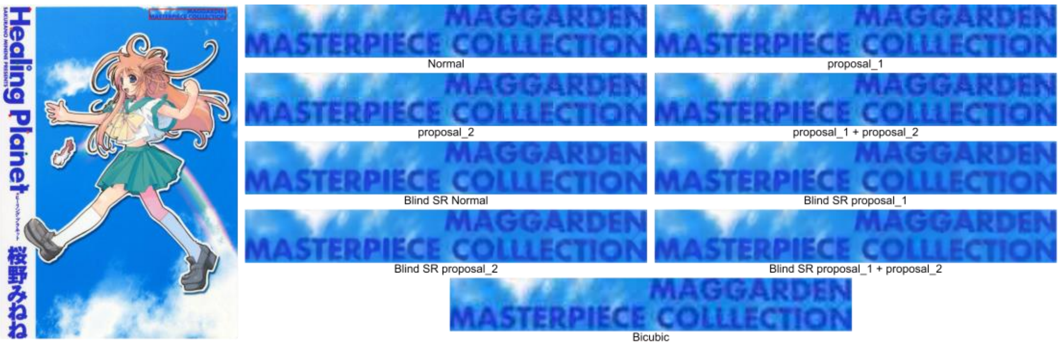

Fig2. Manga109 HealingPlanet x4 (Degraded image saved 10 times with jpeg quality 30)

5. Conclusion

In this study, the accuracy of image restoration was visually improved by sharpening the target image and by appropriate discriminator learning with filters. Since these modifications can be applied without significant changes to the learning method, it is believed that they can be easily applied to other methods. In the future, we are considering super-resolution techniques that take advantage of the frequency separation characteristics of the wavelet transform used to generate the sharpened image.

References

[1] Xintao Wang, Liangbin Xie, Chao Dong, Ying Shan: Real-ESRGAN: Training Real-World Blind Super-Resolution with Pure Synthetic Data, *arXiv:eess.IV*, 2021

[2] F, Cotter: Uses of Complex Wavelets in Deep Convolutional Neural Networks, https://doi.org/10.17863/CAM.53748, 2020

[3] Kiyoharu Aizawa, Azuma Fujimoto, Atsushi Otsubo, Toru Ogawa,Yusuke Matsui, Koki Tsubota, Hikaru Ikuta: Building a Manga Dataset ``Manga109" with Annotations for Multimedia Applications, *IEEE MultiMedia*, 27:2(2020), 8-18

[4] Richard Zhang, Philip Isola, Alexei A. Efros, Eli Shechtman, Oliver Wang: The Unreasonable Effectiveness of Deep Features as a Perceptual Metric, *arXiv:cs.CV*, 2018

A Study of Mask Face Recognition Method Based on Self-Supervised Learning

Jintaro KAWAI[1*] and Hiroyuki KAMATA[2]

[1]Graduate School of Science and Technology, Meiji University, Japan

[2]School of Science and Technology, Meiji University, Japan

*ce221022@meiji.ac.jp, kamata@meiji.ac.jp

Abstract. In this study, we propose a method to authenticate masked face images with higher accuracy even when a depth camera is not used. Prior research has proposed methods to improve robustness to the presence or absence of masks by re-training with a synthetic dataset of masks or by knowledge distillation. However, they have yet to achieve practical accuracy. A method for dealing with masked faces by applying self-supervised learning is proposed in this study. In the proposed method, the machine learning model is designed to treat "masked face" and "unmasked face" of the same person as more similar by applying self-supervised learning. By this method, we can improve the recognition accuracy for masked face images while maintaining the accuracy for normal face images.

Keywords: Face Recognition, masked/unmasked face, Deep Metric Learning

1. Introduction

Face recognition is becoming widely accepted in society because of its convenience. However, due to the spread of infectious diseases, people are wearing masks more than before. This has made it necessary to recognize masked faces, but it has been reported that face recognition models that do not use depth cameras have lower accuracy in recognizing masked faces [1]. Against this background, methods have been proposed that improve robustness to the presence or absence of masks without using a depth camera by retraining the model with face images in which masks are synthesized, or by using knowledge distillation to make the output result of the model when mask images are input closer to the output of normal face images [2, 3]. However, none of these methods have reached practical accuracy, and there are issues that need to be addressed to improve accuracy.

In this study, we propose a method based on self-supervised learning that improves robustness to the presence or absence of masks by treating the embedding vectors of images in which masks are combined with face images in the training data as pseudo labels. This allows the model to learn that masked and unmasked faces of the same person are more similar, thereby improving the recognition accuracy for masked faces.

2. Overview of face recognition

This section outlines the process of face recognition. Face recognition is the task of determining whether a person is identical to a single person to be matched. In practical face recognition, it is necessary to consider the property that the person one wishes to recognate does not appear in the training dataset of the machine learning model. Therefore, in practical face recognition, the following flow of recognition is used.

First, in the training phase, the feature extractor (deep neural network) is trained to output similar embedding vectors for the same person's face image. Specifically, supervised learning is performed on the training face photo data, mainly using ArcFace or its derivatives. After learning is complete, the person is registered in order to determine whom to authenticate. Registration can be accomplished by inputting the face image of the person to be authenticated into the learned feature extractor and acquiring the output embedding vector. When an unknown image is input in this state, the output embedding vector is compared with the previously stored vector to determine if it is the same person.

3. Expemiments

3.1. Proposed Method

In training the aforementioned feature extractor, we propose to apply self-supervised learning to incorporate the dissimilarity of the embedding vectors of masked face image and unmasked face image of the same person into the loss function. The loss function of the proposed method is defined as follows by adding the loss $Loss_{Adacos}$ by Adacos [4], which is the loss function used in existing face recognition, and the loss $Loss_{Mask}$ due to dissimilarity between embedding vectors multiplied by the weight λ are added and defined as follows:

$$Loss_{Total} = Loss_{Adacos} + \lambda \cdot Loss_{Mask} \tag{1}$$

The $Loss_{Adacos}$ is obtained by dissimilarity with the weights designed for each class. In that way, the training samples are trained to approach the weights of the corresponding class. The loss $Loss_{Mask}$ is calculated from the inner product of the embedding vectors as follows:

$$Loss_{Mask} = \frac{1}{N}\sum_{i=1}^{N}(1 - \boldsymbol{W}_{normal} \cdot \boldsymbol{W}_{mask}) \tag{2}$$

where $\boldsymbol{W}_{normal}$ is the L2-normalized embedding vector from the normal image, and $\boldsymbol{W}_{mask}$ is the L2-normalized embedding vector from the mask image.

By calculating the loss in this method, the machine learning model learns that masked and unmasked faces of the same person are more similar, with the aim of improving the robustness against the presence or absence of masks. A schematic diagram of the learning method using the above loss function is shown below in Fig 1.

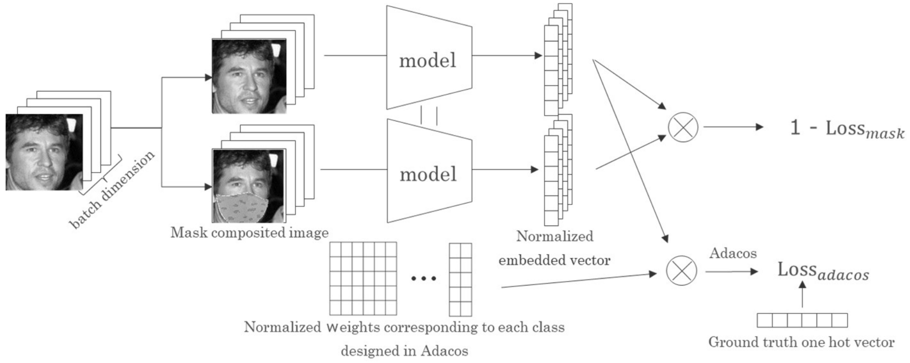

Fig 1. A schematic diagram of the learning method (face image taken from MS1M [5].)

In this study, ResNet50 is used as the model, MS1M[5] is used as the training data set, MaskTheFace[2] is used to synthesize masks during training, and 100 is set for λ in the above equation (1). For the conventional method, ResNet50 is compared with the proposed method by creating a model when retrained with a dataset of face images with synthesized masks and a model trained only with normal images.

3.2. Evaluation Method

We evaluate the performance of the model by asking it to judge whether two input images are of the same person or not. The test dataset consists of identical and non-identical pairs of images created from a dataset of celebrity face images. The datasets used are LFW, which consists of normal face images, MLFW[6], which is a composite of normal face images and masks, and MFR2[2], which contains face images in which masks are actually worn. For the evaluation by MFR2, we show not only the percentage of correct responses but also the histogram of the cosine similarity for each pair. Although most of the previous studies evaluated models by the percentage of correct responses to validation data, we adopted this approach because we believe that when operating models in the real world, models often cannot be trained with images of people to be recognized, and images of people in the test should not be involved in the learning process at all.

4. Results

Table 1 shows the results of a comparative evaluation of the accuracy(ACU) and threshold(TH) of the proposed and conventional methods, using the methods described in Section 3.2. The cosine similarity of the paired images in the MFR2 dataset is shown in Fig 2 as a blue histogram for same-person pairs and an orange histogram for non-same-person pairs.

Table 1. Recognition accuracy[%] for each dataset

	LFW		MLFW		MFR2	
	ACU	TH	ACU	TH	ACU	TH
Normal	99.67	0.306	79.85	0.268	91.05	0.189
Retraining	99.67	0.329	82.07	0.259	92.11	0.152
Proposal	**98.83**	**0.229**	**89.57**	**0.314**	**94.11**	**0.121**

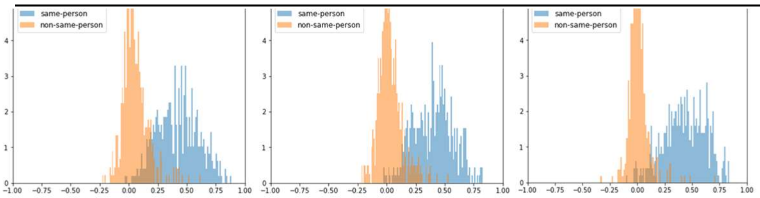

(a) Normal (b) Retraining (c) Proposal

Fig 2. Cosine similarity on the MFR2 dataset for each method

The results show that although the recognition accuracy for normal images is slightly lower than that of the conventional method, the proposed method is able to authenticate images with masks with high accuracy. Fig 2 shows that the proposed method tends to increase the cosine similarity of face image pairs for the same person compared to the conventional method.

5. Conclusion

Based on the results of this study, we have proposed a method for highly accurate recognition of masked faces by incorporating the dissimilarity of embedding vectors of "masked face images" and "unmasked face images" of the same person into the loss function. From the experimental results shown in Fig 2, it can be concluded that the reason for the improved accuracy is that the loss function can output similar embedding vectors for images of the same person, regardless of whether the image is masked or unmasked.

References

[1] NIST: NIST Launches Studies into Masks' Effect on Face Recognition Software, (2020), <https://www.nist.gov/news-events/news/2020/07/nist-launches-studies-masks-effect-face-recognition-software>

[2] Wang, Zhongyuan, et al: Masked face recognition dataset and application, *IEEE Transactions on Biometrics, Behavior, and Identity Science*, volume:5(2023), 298-304.

[3] Huber, Marco, et al: Mask-invariant face recognition through template-level knowledge distillation, *2021 16th IEEE International Conference on Automatic Face and Gesture Recognition*, (2021), 1-8.

[4] Xiao Zhang, Rui Zhao, Yu Qiao, Xiaogang Wang, Hongsheng Li: Adacos: Adaptively scaling cosine logits for effectively learning deep face representations, *Proceedings of the IEEE/CVF Conference on Computer Vision and Pattern Recognition*, (2019), 10823-10832.

[5] Yandong Guo, Lei Zhang, Yuxiao Hu, Xiaodong He, Jianfeng Gao. Ms-celeb-1m: A dataset and benchmark for large-scale face recognition, *ECCV*, volume:9907(2016), 87-102

[6] Wang, C., Fang, H., Zhong, Y., Deng, W: Mlfw: A database for face recognition on masked faces, *Chinese Conference on Biometric Recognition*, Beijing, (2022), 180-188.

Development of a gyrokinetic simulation model toward whole-volume modeling of stellarators

Toseo Moritaka[1*], Robert Hager[2], Seung-Hoe Ku[2], C-S. Chang[2] and Suguru Masuzaki[3]

[1] Plasma Quantum Processes Unit, National Institute for Fusion Science, Gifu, Japan
[2]Princeton Plasma Physics Laboratory, New Jersey, United States
[3]Plasma Multi-phase Matter System, National Institute for Fusion Science, Gifu, Japan

* `moritaka.toseo@nifs.ac.jp`

Abstract. Numerical modeling of plasma transport phenomena in the edge region of magnetic confinement devices is challenging because of the complicated magnetic field structures and various interactions among plasmas, neutrals, and material walls. We are developing novel numerical schemes to realize whole-volume gyrokinetic modeling of stellarators that cover the edge region as well as the core region. The schemes include unstructured mesh generation optimized for the edge magnetic fields, particle-mesh interpolation, and a Poisson solver compatible with the optimized mesh. We are applying these schemes to investigate charged particle motion and divertor particle load under the influence of electrostatic fields around or outside the outermost flux surface in the core region.

Keywords: Gyrokinetic model, Mesh generation, Poisson solver, Particle-in-cell scheme, Magnetic confinement fusion

1. Introduction

The gyrokinetic model is commonly used to demonstrate plasma transport phenomena under self-consistent electrostatic (or electromagnetic) perturbations in global confinement magnetic fields. Since this model separates plasma dynamics into parallel and perpendicular directions relative to the confinement magnetic field, we should properly handle the magnetic field structure in numerical simulations employing the gyrokinetic model. While the gyrokinetic core transport simulations often refer to the magnetic flux coordinates, X-point Gyrokinetic Code (XGC) employs an unstructured mesh and particle-in-cell method to include the edge region of tokamaks where such coordinates are not defined[1]. Recently, the non-axisymmetric version of XGC, namely XGC-S, has been used for linear and non-linear simulations in the core regions of stellarators[2,3,4]. However, extending the gyrokinetic model to the edge regions of stellarators remains challenging due to their complex magnetic field structures.

2. Numerical schemes

The complexity of the magnetic field in stellarators comes not only from the non-axisymmetry but also from the entangled magnetic field lines outside the core region and the helical / island configurations around the divertors. The magnetic flux function can not apply to the entangled magnetic field lines. In addition, the magnetic field lines divert significantly from the torus direction in the helical divertor configuration. Therefore conventional unstructured mesh defined by the flux function on toroidal cross section is not applicable to the edge region of stellarators.

We have developed novel computational schemes for optimizing the spatial mesh to calculate the electrostatic field in the edge region of stellarators[5]. The scheme includes curved surface generation and unstructured mesh generation on the resulting curved surface. The curved surface is generated using a numerical optimization technique to ensure it is locally perpendicular to the confinement magnetic field. This surface effectively solves the gyrokinetic Poisson equation with the perpendicular gradient operator. The unstructured mesh is generated by numerical field line tracing, where crossing points between the curved surfaces and magnetic field lines define mesh vertices. The optimized mesh adaptively refines the crucial regions with magnetic field lines with long connection lengths that connect the closed flux surfaces and the divertors. Field-following interpolation with crossing detection to the curved surface is employed to use the optimized mesh in the particle-in-cell scheme.

The iterative matrix solver using the biconjugate gradient stabilized method is improved to calculate electrostatic fields using the optimized mesh. The geometric multigrid preconditioner uses the hierarchical mesh structure to accelerate the conversion. The Jacobian matrix computed at each mesh vertex is considered to solve the gyrokinetic Poisson equation on the curved surfaces.

3. Application

These numerical schemes, which are being integrated into XGC-S, are first applied to calculate the electrostatic field in the edge region of the Large Helical Device (LHD). In the core region, the global electric field in the radial direction results in the poloidal plasma rotation through the ExB drift motion. Similarly, the electric field in the edge region may generate specific plasma flow around the divertor region. The present simulation model could discuss how the electrostatic field influences the qualitative properties of particle load on the divertors[6] through the ExB and other drift motions.

References

[1] S. Ku, C-S. Chang, R. Hager, *et al.*, Physics of Plasmas **25**, 056107 (2018).

[2] T. Moritaka R. Hager, M. Cole, *et al.*, Plasma **2**, 179 (2019).

[3] M. Cole, R. Hager, T. Moritaka, *et al.*, Physics of Plasmas **26**, 082501 (2019).

[4] T. Moritaka, H. Sugama, M. Cole, *et al.*, Nuclear Fusion **62**, 126059 (2022).

[5] T. Moritaka, M. Cole, R. Hager, *et al.*, Plasma and Fusion Research **16**, 2403054 (2021).

[6] S. Masuzaki, H. Tanaka, M. Kobayashi, *et al.*, Nuclear Materials and Energy **18**, 281 (2019).

Development of Digital Twin Radiation Visualization System

Seiki Saito[1*], Nao Shibata[1], Shigekazu Suzuki[2], Eiji Takada[3]

[1] Yamagata University, Yonezawa, Japan
[2] National Institute of Technology, Fukushima College, Iwaki, Japan
[3] National Institute of Technology, Toyama College, Toyama, Japan

*saitos@yz.yamagata-u.ac.jp

Abstract. This research aims to develop a visualization system for radiation using a digital twin. Currently, radiation measurement instruments only provide localized measurements and lack information about the overall radiation dose distribution in the surrounding space. By constructing a digital twin system, it becomes possible to estimate radiation doses in locations that are not directly measured. In this paper, a framework consisting of three steps is proposed to realize this system: (1) predicting the position of the radiation source using machine learning based on pre-measured dose information, (2) simulating the trajectory of radiation based on the predicted source position, and (3) displaying the simulated radiation trajectory on the HoloLens2, a mixed reality device.

Keywords: Radiation, Digital twin, Monte Carlo simulation, Mixed reality

1. Introduction

Since the accident at the Fukushima Daiichi Nuclear Power Plant, interest in radiation measurement has increased. Radiation is something that cannot be sensed by the five senses. Therefore, it is necessary to measure radiation using measuring instruments, but these instruments are limited to "zero-dimensional measurement," which indicates the radiation dose only at the spot where the instrument is placed, and does not actually provide the total radiation dose distribution in the surrounding space.

A technology that reproduces data in real space on a digital space as if it were its twin is called a digital twin. In this study, we aim to realize a visualization system for radiation utilizing the digital twin. Once the digital twin is realized, real doses in places where no dosimeter is placed can be estimated on a virtual simulation space. As a result, for example, the amount of radiation exposure can be estimated before a worker moves to a new location.

Figure 1(a) shows a radiation shielding experiment and Figure 1(b) shows a simulation space in which the experimental system is reproduced on a computer. In the actual experiment, only the dose at the location where the instrument is placed can be measured. However, if the radiation emitted from the source is simulated, the doses at all calculated locations can be determined. By reflecting the real experimental system in the simulation in real time, we aim to construct a system that can estimate the dose at that instant in a location not actually measured.

In this study, as a first step to realize the proposed system, we contract a framework of following three steps: (1) prediction of radiation source position using machine learning based on pre-measured dose information; (2) Simulation of the trajectory of radiation based on the predicted source position; (3) Displaying the simulated trajectory of radiation on a MR device HoloLens2 [1].

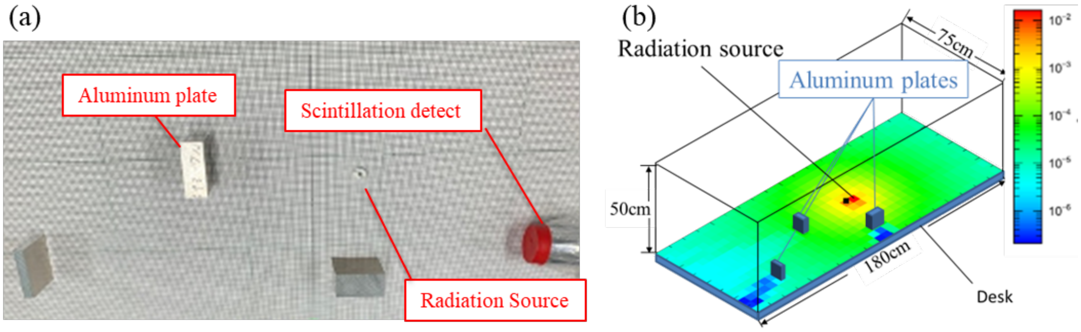

Fig. 1 (a) Radiation shielding experiment actually performed on the desk in the laboratory. (b) Simulation space simulating the experiment.

2. Measurement of Radiation Dose with Positional Data

In order to predict the position of the radiation source, the dose is actually measured at several points in advance. Figure 2 shows the measurement system. A Cs-137 γ-ray source (10 kBq) was used as the radiation source. The radiation source is placed on a desk with an aluminum shield. The dose is measured at several points in the space. A scintillation detector (Canberra NaI (Tl) 802-3x3) and a multi-channel analyzer (Canberra OSPREY-PKG) are used for the measurement. In the obtained energy spectrum, the spectrum in the range of 662 keV±60 keV is integrated. Then, the dose was calculated by subtracting the background value in the range. A VIVE Tracker is placed on the detector to simultaneously measure the position of the scintillation detector. The coordinates $(x^{\mathrm{mes}}, y^{\mathrm{mes}}, z^{\mathrm{mes}})$ of the detector tip are calculated from the detected posture and position information of the VIVE Tracker. Then, a pair of measured doses e^{mes} and position coordinates $\boldsymbol{\gamma}^{\mathrm{mes}} = (x^{\mathrm{mes}}, y^{\mathrm{mes}}, z^{\mathrm{mes}}, e^{\mathrm{mes}})$ are obtained.

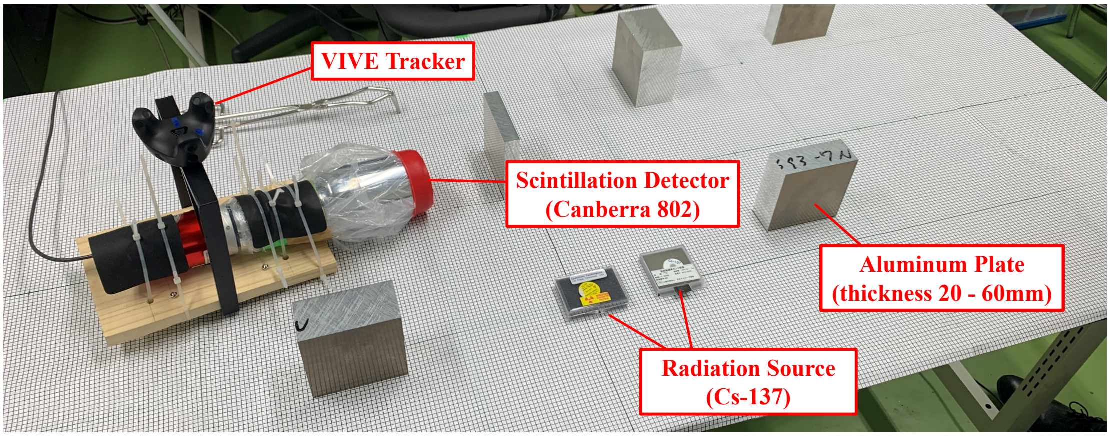

Fig. 2 Measurement system.

3. Machine Learning for Prediction of Position of Radiation Source

A vector $\boldsymbol{\Gamma} = (x, y, z, \varphi)$ that summarizes the position coordinates (x, y, z) of the detector and the radiation particle flux φ at that position is defined. Construct a machine learning model that inputs $\boldsymbol{\Gamma}$ values $\boldsymbol{\Gamma}_1, \boldsymbol{\Gamma}_2, \boldsymbol{\Gamma}_3$ at three coordinate points and outputs radiation source position coordinates (x_o, y_o, z_o). Figure 3 shows the network configuration of the model. There are three hidden layers of 50 nodes, 25 nodes and 10 nodes, respectively. All layers are fully connected. The ReLU function is used as the activation function of the hidden layers, and the linear function is used as the activation function of the output layer.

Training data is generated by PHITS code [2, 3]. Shields are placed in the same position as when the real measurement was performed. One radiation source is placed in a random position. Radiation particle flux φ is calculated at three randomly specified coordinates. The three points and the fluxes are paired with the radiation source position and used as training data.

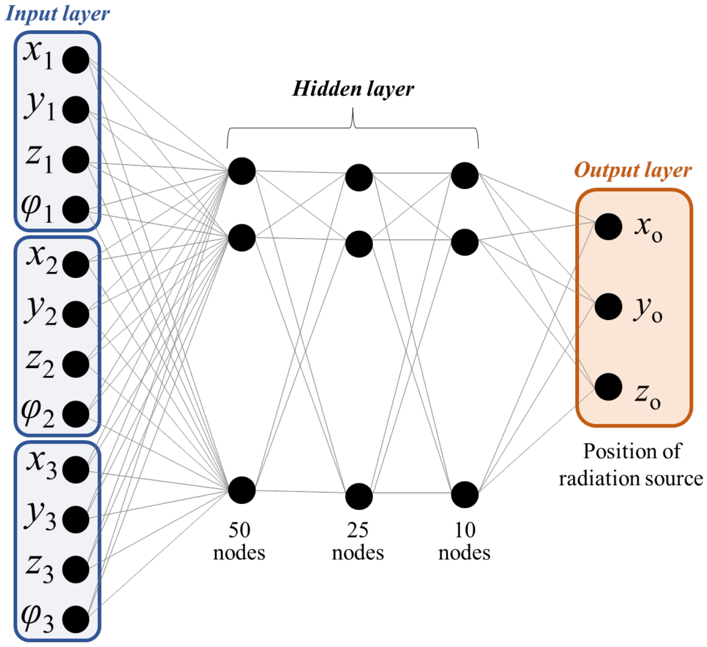

Fig. 3 Network configulation for prediction of position of radiation source.

4. Prediction Results and Visualization

The position of radiation source is predicted by inputting the measured values $\boldsymbol{\Gamma}^{\mathrm{mes}}{}_1$, $\boldsymbol{\Gamma}^{\mathrm{mes}}{}_2$, $\boldsymbol{\Gamma}^{\mathrm{mes}}{}_3$ at the three coordinate points obtained by the measurement described in chapter 2 into the machine learning model constructed in chapter 3. By comparing the measured value e^{mes} with the calculated value φ, the actually measured dose e^{mes} is converted to the radiation particle flux φ before the input. Figure 4(a) shows a photo of actual measurement, and Figure 4(b) shows the result of prediction by the machine learning model. The position can be predicted within the range of a few centimeters of error.

The trajectory of the radiation emitted from the predicted source location is calculated using the PHITS code and displayed on the HoloLens 2. At this time, information on the shielding is scanned by a LiDAR scanner. Figure 5 shows an example of the display. The radiation trajectory is successfully displayed as a red line.

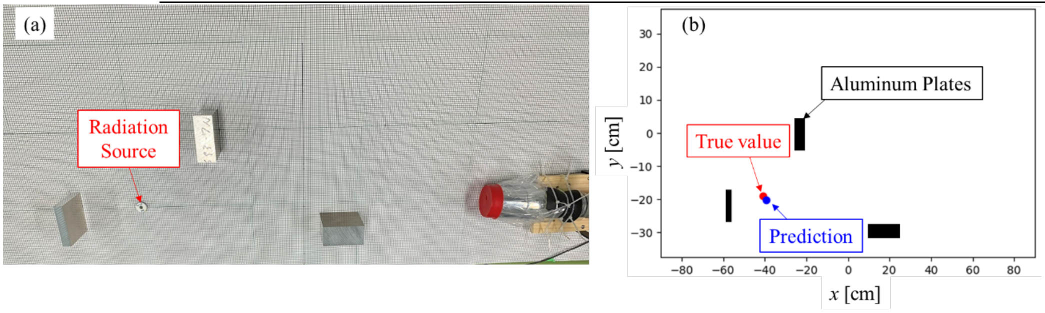

Fig. 4 (a) Photo of actual measurement.
(b) Result of prediction by the machine learning model.

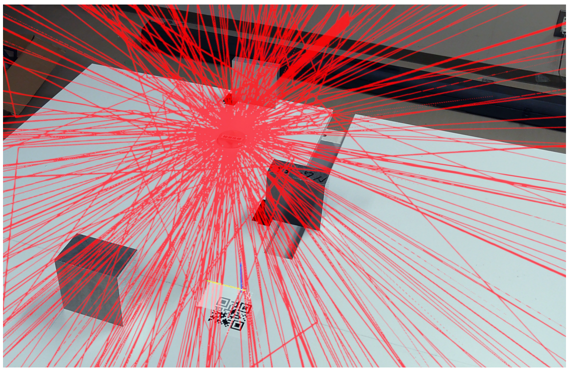

Fig. 5 Example of radiation trajectory display on HoloLens 2.

Acknowledgment

We would like to thank the students of Yamaga University, especially Mr. T. Kakizaki, who was involved in this research as part of his graduation research project. The research was partially supported by Grant-in-Aid for Scientific Research No. 22K03572 from the Japan Society for the Promotion of Science, and by the NIFS Collaborative Research Program NIFS22KIGS002 and NIFS22KISS021. The computations were performed using the JFRS-1 supercomputer system at Computational Simulation Centre of International Fusion En-ergy Research Centre (IFERC-CSC) in Rokkasho Fusion Institute of QST (Aomori, Japan), and Plasma Simulator of NIFS (Toki, Gifu, Japan) .

References

[1] M. Iida, S. Kudo, R. Kawahara, K. Yamaguchi, and S. Saito: *Development of visualization system for radiation by mixed reality technology*, Proc. 40th JSST, pp. 29-31 (2021).

[2] S. Saito and H. Nakamura: *Neutron transmittance on bubble formed tungsten material*, Proc. 38th JSST, pp. 62-64 (2019).

[3] T. Sato, Y. Iwamoto, S. Hashimoto, T. Ogawa, T. Furuta, S. Abe, T. Kai, P. E. Tsai, N. Matsuda, H. Iwase, N. Shigyo, L. Sihver, K. Niita: *Features of Particle and Heavy Ion Transport code System (PHITS) version 3.02*, J. Nucl. Sci. Technol. vol. 55:5-6, pp. 684-690 (2018).

Prediction of recycling hydrogen energy distribution by machine learning based on molecular dynamics simulation

Masato Iida [1], Seiki Saito [1*], Hiroaki Nakamura [2, 3], Keiji Sawada [4], Kazuo Hoshino[5], Masahiro Kobayashi [2, 6], Masahiro Hasuo [7]

[1] Department of Information and Electronics, Graduate school of Science and Engineering, Yamagata University

[2] Department of Research, National Institude for Fusion Science

[3] Department of Electrical Engineering, Graduate School of Engineering, Nagoya University

[4] Department of Material System Engineering, Faculty of Engineering, Shinsyu University

[5] Department of Applied Physics and Physico-Informatics, Fuculty of Science and Technology, Keio University

[6] Department of Fusion Science, Physical Sciences Research Section, The Graduate University for Adcanced Studies

[7] Department of Mechanical Engineering and Science, Graduate School of Engineering, Kyoto University

`*saitos@yz.yamagata-u.ac.jp`

Abstract. In fusion power generation, helium in the plasma is removed by the divertor because it reduces power generation efficiency. The hydrogen ions that contact the divertor are neutralized and return to the plasma as hydrogen atoms and molecules. This process is called recycling. To understand the behavior of recycling hydrogen, it is important to understand the energy of recycling hydrogen. Therefore, we developed a machine learning model to predict the energy distribution of emitted hydrogen from the divertor in this study. The energy distribution of emitted hydrogen is prepared using molecular dynamics (MD) simulations, and the obtained distribution data is used as the teacher data for machine learning.

Keywords: Molecular dynamics simulation, Machine learning, Carbon divertor

1. Introduction

In fusion power generation, the helium produced by the nuclear fusion must be removed because it reduced the efficiency of power generation. The way to remove it is to transport the plasma using magnetic line and contacts the divertor. When the plasma contact the divertor, the hydrogen in the plasma may return to the plasma as neutral hydrogen. This process is called recycling. The effect of the recycling hydrogen on the plasma is related to the energy of the emitted hydrogen from the divertor. In this study, machine learning is used to understand the energy of emitted hydrogen. Firstly, several MD simulations [1-4] of a hydrogen atom incident on the carbon wall calculate the energy of emitted hydrogen, and obtain the energy distribution of emitted hydrogen. Secondly, machine learning model are developed to predict the energy distribution of the emitted hydroten using the obtained distribution as the teacher data. The machine learning model is a simple network consisting of only fully connected neural network.

2. Simulation Model

A carbon amorphous structure consisting of carbon atoms and hydrogen atoms is prepared for the target material. Figure 1 shows the target material. The cyan dots are carbon atoms and the white dots are hydrogen atoms in Figure 1. The size of target is 40 Å ×40 Å ×30 Å. Brenner's

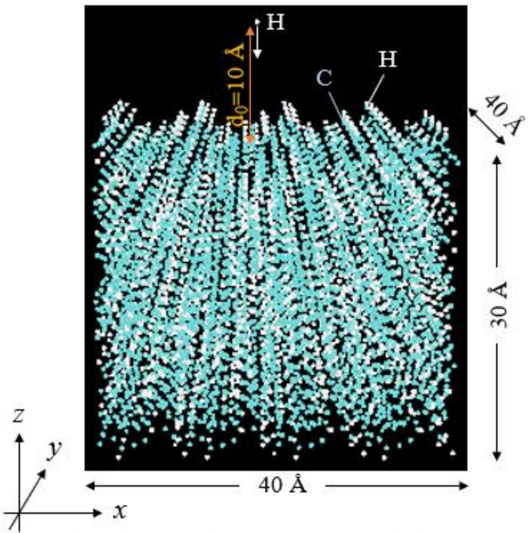

Fig. 1: Carbon target material

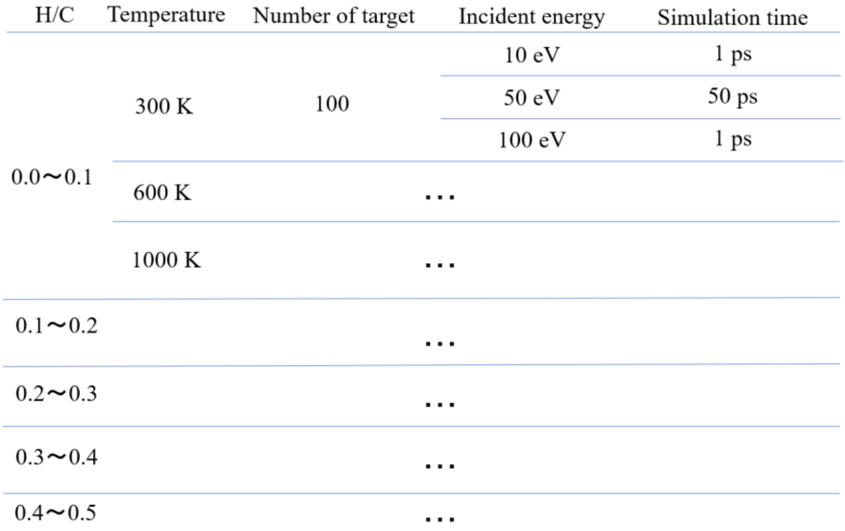

H/C	Temperature	Number of target	Incident energy	Simulation time
0.0〜0.1	300 K	100	10 eV	1 ps
			50 eV	50 ps
			100 eV	1 ps
	600 K		…	
	1000 K		…	
0.1〜0.2			…	
0.2〜0.3			…	
0.3〜0.4			…	
0.4〜0.5			…	

Table 1: Simulation parameters

potential [5] is used for interatomic potential between carbon and hydrogen atoms. One hydrogen atom is injected to the target. The incident angle is set to parallel to z-axis. The position of incidence is random. The parameters of this simulation are varied as shown in Table 1. In total, 45 patterns are calculated. The number of simulations is 1500 for each pattern. The simulation time is set to 1 ps when incident energies are 10 and 100 eV. The simulation time is set to 50 ps when incident energy is 50 eV.

3. Machine Learning Model

The predictions of the energy distribution for emitted atoms and molecules are obtained by machine learning the MD simulation results. The reason for using machine learning is the high calculation cost of MD simulation. For this machine learning, Fully connected neural network are used for prediction. Using H/C, temperature, and incident energy as inputs for machine learning, the translational energy, rotational state and vibrational state distribution of emitted hydrogen are predicted. Emitted hydrogen within 1 ps is predicted with 90 training data and 45 test data. Emitted hydrogen after 1 ps is predicted with 45 training data and 15 test data.

4. Results

The results of machine learning are shown in Figure 2. Figure 2 (a) and (b) are predictions of the energy distributions for emitted atoms and molecules within 1 ps. Figure 2 (c) and (d) are predictions of the energy distributions for emitted molecules after 1 ps. The orange line is the distribution obtained from the simulation and the blue line is the predicted distribution. In this study, simulation results including temperature as a parameter could be predicted by machine learning.

Acknowledgment

The research was partially supported by Grant-in-Aid for Scientific Research, No.22K03572, No.22K18272 and No.23K03362 from the Japan Society for the Promotion of Science, and by the NIFS Collaborative Research Program NIFS20KUTR158, NIFS22KISS021 and NIFS22KIGS002. The computations were performed using the JFRS-1 supercomputer system at Computational Simulation Centre of International Fusion Energy Research Centre (IFERC-CSC) in Rokkasho Fusion Institute of QST (Aomori, Japan), Research Center for Computational Science (Okazaki, Aichi, Japan) and Plasma Simulator of NIFS (Toki, Gifu, Japan) . The ExCELLS Special Collaboration Program of Exploratory Research Center on Life and Living Systems. The NINS program of Promoting Research by Networking among Institutions.

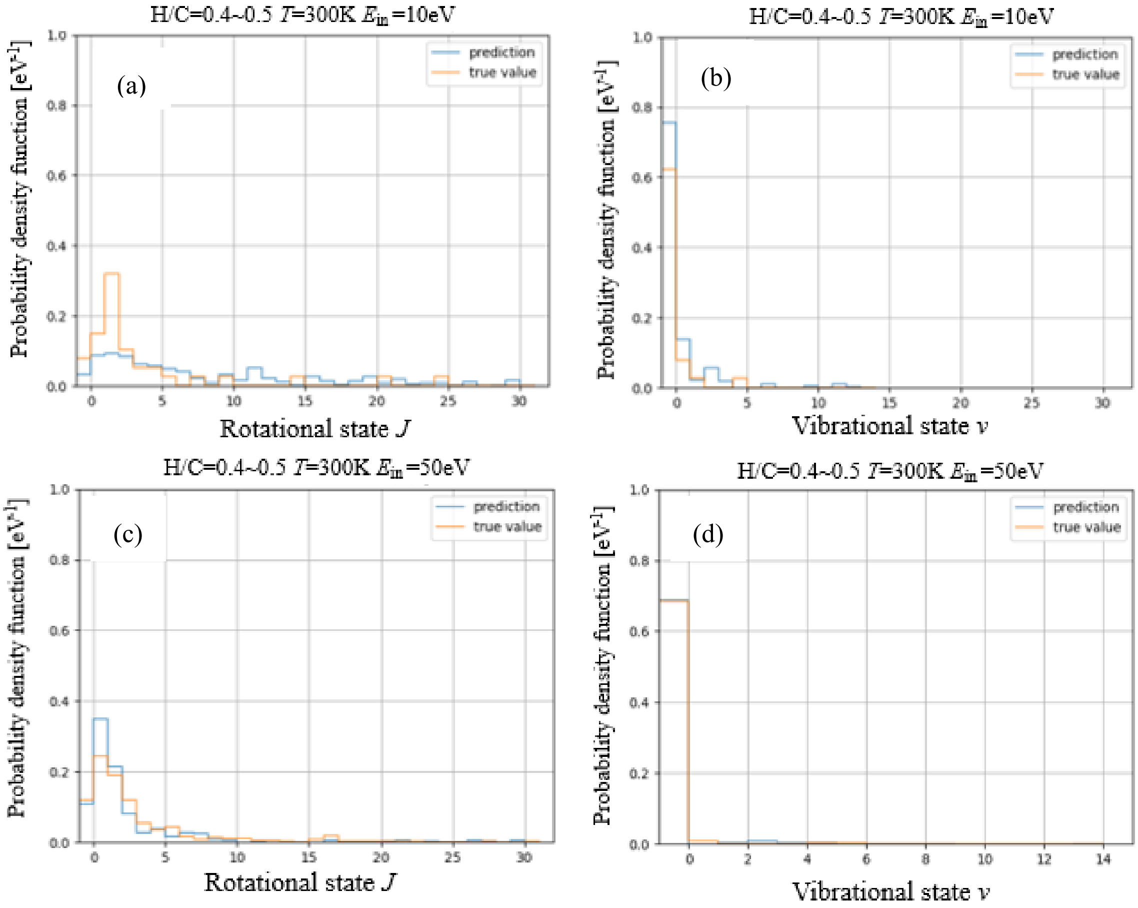

Fig. 2: (a) Prediction of rotational state for emitted molecules within 1 ps

(b) Prediction of vibrational state for emitted molecules within 1 ps

(c) Prediction of rotational state for emitted molecules after 1 ps

(d) Prediction of vibrational state for emitted molecules after 1 ps

References

[1] S. Saito, H. Nakamura, K. Sawada, G. Kawamura, M. Kobayashi, M. Hasuo. Molecular dynamics simulation model of hydrogen recycling on carbon divertor for neutral transport analysis in large helical device. Contributions to Plasma Physics. 2020; e201900152.

[2] K. Sawada, H. Nakamura, S. Saito, G. Kawamura, M. Kobayashi, K. Haga, T. Sawada, and M. Hasuo, Contrib. Plasma Phys. e201900153 (2020).

[3] S. Saito, H. Nakamura, K. Sawada, G. Kawamura, M. Kobayashi, and M. Hasuo, Plasma Fusion Res. **15**, 2403073 (2020).

[4] S. Saito, H. Nakamura, K. Sawada, M. Kobayashi, G. Kawamura, T. Sawada, and H. Masahiro: *Molecular dynamics simulation for hydrogen recycling on tungsten divertor for neutral transport analysis,* Jpn. J. Appl. Phys. **60** SAAB08 (2021).

[5] D. W. Brenner, O. A. Shenderova, J. A. Harrison, S. J. Stuart, B. Ni and S. B. Sinnott: J. Phys. Condens. Matter **14** (2002) 783.

Deep nural network modeling based on capacity computing of Eulerian elasto-plastic simulation

Issei Toida[1,*], Shoki Mori[2], Koji Nishiguchi[1], Tokimasa Shimada[2], Makoto Tsubokura[2], Hiroya Hoshiba[1], Junji Kato[1]

[1]Department of Civil Engineering, Graduate School of Engineering, Nagoya University
[2]Department of Computational Science, Graduate School of System Informatics, Kobe University

* `pv.46c.5138@s.thers.ac.jp`

Abstract. This study uses an Eulerian method and generates training data through massively parallel simulations of elastoplastic dynamics. Based on this training data, we construct a deep-learning model using Convolutional Neural Network (CNN) and verify the accuracy of predicting strain energy in the Taylor bar impact test. We set three different numbers of training data patterns and compare the prediction accuracy to investigate the effect of the number of training data on the prediction accuracy.

Keywords: Eulerian method, Elasto-plastic analysis, Convolutional Neural Network(CNN)

1. Introduction

In the automotive industry, evaluating the collision performance of vehicles is one of the necessary evaluation metrics for assessing the safety of the vehicle. Numerical simulation-based collision analysis is commonly used as the evaluation method. Especially in the upstream design process, it is essential to achieve collaborative design among designers, marketers, and Computer-Aided Engineering (CAE) technicians. Therefore, there is a need for a method that can predict collision performance in real-time with decision-making capability and high computational accuracy.

In this study, we utilize an Eulerian structural analysis method[1] that enables fast and automatic mesh generation to generate a dataset of elasto-plastic analysis results for various structural shapes. We then construct a surrogate model using deep neural networks. As a basic validation, we use the constructed model to predict the strain energy generated during the collision analysis of a rectangular solid with an elliptical hole. Furthermore, we perform accuracy verification to validate the validity and effectiveness of the model built in this study.

2. Numerical method

In this study, we assumed the solid material used in the analysis to be a compressible elastoplastic material, and decomposed the elastoplastic material into elastic deformation component and plastic deformation component through the multiplicative decomposition of the deformation gradient tensor. The yield function was evaluated using the Mises stress-based yield criterion, and the hardening law was assumed to be a linear isotropic hardening law. Additionally, the strain energy, which serves as an indicator of collision absorption energy, was defined as the sum of the strain energy in the elastic component and the strain energy in the plastic component at time t.

In deep learning models, a cuboid image is used as the input variable, and the output value is set as the strain energy. Sigmoid and ReLU activation functions are used in each neuron, and the Adam optimization[3] algorithm is employed for updating the biases and weights. Stochastic Gradient Descent (SGD) is used as the loss function for updating the biases and weights, and the gradients of the loss function are derived using backpropagation[7].

3. Numerical examples

In this study, as a preliminary validation, the two-dimensional Taylor impact test is considered, involving a rectangular elastoplastic solid with an elliptical hole, as shown in Figure 1. The solid is impacted on its lower surface with an initial velocity v = 300 m/s within a computational domain of 2m × 2m.

In this study, as a preliminary validation, two-dimensional image data is used as the input variable. The input images are represented by (128x128) pixel data, as shown in Figure 2.

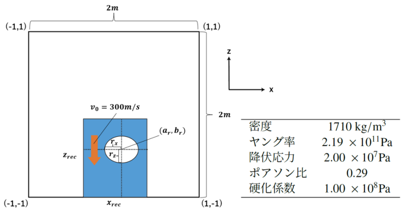

密度	1710 kg/m^3
ヤング率	2.19 × 10^{11}Pa
降伏応力	2.00 × 10^{7}Pa
ポアソン比	0.29
硬化係数	1.00 × 10^{8}Pa

Figure 1: Solid shape, computational domain, and material properties.

Figure 2: Example of input image.

Figure 3 presents the results of accuracy comparison validation, showing the average absolute percentage error (MAPE) and root mean square percentage error (RMSPE) for each training data size. It is important to note that the accuracy validation depicted in Figure 3 utilizes test data. From this figure, it can be observed that when the training data size reaches 3800 cases, the model achieves an MAPE of approximately 4% and an RMSPE of approximately 7%. This indicates that the model can make predictions with a reasonable level of accuracy. Furthermore, it is evident that the prediction accuracy improves as the training data size increases. On the other hand, it can be observed that regardless of the training data size, the RMSPE values are generally higher than the MAPE values. Additionally, it is evident that the prediction accuracy remains unchanged when the training data size exceeds

1500 cases compared to when it is 100 cases. This suggests that increasing the training data alone does not lead to an improvement in prediction accuracy.

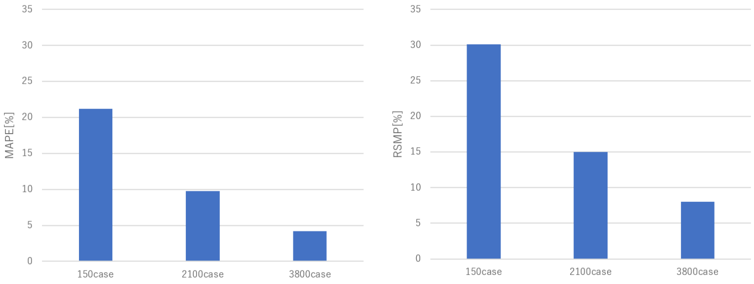

Figure 3: MAPE with different training data sizes.

This can be attributed to the fact that RMSPE is more susceptible to the influence of outlier data, which tends to have larger errors between the test data results and the predictions of the surrogate model, compared to MSPE. It can be inferred that there are a certain number of outlier test data points present in each training data size.

Therefore, in this study, to verify the existence of outliers, scatter plots of test data are created for each training data size. The x-axis represents the output values from the Eulerian structural analysis method, while the y-axis represents the predicted values from the surrogate model.

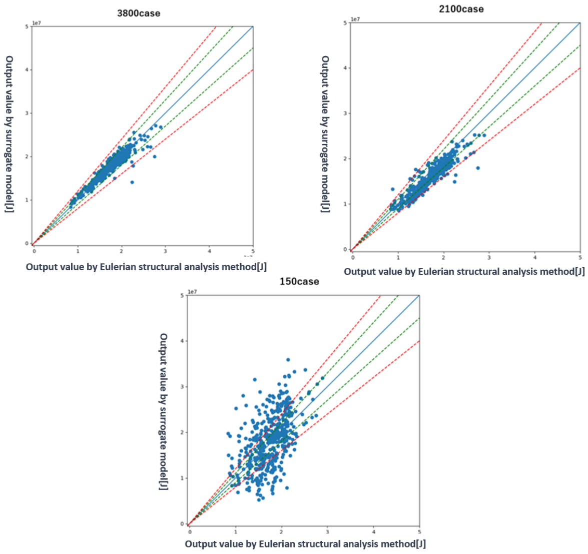

Figure 4: Comparison of scatter plots for different training data sizes and test data.

From Figure 4, it can be observed that a certain number of outliers exist in the test data for all training data sizes. Furthermore, comparing the test data at output values of the Eulerian structural analysis method ranging from 1×10^7[J] to 2×10^7[J], it can be seen that test data above 2×10^7[J] generally exhibit lower prediction accuracy and outliers that deviate from the center.

4. Conclusion

In this study, the Eulerian structural analysis method was utilized to generate training data, and a deeplearning model using CNN was constructed to predict strain energy in the context of the Taylor bar impact test involving a rectangular solid with an elliptical hole. Accuracy validation was performed using test data to investigate the validity and effectiveness of the constructed model.

Future challenges include increasing the training data that is susceptible to the influence of outliers, such as cases with low-positioned elliptical holes. Additionally, it is possible to generate three-dimensional training data as point cloud data, which requires less memory than the pixel data used in this study, to predict strain energy.

References

[1] Benson DJ. COMPUTATIONAL METHODS IN LAGRANGIAN AND EULERIAN HYDROCODES. *Computer Methods in Applied Mechanics and Engineering*. **99**(2-3), pp.235–394, 1992.

[2] Nishiguchi K, Bale R, Okazawa S, Tsubokura M. Full Eulerian deformable solid-fluid interaction scheme based on building-cube method for large-scale parallel computing. *International Journal for Numerical Methods in Engineering*, **117**(2), pp.221–248, 2019.

[3] D.P. Kingma, J. Ba, Adam: A method for stochastic optimization. *arXiv preprint arXiv*. 1412.6980 ,2014

[4] Shimada, T., Nishiguchi, K., Bale, R., Okazawa, S., Tsubokura, M. Eulerian finite volume formulation using Lagrangian marker particles for incompressible fluid–structure interaction problems. *International Journal for Numerical Methods in Engineering*, **123**(5), pp.1294–1328, 2022.

[5] Nishiguchi K, Okazawa S, Tsubokura M. Multimaterial Eulerian finite element formulation for pressure-sensitive adhesives. *International Journal for Numerical Methods in Engineering*, **114**(13), pp.1368–1388, 2018.

[6] WYDER, Philippe M.; LIPSON, Hod. Visual design intuition: predicting dynamic properties of beams from raw cross-section images. Journal of the Royal Society Interface, 2021, 18.184: 20210571

[7] .E. Rumelhart, G.E. Hinton, R.J. Williams, *Learning internal representations by error propagation*, California Univ San Diego La Jolla Inst for Cognitive Science, 1985

Massively Parallel Topology Optimization of Transient Flow Using Building-Cube Method

Ryohei Katsumata[1,*], Koji Nishiguchi[1], Hiroya Hoshiba[1], Junji Kato[1]

[1]Department of Civil Engineering, Graduate School of Engineering, Nagoya University

*`katsumata.ryohei.a3@s.mail.nagoya-u.ac.jp`

Abstract. Recently, topology optimization methods have been adopted not only for structural problems but also for fluid flow problems. Topology optimization for transient flows requires a fine mesh, especially for high Reynolds number flows, which is computationally expensive. Therefore, we propose a transient flow topology optimization method based on the building-cube method (BCM), which is suitable for massively parallel computing. The transient Navier-Stokes equations in the topology optimization procedure are solved by finite volume method, and the sensitivity of the objective function is obtained by sensitivity analysis based on the continuous adjoint method.

Keywords: Topology optimization, Transient flow, Finite volume method, Parallel computing

1. Introduction

Topology optimization is one of the methods to generate an optimal design based on mathematical theory and is the optimization method that allows the most significant degree of freedom. Originally developed for solid mechanics problems, topology optimization has recently been extended to various physical phenomena such as fluids, heat conduction, electromagnetism, and acoustics. Topology optimization of fluid flow problems has been extended from topology optimization for steady Stokes flows [1] to that for steady Navier-Stokes flows. In these fluid topology optimization studies, steady-state conditions are assumed.

In contrast, Deng et al. [2] and Kreissl et al. [3] have proposed topology optimization methods for transient flows. Since topology optimization for such transient flows requires a large computational cost compared to steady-state flows, the mesh resolution is limited to about 500,000 at most in the previous study [4], limiting the number of transient flow problems that can be handled. Therefore, to perform topology optimization for a wider range of transient fluid flow problems, a method suitable for large-scale computations, i.e., a numerical method with high parallel efficiency, is needed.

On the other hand, recent improvements in parallel computer performance have made it possible to perform parallel computations using high-resolution computational meshes. The building-cube method (BCM), a hierarchical Cartesian mesh method, has been proposed [5] as an effective method for such large-scale computations. The BCM has attracted much attention in recent years for simulations of Navier-Stokes flows and coupled fluid-solid interaction problems [6] because of its high parallel efficiency and ease of generating meshes with complex geometries by local subdivision of the mesh.

Based on the above background, we propose transient flow topology optimization using the BCM, which is suitable for massively parallel computations. The transient Navier-Stokes equations for topology optimization are discretized by a cell-centered finite volume method based on the BCM. The sensitivity of the objective function is obtained by a sensitivity analysis based on the continuous adjoint method.

2. Governing equations

In the computational domain Ω, the flow velocity, pressure, and body force at position $\boldsymbol{x} \in \Omega$ and time $t \in [0, T]$ are $\boldsymbol{u}$, p, and $\boldsymbol{f}$, respectively. The governing equations for transient incompressible flow, the equations of motion (Navier-Stokes equations) and the continuity equation can be expressed as follows

$$\rho \frac{\partial \boldsymbol{u}}{\partial t} + \rho (\boldsymbol{u} \cdot \nabla) \boldsymbol{u} = -\nabla p + \mu \nabla \cdot \left(\nabla \boldsymbol{u} + \nabla \boldsymbol{u}^\top \right) + \boldsymbol{f} \,, \quad \text{in } \Omega \times [0, T] \tag{1}$$

$$-\nabla \cdot \boldsymbol{u} = 0 \,, \quad \text{in } \Omega \times [0, T] \tag{2}$$

where ρ is the mass density and μ is the viscosity. The following initial conditions are given for the flow velocity.

$$\boldsymbol{u}(\boldsymbol{x}, 0) = \boldsymbol{u}_0(\boldsymbol{x}) \,, \quad \text{in } \Omega \tag{3}$$

In addition, the following boundary conditions are given on the Dirichlet boundary Γ_D and the Neumann boundary Γ_D.

$$\boldsymbol{u}(\boldsymbol{x}, t) = \boldsymbol{u}_D(\boldsymbol{x}, t) \,, \quad \text{on } \Gamma_D \times [0, T] \tag{4}$$

$$\left[-p\boldsymbol{I} + \mu \left(\nabla \boldsymbol{u} + \nabla \boldsymbol{u}^\top \right) \right] \cdot \boldsymbol{n} = \boldsymbol{g}(\boldsymbol{x}, t) \,, \quad \text{on } \Gamma_N \times [0, T] \tag{5}$$

where $\boldsymbol{I}$ is the unit tensor and $\boldsymbol{n}$ is the outward unit normal vector at the boundary $\partial\Omega$.

In the solid domain, an artificial frictional force [1] is applied so that the flow velocity is $\mathbf{0}$.

$$\boldsymbol{f} = -\alpha \boldsymbol{u} \tag{6}$$

where α is a parameter that represents the impermeability assuming the solid is a porous medium, and is expressed by the following equation using the design variable $\gamma \in [0, 1]$.

$$\alpha(\gamma) = \alpha_{\min} + (\alpha_{\max} - \alpha_{\min}) \frac{q(1-\gamma)}{q+\gamma} \tag{7}$$

where $\alpha_{\min}$ and $\alpha_{\max}$ are the minimum and maximum values of α, respectively. $q \in \mathbb{R}^+$ is a parameter to ensure convexity in the interpolation function of α expressed in the equation (7).

3. Topology optimization problem

Using the above governing equations, the topology optimization problem for transient incompressible Navier-Stokes flow is formulated as follows

$$
\begin{aligned}
&\min J(\boldsymbol{u}, p; \gamma) \\
&\text{s.t.} \begin{cases}
\rho \dfrac{\partial \boldsymbol{u}}{\partial t} + \rho(\boldsymbol{u}\cdot\nabla)\boldsymbol{u} = -\nabla p + \mu\nabla\cdot\left(\nabla\boldsymbol{u} + \nabla\boldsymbol{u}^\top\right) + \boldsymbol{f}, & \text{in } \Omega\times[0,T] \\
-\nabla\cdot\boldsymbol{u} = 0, \quad \text{in } \Omega\times[0,T] \\
\boldsymbol{u}(\boldsymbol{x},0) = \boldsymbol{u}_0(\boldsymbol{x}), \quad \text{in } \Omega \\
\boldsymbol{u}(\boldsymbol{x},t) = \boldsymbol{u}_D(\boldsymbol{x},t), \quad \text{on } \Gamma_D\times[0,T] \\
\left[-p\boldsymbol{I} + \mu\left(\nabla\boldsymbol{u} + \nabla\boldsymbol{u}^\top\right)\right]\cdot\boldsymbol{n} = \boldsymbol{g}(\boldsymbol{x},t), \quad \text{on } \Gamma_N\times[0,T] \\
\displaystyle\int_\Omega \gamma \, \mathrm{d}\Omega \le \theta V_0 \\
0 \le \gamma \le 1
\end{cases}
\end{aligned}
\tag{8}
$$

where $V_0 = \int_\Omega \mathrm{d}\Omega$ is the volume of the whole computational domain Ω, $\theta \in (0,1]$ is the upper bound of fluid volume fraction. Equation (8) represents the equality constraint due to the governing equations and the inequality constraint due to the volume constraint. The external force term $\boldsymbol{f}$ uses the artificial friction force shown in the equations (6)-(7) to treat the computational domain including the solid domain in a unified form. The objective function J is assumed to be the energy dissipation due to the artificial body force and fluid viscosity in this paper and is set to

$$
J(\boldsymbol{u}, p; \gamma) = \int_0^T\int_\Omega \alpha\,\boldsymbol{u}\cdot\boldsymbol{u}\,\mathrm{d}\Omega\mathrm{d}t + \int_0^T\int_\Omega \frac{\mu}{2}\left[\nabla\boldsymbol{u} + (\nabla\boldsymbol{u})^\top\right] : \left[\nabla\boldsymbol{u} + (\nabla\boldsymbol{u})^\top\right]\mathrm{d}\Omega\mathrm{d}t. \tag{9}
$$

4. Numerical methods

As mentioned before, topology optimization for transient flow requires a fine mesh, especially for high Reynolds number flows, and is computationally expensive. Therefore, in this research, the governing equations are discretized using a cell-centered finite volume method based on the BCM, which is suitable for massively parallel computing. As shown in Figure 1, the BCM [5] divides the computational domain into cubic regions, called cubes. Each cube is divided into a Cartesian mesh with the same number of computational cells, and the same number of cubes are distributed to each computational core, with spatial loop processing performed within each cube. This allows each computational core to share the same number of computational cells, thus equalizing the computational load and localizing

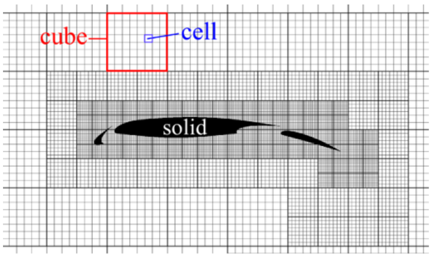

Figure 1: Mesh Division based on the BCM

and continuing memory accesses, which results in high parallel efficiency. In previous research, discretization has been performed mainly using the finite element method, but in this research, discretization is performed using the cell-centered finite volume method [6].

Topology optimization uses the density method to optimize the design domain. The sensitivity of the objective function is obtained using the sensitivity formulation based on the continuous adjoint method using the equations (1)-(5). The adjoint equations in the sensitivity analysis are also discretized using a cell-centered finite volume method based on the BCM. Using the obtained sensitivity, the design variables are updated based on the gradient method, and the optimal solution of the design variables is computed such that the objective function is minimized.

5. conclusion

In this research, we proposed a topology optimization method for transient flow using a cell-centered finite volume method based on the BCM, which is suitable for massively parallel computation. In the presentation, we will demonstrate several numerical examples to verify the proposed method.

References

[1] T. Borrvall, J. Petersson: Topology optimization of fluids in Stokes flow, *International journal for numerical methods in fluids*, 41:1 (2003), 77–107.

[2] Y. Deng, Z. Liu, P. Zhang, Y. Liu, Y. Wu: Topology optimization of unsteady incompressible Navier–Stokes flows, *Journal of Computational Physics*, 230:17 (2011), 6688–6708.

[3] S. Kreissl, G. Pingen, K. Maute: Topology optimization for unsteady flow, *International Journal for Numerical Methods in Engineering*, 87:13 (2011), 1229–1253.

[4] C. Chen, K. Yaji, T. Yamada, K. Izui, S. Nishiwaki: Local-in-time adjoint-based topology optimization of unsteady fluid flows using the lattice Boltzmann method, *Mechanical Engineering Journal*, 4:3 (2017), 17–00120.

[5] K. Nakahashi: Building-cube method for flow problems with broadband characteristic length, *Computational Fluid Dynamics 2002: Proceedings of the Second International Conference on Computational Fluid Dynamics, ICCFD, Sydney, Australia, 15–19 July 2002*, (2003), 77–81.

[6] K. Nishiguchi, R. Bale, S. Okazawa, M. Tsubokura: Full Eulerian deformable solid-fluid interaction scheme based on building-cube method for large-scale parallel computing, *International Journal for Numerical Methods in Engineering*, 117:2 (2019), 221–248.

Modeling of Metal Foams with Adjustable Wall Thickness in Targeted Direction

Naoki Hamano[1,*], Taku Itoh[2,*], Kohei Tateyama[3],
Susumu Nakata[4], Keiko Watanabe[5]

[1]Graduate School of Industrial Technology, Nihon University, Japan
[2]College of Industrial Technology, Nihon University, Japan
[3]Graduate School of Engineering, Muroran Institute of Technology, Japan
[4]College of Information Science and Engineering, Ritsumeikan University, Japan
[5]College of Science and Engineering, Ritsumeikan University, Japan

*`cina22005@g.nihon-u.ac.jp`, `itoh.taku@nihon-u.ac.jp`

Abstract. In this paper, to perform structural analysis simulations using metal foams in various kinds of conditions, a method for generating metal foam models that enable to adjust wall thickness in a targeted direction has been proposed. In the method, the target direction is first set, then the wall thickness of metal foam is determined from a simple equation that represents a relation among near cell structures. In experiments, the results show that the generated metal foam models have thick walls in the targeted direction, in comparison with walls of other directions.

Keywords: Metal foams, Wall thickness, Targeted direction, Shape modeling

1. Introduction

Metal foams have some kinds of valuable properties such as light weight and high capability of shock-absorbing [1]. Because of these properties, metal foams may be applied to various engineering fields, e.g., crash absorbers, and materials of trains and architecture [2]. Hence, evaluation of the performance of metal foams by numerical simulation such as structural analysis is required.

Metal foams mainly have two states based on cell structure, open and closed cells. In addition, intermediate states between open and closed cells also exist. All these states including intermediates can be represented by a method in [3] that has been proposed Sonon et al. We call this Sonon method.

Closed-cell metal foam models generated by Sonon method have quasi-constant thickness walls. Note that the wall thickness of real metal foams are not necessarily quasi-constant. If the wall thickness of metal foam models can be adjusted, structural analysis simulations with more various kinds of conditions may be performed.

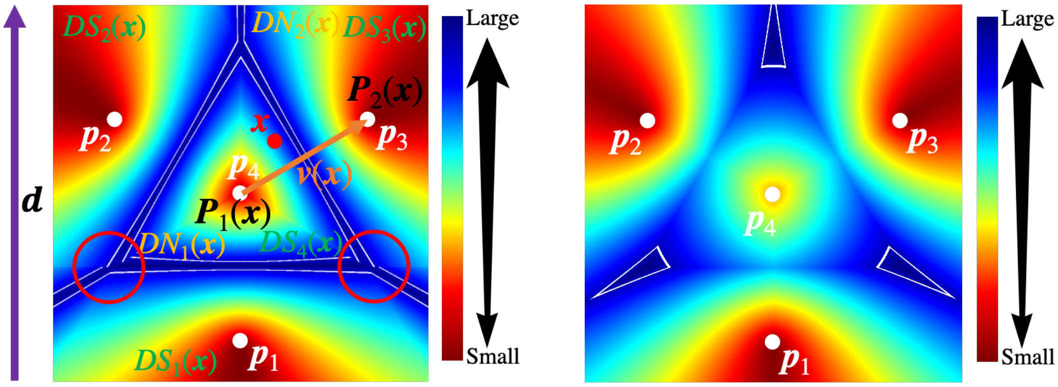

(a) (b)

Figure 1: Distributions of (a) $\hat{O}_{\mathrm{V}}(\boldsymbol{x})$ and (b) $O_{\mathrm{P}}(\boldsymbol{x}) - c$. In (a), $DS_i(\boldsymbol{x})$ based on $\boldsymbol{p}_i$ ($i = 1, 2, 3, 4$), $DN_1(\boldsymbol{x})$, $DN_2(\boldsymbol{x})$, $\boldsymbol{P}_1(\boldsymbol{x})$, $\boldsymbol{P}_2(\boldsymbol{x})$ and $v(\boldsymbol{x})$ are also shown. In (a) and (b), the extracted surfaces are shown as white thin lines. In addition, red circles in (a) are distorted parts of surfaces.

In this paper, we propose a method for generating metal foam models that enable to adjust wall thickness in a targeted direction. In addition, the performance of proposed method is investigated by constructing some metal foam models in experiments.

2. Sonon Method

In this section, we briefly describe about the Sonon method. First, $DS_1(\boldsymbol{x}), DS_2(\boldsymbol{x}), \ldots, DS_n(\boldsymbol{x})$ exist in Ω_{RVE}, where $DS_i(\boldsymbol{x})$ is defined as the i-th signed distance field of Φ_i, and Ω_{RVE} denotes the 3-dimensional (3-D) cubic domain of a representative volume element (RVE) [3]. In addition, Φ_i denotes a closed surface representing the boundary of an inclusion i. Besides, Ω_i^- and Ω_i^+ are the domains inside and outside of Φ_i, respectively. $DS_i(\boldsymbol{x})$ is negative on Ω_i^- and positive on Ω_i^+, and Φ_i can be represented as an implicit representation, $DS_i(\boldsymbol{x}) = 0$.

In the Sonon method, the Voronoï level set function is defined as

$$O_{\mathrm{V}}(\boldsymbol{x}) = DN_2(\boldsymbol{x}) - DN_1(\boldsymbol{x}), \tag{1}$$

where $DN_k(\boldsymbol{x})$ is the k-th neighbor distance field [3]. A quasi-constant thickness closed cell geometry [3] can be extracted by

$$O_{\mathrm{V}}(\boldsymbol{x}) - t = 0, \tag{2}$$

where t is a parameter related to thickness of walls in a closed cell metal foam model.

3. Proposed Method

In this section, we describe a method for generating metal foam models that enable to adjust wall thickness in a targeted direction. The method is based on the Sonon method. As

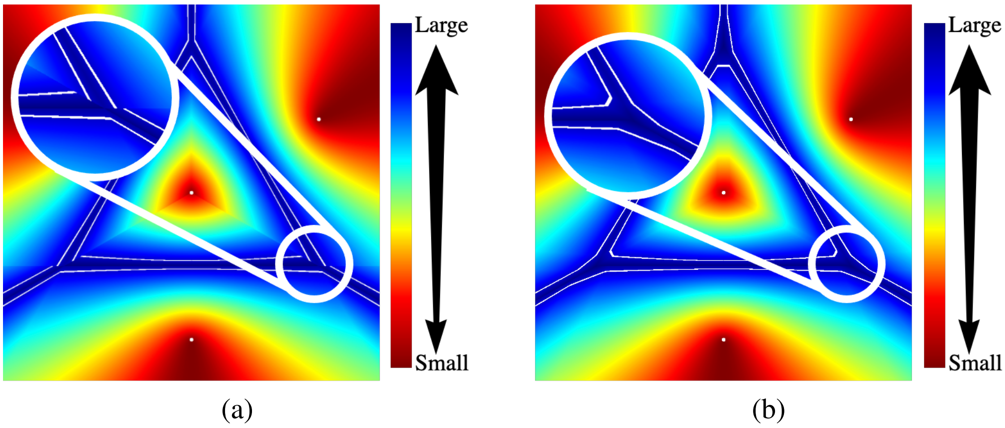

(a) (b)

Figure 2: Enlarged views for distributions of (a) $\hat{O}_{\mathrm{V}}(\boldsymbol{x})$ and (b) $\hat{O}_{\mathrm{VP}}(\boldsymbol{x})$. In (a) and (b), the extracted surfaces are shown as white thin lines.

mentioned in the previous section, the signed distance fields, $DS_1(\boldsymbol{x}), DS_2(\boldsymbol{x}), \ldots, DS_n(\boldsymbol{x})$ exist in Ω_{RVE} in the Sonon method. To generate $DS_1(\boldsymbol{x}), DS_2(\boldsymbol{x}), \ldots, DS_n(\boldsymbol{x})$, we first arrange points $\mathcal{P} = \{\boldsymbol{p}_1, \boldsymbol{p}_2, \ldots, \boldsymbol{p}_n\}$ in Ω_{RVE}. $DS_1(\boldsymbol{x}), DS_2(\boldsymbol{x}), \ldots, DS_n(\boldsymbol{x})$ are generated based on $\boldsymbol{p}_1, \boldsymbol{p}_2, \ldots, \boldsymbol{p}_n$, respectively.

In the proposed method, we modify (2) as follows:

$$\hat{O}_{\mathrm{V}}(\boldsymbol{x}) = O_{\mathrm{V}}(\boldsymbol{x}) - \max(t, \alpha \boldsymbol{d} \cdot \boldsymbol{v}(\boldsymbol{x})) = 0, \tag{3}$$

where $\boldsymbol{v}(\boldsymbol{x}) = (\boldsymbol{P}_2(\boldsymbol{x}) - \boldsymbol{P}_1(\boldsymbol{x}))/|\boldsymbol{P}_2(\boldsymbol{x}) - \boldsymbol{P}_1(\boldsymbol{x})|$, α is a parameter that determines the maximum thickness of walls in closed cell, and $\boldsymbol{d}$ is a targeted direction with $|\boldsymbol{d}| = 1$. In addition, $\boldsymbol{P}_1(\boldsymbol{x})$ and $\boldsymbol{P}_2(\boldsymbol{x})$ denote the points corresponding to $DN_1(\boldsymbol{x})$ and $DN_2(\boldsymbol{x})$, respectively (see Fig. 1(a)). By using (3) to extract surfaces of walls, the thickness of walls is thick in a targeted direction. Note that some distorted parts appear in extracted surfaces in the red circles shown in Fig. 1(a).

Here, we focus on the following function.

$$O_{\mathrm{P}}(\boldsymbol{x}) = \frac{DN_3(\boldsymbol{x}) - DN_2(\boldsymbol{x})}{2} - DN_1(\boldsymbol{x}). \tag{4}$$

Note that, in the Sonon method, $O_{\mathrm{P}}(\boldsymbol{x})$ is originally employed for constructing Plateau borders of open-cell metal foams [3]. Surfaces of Plateau borders can be extracted as $O_{\mathrm{P}}(\boldsymbol{x}) - c = 0$. In Fig. 1(b), the surfaces are shown as white thin lines. In the proposed method, we employ $O_{\mathrm{P}}(\boldsymbol{x})$ to modify the distorted parts. Since the surfaces of Plateau borders, $O_{\mathrm{P}}(\boldsymbol{x}) - c = 0$, appear around the distorted parts of $\hat{O}_{\mathrm{V}}(\boldsymbol{x})$ as shown in Figs. 1(a) and (b), the surfaces of closed-cell metal foams can be extracted by

$$\hat{O}_{\mathrm{VP}}(\boldsymbol{x}) = \min(\hat{O}_{\mathrm{V}}(\boldsymbol{x}), O_{\mathrm{P}}(\boldsymbol{x}) - c) = 0. \tag{5}$$

Enlarged views for distributions of $\hat{O}_{\mathrm{V}}(\boldsymbol{x})$ and $\hat{O}_{\mathrm{VP}}(\boldsymbol{x})$ are shown in Figs. 2(a) and (b), respectively. We see from both figures that the distorted parts are modified by the function $\hat{O}_{\mathrm{VP}}(\boldsymbol{x})$.

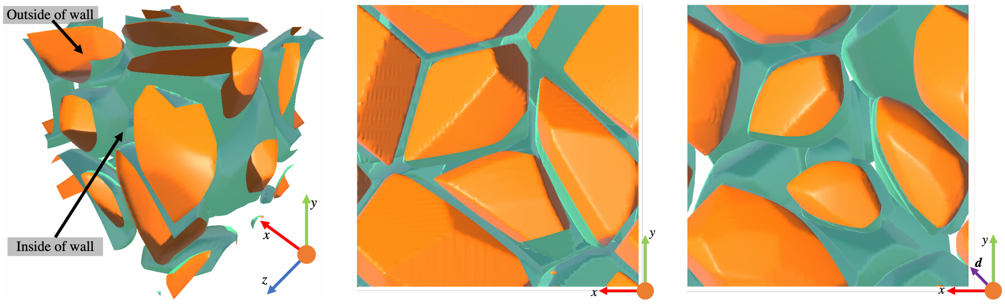

(a) (b) (c)

Figure 3: A result obtained by (a) proposed method with $\boldsymbol{d} = [\sqrt{2}/2, \sqrt{2}/2, 0]^{\mathrm{T}}$. Results viewed from the positive direction of z-axis obtained by (b) original method and (c) proposed method. Note that, in these figures, there are some parts look white because of the lighting in rendering.

4. Results

In this section, we evaluate the wall thickness of metal foam model generated by the proposed method, by comparison with that generated by the original method. First, we show a result obtained by the proposed method in Fig. 3(a). In addition, we also show results viewed from the positive direction of z-axis obtained by the original and proposed methods in Figs. 3(b) and (c), respectively. Note that Figs. 3(a) and (c) are just different perspectives, but they are exactly the same. To obtain these results, we first generate the points $\mathcal{P}$ with $n = 16$ by the Poisson-disk sampling [4] to randomly arrange in Ω_{RVE} defined as $[0, 1] \times [0, 1] \times [0, 1]$ uniformly, and we employ sphere functions of centers $\boldsymbol{p}_i$ as $DS_i(\boldsymbol{x})$ $(i = 1, 2, \ldots, 16)$, respectively. In addition, we set $\boldsymbol{d} = [\sqrt{2}/2, \sqrt{2}/2, 0]^{\mathrm{T}}$, $t = 0.025$, $\alpha = 0.05$ and $c = 0.075$. We see from Figs. 3(a), (b) and (c) that the thickness of walls in the result obtained by the proposed method is thicker than that obtained by the original method, especially for the targeted direction $\boldsymbol{d}$. Other results and further details will be presented at the conference.

References

[1] M. Ashby, T. Evans, N. A. Fleck, J. W. Hutchinson, H. N. G. Wadley, L. J. Gibson: *Metal Foams: A Design Guide*, Butterworth-Heinemann, Oxford, 2000.

[2] F. García-Moreno: Commercial applications of metal foams: Their properties and production, *MDPI*, 9:2 (2016), Art. no. 85.

[3] B. Sonon, B. François, T. J. Massart: An advanced approach for the generation of complex cellular material representative volume elements using distance fields and level sets, *Computational Mechanics*, 56 (2015), 221–242.

[4] D. Duber, G. Humphreys: A spatial data structure for fast Poisson-disk sample generation, *ACM Trans. Graph.*, 25:3 (2006), 503–508.

A Physics-informed neural network-based Surrogate Model for Analyzing Elasticity Problems in Plates with Holes

Zhongjiang Han[1,*], Jiarui Ou[1], Koji Koyamada[2]

[1]Kyoto University
[2]Osaka SeiKei University

*`zhongjianghan@gmail.com`

The full paper of this paper has been published in Journal of Advanced Simulation in Science and Engineering (JASSE).

DOI: `https://doi.org/10.15748/jasse.11.21`

Effects of Gaussian noise for applying the dynamic network biomarker theory to single-cell RNA-seq data

Shota Yonezawa[1,2], Kensuke Sasaki[3], Takayuki Haruki[4,2,*], Keiichi Koizumi[2],
Tomonobu M. Watanabe[3], Kuniya Abe[5], Yuhki Tada[5], Yuukou Horita[4]

[1]Graduate School of Science and Engineering, University of Toyama
[2]Research Center for Pre-Disease Science, University of Toyama
[3]RIKEN Center for Biosystems Dynamics Research
[4]Faculty of Sustainable Design, University of Toyama
[5]RIKEN BioResource Research Center

*`haruki@sus.u-toyama.ac.jp`

The full paper of this paper has been published in Journal of Advanced Simulation in Science and Engineering (JASSE).

DOI: `https://doi.org/10.15748/jasse.11.147`

Aerodynamics research of the gliding flight mechanism of a flying snake supposed as a 2D tandem model

Daiki Hirayama[1*], Ichiro Nakane[2]

[1]Graduate School of Engineering, Kanagawa Institute of Technology
[2]Department of Mechanical Engineering, Kanagawa Institute of Technology
*S2281004@kait.jp

Abstract. The body of snakes are generally unsuitable for a gliding flight. However, a flying snake deforms its round body into a semicylindrical shape and glides in the air without stalling. We discuss the gliding flight mechanism of a flying snake supposed as a 2D tandem model by computer simulation and wind tunnel test. In these results, the maximum lift coefficient is 1.3 and the lift-drag ratio is 2.5 in calculation or 2.2 in measurement. Moreover, we found the pitching moment can be reduced to zero by slightly moving the center of gravity. This characteristic contributes to longitudinal stability and the favorable increase of glide ratio.

Keywords: Flying snake, Gliding flight, Computer simulation, Wind tunnel test

1. Introduction

Snakes can move in water as well as on land, climb a tree, and enter extremely small places. Therefore, a snake-like robot is expected to be put into practical use, and in fact, it is being used for exploration at the Fukushima nuclear power plant on a trial basis. And currently, a flying snake has attracted research attention from the viewpoint of biomimetics. If the gliding flight ability is added to a snake-like robot, the scope of its activities is expanding significantly.

In order to glide in the air, an object must generate large lift, suppress drag, and have longitudinal, lateral and directional stability. However, concerning a flying snake, in particular, it does not have a body part that can be substituted as wing as other gliding animals, e.g., the Japanese giant flying squirrel, and seems not to have a body shape that can maintain a posture stably during gliding. Therefore, the gliding mechanism of a flying snake remains unclear. Thus, as the first step, we made a 2D model of a flying snake and try to clarify the characteristics of the lift, drag and pitching moment. Herein, we discuss the glide ratio and longitudinal stability of a flying snake to realize an unprecedented gliding cable-like object.

2. Overview of the simulation and measurement with a 2D tandem model

Socha *et al.*[1] reported that a flying snake transforms its round body into a semi-cylindrical cross-sectional shape like a wing to generate lift by opening its ribs. In their movies, the flying snake swings its tail around in all cases and wiggles its body in many cases during the gliding flight. However, the wiggling body of it is sometimes stationary. Therefore, we suppose that the wiggling motion is not always necessary to glide, and use a stationary 2D tandem model which dimensions were determined according to the paper by Holden *et al.*[2]. As shown in

Fig.1(a), this model represents the front and rear portions of the S-shaped body of the flying snake during its glide, which have a significant effect on its glide. Fig.1(b) shows the mesh for simulation of flow around this model by Ansys FLUENT[3], and Fig.1(c) shows the cross-sectional shape of the model for wind tunnel test. The dimensions are not shown in Fig.1(b), but are the same as in Fig.1(c). The model for wind tunnel test was made with a 3D printer in 25 sections per each portion. In other words, this model was made by connecting 25 pieces of 5 cm thick with the cross-sectional shape shown in Fig.1(c). Three carbon pipes connecting each piece passed through the round holes in Fig.1(c).

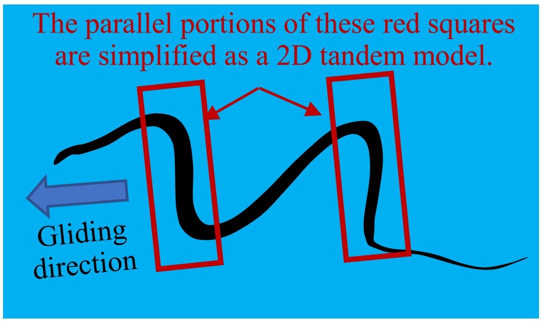

(a) S-shaped gliding posture and diagram of a stationary 2D tandem model

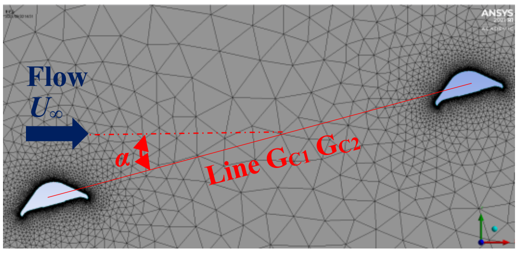

(b) The mesh for simulation of flow around the 2D tandem model by Ansys FLUENT[3] (α=-15°) (The calculation area is 10m × 10m, and the model dimensions are shown in Fig.1(c))

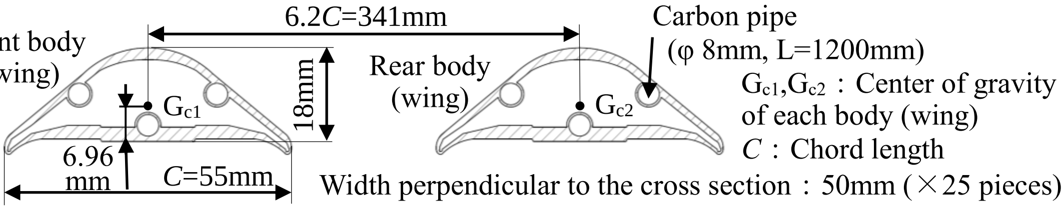

(c) The cross-sectional shape of the 2D tandem model for wind tunnel test

Fig.1 Schematic diagram of a 2D tandem model for the calculation and measurement

The computer simulation of flow around this 2D model were carried out as unsteady and laminar flow using Ansys FLUENT[3]. The time step of unsteady calculation is 0.1s and the total time is 100s. The unsteady calculated values of the lift, drag and pitching moment were averaged for this total time as the representative value. To evaluate this calculation, the wind tunnel test was also carried out under the same conditions as the calculation. For the calculation and measurement, the angle of attack α was changed every 3° between −15° and 90°, and the Reynolds number Re ($=U_\infty C/\nu$) was set as 6.0×10^4. Note that Re calculated from an average maximum velocity during the gliding of the flying snake, as measured by Socha *et al.*[1], is Re $=1.5\times10^4$. However, herein, Re was increased within the same order of magnitude without turbulent transition, considering the model's manufacturing and measurement precision. In our previous report[4], we confirmed that such a change in Re does not affect the phenomenon.

3. Results and Discussion

Aerodynamic coefficients obtained by the computer simulation and wind tunnel test are shown in Fig.2. L is the lift, D is the drag, and M is the moment around the center of gravity G_C, which is the midpoint between G_{C1} and G_{C2} shown in Fig.1(c). The calculation and measurement results agree well except around α=0°, where the support rod connecting the front and rear wings has a significant effect in the wind tunnel test. The maximum lift is generated at α = 27° and 36° in the calculation and measurement respectively, and both have C_L values of 1.3.

The lift–drag ratios also culminate at α=27° (L/D=2.5) and 30° (L/D=2.2) in the calculation and measurement, respectively. Therefore, $\alpha \approx$27° or 30° is optimum during gliding.

The pitching moment coefficient C_M, which affects the longitudinal stability, is a large positive moment around α=0°, and is a large negative moment around α=27°. This change in C_M is suitable for the gliding flight. When a flying snake jumps in the air horizontally, the positive pitching moment causes the snake to turn downward, reduce drag and accelerate due to gravity. Then, the angle of attack α increases, causing the snake to turn upward by the negative pitching moment and glide horizontally. In addition, these characteristics of C_M are consistent with both the previously reported results[4] for only one body of the flying snake and the fact that the effect of the front wing on the rear wing is large at α=0° and decreases as α increases.

Furthermore, based on the above calculation results without the influence of the support rod around α=0°, we discuss the longitudinal stability. Okamoto and Ebina[5] found the point of zero-pitching moment over a wide range of the angle of attack in the wind tunnel test with the model of a beetle wing. They claimed that this pitching moment characteristic makes it easy to change the angle of attack, and that a stable posture can be maintained even if the angle of attack is changed. Thus, similar to their study, the lines of action of wind pressure at each angle of attack are shown in Fig.3 to discuss the longitudinal stability. Fig.3 shows that the lines are concentrated on four points: a red circle mark (α=−15° to −3°), a green circle mark (α=0° to 42°), a blue circle mark (α=45° to 60°) and G_C (α=63° to 90°). In particular, the lines concentrate on the green mark point over the wide range of α. Thus, it is possible to make the pitching moment zero by moving the center of gravity to these mark points, and becomes easier to maintain posture during gliding. In fact, Fig.4 shows the pitching moment coefficient C_{MA} calculated when the center of gravity was moved according to α in these mark points in Fig.3. Fig.4 shows that the magnitude of the pitching moment is close to zero.

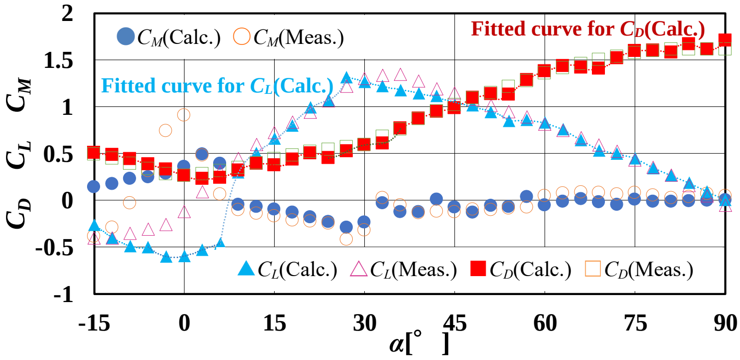

$$C_L=\frac{L}{\frac{1}{2}\rho U_\infty^2(2C)}\qquad C_D=\frac{D}{\frac{1}{2}\rho U_\infty^2(2C)}\qquad C_M=\frac{M}{\frac{1}{2}\rho U_\infty^2(2C)C}$$

Fig.2 Aerodynamic coefficients of the 2D tandem model with fitting curves to calculation results

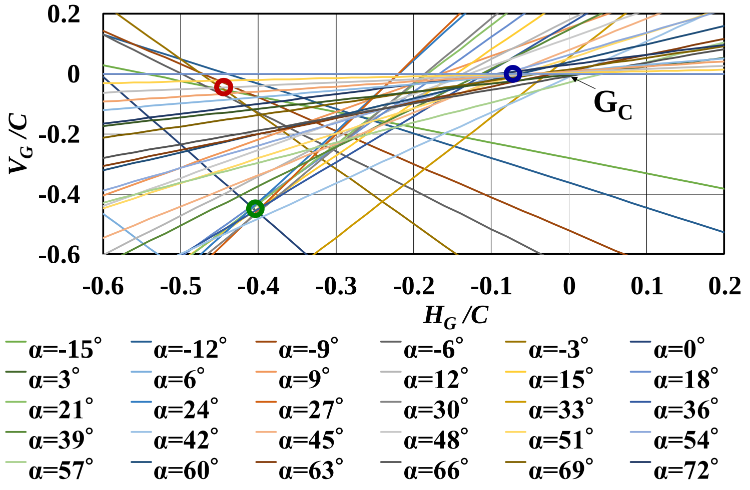

Fig.3 Change in the line of action of wind pressure according to α

Based on the above-mentioned results, we simulated the gliding behavioral characteristics by a first order Eulerian method with the time step of 0.01s, when a flying snake maintains zero pitching moment and always glides with a constant attitude angle β. This attitude angle β is the angle between the horizontal plane and line G_{C1} G_{C2} as shown in Fig.1. This result is shown in Fig.5. In accordance with the measured results of Socha *et al.*[2], a flying snake jumps at an initial velocity of 1.7 m/s, and the wing surface loading is assumed as 29 N/m^2. C_L and C_D were determined by the polynomial equations fitted to the calculation results shown in Fig,2. Fig.5 shows that the gliding trajectory fits within the range from the longest to shortest trajectory of the measured results of Socha *et al.*[1], when β equals to 20°, 25° and 30°. However, the calculated results with constant β fall far short of the longest gliding trajectory of the measurement[1] and maximum glide ratio(L/D=2.5). We predict that a flying snake controls β to be optimal α.

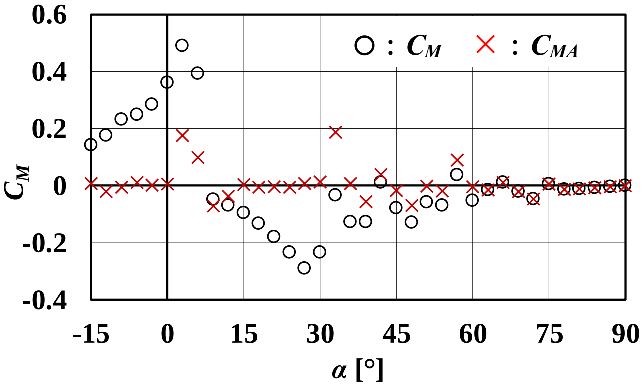

Fig.4 Change in C_M due to moving the center of gravity as shown in Fig.3 (○→○→○→G_C)

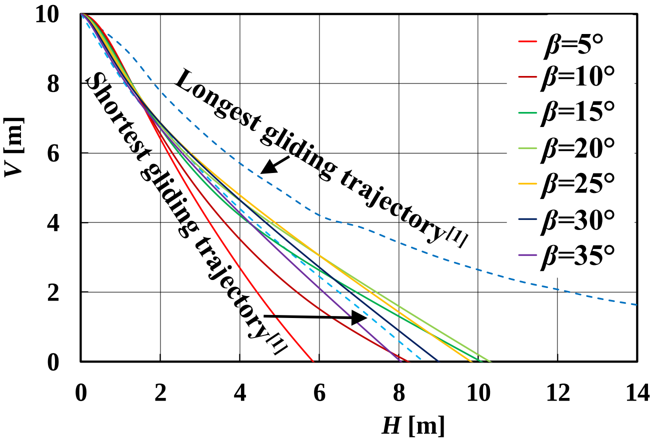

Fig.5 Gliding trajectory at constant attitude angle β

4. Conclusion

The posture of a flying snake during gliding was modeled as 2D tandem wings, and the glide and stability characteristics were clarified through the computer simulation and wind tunnel test. As a result, the maximum lift coefficient is 1.3 and the lift–drag ratio is 2.5 in calculation or 2.2 in measurement. The shape of the snake's body is suitable for reducing the pitching moment to zero by slightly moving the center of gravity. Consequently, in the case of a cable-like object with a shape similar to that of a flying snake, it was found that this object has the potential to glide with longitudinal stability at the glide ratio of about 2.5, even when its body is stationary without wiggling. However, of course, the glide ratio increases when the wing loading is less than the average value 29 N/m^2[1], and decreases when the wing loading is greater.

References

[1] Socha, J. J., O'Dempsey, T., LaBarbera, M. : A 3-D kinematic analysis of gliding in a flying snake, Chrysopelea paradise, *J. Exp.Biol.*, 208 (2005), pp. 1817–1833.

[2] Holden, D., Socha, J. J., Cardwell, N. D., Vlachosetc, P. P. : Aerodynamics of the flying snake Chrysopelea paradisi: how a bluff body cross-sectional shape contributes to gliding performance, *J. Exp.Biol.*, 217 (2014), pp. 382–394.

[3] https://www.cybernet.co.jp/ansys/product/lineup/fluent/, (accessed 2023-07-16). (in Japanese)

[4] Nakane, I., Shimizu, K. : Aerodynamics research of the gliding flight mechanism of a flying snake, *J. of Japan Soc. Aero. Space Sci.,* 71(2023), vol.1, pp. 43–50. (in Japanese)

[5] Okamoto, M., Ebina, K. : Effectiveness of Large-Camber Circular Arc Airfoil at Very Low Reynolds Numbers, *Trans. Japan Soc. Aero. Space Sci.*, 59(2016), pp. 295–304.

Comparison of UKF and EKF for a flow in a volume-changing cylinder

Teruyoshi Sadahiro[1,2,*] and Iori Sakino[2]

[1]Dept. of Science and Technology, Facaulty of Science and Technology, Oita University
[2]Dept. of Innovative Engineering, Facaulty of Science and Technology, Oita University

*`sadahiro@oita-u.ac.jp`

Abstract. Particle Image Velocimetry (PIV) is a measurement method for flow fields.In PIV, if density of tracer particles and working fluid are different, tracker particles are difficult to follow the working fluid, then the measurement is fail. Purpose of this study is to show an effectiveness of UKF compared with EKF for a flow in a volume-changing cylinder. Simulation results show that UKF is more effective than EKF for the scenario.

Keywords: Flow Measurements, PIV, EKF, UKF

1. Introduction

Particle Image Velocimetry (PIV) is a measurement method for flow fields [1]. To measure velocities in a flow filed, small tracker particles are drifted in the flow field, and some flow filed images are taken in some time intervals. Then the flow velocities are calculated by matching of tracker particles or particle-patterns in the time-elapsed flow filed images. Therefore PIV has a potential to be able to measure a lot of flow velocities simultaneously in the flow field. But, PIV is an indirect measurement method, it has some drawbacks.

In PIV, if density of tracer particles and working fluid are different, tracker particles are difficult to follow the working fluid, then the measurement is fail. Iida et al. [2] have addressed the problem using Extended Kalman Filter (EKF). By the way, in the recent decade, nonlinear Kalman Filters like UKF (Unscented Kalman Filter) are widely used and shown their fine performance [3].

Purpose of this study is to show an effectiveness of UKF compared with EKF fora flow in a volume-changing cylinder. This flow filed makes a situation described above.

2. Flow in a volume-changing cylinder

Force for tracer particles are gotten from Basset Boussinesq Oseen equation as follows:

$$\frac{4}{3}\pi r^3 \rho_p \ddot{X}_p = \frac{4}{3}\pi r^3 \rho_f \ddot{X}_f + \frac{1}{2}\cdot\frac{4}{3}\pi r^3 \rho_f \dot{U}_R + \frac{C_D}{2}\pi r^2 \rho_f |U_R| U_R, \tag{1}$$

where $r, \rho_p, \rho_f, X_p, X_f, U_R$, and C_D are radius of particles, density of particles, density of working fluid, positions of a particle, positions of working fluid, relative velocity, i.e. $\dot{X}_f - \dot{X}_p$, and drag coefficient, respectively. C_D depends on Reynolds number $Re_p = \frac{|U_R|d}{\nu}$ where ν is the kinematic viscosity of the working fluid and $d = 2r$, and is shown as follows [4]:

$$C_D = \frac{24}{Re_p}, \qquad \text{if } Re_p < 1, \tag{2}$$

$$C_D = \frac{24}{Re_p}(1 + 0.15 Re_p^{0.687}), \qquad \text{if } Re_p > 1. \tag{3}$$

In this study, air is used as the working fluid and ρ_p is defined as 246 kg/m^3. The velocity and density of the working fluid are also defined as follows:

$$\dot{X}_f = \sin(\beta t), \tag{4}$$

$$\rho_f = \frac{\rho_0}{5 - 4\cos(\beta t)}, \tag{5}$$

where the parameters ρ_0 and β are set to 1.23 kg/m^3 and 2π, respectively.

Using Eq.(1), Eq.(4), and Eq.(5), the equation of the system is shown as follows:

$$\begin{cases} X_p(k+1) = X_p(k) + \dot{X}_p(k)\Delta t + J(k)\Delta t^2/2 \\ \dot{X}_p(k+1) = \dot{X}_p(k) + J(k)\Delta t \\ \dot{X}_f(k+1) = \dot{X}_f(k) + \ddot{X}_f(k)\Delta t \\ \ddot{X}_f(k+1) = \ddot{X}_f(k) + \tilde{\alpha}_f \\ \rho_f(k+1) = \rho_{f(k)} + \dot{\rho}_f(k)\Delta t \\ \dot{\rho}_f(k+1) = \dot{\rho}_f(k) + \tilde{\alpha}_\rho \end{cases}, \tag{6}$$

$$J(k) = l(k)(\dot{X}_p(k) - \dot{X}_f(k)) + m(k)\ddot{X}_f(k), \tag{7}$$

$$l(k) = \frac{9\rho_f(k)\nu}{(2\rho_p + \rho_f(k))r^2}, \tag{8}$$

$$m(k) = \frac{3\rho_f(k)}{2\rho_p + \rho_f(k)}, \tag{9}$$

where $\tilde{\alpha}_f$ and $\tilde{\alpha}_p$ are system noise for $\ddot{X}_f$ and $\dot{\rho}_f$, respectively. And Δt and r is set to 0.01 s and 100 μm, respectively. ν is resolved using Sutherland's formula of viscosity and equation of adiabatic process as follows:

$$\nu = \frac{\mu}{\rho_{f(k)}}, \tag{10}$$

$$\mu = \frac{T_0 + C}{T + C}\left(\frac{T}{T_0}\right)^{1.5} \mu_0, \tag{11}$$

$$T = \left(\frac{\rho}{\rho_0}\right)^{\gamma - 1} T_0, \tag{12}$$

where T is temperature of the working fluid, and γ is heat capacity ratio that set to 1.4. And the parameters μ_0, C, and T_0 are set to 1.8286×10^{-6} Pa·s, 120 K, and 288.15 K, respectively.

The state of the system is defined as follows:

$$\boldsymbol{x} = \begin{bmatrix} X_p & \dot{X}_p & \dot{X}_f & \ddot{X}_f & \rho_f & \dot{\rho}_f \end{bmatrix}^T . \tag{13}$$

And, in the system, it is assumed that X_p and $\dot{\rho}_f$ are observed.

3. Simulation results

Simulation results using EKF [2] and UKF are shown in Fig. 1. In this simulation, variance of system noise for $\ddot{X}_f$ and $\dot{\rho}_f$ are set to 0.5 and 0.001, respectively. In this scenario, both EKF and UKF can be estimated the state although the velocity of particle and the velocity of working fluid are different, i.e. they have some phase error. Comparing results of two methods, the velocity of particle of UKF is more smooth than one of EKF, and the velocity of fluid of UKF is more accurate estimation than one of EKF. Therefore, the results show that UKF is more effective than EKF for the scenario.

References

[1] R. Adrian: Twenty years of particle image velocimetry, *Experiments in Fluids*, 39 (2005), pp.159–169.

[2] S. Iida, K. Ogawara, and J.Yokouchi: Estimation of Fluid Velocity by Tracking a Particle which Does Not Follow the Flow, *Transactions of the Japan Society of Mechanical Engineers. B.(in Japanese)*, 60:578 (1994), pp.3242–3248.

[3] M. Yamakita: What is UKF (Unscented Kalman Filter)?, *Transactions of the Institute of Systems, Control and Information Engineers (in Japanese)*, 50:7 (2006), pp.261–266.

[4] S. Kawano and H. Hashimoto: Drag Coefficient of a Spherical Encapsulated Liquid Drop, *Transactions of the Japan Society of Mechanical Engineers. B.(in Japanese)*, 57:534 (1991), pp.441–446.

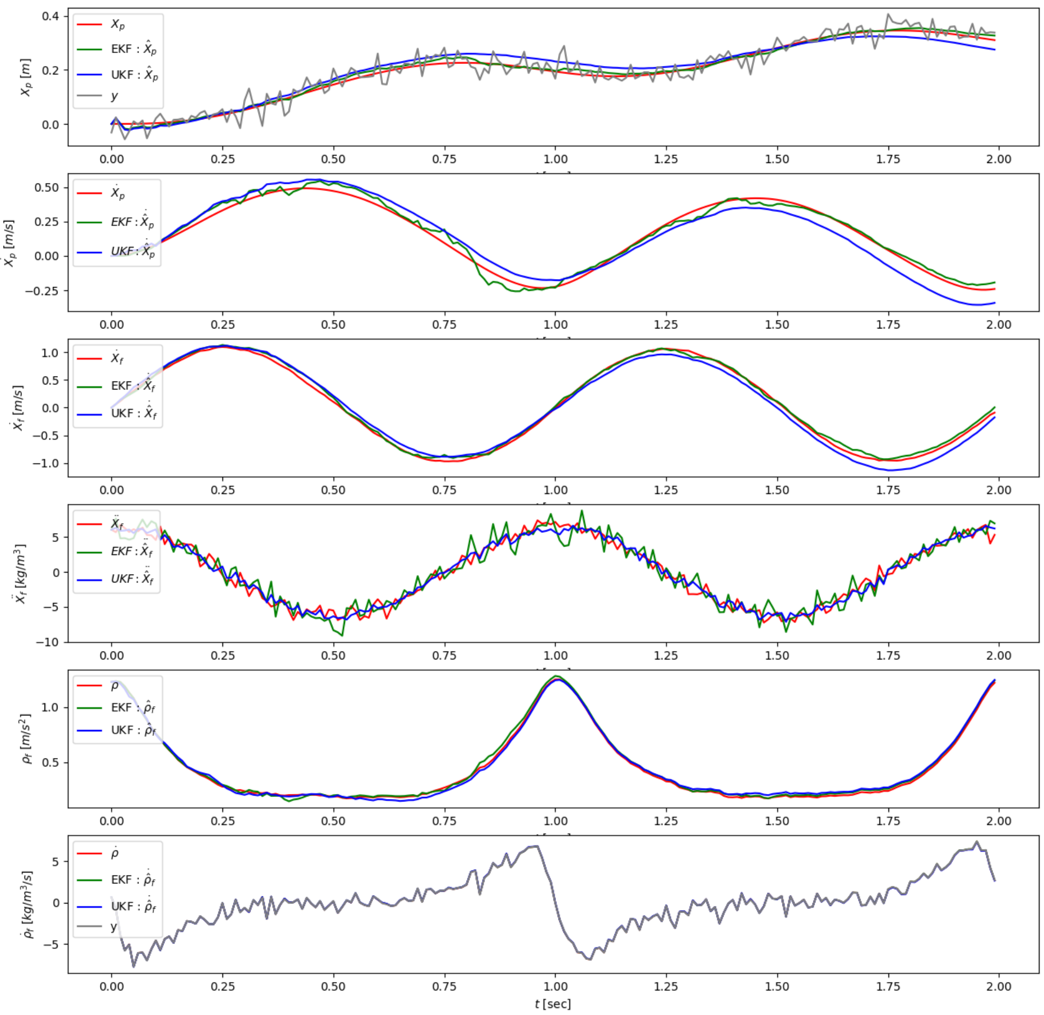

Figure 1: Comparison graphs to estimate the state of a flow in a volume-changing cylinder using EKF and UKF; In this figure, X_p, X_f and ρ_f means positions of a particle, positions of working fluid, and density of working fluid, respectively. And the state of the system is $\boldsymbol{x} = \begin{bmatrix} X_p & \dot{X}_p & \dot{X}_f & \ddot{X}_f & \rho_f & \dot{\rho}_f \end{bmatrix}^T$. In the system, it is assumed that X_p and $\dot{\rho}_f$ are observed. And variance of system noise for $\ddot{X}_f$ and $\dot{\rho}_f$ are set to 0.5 and 0.001, respectively. Comparing results of two methods, the velocity of particle of UKF is more smooth than one of EKF, and the velocity of fluid of UKF is more accurate estimation than one of EKF.

Material extrusion-based additive manufacturing with multi-legged robot for large scale fabrication

Koki Jimbo[1,*]

[1]Department of Advanced Machinery Engineering, School of Engineering, Tokyo Denki University

*`kjimbo@mail.dendai.ac.jp`

The full paper of this paper has been published in Journal of Advanced Simulation in Science and Engineering (JASSE).

DOI: `https://doi.org/10.15748/jasse.11.222`

Computational Fluid Dynamics Analysis of Flying Snakes Using OpenFOAM

Takeru Moriyama[1*] and Taro Fujikawa[1]

[1]Graduate School of Science and Technology for Future Life, Tokyo Denki University

*`23fmr56@ms.dendai.ac.jp`

Abstract. The purpose of this study is to reveal the effect of changes in the angle of attack of the flying snake on the lift-drag ratio. In this paper, we perform a computational fluid dynamics analysis of a 3D flying snake model using OpenFOAM. As a result, the maximum lift-drag ratio was observed under the condition of 20 deg angle of attack. The velocity distribution suggests that changing the angle of attack of the flying snake was found to be effective in increasing the lift-drag ratio.

Keywords: CFD, Flying Snake, OpenFOAM

1. Introduction

The snake type robot is being studied as a robot to work in a variety environments. Existing snake type robots, however, are difficult to move over uneven terrain. One of the methods to deal with moving over all uneven terrain is aerial transfer. Therefore, we focus on the flying snake. The flying snake can glide without special organs such as wings. It has been reported that the flying snake glides by a bluff body cross-sectional shape and undulation [1], [2], [3]. It has also been suggested that the upstream body section of a flying snake influences the downstream body section [4]. However, no analysis of the flow around a 3D model of the flying snake has been conducted. Therefore, this paper reveals the effect of changes in the angle of attack of the flying snake on glide performance by computational fluid dynamics analysis of a 3D model of the flying snake using OpenFOAM.

2. Analysis Method

2.1. Creation of the flying snake model

The analysis performed in this study is computational fluid dynamics analysis using OpenFOAM. The model used in the analysis was created on Inventor(ver. 2021), Autodesk's 3D CAD software. The cross-sectional shape of the model was based on the coordinate data of the point cloud provided by Krishnan*et al* [5]. to mimic the cross-sectional shape of a flying snake gliding. The bending shape of the model was created based on aerial serpenoid curve defined by Yeaton *et al* [3].

Table 1 shows the parameters used to create the simulation model. Figure 1 indicates the top and side views and cross-sectional shape of the model. In this study, the model was created using the maximum horizontal bending angle θ_m and horizontal spatial period ν_θ determined with reference to previous research [3]. The maximum horizontal bending angle is the maximum value of θ shown in Fig. 1 (a). The spatial period in the horizontal direction is the swell period seen from the top of the model. Snout-to-Vent-Length (SVL) is the length from the snout to the total outlet. SVL was determined based on the average value of flying snakes as shown in previous research [6]. In this study, The model is constant cross-sectional area and no tail. The angle of attack was set to 0, 10, 20, 30, and 40 deg, and the analysis results were compared.

Table 1: Parameters for creating a flying snake model

Parameter Definition	Variables	value
Maximum horizontal bending angle	θ_m	93 deg
Horizontal spatial period	ν_θ	1.4
SVL	L	692.60 mm
Body width	L_b	20.60 mm

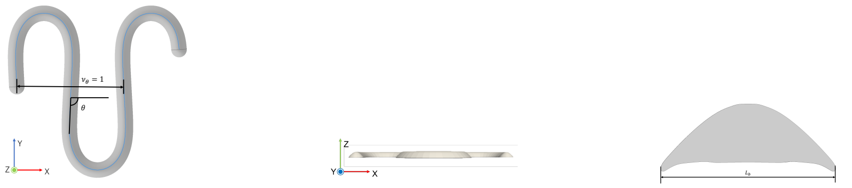

(a) Top View (b) Side view (c) Cross-sectional shape

Fig. 1: Simulation model

2.2. Analysis conditions

In this study, we performed unsteady analysis of an incompressible viscous fluid in three dimensional space using OpenFOAM (v2012 and v2212). The analysis determined the lift and drag coefficient of the model. The solver used in the analysis is the pisoFoam, which is calculated by the PISO method. The fluid is set with a kinematic viscosity of 1.5×10^{-5} $\mathrm{m^2/s}$ and an inflow velocity of 8.0 m/s. Simulation times are set to 0.4 s and the time step is 1.0×10^{-5} s. Figure 2 indicates the computational space. The center point of the model area is consistent with the origin. The boundary surfaces other than the inlet and outlet were set to the slip condition. The analysis space is divided into 50, 36, and 29 sections in the X, Y, and Z-axis directions respectively. The length of one side of the mesh around the body was further divided by 1/16. The size of simulation model is shown in Table 2. The Reynolds number for this study is 10986.67 when the representative length is the cross-section of the body. This value is within the range of Reynolds numbers shown in a previous study [2].

Table 2: Value related to the analysis space setting

Model Name	Model Length	Model Width
Simulation Model	237 mm	227 mm

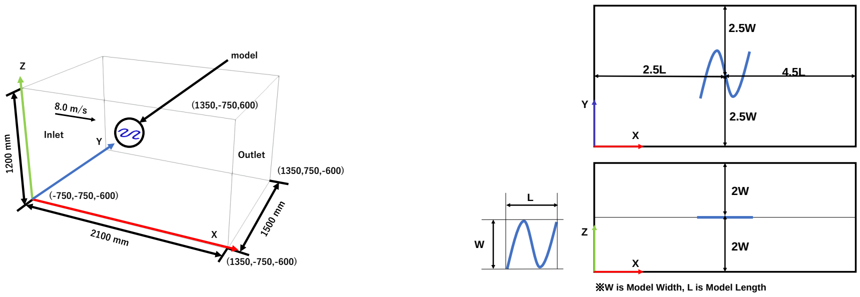

(a) Computational space size

(b) setting Parameter

Fig. 2: Computational space

3. Results and Discation

Figure 3 indicates the lift-drag ratio. Figure 4 indicates the velocity distribution. The lift-drag ratio is maximum value at an angle of attack of 20 deg. The velocity distribution showed that the flow generated in the body section of upstream increased the velocity on the top surface of the body section of the downstream. For this reason, lift of the downstream body section was increasing. This result suggests that changing the angle of attack of the 3D model has the effect of increasing the lift-drag ratio by changing the wake of each body section.

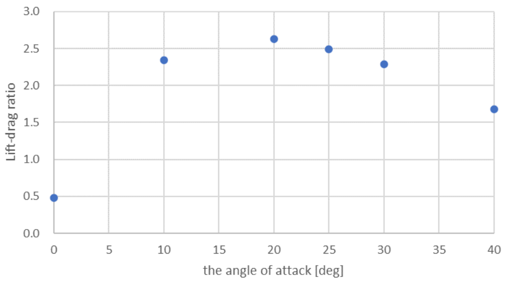

Fig. 3: The lift-drag ratio

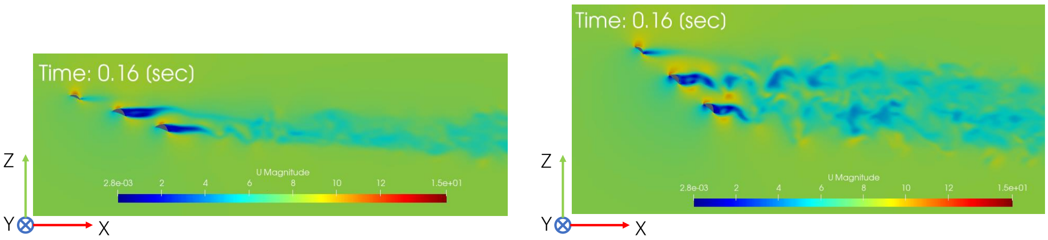

(a) 20 deg

(b) 40 deg

Fig. 4: The velocity distribution

4. Conclusions

In this study, a computational fluid dynamics analysis of the 3D flying snake model was conducted using OpenFOAM. As a result, the lift-drag ratio was maximum at an angle of attack of 20 deg for the model used in this paper. The velocity distribution suggested that changing the angle of attack of the 3D flying snake model has the effect of increasing the lift-drag ratio by wake of each body section interaction.

References

[1] Anush Krishnan, *et al.*: Lift and wakes of flying snakes, *AIP Publishing*, 26:3 (2014), 1–19.

[2] Daniel Holden, *et al.*: Aerodynamics of the flying snake Chrysopelea paradisi:how a bluff body cross-sectional shape contiributes to gliding performance, *The Journal of Experimental Bioloogy*, 217:3 (2014), 382–394.

[3] Isaac J. Yeaton, *et al.*: Undulation enables gliding in flying snakes, *NaturePhysics*, 16:9 (2020), 1–9.

[4] K. Miklasz, *et al.*: Effects of Body Cross-sectional Shape on Flying Snake Aerodynamics, *Experimental Mechanics*, 50:9 (2010), 1335–1348.

[5] Anush Krishnan, *et al.*:https://figshare.com/articles/dataset/Body_cross_section_of_the_flying_snake_Chrysopelea_paradisi/705877.

[6] John J Socha, Tony O'Dempsey, Michael LaBarbera: A 3-D kinematic analysis of gliding in a flying snake, Chrysopelea paradisi, *The Journal of Experimental Biology*, 208:10 (2005), 1817–1833.

JSST 2023

Fast and accurate symmetric rank-*k* operation

Yuki Uchino[1,*] and Katsuhisa Ozaki[2]

[1]Graduate School of Engineering and Science, Shibaura Institute of Technology
[2]Department of Mathematical Sciences, Shibaura Institute of Technology

*`nb22105@shibaura-it.ac.jp`

Abstract. We propose an alternative approach for one of the symmetric rank-k operations A^TA for a real $k\times n$ matrix A. For matrix multiplication, an accurate numerical algorithm using error-free transformation has been proposed. That algorithm offers advantages in terms of computing speed, high parallelism, and reproducibility. However, the product A^TA should be computed at half the cost of a general matrix product, which is impossible with that algorithm. Therefore, we propose an algorithm based on error-free transformation having approximately half the cost of a general matrix product.

Keywords: accurate numerical computation, matrix multiplication, floating-point arithmetic

1. Introduction

This study investigates the matrix multiplications of A^TA for a $k \times n$ floating-point matrix A. The routine `syrk` for A^TA is provided in the Level-3 BLAS (Basic Linear Algebra Subprograms) library and is usually used by matrix decomposition algorithms, such as the Cholesky decomposition algorithm and the Cholesky-QR algorithm, and various machine learning algorithms, such as the regression algorithm, the Support Vector Machine (SVM) algorithm, the Principal Component Analysis (PCA) algorithm, and the k-means clustering algorithm. Ozaki et al. proposed an accurate algorithm (herein called Ozaki's scheme) for matrix multiplication that uses error-free transformations of the matrix product [1]. The algorithm can exploit lower-precision floating-point arithmetic and routines from BLAS. Ozaki's scheme offers advantages in terms of computing speed due to the lower-precision floating-point arithmetic and high parallelism provided by routines from BLAS. In addition, it is possible to obtain reproducible results. Generally, A^TA is computed at half the cost of a general matrix product. However, the original Ozaki's scheme has a higher computation cost because it does not exploit the symmetry of the result. In the present study, we propose an alternative approach for Ozaki's scheme for A^TA. The proposed method has approximately half the cost of a general matrix product. Thus, the proposed method is faster than the original Ozaki's scheme, as demonstrated through numerical experiments.

2. Ozaki's scheme

Let $\mathbb{F}$ be a set of binary floating-point numbers defined in IEEE 754 [2]. Suppose $B \in \mathbb{F}^{n\times k}$ and $C \in \mathbb{F}^{k\times m}$. For $d \in \mathbb{N}$, Ozaki's scheme transforms BC into an unevaluated summation of matrix products:

$$BC = \sum_{p=1}^{d}\sum_{q=1}^{d} B_p C_q, \quad B_p \in \mathbb{F}^{n\times k}, \quad C_q \in \mathbb{F}^{k\times m},$$

where

$$B = \sum_{p=1}^{d} B_p \quad \text{with} \quad |(B_p)_{ij}| > |(B_{p+1})_{ij}| \quad \text{if} \quad (B_p)_{ij} \neq 0$$

and C takes a similar form. Through this approach, $B_p C_q$ for $p, q \leq d-1$ can be evaluated using floating-point arithmetic without rounding error if neither overflow nor underflow occurs. To reduce the computation cost, the scheme approximates BC as follows:

$$\sum_{p=1}^{d-1}\sum_{q=1}^{d-p} B_p C_q + \sum_{p=1}^{d} B_p \left(\sum_{q=d-p+1}^{d} C_q \right). \tag{1}$$

For simplicity, we will omit terms less than $O(mn)$ from the operations count. The computation (1) requires $(d^2 + d)nkm$ flops.

Now, let $B := A^T$ and $C := A$. Then, (1) can be rewritten as

$$\sum_{p=1}^{d-1}\sum_{q=1}^{d-p} A_p^T A_q + \sum_{p=1}^{d} A_p^T \left(\sum_{q=d-p+1}^{d} A_q \right), \tag{2}$$

where $A_p^T A_p$ for $p \leq \lfloor d/2 \rfloor$ can be computed in kn^2 flops by using `syrk` from BLAS and $A_p^T A_q + A_q^T A_p$ for $p + q \leq d - 1$ can be computed in $2kn^2$ flops by using `gemm` or `syr2k` from BLAS. Figure 1 illustrates (2) for $d = 4$. Thus, (2) is performed in $(d^2 + 3d)/2 \cdot kn^2$ flops. The product $A^T A$ should be computed at half the cost of the general matrix product.

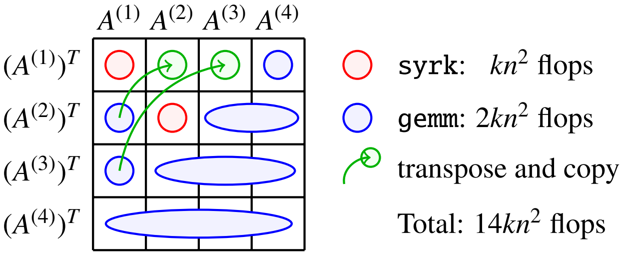

Figure 1: Ozaki's scheme for $A^T A$ with $d = 4$

However, (2) costs dn^3 flops more than that.

ReLAPACK [3] provides the routine `gemmt` which computes only the upper or lower part of a matrix product of general matrices at approximately half the cost of the general matrix product. The routine `gemmt` can be used in multiple libraries, such as the Intel oneAPI Math Kernel Library (oneMKL) [4], OpenBLAS [5], and BLIS [6]. We can compute (2) in $(d^2 + d)/2 \cdot kn^2$ flops by using `gemmt` for all matrix multiplications. However, the concept of `gemmt` is not provided in many libraries or software applications, such as cuBLAS [7], ScaLAPACK [8], MATLAB, or GNU Octave.

3. Proposed method

Let $A_s^e := \sum_{i=s}^{e} A_i$. Our proposed approach approximates $A^T A$ as

$$\sum_{p=1}^{d-1}\sum_{q=1}^{d-p} A_p^T A_q + \sum_{p=\lceil d/2\rceil+1}^{d} \left(A_p^T A_{d-p+1}^{d-\lceil d/2\rceil} + \left(A_{d-p+1}^{d-\lceil d/2\rceil}\right)^T A_p\right) + \left(A_{\lfloor d/2\rfloor+1}^{d}\right)^T A_{\lfloor d/2\rfloor+1}^{d} \tag{3}$$

instead of using (2). Since the computation of (3) only uses `syrk` and `gemm`, our approach can be implemented using routines and built-in functions, such as those in cuBLAS, ScaLAPACK, MATLAB, and GNU Octave, unlike the approach using (2) with `gemmt`. Figure 2 depicts (3) for $d = 4$. The computation of (3) is performed in $(d^2 + 3d)/2 \cdot kn^2$ flops if d is even and $(d^2 + d)/2 \cdot kn^2$ flops otherwise. Thus, by using (3), we can compute $A^T A$ at approximately half the cost of a general matrix product.

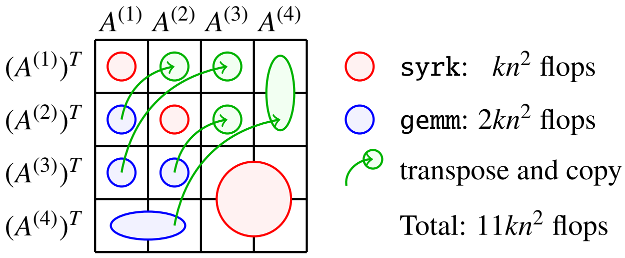

Figure 2: Our proposed approach with $d = 4$

4. Numerical results

We tested three approaches for Ozaki's scheme, (M1) based on (2) with `dgemm` and `dsyrk`, (M2) based on (2) with `dgemmt`, and (M3) based on (3) with `dgemm` and `dsyrk`, using oneAPI DPC++/C++ Compiler 2023.0.0 and oneMKL 2023.0.0 on a personal computer with an Intel Core i9-10900X CPU (3.70 GHz) and Windows 10 operating system. The test matrix A is generated as $a_{ij} = m_{ij} \cdot 2^{e_{ij}}$ with uniformly distributed random numbers $m_{ij} \in [0, 1]$ and $e_{ij} \in [1, 500]$ for all (i, j). Figure 3 shows the computing time ratios of M2 and M3 to M1 and indicates that M2 and M3 are 1.1–1.4 times faster than M1.

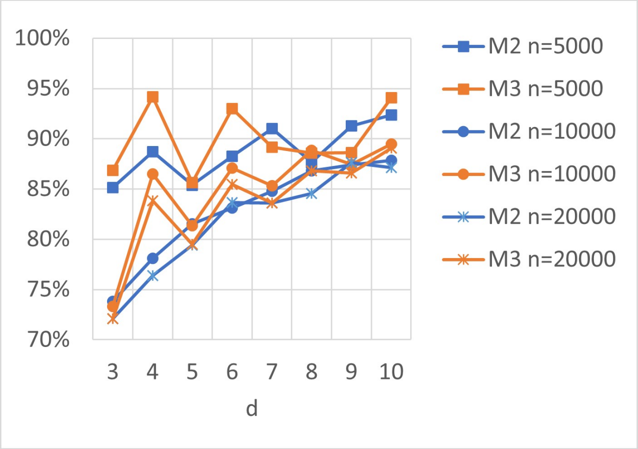

Figure 3: Computing time ratios of M2 and M3 to M1

References

[1] K. Ozaki, T. Ogita, S. Oishi, S.M. Rump: Error-free transformation of matrix multiplication by using fast routines of matrix multiplication and its applications, *Numer. Algorithms*, 59:1 (2012), 95–118.

[2] IEEE Std 754-2008: *IEEE Standard for Floating-Point Arithmetic*, IEEE Computer Society, 2008.

[3] E. Peise, P. Bientinesi: Recursive Algorithms for Dense Linear Algebra: The ReLAPACK Collection, *CoRR*, abs/1602.06763 (2016).

[4] Intel oneAPI Math Kernel Library, `https://www.intel.com/content/www/us/en/developer/tools/oneapi/onemkl.html`.

[5] Z. Xianyi, M. Kroeker: OpenBLAS: An optimized BLAS library, `http://www.openblas.net/`.

[6] Field G. Van Zee, Robert A. van de Geijn: BLIS: A Framework for Rapidly Instantiating BLAS Functionality, *ACM Trans. Math. Softw.*, 41:3 (2015), 14:1–14:33.

[7] NVIDIA: The cuBLAS library, `https://docs.nvidia.com/cuda/cublas/`.

[8] Scalable Linear Algebra PACKage (ScaLAPACK), `http://www.netlib.org/scalapack/`.

Computation method for an upper bound of the maximum norm of a matrix product

Yaxuan Zhao[1,*], Katsuhisa Ozaki[2], Yuki Uchino[1]

[1]Graduate School of Engineering and Science, Shibaura Institute of Technology
[2]Department of Mathematical Sciences, Shibaura Institute of Technology

*`mf22086@shibaura-it.ac.jp`

Abstract. This paper discusses algorithms producing an upper bound of the maximum norm of a matrix product using only standard floating-point arithmetic. This upper bound plays an essential role in verified numerical computations. This paper compares several implementations using a priori error estimates and discusses which methods are fast and efficient for verified numerical computations. Besides, this paper proposes a new method that combines block matrix computations and the running error.

Keywords: a priori error estimates, verified numerical computations, rounding error

1. Introduction

It is necessary to compute an upper bound of the maximum norm of a matrix product for many problems in verified numerical computations, such as linear systems, eigenvalue problems, and singular value decomposition, among others. Several methods have been developed for this purpose. One of the well-known methods is to obtain an enclosure of a matrix product using directed roundings. This method requires two matrix multiplications. An a priori error analysis can be applied to reduce the cost of the computations, and the upper bound with one matrix multiplication is then obtained.

This study discusses how to apply the a priori error analysis. First, the superblock family of algorithms [1] and a fast and accurate block summation algorithm [2] are reviewed. A method that combines block matrix computations and running error analysis is proposed. This method alternatively works without applying accurate summation algorithms.

2. Notation and previous study

This paper uses binary floating-point numbers based on IEEE 754, a standard for floating-point arithmetic [3]. Let $\mathbb{F}$ be a set of binary floating-point numbers. Typically, $\mathbb{F}$ is the set of binary32 or binary64 defined in IEEE 754. The notation $\mathtt{fl}(\cdot)$ indicates a computed result using floating-point arithmetic, where the rounding mode is rounding to nearest (ties to even). Let u be the roundoff unit, e.g., $u = 2^{-53}$ for binary64. A inequality $A \leq B$ for matrices A and B indicates $a_{ij} \leq b_{ij}$ for all i and j. $|A|$ means that for $A \in \mathbb{F}^{m\times n}$ the absolute value for all elements is taken. It should be noted that this notation for a square matrix never indicates the matrix determinant in this paper. It is assumed that neither overflow nor underflow occurs in $\mathtt{fl}(\cdot)$ for simplicity, but it can be treated using the underflow unit easily.

2.1. Rounding error in matrix multiplication

The error estimation theorem is introduced for the dot product of two vectors by Lange and Rump [4]. A binary tree is used to image the arithmetic order of the dot product. It is assumed that each binary tree for dot products in a matrix multiplication is the same. If the order of the computation is recursive, $c := n$ in Theorem 1.

Theorem 1. *For $A \in \mathbb{F}^{m\times n}$ and $B \in \mathbb{F}^{n\times p}$,*

$$|\mathtt{fl}(AB) - AB| \leq cu|A||B|, \quad \lceil \log_2 n \rceil \leq c \leq n \tag{1}$$

is satisfied where the constant c is the height of the binary tree for the dot product.

Let b be a block size, that is, $A_i \in \mathbb{F}^{m\times b}$ and $B_i \in \mathbb{F}^{b\times p}$ such that

$$A = [A_1\ A_2\ A_3\ \ldots], \quad B = \begin{bmatrix} B_1 \\ B_2 \\ B_3 \\ \vdots \end{bmatrix}.$$

Assume that n is dividable by b for simplicity. If a block computation is applied such that

$$C := \mathtt{fl}(A_1B_1 + A_2B_2 + \cdots + A_sB_s), \quad s := n/b,$$

then from [4], one has

$$|C - AB| \leq (b + s - 1)u|A||B|. \tag{2}$$

It should be noted that if b and s are approximately $\sqrt{n}$, then $b + s \approx 2\sqrt{n}$. It is very effective for large n compared to (1) with $c := n$. On the other hand, if b is small, the performance of the matrix multiplication is low.

Next, the superblock family of algorithms [1], a kind of recursive block computation, is introduced. The constant of the error bound of the algorithm is simplified using a technique in [4].

Theorem 2. *For $A \in \mathbb{F}^{m\times n}, B \in \mathbb{F}^{n\times p}$, let T be a result computed by the t-level superblock family algorithm. Define $\gamma_\ell := \ell u/(1 - \ell u)$ for $\ell < u^{-1}$. Then,*

$$|T - AB| \leq (\gamma_{t\lceil \sqrt[t]{n} - t + 1\rceil})|A||B| \tag{3}$$

is satisfied.

It should be noted that if $t = 3$ and the block size for the matrix multiplication is approximately $\sqrt[3]{n}$, then one obtains

$$|T - AB| \lesssim 3\sqrt[3]{n}u|A||B|.$$

2.2. Fast and accurate block summation

Here we introduce the block matrix multiplication based on Fast and Accurate Block summation (FABsum), a block summation algorithm using an accurate summation algorithm [2]. Let T be a computed result by block matrix multiplications using FABsum. A matrix Δ is defined as

$$\Delta := \sum_{i=1}^{s} \mathtt{fl}\,(A_i B_i) - T.$$

If a pure floating-point arithmetic for the sum is applied, then one obtains

$$|\Delta| \le (n-1)u \sum_{i=1}^{s} |\mathtt{fl}\,(A_i B_i)\,|. \tag{4}$$

If accurate summation algorithms are applied, $(n-1)u$ in (4) can be significantly small. The error bound of the block matrix computations then becomes

$$|T - AB| \le bu|A||B| + |\Delta|. \tag{5}$$

This paper applies an algorithm written in Corollary 4.7 in [5], which is an algorithm that produces an approximation of the dot product and its error bound.

2.3. Upper bound of $\|AB\|_\infty$

The popular method for an enclosure of AB is

$$T_d := \mathtt{fl}_\nabla(AB) \le AB \le \mathtt{fl}_\Delta(AB) =: T_u, \tag{6}$$

which involves two matrix multiplications. Here $\mathtt{fl}_\nabla(\cdot)$ and $\mathtt{fl}_\Delta(\cdot)$ mean a computed result with rounding downward and rounding upward, respectively. An upper bound of $\|AB\|_\infty$ is then obtained as

$$\|AB\|_\infty \le \mathtt{fl}_\Delta(\|T\|_\infty), \quad T := \max(|T_d|, |T_u|) \tag{7}$$

where the function max produces a matrix whose elements are the componentwise maximum. If the form (1) is obtained, $\|AB\|_\infty$ is bounded by

$$\|AB\|_\infty \le \|\, |\mathtt{fl}(AB)| + cu|A||B|\, \|_\infty = \max(|\mathtt{fl}(AB)|e + cu|A|(|B|e)), \tag{8}$$

where $e = (1, 1, \ldots, 1)^T \in \mathbb{F}^p$. Hence, the cost for (8) is only a matrix multiplication. An important point in this paper is that computation times in the methods in Subsections 2.1 and 2.2, and the proposed method should be faster than that in (6). The reason is that the upper bound (7) tends to be smaller than that produced by the algorithms in Subsections 2.1 and 2.2, and the proposed method. The performance of the block matrix multiplication and the overhead of the summation must be carefully monitored because the computation times depend on the block size.

3. Proposed method

This paper aims to reduce the upper bound of $|\Delta|$ without applying accurate summation algorithms. The main contribution is avoiding to estimate

$$|A||B| \quad \text{and} \quad |\mathtt{fl}\,(A_iB_i)\,|$$

for the error bound of the sum. By considering the error in the sum step-by-step, a small error bound for the sum can be obtained. The following is a brief description of the proposed algorithm.

Algorithm 1 Proposed method for computing AB and the upper bound of the maximum norm of AB.

```
Input: Matrices $A \in \mathbb{F}^{m \times n}$, $B \in \mathbb{F}^{n \times p}$, block size $b$, and $s = n/b$
Output: The upper bound of the maximum norm of $AB$
$C = \mathtt{fl}(A_1 * B_1)$;
$E = O$;                                                  ▷ $O$ is the zero matrix
for $i = 2, \dots, s$ do
    $T = \mathtt{fl}(A_i * B_i)$;
    $C = \mathtt{fl}(C + T)$;
    $E = \mathtt{fl}_\triangle(E + u|C|)$;
end for
$N = \max(\mathtt{fl}_\triangle(|C|e + Ee + bu|A|(|B|e)))$;   ▷ $e := (1, 1, \dots, 1)^T \in \mathbb{F}^p$
```

Detailed numerical examples will be shown at the conference presentation.

References

[1] A.M. Castaldo, R.C. Whaley, A.T. Chronopoulos, Reducing Floating Point Error in Dot Product Using the Superblock Family of Algorithms, *SIAM J. Sci. Comput.*, 31:2 (2009), 1156–1174.

[2] P. Blanchard, N.J. Higham, T. Mary, A Class of Fast and Accurate Summation Algorithms, *SIAM J. Sci. Comput.*, 42:3 (2020), A1541–A1557.

[3] IEEE Std 754-2008: *IEEE Standard for Floating-Point Arithmetic*, IEEE Computer Society, 2008.

[4] M. Lange, S.M. Rump, Sharp Estimates for Perturbation Errors in Summations, *Math. Comp.* 88 (2019), 349–368.

[5] T. Ogita, S.M. Rump, S. Oishi, Accurate Sum and Dot Product, *SIAM J. Sci. Comput.*, 26:6 (2005), 1955–1988.

Tight enclosure of a matrix product based on BLAS

Katsuhisa Ozaki[1,*]

[1]Department of Mathematical Sciences, Shibaura Institute of Technology, Japan

*ozaki@sic.shibaura-it.ac.jp

Abstract. Herein, enclosure methods of a matrix product for two given floating-point matrices are proposed. Several enclosure methods are based on general matrix multiply in Basic Linear Algebra Subprograms. The number of matrix multiplications is related to the tightness of the radius of an interval matrix and computation time. Existing methods require one, two, three, and five matrix multiplications. Herein, we propose a new enclosure method involving four or five matrix multiplications.

Keywords: Verified numerical computations, Matrix multiplication, Floating-point arithmetic

1. Introduction

Recent architectures are capable of performing floating-point arithmetic at a fast rate. However, the finite precision of binary floating-point numbers, typically defined by IEEE 754 [1] affords a rounding error issue. The verified numerical computations field guarantees the reliability of computed results using only numerical computations. Our goal is to develop efficient enclosure methods for matrix multiplication. Numerical computations are used to enclose the matrix product within an interval matrix. This technique is crucial in verified numerical computations for problems related to numerical linear algebra, such as linear systems, eigenvalue problems, and singular value decomposition.

There are several methods enclosing a matrix product, including methods involving one [2], two, and three and five [3] matrix multiplications. Herein, we propose new enclosure methods involving four or five matrix multiplications. Numerical examples demonstrate that the proposed method with four matrix multiplications produces a tighter interval matrix than the previous method with five matrix multiplications. In addition, the new method with five matrix multiplications produces tight results compared to the previous methods with five matrix multiplications.

2. Notations

Let $\mathbb{F}$ be a set of binary floating-point numbers as defined in IEEE 754 [1]. We define a constant u as the unit round off. The notation $\mathtt{fl}(\cdot)$ indicates a result computed by floating-point arithmetic. For simplicity, we assume that neither overflow nor underflow occurs in $\mathtt{fl}(\cdot)$. A matrix inequality is satisfied elementwise. An interval matrix is denoted with a bold letter. There are two forms for the representation of interval; One is the inf-sup form, i.e.,

$$\mathbf{A} = [\underline{A}, \overline{A}] = \{A \in \mathbb{R}^{m\times n},\ \underline{A} \le A \le \overline{A}\}, \quad \underline{A},\ \overline{A} \in \mathbb{R}^{m\times n}.$$

The other is the mid-rad form, i.e.,

$$\mathbf{A} = \langle C, R\rangle = \{A \in \mathbb{R}^{m\times n}, C - R \le A \le C + R\}, \quad C, R \in \mathbb{F}^{m\times n}, \quad R \ge O \text{ (the zero matrix)}.$$

The notations $\mathtt{fl}_{\triangledown}(\cdot)$ and $\mathtt{fl}_{\vartriangle}(\cdot)$ indicate a computed result with rounding downward and rounding upward as the rounding mode of the floating-point arithmetic. These are defined in IEEE 754 as “Round-to-Negative-Infinity” and “Round-to-Positive-Infinity”, respectively.

3. Enclosure of a matrix product

For $A \in \mathbb{F}^{m\times n}$ and $B \in \mathbb{F}^{n\times p}$, Lange and Rump [4] derived the error bound of the matrix multiplication:

$$|AB - \mathtt{fl}(AB)| \le cu|A||B|, \quad \lceil \log_2 n\rceil \le c \le n, \quad c \in \mathbb{N}. \tag{1}$$

The constant c depends on the height of the binary tree (the calculation order of the dot product is imaged by a binary tree). From (1), we have

$$AB \in \langle \mathtt{fl}(AB),\ cu|A||B|\rangle. \tag{2}$$

Let vectors $e \in \mathbb{F}^p, f \in \mathbb{F}^m, g, h \in \mathbb{F}^n$ be defined as follows:

$$e = (1, 1, \dots, 1)^T, \quad f = (1, 1, \dots, 1)^T, \quad g_j = \max_i |a_{ij}|, \quad h_i = \max_j |b_{ij}|.$$

Ogita and Oishi [5] proposed a method for producing an upper bound of $|A||B|$ as

$$|A||B| \le \min(|A|he^T, fg^T|B|) \le \mathtt{fl}_{\vartriangle}\left(\min(|A|he^T, fg^T|B|)\right) =: T, \tag{3}$$

where the function min produces a matrix with a componentwise maximum. Then, from (2) and (3), AB is enclosed by

$$\langle \mathtt{fl}(AB), T\rangle, \tag{4}$$

where only matrix multiplication is required. The popular enclosure method with two matrix multiplications using directed rounding is given as follows:

$$AB \in [\mathtt{fl}_{\triangledown}(AB), \mathtt{fl}_{\vartriangle}(AB)]. \tag{5}$$

Next, we briefly introduce the existing enclosure methods [3]. We split the matrices as follows:

$$A = A_1 + A_2, \quad B = B_1 + B_2, \tag{6}$$

where

$$\mathtt{fl}(A_1B_1) = A_1B_1, \quad |(a_1)_{ij}| \geq |(a_2)_{ij}| \text{ for } (a_1)_{ij} \neq 0 \text{ and } |(b_1)_{ij}| \geq |(b_2)_{ij}| \text{ for } (b_1)_{ij} \neq 0. \tag{7}$$

Then, from (1) and (6), we have

$$AB \in \langle \mathtt{fl}(A_1B_1) + \mathtt{fl}(A_1B_2) + \mathtt{fl}(A_2B), cu|A_1||B_2| + cu|A_2||B| \rangle. \tag{8}$$

Apply similar techniques in (3) and (4), we obtain matrices T_1 and T_2 without computing a full matrix multiplication such that $cu|A_1||B_2| \leq T_1$ and $cu|A_2||B| \leq T_2$. Then, we have

$$AB \in \langle \mathtt{fl}(A_1B_1) + \mathtt{fl}(A_1B_2) + \mathtt{fl}(A_2B), \mathtt{fl}_{\triangle}(T_1 + T_2) \rangle, \tag{9}$$

which involves three full matrix multiplications. Notably, the following may be satisfied:

$$\mathtt{fl}(A_1B_1) + \mathtt{fl}(A_1B_2) + \mathtt{fl}(A_2B) \notin \mathbb{F}^{m \times p}.$$

The other method based on (6) is to enclose AB by

$$AB \in [\mathtt{fl}_{\triangledown}(\mathtt{fl}(A_1B_1) + A_1B_2 + A_2B), \mathtt{fl}_{\triangle}(\mathtt{fl}(A_1B_1) + A_1B_2 + A_2B)], \tag{10}$$

which requires five matrix multiplications.

4. Proposed methods

4.1. Enclosure method with four matrix multiplications

We use a technique in [6] to split the matrices A and B as follows:

$$A = A_1 + A_2 + A_3, \quad B = B_1 + B_2, \tag{11}$$

where $A_1B_1 = \mathtt{fl}(A_1B_1)$ and $A_2B_1 = \mathtt{fl}(A_2B_1)$. Moreover, we obtain (7) and

$$|(a_2)_{ij}| \geq |(a_3)_{ij}| \text{ for } (a_2)_{ij} \neq 0. \tag{12}$$

We compute

$$AB = A_1B_1 + A_2B_1 + (A - A_3)B_2 + A_3B = \mathtt{fl}(A_1B_1) + \mathtt{fl}(A_2B_1) + \mathtt{fl}(A - A_3)B_2 + A_3B. \tag{13}$$

Notably, $A - A_3 \in \mathbb{F}^{m \times n}$. We enclose $\mathtt{fl}(A - A_3)B_2$ and A_3B using (3) and (4). This enclosure method involves four matrix multiplications.

4.2. Enclosure method with five matrix multiplications

We also employ the technique in [6] to split A and B as follows:

$$A = A_1 + A_2 + A_3 + A_4, \quad B = B_1 + B_2 \tag{14}$$

where $A_1B_1 = \mathtt{fl}(A_1B_1)$, $A_2B_1 = \mathtt{fl}(A_2B_1)$ and $A_3B_1 = \mathtt{fl}(A_3B_1)$. Moreover, We obtain (7), (12), and $|(a_3)_{ij}| \geq |(a_4)_{ij}|$ for $(a_3)_{ij} \neq 0$. We compute

$$\begin{aligned} AB &= A_1B_1 + A_2B_1 + A_3B_1 + (A - A_4)B_2 + A_4B \\ &= \mathtt{fl}(A_1B_1) + \mathtt{fl}(A_2B_1) + \mathtt{fl}(A_3B_1) + \mathtt{fl}(A - A_4)B_2 + A_4B. \end{aligned} \tag{15}$$

Similarly, we have $A - A_4 \in \mathbb{F}^{m \times n}$. We enclose $(A - A_4)B_2$ and A_4B using (3). This enclosure method involves five matrix multiplications.

5. Numerical examples

In this section, we use Intel Core i7-8555U and MATLAB 2022a for numerical examples. We set $A, B \in \mathbb{F}^{n\times n}$ as $A = \texttt{randn}(n)$ and $B = \texttt{randn}(n)$. Tables 1 and 2 indicate computing times (average of ten runs) and the average of computed radii, respectively, where M1, M2, M3, M4, and M5 indicate the methods in (5), (9), (10), (13), and (15), respectively.

Table 1: Comparison of computing times (sec)

size	M1	M2	M3	M4	M5
3000	1.0439e+01	1.7613e+01	2.6073e+01	2.4061e+01	2.8967e+01
5000	2.3833e+01	3.9644e+01	6.0813e+01	5.2907e+01	6.5399e+01
10000	1.1767e+02	1.8560e+02	2.9512e+02	2.6044e+02	3.2495e+02

Table 2: Comparison of computed radii

size	M1	M2	M3	M4	M5
3000	1.7824e-12	4.2083e-16	3.6276e-18	3.2877e-18	1.5411e-19
5000	3.0115e-12	7.3950e-16	6.7042e-18	5.7773e-18	4.5136e-19
10000	6.0853e-12	3.3108e-15	3.1474e-17	1.9399e-17	3.2332e-18

We cannot explain how to obtain (11) and (14) and introduce sufficient numerical examples owing to the page limit restriction. These will be shown in the conference presentation.

References

[1] 754-2019 - IEEE Standard for Floating-Point Arithmetic, IEEE, 2019.

[2] K. Ozaki, T. Ogita, S. M. Rump, S. Oishi: Fast algorithms for floating-point interval matrix multiplication, *Journal of Computational and Applied Mathematics*, 236 (2012), 1795–1814.

[3] K. Ozaki, T. Ogita, S. Oishi: Tight and efficient enclosure of matrix multiplication by using optimized BLAS, *Numerical Linear Algebra With Applications*, 18:2 (2011), 237–248.

[4] M. Lange and S.M. Rump: Sharp estimates for perturbation errors in summations, *Mathematics of Computation*, 88 (2019), 349-–368.

[5] T. Ogita, S. Oishi: Fast inclusion of interval matrix multiplication, *Reliable Computing*, 11:3 (2005), 191–205.

[6] K. Ozaki, T. Ogita, S. Oishi, S. M. Rump: generalization of error-free transformation for matrix multiplication and its application, *Nonlinear Theory and its Applications*, 4:1 (2013), 2–11.

Single shot machine learning based phase retrieval for the X-ray phase imaging

Ryosuke Ueda[1,*] and Atsushi Momose[1]

[1]Institute of Multidisciplinary Research for Advanced Materials, Tohoku University

*`ryosuke.ueda.a7@tohoku.ac.jp`

The full paper of this paper has been published in Journal of Advanced Simulation in Science and Engineering (JASSE).

DOI: `https://doi.org/10.15748/jasse.11.188`

Development of AR Visualization Teaching Materials for 3D Scatter Radiation Distribution in an X-ray Examination Room Using a Head-Mounted Display

Toshioh Fujibuchi[1*], Hiroyuki Arakawa[1], Takashi Yoshinaga[2]

[1] Department of Health Sciences, Faculty of Medical Sciences, Kyushu University

[2] Steampunk Digital, Co. Ltd.

*`fujibuchi.toshioh.294@m.kyushu-u.ac.jp`

Abstract. In this study, we developed an AR application to visualize the scatter radiation distribution during X-ray imaging and X-ray CT examinations to address the increasing occupational radiation exposure risks faced by medical radiation practitioners due to the growing use of radiological imaging. Monte Carlo simulation codes were employed to simulate the scatter radiation distribution, and the accuracy was validated by comparing the results with measured data. Subsequently, we developed an application using Quest2 and HoloLens2 to visualize the scatter radiation distribution in X-ray rooms and X-ray CT rooms, respectively. The difference between the scatter radiation measurement values obtained from Monte Carlo simulation and survey meters was within an average of 10%. Three-dimensional scatter radiation distributions were successfully displayed with a sense of immersion and stereoscopic vision.

Keywords: Augumented rearity, Monte carlo simulation, Radiography, Computed tomography, Head-mouted display

1. Introduction

The use of radiological imaging continues to increase both domestically and internationally. In Japan, the number of X-ray CT devices per million people was 111.5 in 2017, which is higher than in other major countries [1]. Consequently, there is a possibility of occupational exposure to radiation for medical practitioners, such as physicians, radiological technologists, and nurses, who may enter the examination room during imaging procedures [2].

Understanding the distribution of scatter radiation is crucial for radiation protection measures during X-ray examinations. However, scatter radiation is invisible, making it difficult to visualize. Moreover, as radiation spreads in three dimensions, the recognition and understanding of scatter radiation spread using two-dimensional distributions have limitations. Previous studies have utilized Monte Carlo simulation codes to simulate scatter radiation distribution and displayed them in three dimensions using augmented reality (AR) technology on PC screens or iPads [3, 4]. By visualizing and displaying the three-dimensional scatter radiation distribution in real size using a head-mounted display, it is possible to enhance immersion, stereoscopic vision, and realism, thus facilitating intuitive recognition of dangerous and safe positions during assistance.

The objective of this study is to develop an AR application that visualizes the scatter radiation distribution during X-ray imaging and X-ray CT examinations, compatible with head-mounted displays.

2. Materials and Methods

2.1 Simulation of scatter radiation distribution

PHITS was used as the Monte Carlo simulation code[5]. X-ray imaging devices and X-ray CT devices were replicated, and the three-dimensional scatter radiation distribution in the room was measured at more than 20 points using an ionization chamber survey meter and compared with the simulation results. After verifying the calculation accuracy, the three-dimensional scatter radiation distribution when irradiating an ICRP 110 voxel phantom representing a patient model with X-rays was calculated [6]. The calculation results were imported into the Unity 2019.4.26f1 game development engine to create an AR application.

2.2 Display of scatter radiation volume data in X-ray imaging rooms

MetaQuest2 (Meta) was used as the AR device to augment the scatter radiation volume data in real space. The axes of x, y, z cross-sections and the color scale of the dose can be adjusted arbitrarily using a controller. Additionally, the virtual space can be scaled down to enable tabletop exercises.

2.3 Display of three-dimensional scatter radiation distribution in X-ray CT rooms

HoloLens2 (Microsoft) was used as the AR device. AR markers were placed at the isocenter of the gantry, and the coordinates of the real space and 3D objects were adjusted.

3. Results

3.1 Accuracy of the Simulation

The difference between the measured scattering values using the survey meter for Monte Carlo simulations was within an average of 10%.

3.2 Display of Scattering Volume Data in X-ray Imaging Room

Figure 1 shows the AR image inside the X-ray imaging room. The image appears with a black background, but it is possible to display real-space images in pass-through mode.

3.3 Display of 3D Scattering Distribution in X-ray CT Room

Figure 2 shows the 3D scattering distribution image in the X-ray CT room. The real-space device and the 3D scattering distribution could be overlaid and displayed. With Hololens2, once the AR marker is recognized, the 3D object remains visible and aligned even when moving away from the line of sight.

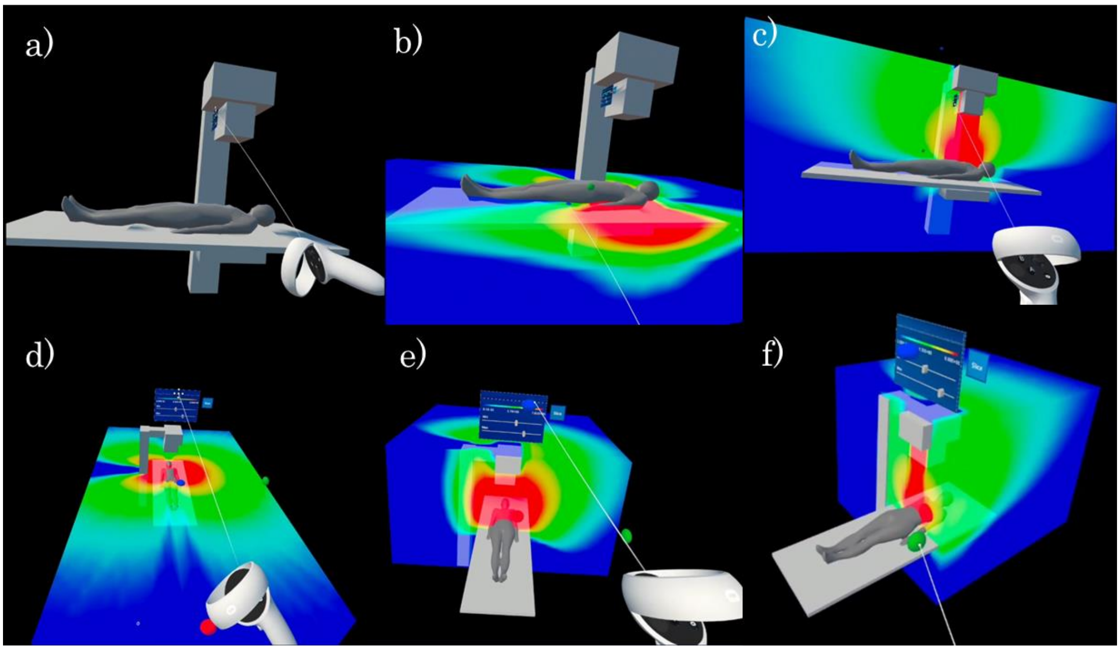

Figure 1: Display of Scattering Volume Data during Supine X-ray Irradiation using Quest 2

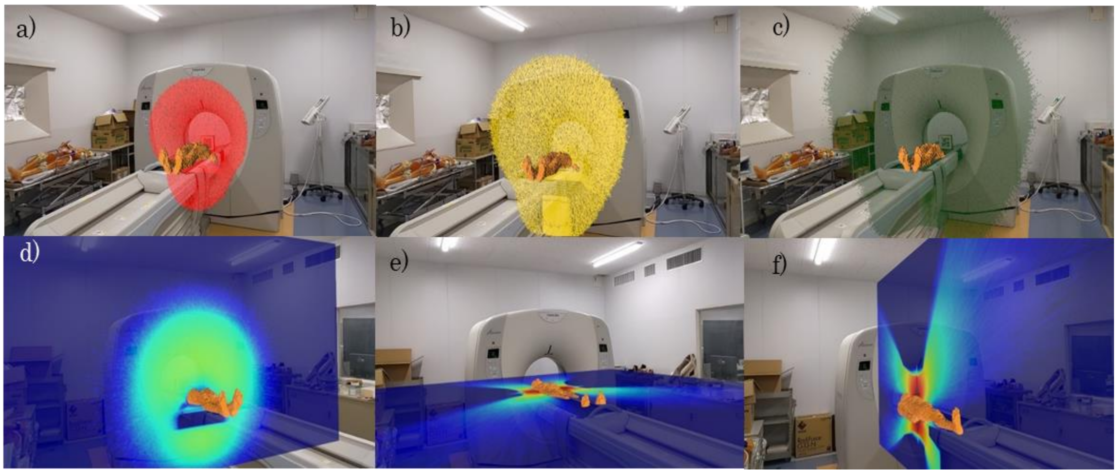

Figure 2: Display of Scattered radiation in CT room displayed for each 3D dose and each cross sections using Hololens 2

4. Disucussion

The use and challenges of AR applications involve increasing the sense of presence by displaying scattering rays at actual size and allowing real-time observation in the actual inspection location. Additionally, by overlaying 2D and 3D representations, it becomes possible to compare the differences in perception due to the display methods. Therefore, it is expected to facilitate users' understanding of the spread of scattering rays. In radiation protection education, the principle of ALARA (As Low as Reasonably Achievable) outlined by the International

Commission on Radiological Protection is crucial. However, if the created AR application is used solely for healthcare professionals and students with limited opportunities for radiation protection education, there is a possibility of excessive fear, false reassurance, or misconceptions regarding radiation exposure. Therefore, it is necessary to consider evaluation methods when using this AR application for radiation protection education, such as conducting lectures on dose limits during medical radiation exposure and occupational exposure.

5. Conclusion

We have developed an AR application that visualizes the scattering distribution during X-ray imaging and CT examinations in real-space and allows observation from any position and angle, providing a sense of presence. By using this application with an AR head-mounted display in the CT examination room, intuitive understanding of the spread of scattering rays and locations with high dose rates could be achieved. In the future, it is necessary to further improve the usefulness of the AR application by considering display methods and evaluation methods for radiation protection education.

References

[1] OECD, Health at a Glance 2019: *OECD Indicators*, OECD publishing (2019), Paris.

[2] T. Fujibuchi, K. Fujita, T. Igarashi et al.: Proposal for Reduction Measures of Eye Lens Exposure Based on Actual Exposure Management in Radiation-exposed Medical Staff, *Japanese Journal of Radiological Technology*, 77 (2021), 161-171.

[3] T. Fujibuchi: Radiation protection education using virtual reality by visualization of scatter distribution in radiological examination, *Journal of Radiological Protection*, 41 (2021), S317.

[4] K. Nishi, T. Fujibuchi, T. Yoshinaga, Development of an application to visualise the spread of scattered radiation in radiography using Augmented Reality, *Journal of Radiological Protection*, 11(2020), 1299-1310.

[5] T. Sato, Y. Iwamoto, S. Hashimoto, et al.: Features of Particle and Heavy Ion Transport code System (PHITS) version 3.02, *Journal of Nuclear Science and Technology*, 55 (2018), 684-690

[6] ICRP, 2009. Adult Reference Computational Phantoms. ICRP Publication 110.

[7] ICRP, Recommendations of the International Commission on Radiological Protection, ICRP Publication 60, *Ann. ICRP*, 21 (1990)

Investigation of patient release examination training in nuclear medicine using Mixed Reality

Hiroyuki Arakawa[1,*] , Toshioh Fujibuchi[1], Yoshihiro Okada[2], Kosuke Kaneko[3],
Toshiko Tomisawa[4]

[1]Department of Health Sciences, Faculty of Medical Sciences, Kyushu University
[2]Innovation Center for Educational Resources, Kyushu University Library
[3]Robert T.Huang Entrepreneurship Center, Kyushu University
[4]Department of Nursing Science, Graduate School of Health Sciences, Hirosaki University

[*]`arakawa.hiroyuki.306@m.kyushu-u.ac.jp`

The full paper of this paper has been published in Journal of Advanced Simulation in Science and Engineering (JASSE).

DOI: `https://doi.org/10.15748/jasse.11.125`

Study on effect of oxygen concentration in water radiolysis using Geant4-DNA

Tsukasa Aso[1*], Shun Fukagawa[1], Yoshiyuki Hirano[2], Masanori Hara[3], Susumu Fujiwara[4]

[1] National Institute of Technology, Toyama College
[2] Nagoya University
[3]University of Toyama
[4] Kyoto Institute of Technology

`*aso@nc-toyama.ac.jp`

Abstract. The effect of the presence of dissolved molecular oxygen in water radiolysis was studied using a Geant4-DNA Monte Carlo simulation. The simulation included physics and chemistry processes, in which 72 chemical reaction channels were registered including reactions of dissociated molecules with dissolved oxygen in water. In order to verify the chemical reactions, time dependent yields of OH radical and e_{aq}^- by 5 MeV proton irradiation were calculated for two different oxygen concentrations. In addition, time dependent yields of several molecular species by 4.5 keV electron irradiation were calculated to study a production of O_2^- and HO_2 radicals, which is hypothesized to be linked to the oxygen sensitization effect in biological systems.

Keywords: Geant4-DNA, Oxygen concentration, Reactive oxygen species

1. Introduction

Ionizing radiation induces DNA damages through direct interactions of radiation particles and indirect interactions of reactive oxygen species (ROS) created in water radiolysis. For low LET radiation particles such as electron and proton, it is commonly known that the indirect effect takes place comparable or more contribution to DNA damages through abstraction of deoxyribose hydrogens by hydroxyl (OH) radicals than the direct effect. In addition, the radiosensitivity of biological systems is strongly affected by the target oxygenation. There are two mechanisms are considered that increase DNA damages by production of the superoxide anion (O_2^-) and its protonated form (HO_2), and the inhibition of the subsequent biological DNA repair process by the existence of oxygen species. However, the nanoscopic mechanism is still not completely understood.

To study the effect of the presence of dissolved molecular oxygen in water radiolysis, the Geant4-DNA Monte Carlo simulation was used to calculate the transport of particle radiation in water and the chemical reactions of water radiolysis [1-4]. The results are presented in the time dependent yields of chemical species for several oxygen concentrations and compared with the results reported in [5].

2. Materials and Methods

The Geant4-DNA is an extension of Geant4, which can simulate electromagnetic physics and water radiolysis in atomic scale including diffusions and reactions of chemical species. The Geant4 version 11.1.0 was used in this study. We utilized the "scavenger" example code in the Geant4 distribution, in which the G4EmDNAPhysics_option2 and the EmDNAChemistry were activated in the physics-list for the physics and chemistry processes. We revised the dissociation channels and the reaction table for chemical species in the EmDNAChemistry to be identical to that of G4EmDNAChemistry_option3 which consists of 72 reactions including production channels of O_2^- and HO_2 radicals and its reaction rates (k). We additionally registered four reactions for H, e_{aq}^-, O, and O^- with dissolved oxygen in water. The concentration of molecular oxygen dissolved in water, C_{O_2} [mole/dm^3], is calculated by $C_{O_2} = pO_2 \cdot H_c$ with the partial pressure of oxygen, pO_2 [atm], and $H_c = 1.3 \times 10^{-3}$ [mole/(L · atm)] being the coefficient of Henry's law for oxygen solubility in water. The reaction rate related to the dissolved oxygen is then recalculated as $C_{O_2} \cdot k$ [s^{-1}].

The simulation was performed assuming in an infinite simulation space filled with water, while the primary particle track was only simulated inside a cubic volume of 5 μm side. The G-value was calculated as the yield of chemical species averaged in 100 eV energy deposits.

3. Results and discussion

Figure 1 shows the result of the time dependent yields of OH radical and e_{aq}^- by 5 MeV proton irradiation, in which the result in [5] is also shown for comparison. Although the initial yield of OH radical in this study is about 10% larger than that in [5], it becomes consistent each other after the 1 ns diffusion time. The presence of oxygen does not affect to the yield of OH radical, whilst it strongly consumes the e_{aq}^-. This is because the OH radical does not have direct reaction channel with oxygen, however, e_{aq}^- directly reacts with oxygen through $e_{aq}^- + O_2 \rightarrow O_2^-$. The effect of dissolved oxygen to the time dependent yields of e_{aq}^- in this study agrees well with the result in [5].

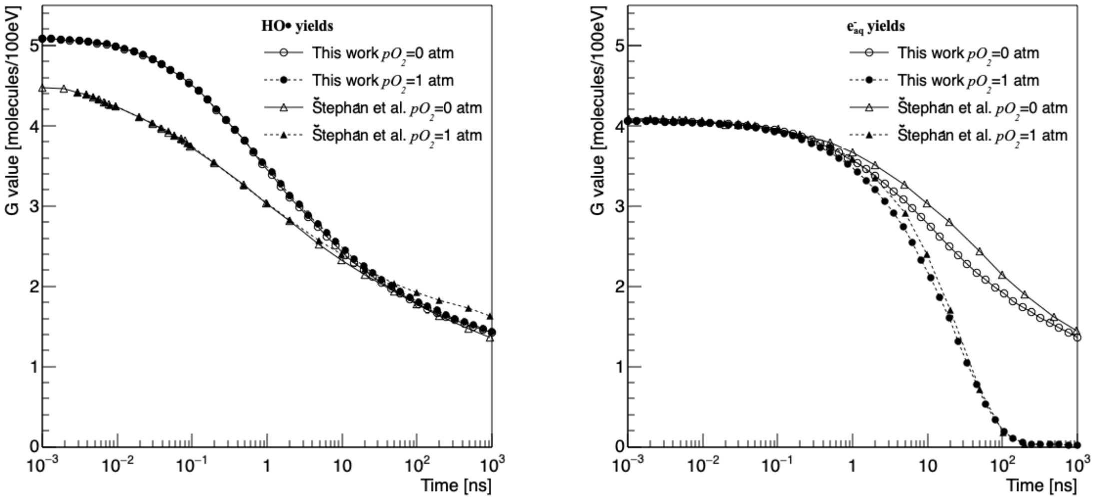

Fig. 1 Comparison of time dependent yields for OH radical and e_{aq}^- by 5 MeV proton irradiation in water with complete anoxia (open symbol) and with an oxygen concentration of 1 atm (closed symbol) for this work (circle) and Štephán et al. [5] (triangle), respectively.

Figure 2 shows time dependent yields of several chemical species by 4.5 keV electron irradiation for oxygen concentrations of 0% (complete anoxia) and 21% (fully aerated condition), respectively. Since there are direct reaction channels with dissolved oxygen for e_{aq}^- (e_{aq}^- $+ O_2 \rightarrow O_2^-$) and H radical ($H + O_2 \rightarrow HO_2$), the molecular oxygen dissolved in water for the 21% oxygen concentration almost consumes e_{aq}^- and H radical within 1 μs. On the other hand, these reactions produce O_2^- and HO_2 radicals. The yields of these species increase from 1 ns to 1 μs and lead to a saturation in conjunction with consumption of e_{aq}^- and H radical.

These results confirm productions of two ROSs, O_2^- and HO_2 radicals, in oxygen dissolved water, which is not occur in anoxic conditions. Further studies are required to explain the oxygen sensitization effect in biological systems by taking account for contributions of these ROSs to DNA damages.

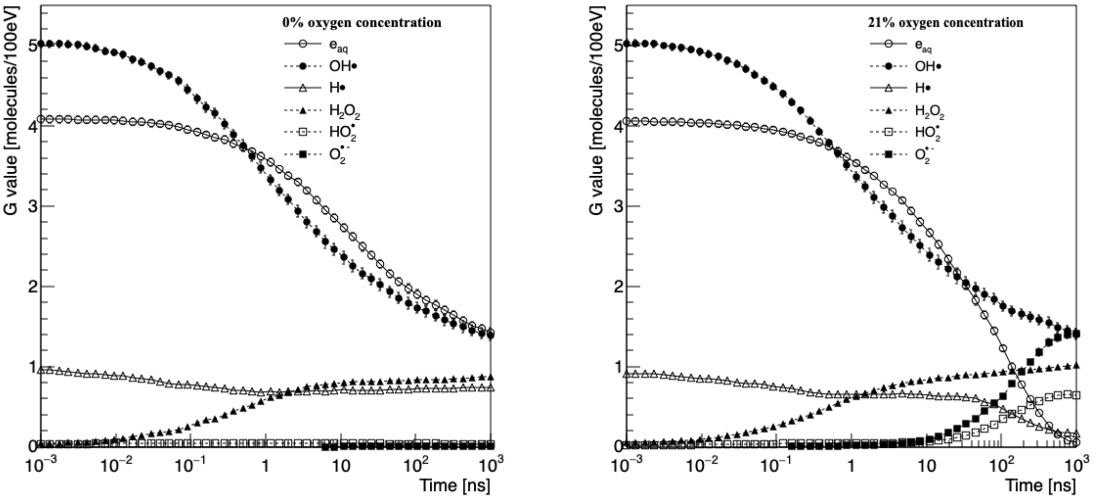

Fig. 2 Comparisons of the time dependent yields for several chemical species by 4.5 keV electron irradiation in water with a partial oxygen pressure of 0% (left) and 21% (right), respectively.

References

[1] S. Incerti et al.: Geant4-DNA example applications for track strucrue simulation in liquid water: a report from the Geant4-DNA project, *Med. Phys.*,45 (2018), e722-e739.

[2] M. A. Bernal et al.: Track structure modeling in liquid water: A review of the Geant4-DNA very low energy extension of the Geant4 Monte Carlo simulation toolkit, *Phys. Med.*, 31(2015), 861-874.

[3] S. Incerti et al.: Comparison of Geant4 very low energy cross section models with experimental data in water, *Med. Phys.*, 37(2010), 4692-4708.

[4] S. Incerti et al.: The Geant4-DNA project, *Int. J. Model. Simul. Sci. Comput.*, 1(2010), 157-178.

[5] V. Štepán and M. Davídková: Impact pf oxygen concentration on yields of DNA damages caused by ionizing radiation, *J. Phys. Conf. Ser.*, 101(2008), 12015.

Calorimetric Evidence of New Temperature Anomaly In Trehalose Dihydrate

Soichi Tatsumi[1,*], Reon Oka[1], Yasunari Yato[1], Keisuke Yamakawa[1], Yasuo Saruyama[1], Haruhiko Yao[1]

[1]Faculty of Materials Science and Engineering, Kyoto Institute of Technology

*`statsumi@kit.ac.jp`

Abstract. The thermal properties of trehalose dihydrate were investigated in an environment where water does not evaporate. We found thermal anomalies at around 80 ° C (LTA) and around 160° C (HTA). We confirmed that LTA disappeared by completing HTA and the glass transition derived from trehalose hydrate appeared around 20 ° C after the disappearance of LTA. It suggests the emergence of trehalose hydrate with about 1.3 water molecules per 1 trehalose. Therefore, we concluded that HTA is caused by the high-temperature phase separation of trehalose hydrate.

Keywords: Calorimetric Measurements, Glass transition, trehalose-dihydrate

1. Introduction

Trehalose is a disaccharide formed by the glycosidic linkage of glucose and is found in many plants and animals in nature. This substance is of interest because of its association with an extreme environment survival strategy called cryptobiosis, which is observed in certain microorganisms. For example, the larvae of the polypedilum vanderplanki are known to replace the water in their bodies with trehalose under extremely arid conditions. This mechanism prevents water evaporation and the destruction of body tissues by freezing. In addition, the larvae of the polypedilum vanderplanki can withstand temperatures exceeding 100 ° C for a short period of time in the cryptobiosis state, which is believed to be due to the high glass transition temperature of trehalose and the glassy state[1]. However, as reported in the aforementioned article, the dried larvae contain a small amount of water, and their composition ratio is equivalent to trehalose dihydrate, where trehalose in its natural state is considered to be dihydrate. However the glass transition temperature of trehalose dihydrate is very low at about -20° C[2], so it is not realistic to attribute its high-temperature resistance to the amorphous nature of trehalose. A more detailed study of the properties of trehalose dihydrate is required for a deeper understanding of the mechanism behind cryptobiosis.

In this talk, we will focus on the thermal anomaly around 80 °C (LTA) and the thermal anomaly around 160 ° C (HTA), which are newly discovered thermal properties of trehalose

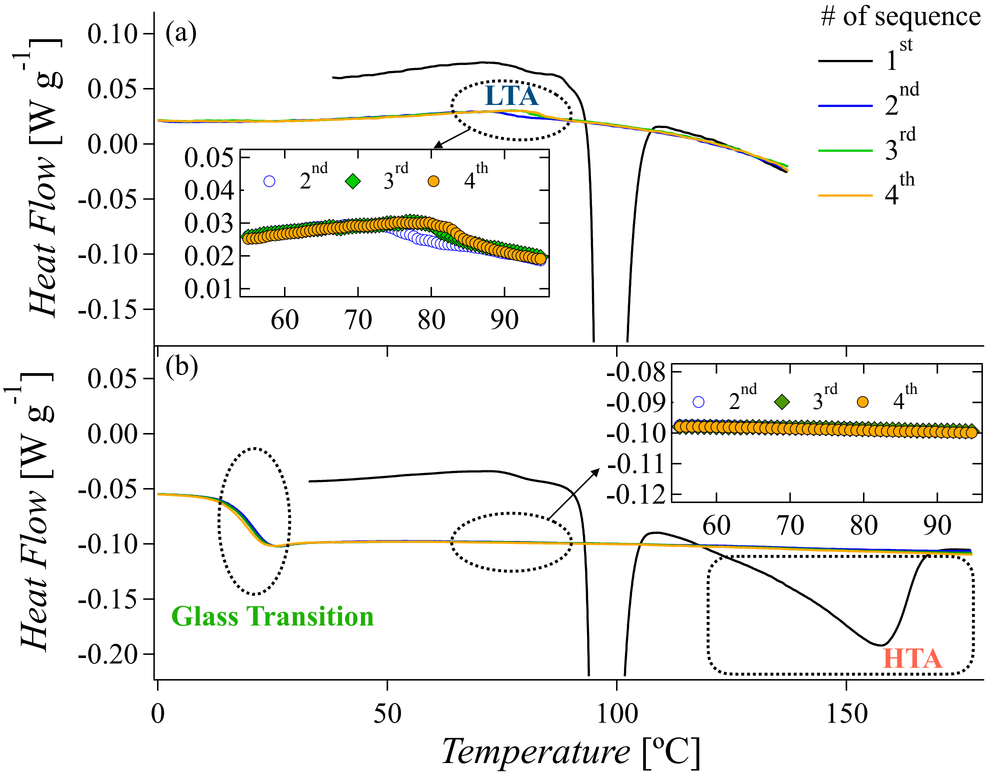

Figure 1: Schematics of thermogram without completion of HTA (a) and with completion of HTA (b). The first runs of both figures indicate the melting of crystalline trehalose dihydrate. While the thermogram shown in Fig.(a) stops the temperature scan at around 130 °C, Fig.(b) goes around 180° to complete HTA. The consequent runs of them indicate the thermal properties of liquid trehalose dihydrate. The inset of Fig. a represents the LTA of liquid trehalose dihydrate with an effect of repetition of measurements. The inset of Fig. b demonstrates the disappearance of LTA with the completion of HTA.

dihydrate and appear only in the direction of temperature increase. This is due to the fact that after the completion of HTA, the glass transition is induced at around 20 °C. This suggests that after the completion of HTA, trehalose hydrate separates into a phase that contains plenty of water and a phase that contains little water.

2. Thermal Analysis & Anneal Effect

Trehalose dihydrate has a melting point of around 100 °C. Once melted, recrystallization is unlikely to occur in a sealed environment. Figure 1 shows the thermograms of melting of crystalline trehalose dihydrate and the thermal behavior of liquid trehalose measured using DSC 2920 (TA Instruments Co., Ltd.). Without and with the completion of thermal anomalies at around 160 °C (HTA), the appearance of thermal anomalies around 80-90 °C (LTA) is changed as shown in the inset. Without completion of HTA(Fig.1(a)), LTA is appeared and shifts to the higher temperature with repetition of temperature scan, while with completion of HTA (Fig.1(b)), LTA disappeared completely as shown in the inset and instead a glass transition appeared around 20 °C.

Next, the properties of LTA were examined in detail in terms of the annealing effect. Figure 2 shows the annealing temperature dependence of the temperature at which LTA develops (T_{LTA}) after annealing at different temperatures for 3 hours. As can be seen from this figure, the thermal anomaly does not disappear but remains even when annealed at a temperature higher than T_{LTA}. This is a very strange result considering that the annealing effect usually has the property of eliminating thermal anomalies that occur at temperatures lower than the annealing temperature.

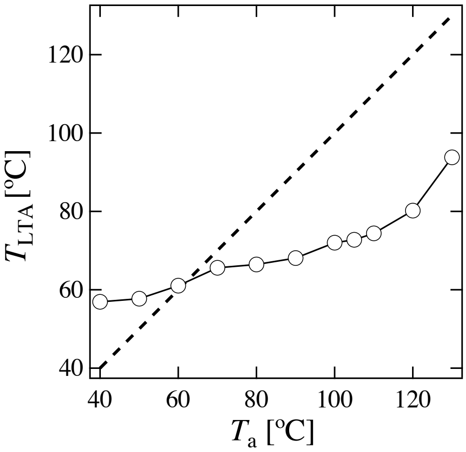

Figure 2: The temperature of LTA (T_{LTA}) as a function of annealing temperature (T_{a}). Dashed line indicate the $T_{\mathrm{LTA}} = T_{\mathrm{a}}$.

3. Summary and Relation with Cryptobiosis

The thermal anomalies we found in trehalose dihydrate have not received much attention in the past. The correlation between the two thermal anomalies, HTA and LTA, is particularly important. As mentioned in the previous section, the appearance of the glass transition at around 20° C in samples with completion of HTA and loss of LTA corresponds to the presence of about 1.3 water molecules for each molecule of trehalose. Therefore, it is suggested that phase separation occurs between trehalose containing a small amount of water and pure water or water-rich trehalose with the completion of HTA. As for the origin of LTA, trehalose dihydrate has a tendency to be homogeneous as a dihydrate near room temperature, and we would like to consider the possibility that a thermal anomaly occurs as a process to resolve the concentration inhomogeneity with temperature change. In the aforementioned previous study, a slow temperature change was important in the high-temperature tolerance experiment of the larvae of polypedilum vanderplanki. Based on our proposal, this corresponds to the request for a condition to change temperature with moderate to maintain a uniform solution state as a property of trehalose dihydrate. In my presentation, I will discuss the above scenario with a more detailed enthalpy analysis, and discuss what kind of approach is possible by numerical calculation.

References

[1] M. Sakurai, et al.: Vitrification is essential for anhydrobiosis in an African chironomid, Polypedilum vanderplanki, *Proc. Nat. Acad. Sci. (USA)*, 105(2008), 5093

[2] O. S. McGarvey, V. L. Kett, and D. Q. M. Craig: An investigation into the crystallization of α,α-trehalose from the amorphous state, *J. Phys. Chem. B* 107 (2003), 6614-6620

[3] Yasunari Yato: High temperature anomaly in liquid trehalose dihydrate, *Master Thesis at Kyoto Institute of Technology*, (2020)

Investigation of the impact of human contact for the onset of pediatrics infectious diseases and Kawasaki Disease

Souta Kunii[1*], Yoshihide Shibata[2], Shinsuke Hoshino[3], Ryusuke Ae [4],
Hiromichi Hamada [5]

[1]Advanced Course for Interdisciplinary Technology Development,
National Institute of Technology, Gifu College
[2]Department of Electrical and Computer Engineering,
National Institute of Technology, Gifu College
[3] Department of Pediatrics, Shiga University of Medical Science
[4] Division of Public Health, Center for Community Medicine, Jichi Medical University
[5] Department of Pediatrics, Graduate School of Medicine, Chiba University

***2022y10@stu.gifu-nct.ac.jp**

Abstract. Kawasaki disease (KD) is a specific disease in children and its mechanism of onset has not been clarified. Bacteria, infections and autoimmune abnormalities are considered as potential causes of pathogenesis in KD [1]. During the COVID-19 epidemic period in 2020, the rapid decrease of KD patients was observed compared with the number of ones in previous years [2]. During the same period, a rapid decrease of pediatrics infectious diseases (PIDs) was also observed [3]. In this study, we focused on the effect of human contacts for KD and PIDs. Data on the population staying at major train stations in each prefecture were used to assess human contacts [4]. We used nationwide KD survey from Jichi medical univ. as KD patients' data [5] and Infectious Disease Weekly Report (IWDR) in national institute of infectious disease in Japan as PIDs patient data [6]. We evaluated the relationship between the decreases of KD, PIDs, and human contact, respectively. As a result, it was found that there was no correlation between decreases of KD and the population staying at major train stations after 19 weeks of 2020 and there were different correlations between decreases of KD and PIDs.

Keywords: Kawasaki disease, Pediatrics infectious disease, human contact, medical and engineering collaboration

1. Introduction

Kawasaki disease (KD) is an acute febrile illness in children and the cause of the disease is still unknown [1]. Before the COVID-19 epidemic period, the number of KD patients was increasing on every year in Japan [5]. However, the number of KD patients in 2020 was 35.6% lower than in one in 2019 [2]. In addition, the number of pediatric infectious diseases (PIDs) during the COVID-19 pandemic periods were lower than in previous years and still continued to the end of 2020 [3].

Bacteria, infections and autoimmune abnormalities are considered as potential causes of pathogenesis in KD [1]. In 2020, the rapid decrease of the number of PIDs and KD patients in Japan was observed. In this study, we focused on the effect of human contacts for KD and PIDs. Data on the population staying at major train stations in each prefecture were used to assess human contacts [4]. We used nationwide KD survey from Jichi medical univ. as KD patients' data [5] and Infectious Disease Weekly Report (IWDR) in national institute of infectious disease in Japan as PIDs patient data [6].

2. Used data and analysis method

For data on KD patients, we used the 25th and 26th national KD survey conducted by Jichi Medical University. These include data on gender, age, and other characteristics of patients from 2017 to 2020. The Infectious Disease Weekly Report (IDWR) [6] was used for data on PIDs patients. For this study, data on the number of cases of 10 designated pediatric infectious diseases (RS virus infection, Group A streptococcal pharyngitis, Infectious gastroenteritis, Chickenpox, Hand-foot-and-mouth disease, Erythema infectiosum, Exanthem subitum, Herpangina, Mumps, Pharyngoconjunctival fever) from 2017 to 2020 were used as PIDs. Population data in major stations were obtained from Mobile Spatial Statistics [4] provided by NTT DOCOMO inc. For this study, we used data on the population in major stations on 47 prefectures from 2017 to 2020[4]. It should be noted that the age of the population data in the major station ranged from 20s to 40s as data of parents in KD patients. Time periods for evaluation were assumed to be 8, 12, and 18 o'clock.

From these data, we determined the change rate in the number of cases of KD, designated pediatric infectious diseases, and the average population at major train stations in the 47 prefectures at 8:00, 12:00, and 18:00. The definition of the change rate is as follows;

$$\text{the rate of change} = (P_{2020} - P_{2017-2019}) \times 100/(P_{2017-2019}) \cdots (1)$$

where P_{2020} is the values in 2020 and $P_{2017-2019}$ is the averaged value from 2017-2019. Figure 1 shows the change in the population at Shinjuku Station in 2017-2019 and 2020. Population changes in 2017-2019 were small. However, in 2020, the population decrease from 10 to 18 weeks and has recovered after 18 weeks. Therefore, 1-18 weeks was defined as decay phase, and after 18 weeks was defined as recovery phase in this study. We evaluated the correlation between KD, PIDs, and population in both phases.

3. Result and discussion

Scatter plots of the percentage change in KD and population are shown in Figure2. Correlation coefficients are also shown in the upper of Figure 2. Population data was used at 8:00. The blue dots are data during the decay phase and the red dots is data during the recovery phase. Change rate between KD and population was similar during decay phase. On the other hand, Change rate for KD was higher than change rate for population during recovery phase. The reason for this may be due to measures against infectious diseases. It is considered that COVID-19 has changed people's lifestyles. In the decay phase, the correlation coefficient was 0.57, a positive correlation. In the recovery phase, there was no correlation with a correlation coefficient of -0.26.

The correlation coefficients between the 10 PIDs and the population for each week are shown in Figure3. Correlation coefficients are compared for each PIDs. In the decay phase, there was a strong positive correlation in almost PIDs. In the recovery phase, many of the correlation coefficient were positive. However, the correlation coefficient value was various in each PIDs.

The correlation coefficients between KD and PIDs for each week are shown in Figure 4.In the decay phase, there was generally a strong positive correlation. However, in the recovery phase, there were large differences in correlation coefficients for each PIDs.

4. Conclusion

There was no correlation between KD and population in recovery phase. There was a positive correlation between PIDs and population. There were different correlations between KD and PIDs for each PIDs. Based on these results, we consider that COVID-19 infection control affected KD onset.

References

[1] R. Ae, N. Makino, K. Kosami, M. Kuwabara, Y. Matsubara, Y. Nakamura, Epidemiology, treatments, and cardiac complications in patients with Kawasaki disease: the Nationwide Survey in Japan, 2017-2018. J Pediatr 2020; 225:23-9.e2.

[2] R. Ae, N. Makino, M. Kuwabara, Y. Matsubara, K.Kosami, T.Sasahara, Y. Nakamura: Incidence of Kawasaki Disease Before and After the COVID-19 Pandemic in Japan: Results of the 26th Nationwide Survey, 2019 to 2020, *JAMA Pediatr*, **176:12** (2022), 1217-1224.

[3] R. Ae, Y. Shibata, T. Furuno, T. Sasahara, Y. Nakamura, H. Hamada, Human mobility and droplet-transmissible pediatric infectious diseases during the COVID-19 pandemic., Int. J. Environ. Res. Public Health, 2022;19(11):6941.

[4] Mobile spatial statics, NTT DOCOMO [Website of mobile spatial statics in NTT DOCOMO]. Available online: https://mobaku.jp (accessed on 5 June 2023).

[5] Nationwide Survey of Kawasaki Disease, Japan [Website of Kawasaki disease Surveillance Data] (in Japanese). Available online: https://www.jichi.ac.jp/dph/inprogress/kawasaki/ (accessed on 9 June 2023).

[6] National Institute of Infectious Disease, Japan [Website of IDWR Surveillance Data]. Available online: https://www.niid.go.jp/niid/en/data.html (accessed on 9 June 2023).

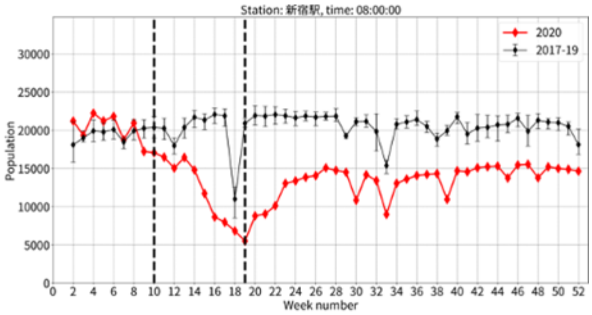

Figure 1 Change of population at Shinjuku station in 2020

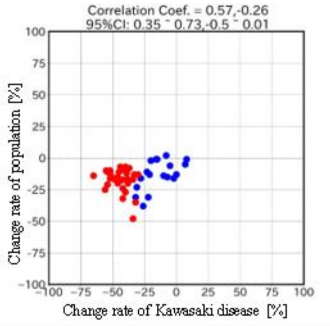

Figure 2 Correlation between percent changes in KD and population at major station.

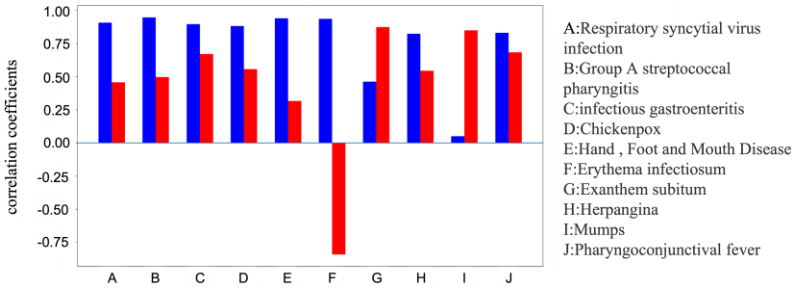

Figure 3 Comparison of correlation coefficients between PIDs and population at major station.

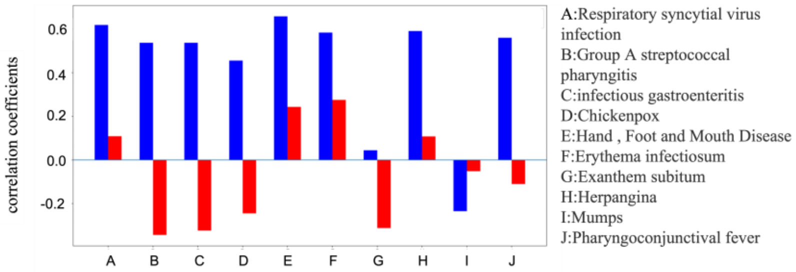

Figure 4 Comparison of correlation coefficients between PIDs and KD.

Trajectory Tracking Control of Lizard-Inspired Single-Actuated Robot based on Inverse Kinematics

Shunsuke Nansai[1,*] and Norihiro Kamamichi[2]

[1]Office for Establishment of New Faculty, Akita University
[2]Department of Robotics and Mechatronics, Tokyo Denki University

*`nansai@gipc.akita-u.ac.jp`

Abstract. The purpose of this paper is to design a trajectory-tracking control system based on inverse kinematics for the Lizard-inspired robot, which is a novel 1-DOF-driven robot. The primary focus of the control system is to converge the position error, the attitude error, and the control input. To accomplish this, we derive recursion formulas for position and posture errors and utilize inverse kinematics to obtain the control input in three steps. The effectiveness of the designed control system is validated through numerical simulations.

Keywords: Single Actuated Robot, Tracking Control, Kinematics

1. Introduction

Mobile mechanisms with limited degrees of freedom have garnered significant attention as an innovative means of achieving compact and lightweight mobile devices [1, 2]. Nonetheless, there are still several challenges that need to be addressed. In response, we have proposed a novel solution called the Lizard-Inspired Single-Actuated robot, which offers a new morphology capable of overcoming these issues [3].

The purpose of this paper is to design a trajectory-tracking control system based on inverse kinematics. This paper is a first step in designing an advanced control system for a lizard-inspired robot. A linear trajectory close enough to the robot is chosen as a reference trajectory to design a control system that does not consider input and state constraints. For this purpose, we first formulate the forward kinematics of the robot. Then, we derive the recursion formulas for the position and attitude errors. Then, we consider the recursion formulas in three steps to converge the position error, the posture error, and the control input, and determine the control input by inverse kinematics. The effectiveness of the designed control system is verified through numerical simulation.

2. Kinematics

In this section, the forward kinematics is formulated. Figure 1 shows a schematic figure of the robot. In Fig. 1, let l be the length of $\overrightarrow{P_1P_2}$ and $\overrightarrow{P_3P_4}$ with $l = 0.1$ m, and let d be the

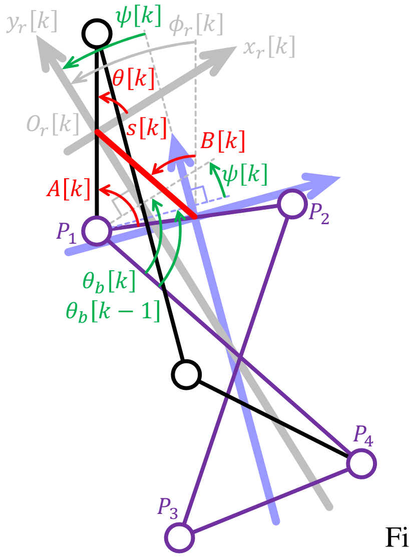

Figure 1: Schematic of the lizard-inspired robot.

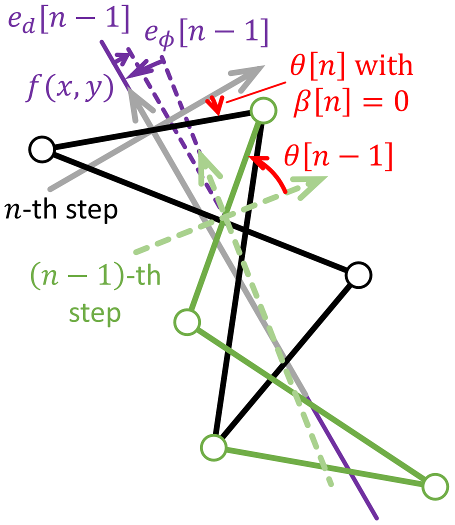

Figure 2: The schematic figure of the control strategy. When the robot converges to the reference trajectory at the n-th step, the control input at or before the n-1st step is determined so that all three of the position error, attitude error, and control input converge.

length of $\overrightarrow{P_2P_3}$ and $\overrightarrow{P_1P_4}$ with $d = 0.2$ m.

We now formulate $\theta[k]$ as $\theta[k] = (-1)^k\alpha + \beta[k]$ for $k = 0, \cdots, n$. In this equation, α [rad] is the amplitude. $\beta[k]$ [rad] is the bias of the amplitude and is the control input in this study. k, $(k = 0, \cdots, n)$ is the number of times the support legs are switched. From Fig. 1, the turning angle is generalized as follows [3]:

$$\psi[k] = (-1)^k\left(\theta_b[k] - \theta_b[k-1]\right), \quad k = 1, \cdots, n. \tag{1}$$

$$\theta_b[k] = \cos^{-1}\left(\frac{l}{d}\cos\theta[k]\right).$$

The stride length is also generalized as follows [3]:

$$s[k] = \operatorname{sgn}(A[k])\, l \sin\left(\frac{A[k]}{2}\right), \qquad k = 1, \cdots, n. \tag{2}$$

$$A[k] = \theta[k] - \theta[k-1] + \phi[k].$$

Where, sgn(·) is a sign function. The posture is formulated as follows [3]:

$$\phi_r[k] = \sum_{n=1}^{k}\psi[n] + \phi_r[0]. \tag{3}$$

An angle between the stride length and the y-axis of the absolute coordinate is formulated as follows:

$$B[k] = \frac{A[k]}{2} + \theta[k-1] + \phi_r[k-1], \quad k = 1, \cdots, n.$$

3. Control System Design based on Inverse Kinematics

In this section, we present the design of a trajectory-tracking control system using inverse kinematics. Our study focuses on a linear trajectory, assuming that the distance between the reference trajectory and the robot is sufficiently close. Our goal is to develop a control system that converges not only the distance and posture but also the control input. To achieve this, we first derive the recursion formulas for the error in both distance and attitude. From Fig. 2, the distance error $e_d[k]$ and the posture error $e_\phi[k]$ are formulated as follows:

$$e_d[k+1] = e[k] + s[k+1]\sin\left(\phi_{ref} - B[k+1]\right), \tag{4}$$

$$e_\phi[k+1] = e_\phi[k] - \psi[k+1]. \tag{5}$$

Figure 2 illustrates that for a single input, three state quantities need to converge: distance, posture, and input. Consequently, three steps are necessary to achieve convergence for all of them. In this study, we derive the forward kinematics for these three steps as follows:

$$\begin{bmatrix} e_d[k+3] \\ e_\phi[k+3] \end{bmatrix} = \boldsymbol{f}(\boldsymbol{U}) = \begin{bmatrix} e[k] + \sum_{n=k+1}^{k+3} s[n]\sin\left(\phi_{ref} - B[n]\right) \\ e_\phi[k] - \sum_{n=k+1}^{k+3} \psi[n] \end{bmatrix}, \tag{6}$$

where, $\boldsymbol{U} = [\beta[k+1], \beta[k+2]]^T$, and it is the input vector of 2 steps. In (6), $\beta[k+3] = 0$ under the condition of the control target. By inverse kinematics, the input vector is obtained as follows:

$$\boldsymbol{U} = \boldsymbol{f}^{-1}(0,0).$$

$\beta[k+1]$ included in $\boldsymbol{U}$ is defined as the control input.

4. Numerical Simulation

The effectiveness of the designed trajectory-tracking control system is verified by numerical simulation. MATLAB R2021b (9.11.0.1769968) 64-bit (win64) performed the numarical simulation. The simulation time was $6\pi/10$[s], sampling interval was set to $\pi/10$[s]. And, the initial location and posture of the robot were the origin and 0 rad. Amplitude α [rad] was set to $\pi/4$ rad. The reference trajectory was set as follows $\sqrt{3}x+y+0.05 = 0$. The simulation results are shown in Figs. 3-5. Figure 3 shows that the robot follows the reference trajectory with the designed control system. Figures 4-5 show that all three (the distance error, the attitude error, and the input) converge to zero at the third step. Thus, it can be confirmed that the trajectory-tracking control of the robot can be designed by inverse kinematics. The red lines are the simulation results of the methods in [3], which confirm that the proposed method in this paper can converge faster without overshooting.

5. Conclusion

In this paper, we present the design of a trajectory-tracking control system based on inverse kinematics, representing the initial phase of an advanced control system for a Lizard-Inspired Single-Actuated Robot. Initially, we formulate the forward kinematics of the robot.

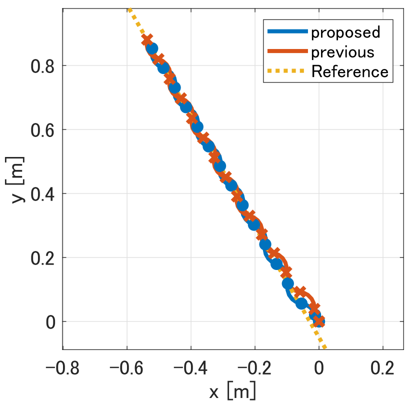

Figure 3: The trajectory of the robot

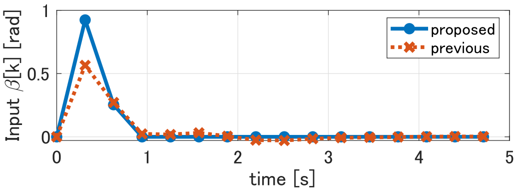

Figure 4: The time variation of the control input $\beta[k]$.

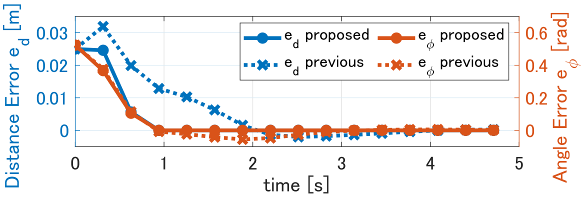

Figure 5: The time variation of the distance error $e_d[k]$ and the posture error $e_\phi[k]$.

Subsequently, we derive recursion formulas for the position and posture errors and formulate the inverse kinematics to ensure convergence of the position error, posture error, and control input to zero by the third step. The effectiveness of the designed control system is confirmed through numerical simulations, demonstrating the convergence of the position error, attitude error, and control input to zero at the third step.

Our future work aims to design a more advanced model predictive control system that accounts for input and state constraints. Additionally, we intend to develop a control system capable of following not only straight trajectories but also arbitrarily curved trajectories.

Acknowledgment

This work is funded by JSPS KAKENHI grant number 21K14107.

References

[1] D. Zarrouk, R.S. Fearing: 1star, a one-actuator steerable robot, *Proceedings of 2014 IEEE International Conference on Robotics and Automation (ICRA)*, Hong Kong, (2014), 2569–2569.

[2] Y. Kawakami, N. Kamamichi: Motion Analysis of Lizard Type Quadruped Robots, *Proceedings of JSME annual Conference on Robotics and Mechatronics*, (2013), 2P1-F04.

[3] S. Nansai, N. Kamamichi: Tracking Control of Lizard-Inspired Single-Actuated Robot Utilizing Posture Compensation, *Proceedings of SICE International Symposium on Control Systems 2023*, (2023), 3M7-2.

Wall walking of lizard-inspired single-actuated robot

Haruki Kanakubo[1*], Shunsuke Nansai[2], Norihiro Kamamichi[1]

[1]Department of Robotics and Mechatronics, Graduate School of Science and Technology for Future Life, Tokyo Denki University

[2]Office for Establishment of New Faculty, Akita University

*22fmr06@ms.dendai.ac.jp

Abstract. This study aims to develop a quadruped robot that can walk on horizontal and vertical planes with a minimum of actuators. Focusing on the motion of lizards that move quickly by utilizing the flexion of torso than legs, a lizard-type quadruped robot using a crossed four-bar linkage mechanism and single actuator is developed. In addition, to achieve adsorption to a wall surface, a suction mechanism is applied. The motion of the experimental robot is verified through experiments.

Keywords: Quadruped robot, 1-DOF driving robot, Adsorption

1. Introduction

In general, leg-type mobile robots have a multi-degree of freedom leg structure and a large number of actuators. Therefore, the complexity of the mechanism and control becomes an issue. On the other hand, as a study of another perspective, mobile robots with a minimum number of actuators have been studied. Examples include a robot that uses only one motor to generate wave-like motion [1] and a robot that can rotate multiple legs simultaneously [2]. Fewer actuators have the advantages for constructing small and lightweight robots and for easy motion analysis.

Inspired by the movement of lizards, which move more quickly by utilizing the flexion of their torso than their legs, this study aims to realize a walking motion of a robot using a crossed four-bar link mechanism [3]. This robot can be driven by a single motor and can move in a flat plane. In addition, by introducing a suction mechanism, the lizard-inspired robot can walk on the vertical planes such as walls and glass windows. In this paper, the design and development of the robot system and its verification results are described.

2. Motion algorithm

Figure 1 shows the motion algorithm for the lizard-inspired quadruped walking robot. The robot consists of a crossed four-bar linkage mechanism and moves by operating single motor mounted on the drive joints. If tip positions of a pair of diagonal legs are fixed by adsorption, the remaining degree of freedom is one. Thus, the moving legs are moved in tandem by the single motor. The moving sequence is shown below:

(1) The moving legs is moved forward while keeping the diagonal pair of legs fixed.
(2) The fixed and moving legs are switched respectively.
(3) The switched moving legs moved forward as a symmetrical movement with (1).
(4) The fixed and moving legs are switched respectively, and the above steps are repeated.

The motion of the robot is easily analyzed based on kinematic modeling. Walking simulations of above moving sequence is shown in Figure 2. As shown in Figure 2(a), a straight motion of the lizard-type robot can be realized by moving the drive joints symmetrically with the same angle. As shown in Figure 2(b), a turning motion can be realized by moving the drive joints asymmetrically with an offset angle.

3. Development of experimental robot

The lizard-type robot is operated by single servo motor that drives a crossed four-bar linkage mechanism. The fixed legs are switched with adsorption by negative pressure suction. A schematic diagram of the pneumatic control system for controlling adsorption is shown in Figure 3. The proposed pneumatic control system consists of a vacuum pump, a solenoid valve and suction pads. As shown in the walking algorithm, the left front leg and the right hind leg, or the right front leg and the left hind leg move in pairs at the same time. Therefore, the negative pressure of the vacuum pump is switched and controlled by two solenoid valves connected to each diagonal leg.

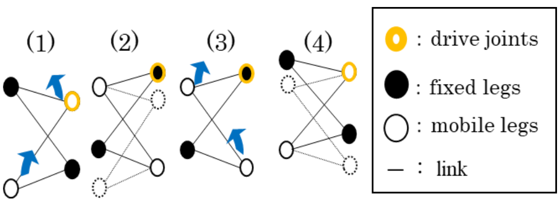

Fig. 1 Motion pattern of the robot

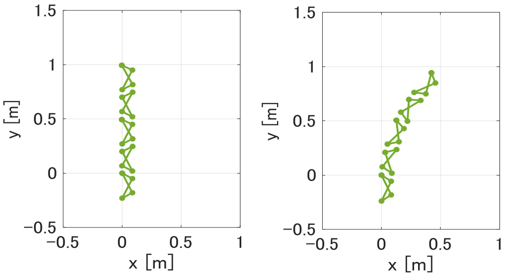

(a) Forward motior (b) Turning motion

Fig. 2 Simulation results

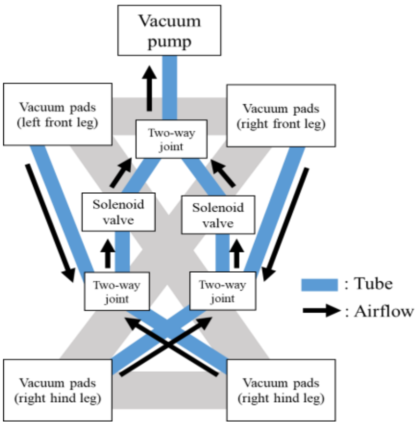

Fig. 3 Pneumatic control system

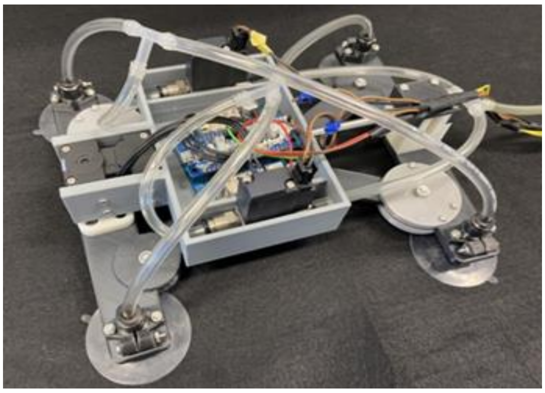

Fig. 4 Fabricated experimental robot

Figure 4 shows a fabricated experimental robot. A crossed four-bar linkage frame and motor fixing parts of the experimental robot were fabricated using a 3D printer. Other main components include a servo motor (XM430-W350-R, ROBOTIS), a microcontroller board (OpenCM 9.04, ROBOTIS), a solenoid valve (V030E1-PSL DC12V, Koganei), and a vacuum pump (DP0110-X1, Nitto Koki). Table 1 shows Robot parameters. Total weight of the robot is 654 g.

4. Experiments

Figure 5 shows the results of the walking experiment on a vertical plane. In this experiment, the robot is climbing up the vertical plane in a straight motion while adsorbing on the vertical acrylic plate. The walking operation is shown below:

(1) The motor is rotated for π/9 rad while the suction cups of fixed legs are absorbed.
(2) The suction cups of moving legs are also absorbed, and the four legs are adsorbed to the vertical plane.
(3) The previous fixed legs are released and the moving legs are switched to the fixed legs.

For each operation, (1) was performed at 0.5 s, (2) at 0.5 s, and (3) at 1.0 s. As observed from the sequence of photographs in Figure 5, the forward motion on the vertical plane was verified as same as simulation. In addition, it was confirmed that the weight of the experimental robot can be supported by vacuum suction.

Next, Figure 6 shows the results of the turning motion on the horizontal plane. The walking method is the same as the forward motion, but the rotation angle is offset from the center by π/9 rad. As shown in the photograph, the robot turned at a constant curvature with moving forward.

In the turning experiment on the vertical plane, the legs sometimes lifted off due to the weight of the robot and distortion of the linkage structure. To solve this problem, improvements of the mechanical structure to prevent distortion or to optimize weight balance are under consideration.

Table 1 Robot parameters

Part name	Numerical value
Weight	654 g
Size	240 mm×200 mm×75 mm
Link length of across part	200 mm
Link length of parallel part	100 mm

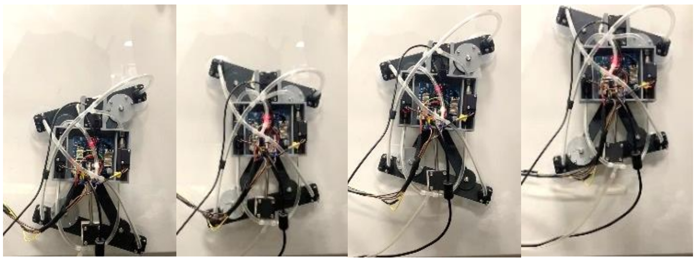
0 s 2 s 4 s 6 s

Fig. 5 Forward motion on vertical plane

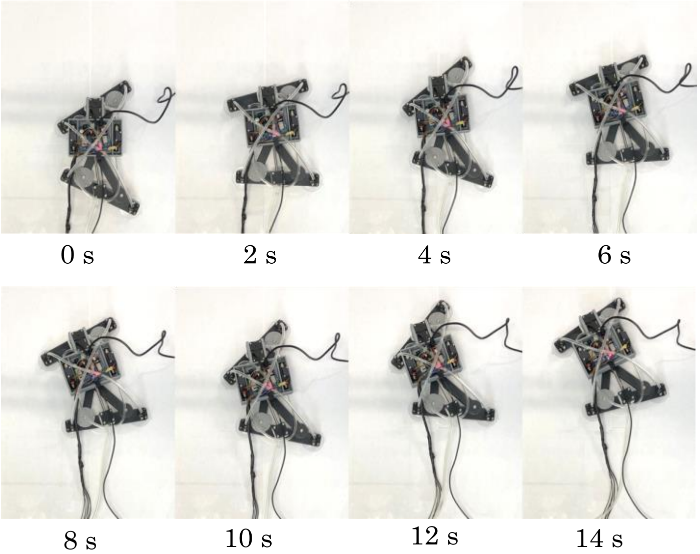

Fig. 6 Turning motion on horizontal plane

5. Conclusion

In this study, a lizard-inspired quadruped robot that can walk on horizontal and vertical planes with a minimum of actuators was designed and constructed. The walking motion on the vertical plane was verified through experiments.

In the future, the experimental robot is improved to realize a stand-alone motion with a built-in vacuum pump and power source. In addition, motion generation and control algorithms including obstacle avoidance are investigated.

References

[1] David Zarrouk, Moshe Mannetal, Nir Degani, Tal Yehuda, Nissan Jarbi and Amotz Hess, "Single actuator wave like robot (SAW): design, modeling, and experiments," *Bioinspiration &Biomimetics*, 11:4 (2016), 046004 pages.

[2] David Zarrouk and Ronald S. Fearing, "Controlled in plane locomotion of a hexapod using a single actuator," *IEEE Transactions on Robotics*, 31:1 (2015), pp. 157-167.

[3] Shouhei Noji, Shunsuke Nansai, Norihiro Kamamichi and Hiroshi Itoh "Modeling and Control of a Lizard-Inspired Single-Actuated Robot," *IEEE Robotics and Automation Letters*, 7:3 (2022), pp. 6399-6406.

Numerical Simulation of Butterfly-style Flapping Robot for Turning Flight with Lead-lag Motion

Hajime Endo[1*], Taro Fujikawa[1], Koki Kikuchi[2]

[1]Advanced Multidisciplinary Engineering, Graduate School of Advanced Science and Technology, Tokyo Denki University
[2]Department of Advanced Robotics, Faculty of Advanced Engineering, Chiba Institute of Technology

*`22udq01@ms.dendai.ac.jp`

Abstract. Flapping flight is a common method in nature, and its mechanism is getting attention. We research the flapping flight mechanism treating butterflies as the target. A butterfly makes its lead-lag angle asymmetry during turning flight. In this research, we construct a simulation experiment to quantitatively analyze the lead-lag angles required for turning flight, attitude angles, and moment. As a result, it was clear that a butterfly-style flapping robot turns with asymmetric lead-lag angles.

Keywords: Flapping robot, Lead-lag motion, MAV, CFD

1. Introduction

Flapping flight is a common method in nature, and its mechanism is getting attention. Flapping flight is a useful method for small flying robots, and robots modeled of birds and insects were developed [1], [2]. Here, a butterfly's flight is characterized by lower flapping frequency compared with other insects, and its wings have low degrees of freedom during flight. Due to those reasons, we think that the feasibility of developing a small-scale flapping robot inspired by butterflies is a high possibility, and we research flapping flight mechanisms treating butterflies as the target. The latest butterfly-style flapping robot that we have developed is currently capable of only flying straight, and we need to find a method of turning flight. Additionally, a butterfly makes its lead-lag angle asymmetry during turning flight, and the experiment with hardware suggests the relationship between lead-lag angles and turning flight [3]. Based on this relationship, new turning motion methods with lead-lag motion was researched [4], however, it is difficult to demonstrate the relationship between small lead-lag angle variation and turning motion through actual machine experiments. In this paper, we construct simulations to quantitatively analyze the lead-lag angles required for turning flight, attitude angles, and moments of a butterfly-style flapping robot.

2. Method

2.1. Lead-lag motion

Figure 1(a) shows a currently developed butterfly-style flapping robot. This robot is capable of achieving its flapping angle of approximately 90 degrees by the flexibilities of its elastic links, enabling takeoff from 0 m/s [5]. By using elastic links, the fore wings of the robot's wings have a front/rear direction degree of freedom. We called this motion a lead-lag motion. Here, We define the forward lead-lag motion as a positive direction, and the rotation angle θ [deg] (as shown in Fig. 1(b)) as lead-lag angles.

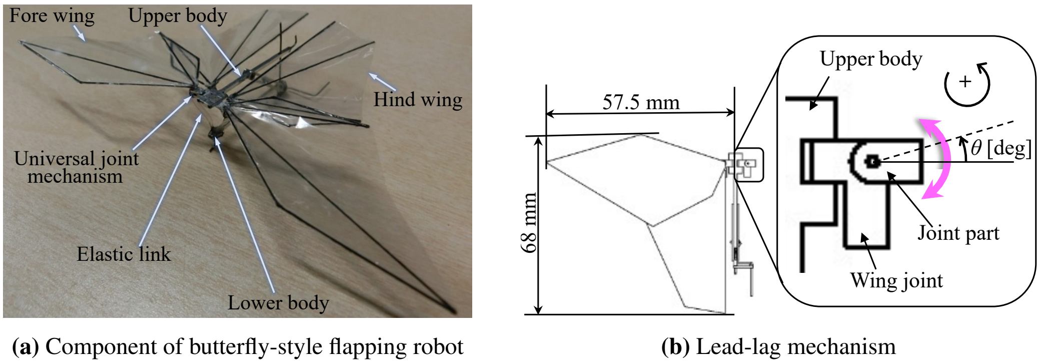

(a) Component of butterfly-style flapping robot

(b) Lead-lag mechanism

Fig. 1: Developed butterfly-style flapping robot

2.2. Simulation models

Examples of the model for simulation are shown in Fig. 2, 3. The model was designed by SOLIDWORKS 2021 based on the actual size of a swallowtail butterfly (*Papilionidae*). Additionally, to restrain fluctuation of roll angle, the models have flapping angles of 10 deg. Three models were made: Model N with lead-lag angles of both wings designed to be 0 deg, Model L with a lead-lag angle of the left side wing designed to be 10 deg, Model R with a lead-lag angle of the right side wing designed to be 10 deg.

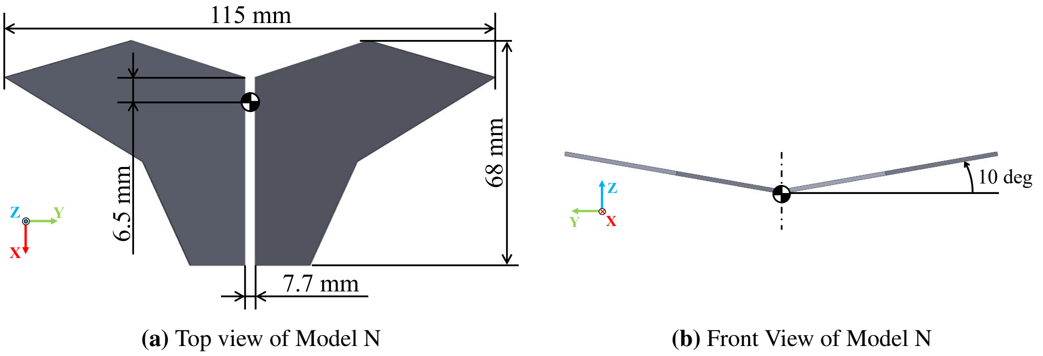

(a) Top view of Model N

(b) Front View of Model N

Fig. 2: 3D CAD model without lead-lag angle

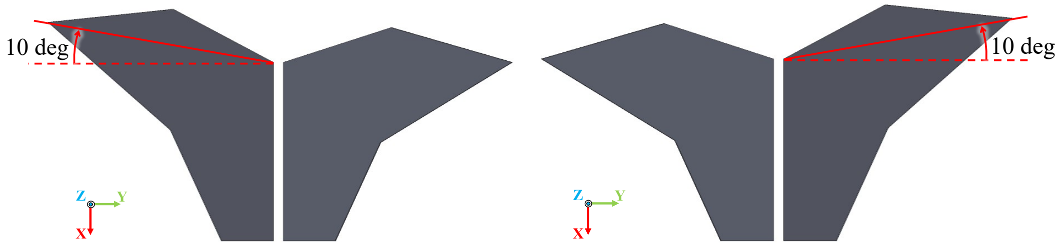

(a) Top view of Model L **(b)** Top view of Model R

Fig. 3: 3D CAD model without lead-lag angle

2.3. Simulation parameters

In this simulation, we conduct a three-dimensional moving boundary fluid analysis using overset grid in OpenFOAM, which is open source computational fluid dynamics tool. We obtain a trajectory of the model's center of gravity(CoG) in gliding. The courant number is set to 1, and the time step is automatically calculated. Computational space is shown in Fig. 4. This computational space is a cube with a side length of 2.0 m.

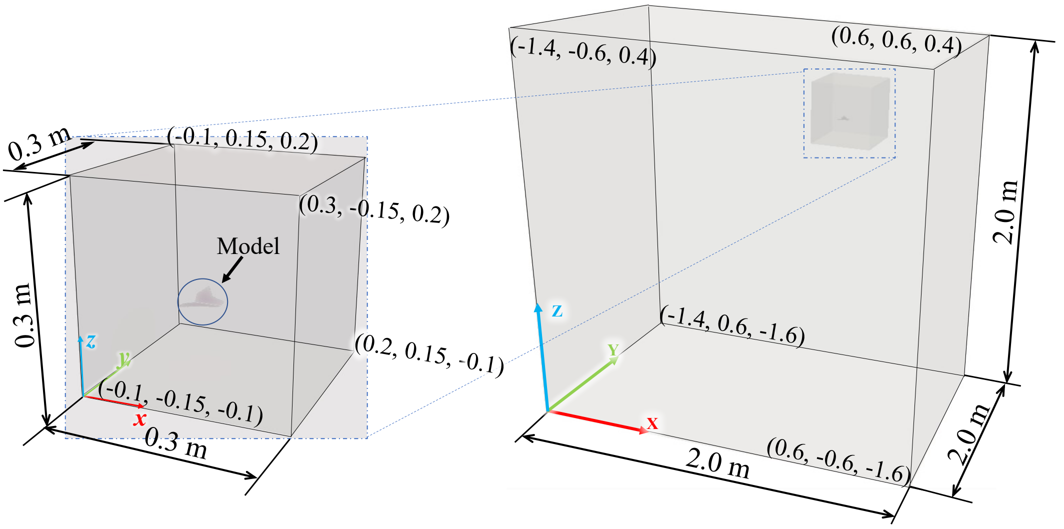

Fig. 4: Computational space

3. Results and discussion

The trajectory of the model's CoG on XZ plane is shown in Fig. 5(a). The glide distance of Model N is the longest on XY plane. The trajectory of the model's CoG on XY plane is shown in Fig. 5(b). In these results, we confirm that Model L turns right, and Model R turns left.

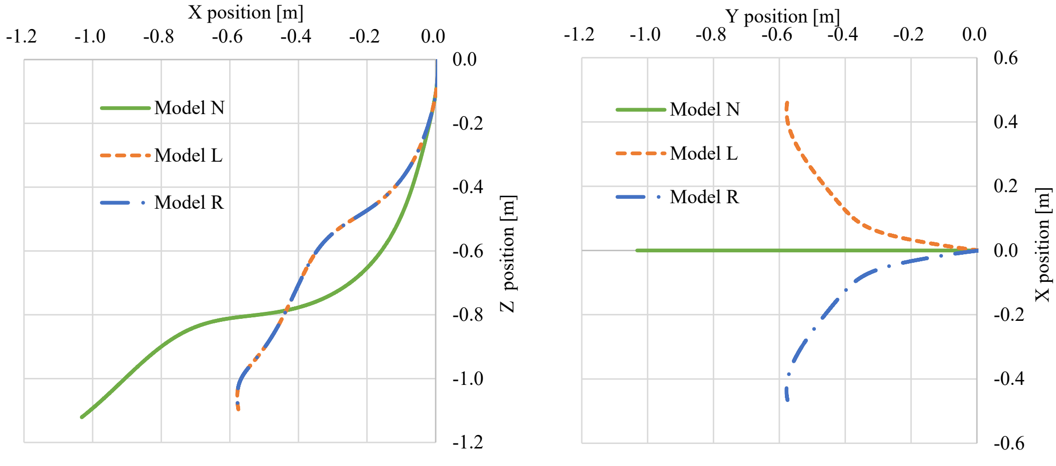

(a) Trajectory of CoG on XZ plane **(b)** Trajectory of CoG on XY plane

Fig. 5: Trajectory of CoG

4. Conclusions

In this research, we confirm the effect of lead-lag motion on the gliding of a butterfly-style flapping robot. We compare the flight trajectories of models without lead-lag angles of wings with the model with the lead-lag angle of a side wing. As a result, the model with the lead-lag angle of the left wing turns right, and the model with the lead-lag angle of the right wing turns left. From the above, it was clear that a butterfly-style flapping robot turns with asymmetric lead-lag angles.

References

[1] E. Ajanic, A. Paolini, C. Coster, *et al.*: Energy extraction performance of tandem flapping foil undergoing elliptical motion trajectory, *Ocean Engineering*, 268 (2023), 1–12.

[2] L. Qian, L. Haoze, S. Huan, *et al.*: An Aerial–Wall Robotic Insect That Can Land, Climb, and Take Off from Vertical Surfaces, *Reserch*, (2023), 1–15.

[3] Y. Ozawa, T. Fujikawa, K. Kikuchi, *et al.*: Analysis of Turning Motion for Developing a Butterfly-Style Flapping Robot, *MM Science J*, (2018), 2198–2204.

[4] H. Endo, T. Fujikawa: Development of a Turning Control Mechanism for a Butterfly-style Flapping Robot with Lead-Lag Motion, *the 2022 JSME Conference on Robotics and Mechatronics*, (2022), 1–4.

[5] T. Fujikawa, Y. Sato, T. Yamashita, *et al.*: Development of a lead-lag mechanism using simple flexible links for a small butterfly-style flapping robot, *2010 World Automation Congress*, (2010), 1–6.

JSST 2023

Numerical studies on preconditioned iterative solvers with minimal residual smoothing

Arisa Kawase[1,*] and Kensuke Aihara[2]

[1]Graduate School of Integrative Science and Engineering, Tokyo City University
[2]Department of Computer Science, Tokyo City University

*g2381420@tcu.ac.jp

Abstract. Lanczos-type iterative methods are effective for solving large sparse linear systems; however, its residual 2-norms often oscillate. *Minimal residual smoothing* was proposed to prevent oscillations and generate a monotonically decreasing residual sequence. However, the error 2-norms after smoothing can increase. Herein, we show that the error 2-norms tend to expand, particularly when the condition number of the coefficient matrix is large. To overcome this problem, we use residual smoothing in combination with preconditioning, which is a well-known technique for reducing the condition number.

Keywords: linear systems, Lanczos-type solver, residual smoothing, preconditioning

1. Introduction

We consider solving a large sparse linear system $A\boldsymbol{x} = \boldsymbol{b}$, $A \in \mathbb{R}^{n\times n}$, $\boldsymbol{b} \in \mathbb{R}^n$ that frequently appears in scientific computing. Lanczos-type solvers, such as the CG [1] and Bi-CG [2] methods, update the approximate solutions by expanding the Krylov subspace; however, they do not monotonically approach the exact solution, and the residual 2-norms often oscillate. This causes severe propagation of rounding errors, thus leading to deterioration of convergence and loss of attainable accuracy of the approximate solutions. It may also provide an approximate solution that does not satisfy the required accuracy when the number of iterations are fixed. Residual smoothing was developed to improve convergence behavior [3, 4]. This technique transforms the residuals generated by an iterative method into alternative residuals that exhibit smooth convergence behavior. By setting the parameters for minimizing the residual 2-norms for each iteration, they can decrease monotonically.

In this study, first, we performed numerical experiments to show that the error 2-norms after smoothing can be magnified, whereas the residual 2-norms decrease smoothly. Additionally, we analyzed this phenomenon theoretically, and clarified that the error 2-norms can expand if the condition number of A is large. Next, we improved the convergence behavior of the error 2-norms by applying preconditioning [5] which is useful for reducing the condition number. Through numerical experiments with both residual smoothing and preconditioning, we investigated the convergence behavior of the error 2-norms.

2. Minimal residual smoothing and error norm behavior

Let $\boldsymbol{x}_k$ and $\boldsymbol{r}_k = \boldsymbol{b} - A\boldsymbol{x}_k$ be the kth approximation and corresponding residual, respectively, generated by an iterative method. Thus, the following transformation yields a new approximation $\boldsymbol{y}_k$ and the corresponding smoothed residual $\boldsymbol{s}_k = \boldsymbol{b} - A\boldsymbol{y}_k$:

$$\boldsymbol{y}_k = \boldsymbol{y}_{k-1} + \eta_k(\boldsymbol{x}_k - \boldsymbol{y}_{k-1}), \quad \boldsymbol{s}_k = \boldsymbol{s}_{k-1} + \eta_k(\boldsymbol{r}_k - \boldsymbol{s}_{k-1}), \tag{1}$$

where $\boldsymbol{y}_0 = \boldsymbol{x}_0$ and $\boldsymbol{s}_0 = \boldsymbol{r}_0$, and the scalar parameter η_k is set to minimize the residual 2-norms $\|\boldsymbol{s}_k\|_2$, as follows.

$$\eta_k = -\frac{\boldsymbol{s}_{k-1}^\top(\boldsymbol{r}_k - \boldsymbol{s}_{k-1})}{\|\boldsymbol{r}_k - \boldsymbol{s}_{k-1}\|_2^2}. \tag{2}$$

This is called minimum residual smoothing, and $\|\boldsymbol{s}_k\|_2 \le \|\boldsymbol{r}_k\|_2$ and $\|\boldsymbol{s}_k\|_2 \le \|\boldsymbol{s}_{k-1}\|_2$ hold.

In the preliminary experiments with various test matrices, we found that the error 2-norms tend to increase for ill-conditioned matrices. Analyzing the relationship between the error 2-norms before and after minimal residual smoothing (i.e., $\|\boldsymbol{x}^* - \boldsymbol{x}_k\|_2$ and $\|\boldsymbol{x}^* - \boldsymbol{y}_k\|_2$), we obtained the following result, where $\boldsymbol{x}^*$ is the exact solution.

Proposition 1. *For the error 2-norms before and after performing* (1) *with* (2)*, it holds that*

$$\frac{\|\boldsymbol{x}^* - \boldsymbol{y}_k\|_2}{\|\boldsymbol{x}^*\|_2} \le \|A^{-1}\|_2\|A\|_2\frac{\|\boldsymbol{x}^* - \boldsymbol{x}_k\|_2}{\|\boldsymbol{x}^*\|_2}. \tag{3}$$

From (3), we observe that the relative error 2-norms after smoothing can be large, even if those before smoothing are sufficiently small, when the condition number $\|A^{-1}\|_2\|A\|_2$ is large. Essentially, $\|\boldsymbol{x}^* - \boldsymbol{y}_k\|_2$ is of the same order of magnitude as $\|\boldsymbol{x}^* - \boldsymbol{x}_k\|_2$ if the condition number is sufficiently small. Therefore, we improved the convergence behavior of $\|\boldsymbol{x}^* - \boldsymbol{y}_k\|_2$ by applying a preconditioning technique to reduce the condition number.

The primary purpose of preconditioning is to achieve faster convergence by converting a linear system into an easier problem-to-solve. Thus, these results represent a novel aspect of preconditioning when used with minimal residual smoothing. Numerical experiments and a detailed discussion will be presented at the JSST2023 meeting.

Acknowledgements. The authors would like to thank the reviewers for their careful reading. This study was partly supported by JSPS KAKENHI Grant Number JP20H04195.

References

[1] M. R. Hestenes and E. Stiefel, Methods of conjugate gradients for solving linear systems, J. Research Nat. Bur. Standards, **49** (1952), 409–436.

[2] R. Fletcher, Conjugate gradient methods for indefinite systems, Lecture Notes in Math, **506** (1976), 73–89.

[3] R. Weiss, Parameter-Free Iterative Linear Solvers, Akademie Verlag, Berlin, 1996.

[4] W. Schönauer, Scientific Computing on Vector Computers, Elsevier, Amsterdam, 1987.

[5] Y. Saad, Iterative Methods for Sparse Linear Systems, 2nd. edn., SIAM, Philadelphia, 2003.

Iterative refinement for an eigenpairs subset of a real generalized symmetric-definite eigenproblem

Takeshi Terao[1,*]

[1]Research Institute for Information Technology, Kyushu University

*`terao.takeshi.412@m.kyushu-u.ac.jp`

Abstract.

This paper considers an iterative refinement for an eigenpairs subset of a real generalized symmetric-definite eigenproblem. An iterative refinement method for a subset of eigenpairs to a standard eigenproblem is proposed. The method uses the compact WY representation of the computed eigenvector matrix. Therefore, we consider the compact WY representation for B-orthogonal columns, and apply it to the iterative refinement for the generalized eigenproblem.

Keywords: Eigenvalue problem, Iterative refinement, Accurate computation

1. Introduction

A real generalized symmetric-definite eigenproblem for a symmetric matrix $A \in \mathbb{R}^{n\times n}$ and a symmetric positive definite matrix $B \in \mathbb{R}^{n\times n}$ is $A\boldsymbol{x}_j = \lambda_j B\boldsymbol{x}_j$, where an eigenvalue $\lambda_j \in \mathbb{R}$ and an eigenvector $\boldsymbol{x}_j \in \mathbb{R}^n$. This paper considers

$$AX = BXD,$$

where $D = \mathrm{diag}(\lambda_1, \dots, \lambda_k) \in \mathbb{R}^{k\times k}$ is a diagonal matrix and $X = [\boldsymbol{x}_1, \dots, \boldsymbol{x}_k] \in \mathbb{R}^{n\times k}$ is a rectangular B-orthogonal matrix. Here, we assume that $|\lambda_i| > |\lambda_j|$ for $1 \le i < j \le k \le n$.

Numerical computations produce approximations $\hat{D} \approx D$ and $\hat{X} \approx X$ such that

$$A\hat{X} \approx B\hat{X}\hat{D}, \quad \hat{X}^T B\hat{X} \approx I_k,$$

where $I_k \in \mathbb{R}^{k\times k}$ is the identity matrix. When $k = n$, Ogita and Aishima proposed an excellent iterative refinement method based on matrix multiplication [1, 2]. The proposed method is applicable to the case as $k < n$. In other words, since the proposed method works on eigenpair subsets, it can be applied to the problem of large sparse matrices. This paper presents the algorithm of the proposed method. Convergence and computational performance will be presented in the presentation.

2. The proposed method

First, an introduction to the compact WY representation [3, 4] for a rectangular B-orthogonal matrix is detailed. Let $X \in \mathbb{R}^{n \times k}$ be the B-orthogonal columns, and the proposed method produces the B-orthogonal matrix $H \in \mathbb{R}^{n \times n}$. Suppose that $R \in \mathbb{R}^{n \times n}$ is the Cholesky factor of B such that $B = R^T R$. Then, the matrix $Q = RX$ has orthogonal columns, and the compact WY representation can be applied to Q. Then, the orthogonal matrix $G = I - YTY^T$ can be generated from Q and $H = R^{-1}G$ is satisfied. Here, $Y = Q - I_{(n,k)}$ and $T = -Y_1^{-T}$, where $I_{(n,k)} \in \mathbb{R}^{n \times k}$ is a rectangular identity matrix and $Y_1 \in \mathbb{R}^{k \times k}$ is a top block of Y. The following is the proposed algorithm that improves the accuracy of an eigenpairs subset for the generalized eigenvalue problem.

Algorithm 1 Refinement for an approximate eigenpair subset

```
Require: $A \in \mathbb{R}^{n \times n}$, $B \in \mathbb{R}^{n \times n}$, $\hat{X} \in \mathbb{R}^{n \times k}$, and $\hat{D}^{(p)} \in \mathbb{R}^{k \times k}$ with $k \leq n$
    $\hat{H}$ = CompactWY_B($\hat{X}, R$)    % Compact WY representation for B-orthogonal matrix
    $S = \hat{H}^T(A\hat{X} - B\hat{X}\hat{D})$
    $t_j = \hat{\boldsymbol{x}}_j^T B \hat{\boldsymbol{x}}_j$ for $1 \leq j \leq k$
    $\hat{d}_{jj} \leftarrow \hat{d}_{jj} + s_{jj}/t_j$ for $1 \leq j \leq k$
    $\tilde{e}_{ij} = \begin{cases} (1 - t_j)/2, & i = j \\ \dfrac{s_{ij}}{\hat{d}_{jj} - \hat{d}_{ii}}, & \text{otherwise} \end{cases}$ for $1 \leq i, j \leq k$
    $\tilde{e}_{ij} = s_{ij}/\hat{d}_{jj}$ for $k + 1 \leq i \leq n, 1 \leq j \leq k$
    $\hat{X} \leftarrow \hat{X} + \hat{H}\tilde{E}$
Ensure: $\hat{X} \in \mathbb{R}^{n \times k}$ and $\hat{D} \in \mathbb{R}^{k \times k}$
```

References

[1] Takeshi Ogita and Kensuke Aishima. Iterative refinement for symmetric eigenvalue decomposition. *Japan Journal of Industrial and Applied Mathematics*, 35:1007–1035, 2018.

[2] Takeshi Ogita and Kensuke Aishima. Iterative refinement for symmetric eigenvalue decomposition ii: clustered eigenvalues. *Japan Journal of Industrial and Applied Mathematics*, 36:435–459, 2019.

[3] Yusaku Yamamoto. Aggregation of the compact wy representations generated by the tsqr algorithm. In *Conference talk presented at SIAM Applied Linear Algebra*, 2012.

[4] Grey Ballard, James Demmel, Laura Grigori, Mathias Jacquelin, Hong Diep Nguyen, and Edgar Solomonik. Reconstructing householder vectors from tall-skinny qr. In *2014 IEEE 28th International Parallel and Distributed Processing Symposium*, pages 1159–1170. IEEE, 2014.

Benchmark results for point cloud isosurfaces implemented on VisAssets

Hideo Miyachi[1*], Shintaro Kawahara[2], Kazuo Kashiyama[3]

[1]Department of Information Systems, Tokyo City University
[2]Japan Agency for Marine-Earth Science Technology (JAMSTEC)
[3]Department of Civil and Environmental Engineering, Chuo University

*`miyachi@tcu.ac.jp`

Abstract. We have been developing VisAssets, a framework for general-purpose scientific visualization on the game engine Unity, and implementing point cloud isosurfaces for large-scale data. We compared the performance of the proposed point cloud isosurfaces with that of isosurfaces that generate triangles using the Marching cubes method. The results showed that the point cloud isosurfaces performed better than the isosurfaces of the conventional method in terms of memory consumption, isosurface generation speed, and rendering speed for large-scale data.

Keywords: Large scale visualization, Point cloud isosurfaces, Unity, VisAssets

1. Introduction

We are developing a framework for general-purpose scientific visualization on the game engine Unity, which is called VisAssets[1]. The feature of this framework is that visualization applications can be constructed by hierarchically instantiating assets which implement subdivided visualization elements on the Unity Editor, following the concept of data flow in visual programming. In addition, another advantage is easy to add VR/AR functions by building applications on Unity. Furthermore, we are currently implementing large-scale visualization functionality into this framework. In this paper, we report benchmark results of point cloud isosurfaces processing on the isosurface extended to unstructured data.

2. Point cloud isosurfaces

The large-scale data described here assumes numerical results with an amount of resolution that exceeds the number of pixels on the display screen. Under such conditions, even if isosurfaces are generated, most of the surfaces will be contained in a single pixel. If the isosurfaces have complex shape, some surfaces will be hidden behind the surface and not reflected in the display by hidden surface removal. This means that computational costs are wasted in the generation of surfaces not involved in the display and in the shading process. Therefore, for high-density numerical calculations, it is effective to check the visibility by hidden surface removal in advance and generate isosurfaces only for visible cells[2]. The process is shown in Fig.1.

For illustration, the figure is shown in two dimensions. In Fig.1, sphere-like isosurfaces are generated. In the Marching cubes method, the isosurfaces are generated as triangles while considering the pattern of the isosurfaces in each cell. On the other hand, at first, the proposed method determines only whether isosurfaces exist in a cell (Fig.1(1)). The second, a point (or an alternative such as a sphere) is placed at the center of gravity of the cell where the isosurfaces exist. Using the alternative objects, the visibility of each cell is determined by rendering from 26 surrounding directions (Fig.1(2)), and invisible points are removed. As a result, only visible points survived as shown in Fig.1(3). Finally, surfaces are generated using the Marching cubes method for only the visible points (Fig.1(4)). However, in this benchmark, the last process (Fig.1(4)) is omitted and the isosurfaces are displayed as a point cloud in the state of Fig.1(3) for the benchmark. In this case, the point is shaded at rendering by using the normal of the point. The normal is given as the average of look-at-from vectors in the visible view position multiplied by -1.

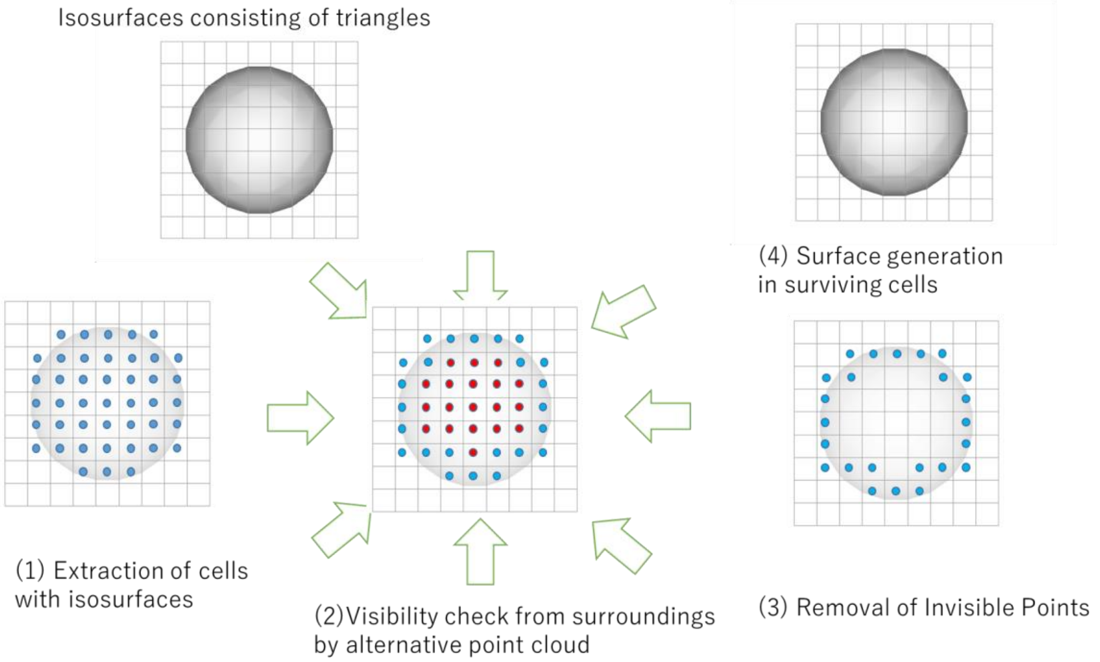

Fig.1 Procedure of point isosurface generation in [2]

3. Benchmark

Unstructured data consisting of hexahedral cells was used for benchmarking. One block contains 1000 hexahedral cells of size 10×10×10, as shown in Fig.2(a). A physical quantity R is defined on each node, where R gives the distance from the center of the block. The value of R has a definition range from 0 to $\sqrt{3}$. Fig.2(a) visualizes the isosurface with a threshold value equal to the median value of $R=\sqrt{3}/2$. The benchmark uses a large data set of N×N×N replicates of this block. Fig.2(b) shows the isosurfaces visualization of the data when N=3. Table 1 shows the computer environment used for the benchmark.

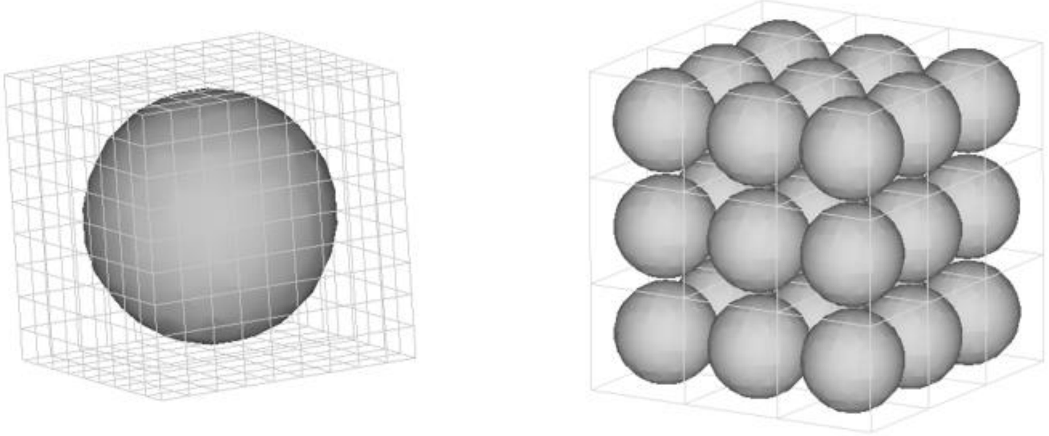

(a) a block data

(b) N×N×N blocks data (N=3)

Fig.2 Benchmark data

Table 1 Computer Environment for the benchmark

OS	Windows 10 Home 21H2 19044.2468
CPU	Intel Core i7-8750H@2.20GHz
Memory	Physical memory: 32GB Virtual memory about 45GB (Available C drive space)
Storage	System Drive (C): SAMSUNG MZVLB512HAJQ-00000 Work Drive (W): SanDisk Extreme Pro 55AF SCSI Disk Drive
GPU	NVIDIA GeForce GTX 1070 with Max-Q Design Driver 30.0.15.1179

Benchmarks were performed with four different numbers of blocks N=10, 20, 30, and 40. The number of triangles and the number of points constituting the isosurface for an increase in the number of grids are shown in Fig.3. While the number of triangles increases in proportion to the increase in the number of grids for isosurface with triangles, the number of points is significantly less than the number of triangles constituting the isosurfaces, since the calculation of internal invisible cells is removed.

Figure 4 shows the processing time for isosurface with triangles and with points versus the number of grids. This is the time from the completion of data loading to finishing the first visualization. On both isosurfaces, the time increase as the number of grids increases, but the rate of increase for isosurface with points is lower than isosurface with triangles. For N=40, the isosurface with triangles takes 1488 seconds (about 25 minutes), while the isosurface with points takes 207 seconds, seven times faster. The isosurface with points also consumes less memory, and for N=42 or greater, surface isosurface with triangles are out-of-memory and cause errors, but the isosurface with points cannot cause errors.

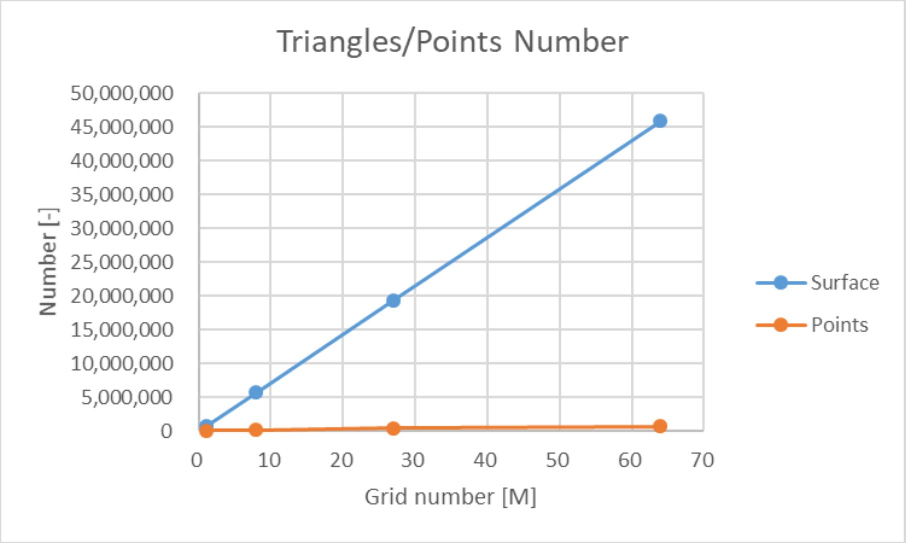

Fig.3 Number of triangles/points against the number of grids

The rendering speeds for the second and subsequent rendering processes, i.e., when rotating the display object, etc., are shown in Fig.5. The isosurface with triangles is rendered at the maximum speed of 400 FPS when N=10, but the speed drops to 33 FPS when N=40. On the other hand, the isosurface with points keeps a constant speed of 400 FPS.

Figure 6 shows the visualization images for N=20. The left image is the isosurface with triangles, and the right image is the isosurface with points. Gaps are generated in the isosurface with points. Although we did not evaluate the image quality in this work, we understand that the quality of the two images is not the same as the current settings. The data set used for this benchmark has a data distribution that generates isosurface with many hidden surfaces, which is advantageous for isosurface with points.

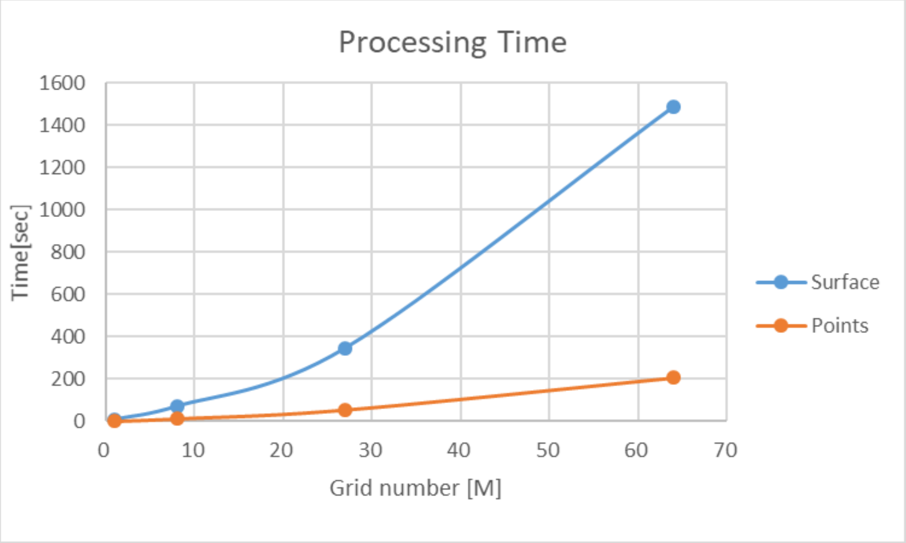

Fig.4 Isosurface processing time against the number of grids

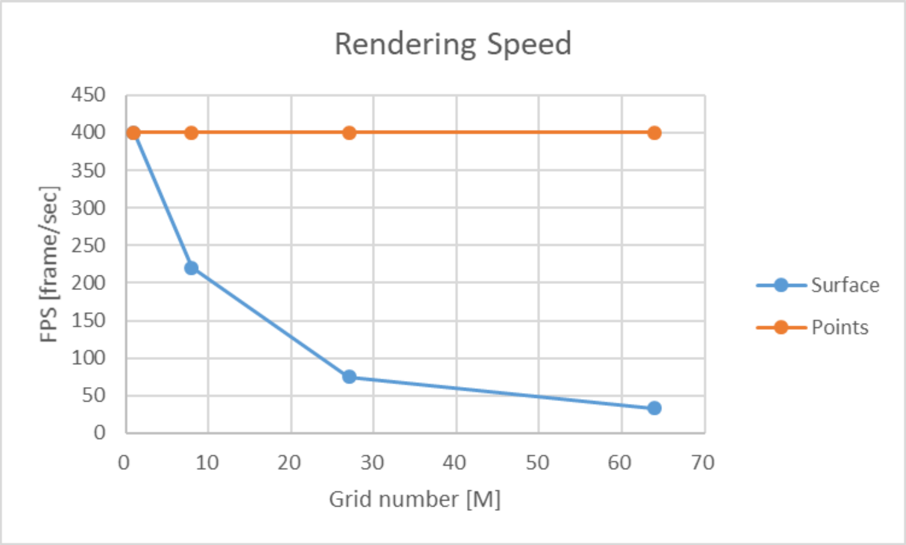

Fig.5 Rendering speed against the number of grids

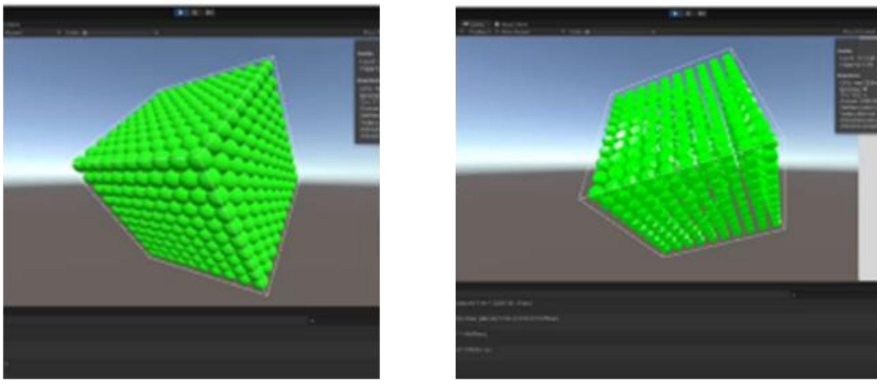

(a) triangles (b) points

Fig.6 Visualized images at N=20

5. Conclusion

We measured the performance of point cloud isosurfaces, which has been implemented in VisAssets: a visualization framework on Unity game engine, using data with 60 million cells of hexahedral elements. Compared to isosurfaces with triangles generated by Marching cubes method, point cloud isosurfaces showed superior performance in three indices: memory consumption, processing speed, and rendering speed. However, the distribution condition of the isosurface in this benchmark was favorable to the proposed point cloud isosurface. In addition, we did not evaluate the image quality of the visualization displayed by the point cloud isosurfaces and found that the point cloud isosurfaces have gaps among the isosurfaces under the current settings. The image quality needs to be improved.

Acknowledgments

This work was supported by JSPS KAKENHI Grant Numbers 21K11916 and 22K12054.

References

[1] Hideo Miyachi, Shintaro Kawahara: Development of VR Visualization Framework with Game Engine, *Journal of Advanced Simulation in Science and Engineering*, Vol.12, No.2 (2020), pp.59-68 (in Japanese).

[2] Hideo Miyachi, Daisuke Matsuoka, Yoji Matsumoto: An alternative visualization pipeline for large-scale data sets by using early visibility test point rendering, *International Journal of Modeling, Simulation, and Scientific Computing*, Vol.9, No.3 (2018), pp.1840004-11.

Simulation Analysis of the Transport of Dust Particles Injected by the Multi-Species Impurity Powder Dropper in the Large Helical Device

Mamoru Shoji[1,2*], Gakushi Kawamura[1,2], Roman Smirnov[3], Yasunori Tanaka[4]

[1]National Institute for Fusion Science, National Institutes of Natural Science
[2]Fusion Science Program, Graduate University for Advanced Studies, SOKENDAI
[3]Department of Mechanical and Aerospace Engineering, University of California at San Diego
[4]Institute of Science and Engineering, Kanazawa University

*`shohji.mamoru@nifs.ac.jp`

The full paper of this paper has been published in Journal of Advanced Simulation in Science and Engineering (JASSE).

DOI: `https://doi.org/10.15748/jasse.11.12`

Advanced virtual-reality visualization for analysis of fusion plasma simulation data

Hiroaki Ohtani[1,2*], Shintaro Kawahara[3]

[1]Sensing and Intellectualizing Technology Unit, National Institute for Fusion Science
[2]Fusion Science Program, Graduate Institute for Advanced Studies, SOKENDAI
[3]Center for Earth Information Science and Technology, Japan Agency for Marine-Earth Science and Technology
*`ohtani.hiroaki@nifs.ac.jp`

Abstract. This paper reports on enhancements of virtual reality (VR) visualization software for CAVE Systems "VFIVE" to research plasma physics in the periphery region of a fusion reactor. Visualizing streamlines from predefined starting points enables us to trace the magnetic field and plasma flow streamlines toward the divertor plates. Various kinds of streamline representations help us to understand the structures and relationships of the vector fields. Fusion visualization integrally displays the results by VFIVE, and a 3-D model rendered by Unity to figure out intuitively the physics of plasma. These developments open a new path for simulation science.

Keywords: Virtual reality visualization, fusion visualization, simulation data, 3-D model

1. Introduction

High-temperature fusion plasma is magnetically confined in a finite space, and special non-uniformity and a strong gradient are generated in the plasma temperature, density profile, magnetic field profile, and so on. In addition, fusion plasma is an open system because energy is supplied to the finite space from outside into the plasma, and energy flows out through the boundary of the plasma. Since the plasma has strong nonlinearity and non-equilibrium in addition to these properties, various and complex phenomena take place [1]. It is useful to apply visualization by virtual reality (VR) technologies to the investigation of complex three-dimensional (3-D) structures and the time variation of plasma [2,3]. This paper reports that the VR visualization software for CAVE Systems "VFIVE" [4,5,6] is enhanced.

2. Visualization software

VFIVE is one general-purpose VR visualization software for CAVE systems and is developed for visualizing simulation data in the Cartesian coordinate system by several visualization methods, such as streamline, arrow, isosurface, contour plot, and so on. To research plasma flow and magnetic field structure in the periphery region between core plasma and the plasma-facing wall, we add several functions to the VFIVE: 1) streamlines from predefined starting points, 2) new streamline representations, and 3) a fusion display of visualization results by VFIVE and the 3-D model rendered by Unity [7]. Although VFIVE itself can start to draw streamlines from the point which a controller specifies, it is a little difficult to decide the specific points by the controller in the 3-D VR space. Function 1) enables us to trace the magnetic field and plasma flow streamlines toward the divertor plates and find their origins, since we can calculate the backward streamlines from the starting points on the divertor plates. Function 2) provides two new streamline-visualization methods, such as tube and ribbon, in addition to the colored line. Figure 1 shows three types of streamline visualization methods. The line method is a visualization technique already implemented in VFIVE, where a set of vertices that form the streamlines are connected by line segments in a typical drawing style. The tube and ribbon methods are extensions of this technique. In the tube method, cylindrical shapes are used instead of line segments to enhance the visibility of the three-dimensional structure of the streamlines. For each vertex that constructs a streamline, a sphere with the same radius as the cylinder is drawn, ensuring that each cylinder is drawn continuously. In the ribbon method, polygonal surfaces are formed by connecting the ends of line segments (equivalent to leftward and rightward vectors) that are orthogonal to both the forward and upward vectors at each vertex constituting the streamlines, sequentially. The structure and torsion of the tube and ribbon give us an intuitive awareness of the structures and relationships of the vector fields. Function 3) is realized by the commercial software “FusionSDK” by FiatLux and Cybernet [8,9,10]. In the role of the same method as function 3) by VFIVE itself, we also add data reading and 3-D model visualization functions to VFIVE to read and visualize a 3-D model of MQO formatted data with visualization results by VIVE by using GLMetaseq [11]. We suppose we can apply these functions to VFIVE visualization by a head-mount display connected to a PC through the CLCL library [12,13].

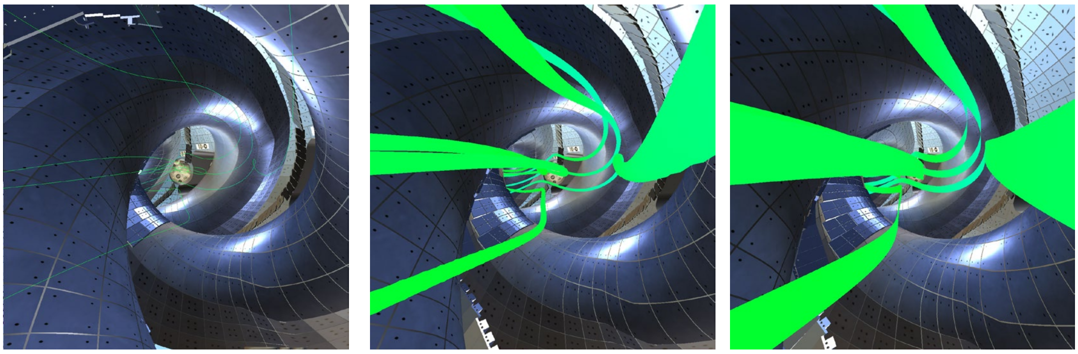

Fig.1 Three types of streamline-visualization methods. Left: line, middle: tube, and right: ribbon. Since figures projected onto 2D plane, difficult to distinguish difference between tube and ribbon methods.

3. Fusion visualization results

Figure 2 shows the fusion visualization of VFIVE visualization and the Unity-rendered 3-D model of the Large Helical Device (LHD) of the National Institute for Fusion Science by FusionSDK. The left figure of Fig. 2 shows the appearance of the LHD 3-D model with simulation box lines shown by VFIVE. The right graphic of Fig. 2 indicates the inside of the LHD vacuum vessel with a magnetic field streamline and a color contour plot of the magnetic field strength. By using visualization functions of VFIVE, it is possible to visualize simultaneously many physical quantities by multiple visualization methods in a realistic 3-D model visualization. It will help fusion plasma researchers to understand the physics of plasma flow in the periphery region by visualizing magnetic field lines, flow velocity vectors, averaged velocity vectors by gradient and curvature drifts with profiles of temperature and particle density.

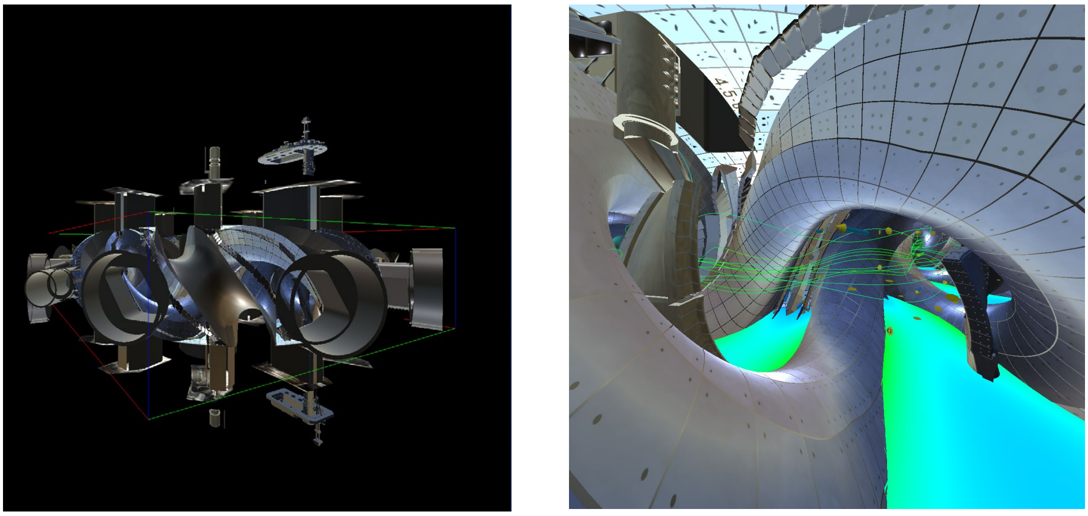

Fig.2 Fusion visualization of VFIVE and LHD 3-D model. Left: appearance of LHD 3-D model with simulation box boundary (green, red, and blue lines show x, y, and z axes). Right: inside LHD vacuum vessel with magnetic field streamline and contour plot of magnetic field strength. Streamline is single line of magnetic field which goes around several times in toroidal direction. Color contour of magnetic field strength drawn on $z = 0$ plane.

4. Summary

We enhance the visualization function of VFIVE to research the plasma physics in the periphery region of a fusion reactor. We are now checking the data transformation of the LHD vessel model data rendered by Unity to MQO formatted data, and the fusion visualization display by GLMetadeq. In the JSST conference, we will report this verification result.

Acknowledgments

This work was performed with the support and under the auspices of the NIFS Collaboration Research program (NIFS22KIIS001), and a part of this study is supported by JSPS Grants-in-Aid for Scientific Research (22K12054).

References

[1] FUSION2030 Fusion Plasma Working Group: Science of fusion plasma and its extent, https://www.nifs.ac.jp/research/Fusion2030/FPWG/fpwg_SciChallenges.html (accessed May 23, 2023)

[2] H. Ohtani, et al: Visualization of dust particle data with plasma simulation results using virtual-reality system. *Contrib. Plasma Phys.*, Vol.56 (2016), pp.692-697.

[3] H. Ohtani, et al: Virtual-reality visualization of loss points of 1 MeV tritons in the Large Helical Device, LHD, *J. Vis.,* Vol. 25 (2022), pp.281-292.

[4] A. Kageyama, et al: Data visualization by a virtual reality system. *In: Proc. 16th international conference on the numerical simulation of plasmas (ICNSP)*, (1998), p.138.

[5] VFIVE: https://www.jamstec.go.jp/ceist/aeird/avcrg/vfive.ja.html (accessed May 23, 2023)

[6] C. Cruz-Neira, et al: Surround-screen projection-based virtual reality: the design and implementation of the CAVE. *In: SIGGRAPH'93: proceedings of the 20th annual conference on computer graphics and interactive*, (1993), pp 135–142.

[7] Unity: https://unity.com/ (accessed May 23, 2023)

[8] Fusion: https://www.fiatlux.co.jp/product/virtual/fusion/ (accessed May 23, 2023)

[9] H. Miyachi, et al: Visualization PSE for multi-physics analysis by using OpenGL API fusion technique, *IEEE Comp. Soc.*, (2005), p.530.

[10] H. Miyachi, et al: Network OpenGL fusion to make effective presentation system, *IEEE Comp. Soc.*, (2007), p.536.

[11] GLMetaseq: http://kougaku-navi.net/ARToolKit/ (accessed May 23, 2023)

[12] S. Kawahara, et al: Development of CAVELib Compatible Library for HMD-type VR Devices, *J. Adv. Sim. Sci. Eng.*, Vol.6 (2019), pp.234-248.

[13] CLCL: https://github.com/kawaharas/CLCL (accessed May 23, 2023)

Characterization of two elementary processes in the formation of amino acid precursors in extraterrestrial space by molecular dynamics simulation

Hiroaki Nakamura[1,2,*], Yoshinori Satake[2], Masayuki Murai[2], Kensei Kobayashi[3], Itsuki Sakon[4], Shunsuke Usami[1,4], Miyuki Yajima[1,5], Yuki Goto[1], Masahiro Kobayashi[1,5], Seiki Saito[6], Hisashi Okumura[5,7,8], Masahiro Kato[1,8,9]

[1]National Institute for Fusion Science, National Institutes of Natural Sciences
[2]Nagoya University
[3]Yokohama National University
[4]The University of Tokyo
[5]SOKENDAI (The Graduate University for Advanced Studies)
[6]Yamagata University
[7]Exploratory Research Center on Life and Living Systems, National Institutes of Natural Sciences
[8]Institute for Molecular Science, National Institutes of Natural Sciences
[9]Hiroshima Synchrotron Radiation Center, Hiroshima University

[*]`hnakamura@nifs.ac.jp`

Abstract. Molecular dynamics simulations are performed to investigate the elementary processes of two scenarios of complex organic substances (“garakuta” molecules) formation: top-down and bottom-up. First, in the top-down scenario, we perform molecular dynamics (MD) simulations of nitrogen bombardment on coronene molecules. As a result, we investigate the chemical reactions of adsorption, reflection, and permeation of nitrogen when the incident energy of nitrogen is 0.3 eV. Next, in a bottom-up scenario, computer simulations are performed in which small molecules are collected, heated, and cooled. As a result, we can create a molecule with a molecular weight of 352. Thus, we demonstrate that we can handle elementary processes in order to obtain a complete picture of the two scenarios.

Keywords: Molecular dynamics simulation, Chemical evolution, Amino acid, Precursor

1. Introduction

In the conventional classical theory of chemical evolution, it was thought that ”large molecules are gradually formed from small molecules through thermodynamic equilibrium reactions on the primitive earth, and functions are subsequently produced [1, 2]. However, since life exists in a non-equilibrium state (dissipative structure), the assumption of thermodynamic equilibrium, which is the basis of classical evolutionary theory, is broken in the first place. Therefore, this classical theory of chemical evolution has been reconsidered, and expectations have been placed on extraterrestrial organic matter as a source of amino acids other than the generation of organic matter from the primitive earth's atmosphere [3, 4].

Against this background, through experiments using accelerators and other simulations, one of the authors (K. Kobayashi) and his colleagues proposed the "Garakuta World Hypothesis" that complex organic substances (named "Garakuta molecules") generated for some reason in extraterrestrial space arrive on Earth and produce amino acids [5]. In this hypothesis, garakuta molecules generated outside of the earth first propagate through space to reach the earth. These molecules are exposed to the hydrothermal environment on the earth, undergo hydrolysis and mutation, and form a molecular population with biochemical functions (a "garakuta world"). This garakuta world evolves, giving rise to the "protein world" and the "RNA world," which combine to evolve into the "ancestor of life."

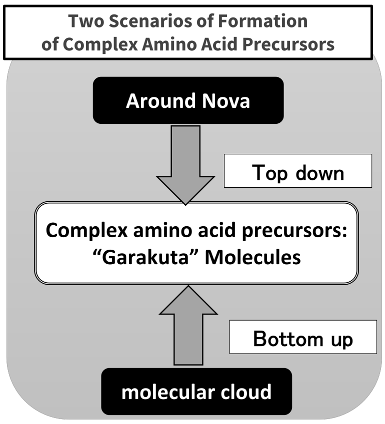

Figure 1: The origin of primordial organic molecules (grarakuta molecules) in the solar system.

As shown in Fig. 1, there are two scenarios for the extraterrestrial process of creating the garakuta molecules, which is the starting point of this series of the garakuta world hypotheses: a bottom-up scenario in which chemical reactions in the molecular clouds in the primordial solar nebula create complex organic molecules and a top-down scenario that organic dust born around the nova in the terminal phase is incorporated into the molecular cloud and become the origin of garakuta molecules [6]. Since the material matching the peak values of the infrared bands obtained from experiments measuring the infrared spectra of interstellar material has not yet been identified, we have not been able to determine the superiority of these two scenarios. Therefore, we perform simulations of nitrogen plasma irradiation of carbon materials using molecular dynamics (MD) method to clarify the superiority and inferiority of the two scenarios.

2. Simulation Models and Results

2.1. Top down scenario

The top-down scenario assumes a process in which organic dust scattered in the vicinity of a nova that has reached the end of its life is incorporated into a molecular cloud and reacts to become the garakuta molecule. We first choose hydrocarbons (coronene: C_{24} H_{12}, Fig. 2) as one of the simplest organic molecules. We perform MD simulation methods to investigate how this hydrocarbon reacts in a molecular cloud composed of nitrogen. In our MD model, a nitrogen atom is injected perpendicular to the coronene at the incident energy E_{in}.

As the simulation results, we clarify the dependence of the three reactions, adsorption, reflection, and penetration, on the incident position when the incident energy of nitrogen is $E_{\mathrm{in}} = 0.3$ eV.

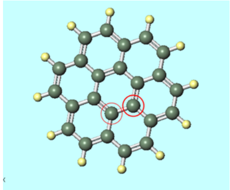

Figure 2: Coronene molecule ($C_{24}H_{12}$). Green represents carbon and yellow represents hydrogen. The coronene is irradiated with nitrogen atoms and the reaction is examined.

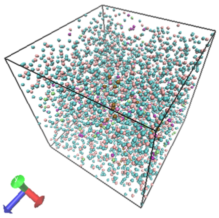

Figure 3: 1000 molecules of water, 100 molecules of carbon monoxide, and 10 molecules of ammonia are initially placed randomly; after heating to 10,000 K and cooling to 10 K, $C_7O_{16}H_{12}$ (molecular weight 352) is formed.

2.2. Bottom up scenario

The bottom-up scenario assumes chemical reactions in the primordial solar nebula. We investigate what kind of reactions occur when small molecules (water, carbon monoxide, ammonia, methane, etc.) are heated by energetic particles. So far, the acceleration experiment by Kobayashi's experiment has provided data on the molecular species produced, depending on the initial composition ratio of small molecules. Therefore, molecular synthesis simulations are performed using the MD method used in the top-down scenario. As shown in Fig.3, when water, carbon monoxide, and ammonia are randomly arranged and the system is heated and then cooled, molecules with a molecular weight of 352 are produced by the MD method.

3. Conclusions

To investigate the characteristics of the two scenarios of the formation of garakuta molecules, we first performed MD simulations of nitrogen bombardment of coronene molecules in the top-down scenario. As a result, we were able to investigate the chemical reactions of adsorption, reflection, and penetration of nitrogen at an incident energy of 0.3 eV of nitrogen. Next, in the bottom-up scenario, computer simulations were performed in which small molecules were collected and they were heated and then cooled. As a result, we were able to create a molecule with a molecular weight of 352. We were able to demonstrate that we could handle the elementary processes to get a full picture of the two scenarios.

Acknowledgments

The computation was performed using Research Center for Computational Science, Okazaki, Japan (Project: 22-IMS-C104) and Plasma Simulator of NIFS. The research was supported by Japan Society for the Promotion of Science (Grant Nos. JP19K14692, JP22H05131, JP23H04609, JP22K18272, JP23K03362), by the NINS program of Promoting Research by Networking among Institutions, by the NIFS Collaborative Research Programs (NIFS22KIIP003, NIFS22KIGS002, NIFS22KISS021) and by the ExCELLS Special Collaboration Program of Exploratory Research Center on Life and Living Systems.

References

[1] S. L. Miller, *Science*, **118**(1953) 528.

[2] G. Schlesinger and S.L. Miller, *J. Mol. Evol.*, **19** (1983) 376.

[3] J.E. Elsila, *et. al.*, *ACS Cent. Sci.*, **2** (2016) 370.

[4] C.R. Cronin, S. Pizzarello, *Science*, **275** (1997) 951.

[5] K.Kobayashi, *et al.*, *Astrobiology: Emergence, Search and Detection of Life* (Ed.: Basiuk, V. A.), p. 175, American Scientific Publishers, Stevenson Ranch, CA, USA (2010)。

[6] I. Endo, I. Sakon, *et al.*, *Astrophys. J.*, **917** (2021) 103.

Molecular dynamics study of defects on fatty acid vesicle induced by magnesium ion

Ryuta Kawanami[1,*] and Susumu Fujiwara[1,*]

[1]Kyoto Institute of Technology

*`d2871005@edu.kit.ac.jp, fujiwara@kit.ac.jp`

The full paper of this paper has been published in Journal of Advanced Simulation in Science and Engineering (JASSE).

DOI: `https://doi.org/10.15748/jasse.11.179`

Molecular dynamics study of OH radical-mediated DNA damage production

Susumu Fujiwara[1*], Ryuta Kawanami[1], Tomoko Mizuguchi[1], Yoshiteru Yonetani[2],
Tsukasa Aso[3], Hiroaki Nakamura[4,5]

[1]Kyoto Institute of Technology
[2]National Institutes for Quantum Science and Technology
[3]National Institute of Technology, Toyama College
[4]National Institute for Fusion Science
[5]Nagoya University

`*fujiwara@kit.ac.jp`

Abstract. Molecular dynamics simulations were performed to evaluate the accessibility of OH radicals to DNA and compared to the experimental DNA-radical reactivity. For the hydrogen abstraction reaction to proceed, the hydrogen of the sugar would need to be accessed at a certain angle by the OH radical to form a water molecule. However, simulation results show that counting only such arrangements results in large deviations from experimental values. This result indicates that in addition to the access angle, the reaction rate of the hydrogen abstraction reaction must also be considered in order to understand the mechanism of the hydrogen abstraction reaction by OH radicals.

Keywords: DNA damage, Hydroxyl (OH) radical accessibility, Hydrogen abstraction, Molecular dynamics simulation

1. Introduction

Hydroxyl (OH) radicals produced in cells by metabolism or radiation can damage DNA [1]. Unrepaired damage accumulates in DNA, causing cell cancer and genetic disease [2]. DNA damage by OH radicals can be divided into two major categories: the addition of OH radicals to the base (85-90%) and the hydrogen abstraction from the sugar moiety (10-15%). Although the fraction of hydrogen abstraction is small, the carbon radicals produced by this process can turn into catastrophic damage. In particular, C1’ is easily changed to an apurinic/apyrimidinic site, and C3’, C4’, and C5’ to strand breaks. Previous studies have shown that hydrogen abstraction reactions are likely to occur in the order C5’ > C4’ > C3’ > C2’ > C1’ [3]. Furthermore, molecular simulations have shown that the difference in reactivity between DNA and OH radicals is mainly due to the difference in solvent accessibility of each hydrogen site [4]. However, the hydration structure of OH radicals is known to be quite unstable and the behavior of water molecules and OH radicals is known to be very different [5]. Therefore, in this study, the hydrogen abstraction reaction is evaluated from the accessibility of OH radicals.

2. Simulation details

We used two types of base sequence of DNA, d(ATATAT) and d(CGCGCG), with 1783 water molecules, and 8 OH radicals. The bsc1 force field of Amber22 was used for DNA and the TIP3P force field for water. Three different models of OH radicals were used [5-7]. The molecular dynamics simulations were performed using Amber22. The initial simulation box was a truncated octahedron of 45.3 Å with periodic boundary conditions. The cutoff distance for the Lennard-Jones interaction and the electrostatic interaction was set to 8 Å. Ten sodium ions (Na^+) were added for electrical neutralization in the PME calculation. After the equilibration of the system, the production run was performed for 100 ns with an integration time step of 2 fs under NPT conditions. Temperature and pressure were set to T = 310 K and P = 1 atm, respectively.

The accessibility of OH radicals was calculated for each sugar hydrogen. The number of times an OH radical came within 3 Å of the hydrogen of each sugar was counted. To efficiently sample the OH configuration, a restraining potential with a flat bottom and a parabolic side up to 8 Å was imposed between the OH radical and the oxygen atom of the sugar moiety.

3. Results and discussion

The relationship between the number of times an OH radical approaches each hydrogen atom (accessibility) obtained from our simulations and the experimental DNA-radical reactivity [3] is shown in Fig. 1. In this figure, black and red circles represent OH radical accessibility with no angle criterion and with angle criterion of 109°±10°, respectively. For the hydrogen abstraction reaction to proceed, sugar hydrogens would need to be accessed by OH radicals at a certain angle (tetrahedral angle ≈ 109.5°) that would form a water molecule. However, counting only such arrangements (red circles in Fig. 1) resulted in large deviations from the experimental values.

To understand the mechanism of hydrogen abstraction by OH radicals, it is necessary to consider the reaction rate of hydrogen abstraction reaction in addition to the angle of access.

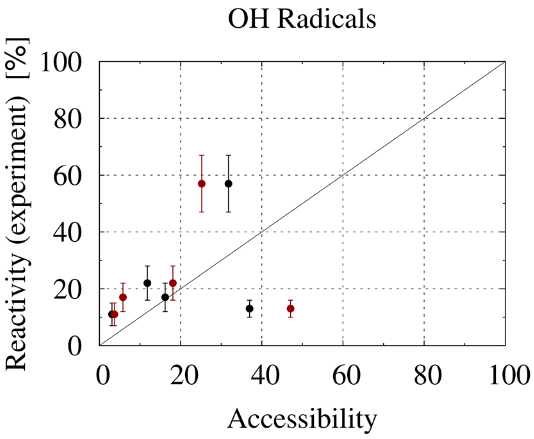

Fig. 1 Relation between OH radical accessibility and the DNA-radical reactivity. Black circles represent OH radical accessibility with no angle criterion and red circles that with angle criterion of 109°±10°.

References

[1] W. K. Pogozelski, T. D. Tullius: Oxidative Strand Scission of Nucleic Acids: Routes Initiated by Hydrogen Abstraction from the Sugar Moiety, *Chemical Reviews*, 98:3 (1998), 1089-1108.

[2] L. P. Candeias, S. Steenken: Reaction of HO· with Guanine Derivatives in Aqueous Solution: Formation of Two Different Redox-Active OH-Adduct Radicals and Their Unimolecular Transformation Reactions. Properties of G(-H)·, *Chemistry Europe*, 6:3 (2000), 475-484.

[3] B. Balasubramanian, W. K. Pogozelski, T. D. Tullius: DNA strand breaking by the hydroxyl radical is governed by the accessible surface areas of the hydrogen atoms of the DNA backbone, *Proceedings of the National Academy of Sciences*, 95:17 (1998), 9738-9743.

[4] Y. Yonetani, H. Nakagawa: Understanding water-mediated DNA damage production by molecular dynamics calculation of solvent accessibility, *Chemical Physics Letters*, 749:16 (2020), 137441.

[5] M. G. Campo, J. R. Grigera: Classical molecular-dynamics simulation of the hydroxyl radical in water, *The Journal of Chemical Physics*, 123:8 (2005), 084507.

[6] B. Fiser, B. Jójárt, I. G. Csizmadia, B. Viskolcz: Glutathione – Hydroxyl Radical Interaction: A Theoretical Study on Radical Recognition Process, *PLOS ONE*, 8:9 (2013), e73652.

[7] E. Lindahl, B. Hess, D. van der Spoel: GROMACS 3.0: a package for molecular simulation and trajectory analysis, *Molecular Modeling Annual*, 7 (2001), 306-317.

Understanding from solution-enclosures - Using elliptic equations as a case study

Kazuaki Tanaka[1,*]

[1]Global Center for Science and Engineering, Waseda University

[*]`tanaka@ims.sci.waseda.ac.jp`

Abstract. Rigorous numerical computation has enabled us to derive precise and definitive solution enclosures for various equations. However, the information we seek extends beyond these inclusions, even when they are relatively minuscule. In this presentation, we will posit that a desired problem can be modeled by a specific equation. Subsequently, we will discuss possible objectives in understanding the solutions to this equation and explore the insights we can glean from the information provided by the solution enclosures. Finally, we will conclude by presenting several examples that employ elliptic equations.

Keywords: Rigorous numerical computation, Solution-enclosures, Elliptic equations

1. Introduction

Solving equations of the form

$$F(x) = 0 \tag{1}$$

is a foundational and critical aspect of the natural sciences. Here, F represents a generally nonlinear mapping defined over a subset D of a mathematically defined space X such as a linear space, topological space, or manifold. The range of this mapping is another space, Y.

Rigorous numerical computation (RNC), alternatively known as Verified Numerical Computation, Numerical Verification Method, Computer-assisted proofs, Rigorous numerics, or Self-validating numerical methods, has seen significant developments over several decades. This field has found application in various domains such as linear systems, eigenvalue problems, nonlinear matrix equations, and different types of differential equations, with substantial results. RNC, for an approximate numerically computed solution $\hat{x}$, precisely determines the upper bound r of the error associated with the true solution x. That is to say, it verifies the existence of the true solution x within the range $\|x - \hat{x}\| \leq r$. This characteristic bestows upon RNC a rigor uncommon in standard numerical computations, which often incorporate errors. Moreover, if r is adequately small, not only the existence of the solution, but also the specific “shape” of x can be ascertained, exemplifying the power of numerical computations. However, this level of inclusion information may not suffice, as it doesn't reveal aspects such as the quantity of solutions, uniqueness, sign, and so forth. These attributes are frequently crucial when contemplating the original phenomena originating the equation. More intricate information, like stability (Morse index), nondegeneracy, and sign-changing structure can be of particular importance, especially when the solution x is a function instead of a value.

In this discourse, we will consider RNCs for semilinear elliptic equations as a representative model. The solutions of such equations, which are stationary solutions of the reaction-diffusion model, are deemed crucial.

We will review RNCs for solutions of elliptic equations as presented in the survey [1] and its associated references. The discussion will focus on whether we can derive information related to stability (Morse index), nondegeneracy, and sign-changing structure from solution enclosure information, referencing studies [2,3,4,5,6]. We will outline what can and cannot be achieved with existing methods, and will also present future prospects in this field.

References

[1] Mitsuhiro. T. Nakao, Michael Plum, and Yoshitaka Watanabe, Numerical Verification Methods and Computer-Assisted Proofs for Partial Differential Equations. Springer Series in Computational Mathematics, 2019.

[2] Kazuaki Tanaka, Taisei Asai: A posteriori verification of the positivity of solutions to elliptic boundary value problems, Partial Differential Equations and Application, 3, 9 (2022).

[3] Kazuaki Tanaka: A posteriori verification for the sign-change structure of solutions of elliptic partial differential equations, Japan Journal of Industrial and Applied Mathematics, 38, 731-756 (2021).

[4] Kazuaki Tanaka: Numerical verification method for positive solutions of elliptic problems, Journal of Computational and Applied Mathematics, 370, 112647 (2020).

[5] Kazuaki Tanaka, Kouta Sekine, Makoto Mizuguchi, and Shin'ichi Oishi: Sharp numerical inclusion of the best constant for embedding on bounded convex domain, Journal of Computational and Applied Mathematics, 311, 306–313 (2017).

[6] Kazuaki Tanaka, Kouta Sekine, Makoto Mizuguchi, and Shin'ichi Oishi: Numerical verification of positiveness for solutions to semilinear elliptic problems, JSIAM Letters 7, 73-76 (2015).

The best constants for the projection error on triplet Hilbert spaces

Munehisa Takahashi[1], Kouta Sekine[1], Makoto Mizuguchi[2]

[1]Graduate School of Information and Computer Science, Chiba Institute of Technology
[2]Faculty of Science and Engineering, Chuo University

*s2381028FW@s.chibakoudai.jp

Abstract. The use of projection error constants is a well-known method for error evaluation of spectral methods for Dirichlet boundary value problems for linear elliptic partial differential equations. In this presentation, we propose a method for deriving the best projection error constant in a set of three Hilbert spaces. Furthermore, we derive the inverse of the Aubin-Nitsche trick, and clarify the relationship between the best projection error constant and the eigenvalue problem. As an example of their application, specific projection error constants for the Bessel spectral method are presented.

Keywords: projection error constant, error evaluation, eigenvalue problem

1. Introduction

Numerical computation is an arithmetic method to proof the existence or unique existence of a solution to a given problem (mathematical model), including a rigorous evaluation of rounding errors [1, pp.1-2]. In other words, numerical computation guarantees the validity and reliability of the numerically obtained approximate solution. When solving partial differential equations by computer, discretization errors, rounding errors, and censoring errors occur, but the methods proposed by Nakao [1] and Plum [2] can guarantee accuracy. In particular, Nakao's method is characterized by the use of the projection error constant and the Aubin-Nitsche trick [1, pp.38-39].

Let $V \subset X \subset V^*$ be triplet Hilbert spaces. That is, let V and X be Hilbert spaces, and V and X is defined as

$$V \Subset X \text{ and } \bar{V}^{\|\cdot\|_X} = X. \tag{1}$$

Here, $V \Subset X$ means "V is compactly embedded in X", and $\bar{V}^{\|\cdot\|_X} = X$ means that V is dense in the meaning of the norm of X. The inner product in the Hilbert space V and X is denoted by $(u, v)_V$ and $(u, v)_X$, and the norm derived from the inner product by $\|u\|_V = \sqrt{(u, u)_V}$ and $\|u\|_X = \sqrt{(u, u)_X}$. Let V^* be the dual space of V, and the conjugate pair $\langle \cdot, \cdot \rangle_{V^* \times V}$. Also assume that

$$(u, v)_X = \langle u, v \rangle_{V^* \times V} \tag{2}$$

holds for $u \in X(\subset V^*)$, $v \in V$.

The linear operator $\mathcal{A} : V \to V^*$ is defined by

$$\langle \mathcal{A}u,\, v\rangle_{V^*\times V} := (u,\, v)_V\,,\ u, v \in V. \tag{3}$$

Then, from Riesz representation theorem, $\mathcal{A}$ is isometric isomorphism, and we have

$$\|\mathcal{A}u\|_{V^*} = \|u\|_V,\ u \in V. \tag{4}$$

Also, let

$$D := \{v \in V \mid Av \in X\}\,. \tag{5}$$

We define the linear operator $A : D \to X$ as

$$Au = \mathcal{A}u,\ u \in D. \tag{6}$$

From (3) and (6), for $u \in D$,

$$(u, v)_V = \langle \mathcal{A}u,\, v\rangle_{V^*\times V} = \langle Au,\, v\rangle_{V^*\times V} = (Au,\, v)_X. \tag{7}$$

Let V_n be a finite-dimensional subspace of V and $N = \dim(V_n)$. Also, let $V_\perp := \{u \in V \mid (u,\, v_h)_V = 0,\ v_h \in V_n\}$ be the orthogonal complement of V_n to V. Then, $V_\perp$ is in Hilbert space in topology with V. From the projection theorem, for the inner product $(\cdot,\cdot)_V$ of V, any $u \in V$ can be uniquely decomposed into the form

$$u = u_n + u_\perp,\ u_n \in V_n,\ u_\perp \in V_\perp. \tag{8}$$

In this case, the orthogonal projection $R_h : V \to V_n$ from u to u_n can be defined as

$$((I - R_h)\,u,\, v_h)_V = 0,\ v_h \in V_n. \tag{9}$$

For the orthogonal projection R_h defined by (9), we define th following constant.

Definition 1 (projection error constant)**.** *The C satisfying inequality*

$$\|(I - R_h)v\|_V \le C\|Av\|_X,\ \forall v \in D \tag{10}$$

is called the projection error constant.

Under the orthogonal projection R_h, it is known that the following evaluation is called the Aubin-Nitsche trick [3].

Lemma 2 (Aubin-Nitsche trick)**.** *Let C_1 be a constant satisfying inequality*

$$\|(I - R_h)u\|_V \le C_1\|Au\|_X,\ u \in D. \tag{11}$$

Then, we have

$$\|(I - R_h)u\|_X \le C_1\|(I - R_h)u\|_V,\ u \in V. \tag{12}$$

2. The best projection error constant

To derive the best projection error constant, we first derive the inverse of the Aubin-Nitsche trick.

Lemma 3 (Inverse Aubin-Nitsche trick). *Let C_2 be a constant satisfying inequality*

$$||(I - R_h)u||_X \leq C_2||(I - R_h)u||_V, \ u \in V. \tag{13}$$

Then, we have

$$||(I - R_h)u||_V \leq C_2||Au||_X, \ u \in D. \tag{14}$$

Next, we consider the best constants for C_1 and C_2, and introduce their equivalence.

Lemma 4 (equivalency of best constants). *Let C_1 be a constant satisfying inequality*

$$||(I - R_h)u||_V \leq C_1||Au||_X, \ u \in D. \tag{15}$$

That is

$$C_1 := \sup_{u \in D \setminus \{0\}} \frac{||(I - R_h)u||_V}{||Au||_X}. \tag{16}$$

Let C_2 be a constant satisfying inequality

$$||(I - R_h)u||_X \leq C_2||(I - R_h)u||_V, \ u \in V. \tag{17}$$

That is

$$C_2 := \sup_{u \in V \setminus \{0\}} \frac{||(I - R_h)u||_X}{||(I - R_h)u||_V}. \tag{18}$$

Then we have

$$C_1 = C_2, \tag{19}$$

and the best constant satisfying the above two inequalities is the same.

Since we derived the equivalence of the best constants, the following theorem holds for the relationship between the best constants and eigenvalues.

Theorem 5 (The best projection error constant). *Let $\lambda_\perp^{(1)}$ be the minimum eigenvalue of the following eigenvalue problem*

$$\text{Find}\,(u_\perp, \lambda_\perp) \in V_\perp \times (0, \infty) \ \ \text{s.t.}\,(u_\perp, v_\perp)_V = \lambda_\perp (u_\perp, v_\perp)_X, \ v_\perp \in V_\perp.$$

Then, the best constant C satisfying

$$||(I - R_h)u||_V \leq C||Au||_X, \ u \in D \tag{20}$$

and

$$||(I - R_h)u||_X \leq C||(I - R_h)u||_V, \ u \in V \tag{21}$$

is defined by

$$C := \frac{1}{\sqrt{\lambda_\perp^{(1)}}}. \tag{22}$$

3. Applications

Theorem 5 can be applied to the boundary value problem in $\Omega = \{x^2,\ |x| \leq 1\}$ on the disk using the Bessel function. Let $L^2(\Omega)$ denote the functional space of the 2nd power Lebesgue integrable functions. Then, we define the inner product $(u,\ v)_{L^2(\Omega)} := \int_\Omega u(x)v(x)\ dx$, the norm $\|u\|_{L^2(\Omega)} := \sqrt{(u,\ u)_{L^2(\Omega)}}$. In addition, the first-order $L^2(\Omega)$ Sobolev space is denoted by $H^1(\Omega)$. We define $H_0^1(\Omega) := \{\ u \in H^1(\Omega)\ |\ u = 0 \text{ on } \partial\Omega\ \}$ with the inner product $(u,\ v)_{H_0^1(\Omega)} := (\nabla u,\ \nabla v)_{L^2(\Omega)}$. Also, let $H^{-1}(\Omega)$ be the dual space of $H_0^1(\Omega)$.

We put $V = H_0^1(\Omega)$, $X = L^2(\Omega)$ and $V^* = H^{-1}(\Omega)$. In this case, we consider

$$\begin{cases} -\Delta u &= f \quad \text{in } \Omega \\ \quad u &= 0 \quad \text{on } \partial\Omega \end{cases}. \tag{23}$$

Let $m(\in \mathbb{N})$-th zero point of the $n(\in \mathbb{N} \cup \{0\})$th-order Bessel function $J_n(s)$ be $\tau_{n,m}$. Then, it is known that the eigenvalues of the eigenvalue problem

$$\text{Find } (u,\ \lambda) \in V \times \mathbb{R} \text{ s.t. } (u,\ v)_{H_0^1(\Omega)} = \lambda(u,\ v)_{L^2(\Omega)},\ v \in V$$

are $\tau_{n,m}$ and the eigenfunctions are $J_n(\tau_{n,m}r)e^{in\theta}$.

We assume that $V_n = \mathrm{span}\{J_n(\tau_{n,m}r)e^{in\theta}\}$, and the range of n and m is $0 \leq n \leq N_n,\ 1 \leq m \leq N_m$. Therefore, from the Theorem 5 and the property of the zero point $\tau_{n,m}$ of the Bessel function, we have the best projection error constant

$$C = \frac{1}{\sqrt{\min\{\tau_{0,N_m+1},\ \tau_{N_n+1,1}\}}} \tag{24}$$

satisfying

$$\|(I - R_h)u\|_{H_0^1} \leq C\|\Delta u\|_{L^2}. \tag{25}$$

References

[1] Mitsuhiro T. Nakao, Michael Plum, and Yoshitaka Watanabe. *Numerical verification methods and computer-assisted proofs for partial differential equations*. Springer, 2019.

[2] Michael Plum. Computer-assisted existence proofs for two-point boundary value problems. *Computing*, Vol. 46, No. 1, pp. 19–34, 1991.

[3] Philippe G Ciarlet. *The finite element method for elliptic problems*. SIAM, 2002.

JSST 2023

Performance Evaluation of Neural Networks for various Partial Differential Equation Derivation

Kunqi Hu[1*], Yu Long[1], Koji Koyamada[2]

[1]Kyoto University
[2]Osaka Seikei University

*`hu.kunqi.24w@st.kyoto-u.ac.jp`

Abstract. Recently, the representation ability of neural network (NN) has led to an increased focus on deriving partial differential equations (PDEs) from extensive datasets collected in intriguing scientific phenomena. However, few studies have provided a comprehensive comparison of different layer structures in NN across various PDEs. In this paper, we investigate PDEs that encompass diverse phenomena, employing NN as a fundamental tool for PDE derivation. We utilize two candidate libraries to evaluate the NN's approximating capability and the sequential threshold ridge regression's selection ability. Additionally, we explore various layer structures to ensure sufficient model complexity. The training loss of the NN, regression loss, error between exact and identified coefficients of partial differential terms, and the error between exact and estimated values of discrete spatio-temporal points are used to determine the champion dataset.

Keywords: Neural network, Partial differential equations, Regression analysis

1. Introduction

Many important natural science and engineering technological issues can be attributed to the study of partial differential equations (PDEs). A PDE contains unknown multi-variable functions and their partial derivatives. They are used to formulate problems, and they are either solved manually or by using a computer model. Currently, PDE derivation research from big data is in a basic technological research and development phase.[1]

In this paper, we assume a PDE and consider a set of the PDE solution data at multiple discrete spatio-temporal points as pseudo measurement data. A neural network (NN) is taken as a spatio-temporal model to calculate the partial differential terms. Using the partial differential terms, the coefficients are estimated by regularization regression analysis.

Furthermore, we consider two kinds of partial differential term candidate libraries. One is to verify the approximating ability of the NN and the other is to verify the selecting ability of the sequential threshold ridge regression (STRidge), which is used to narrow down essential partial differential terms. Meanwhile, sufficient layer structures are explored.

2. Related work

2.1. Data-driven PDE derivation

Maziar Raissi et al. employed machine learning techniques to derive PDEs from observed data. In their method, they implemented a learning algorithm that can solve the problem of a data shortage scenario that appears in experiments when measuring data from complex physical phenomena.[2] However, in this method, the partial differential terms that constitute the PDE are determined in advance, so it is considered to be insufficient as a method for PDEs from unknown physical phenomena. In our method, we not only consider situations where the partial differential terms are predetermined but also situations where the correct partial differential terms need to be selected from a wide candidate library.

2.2. Sparse regression methods for differential terms determination

Bongard applied the symbolic regression and the evolutionary algorithm to determine the nonlinear dynamic system.[3] Samuel H. Rudy et al. proposed the PDE-FIND method in which a large library of candidate terms are created, even on higher-dimensional spatial domains.[4] Besides, they applied the STRidge algorithm. We also borrowed the STRidge method and applied it in our experiments.

3. Method

For a PDE equation has exact solution, a spatio-temporal coordinate dataset is created according to its space dimension and time span. Take a one-dimensional PDE as an example, its space dimension x will have 100 steps as well as its time span t. Furthermore, we conduct random sampling on the dataset. Therefore, for an 80% sampling rate dataset, it will totally have 8000 input point data. By employing the exact solution, 8000 corresponding output point data are obtained. These discrete spatio-temporal points are put into the PDE equation to generate training data.

A fully-connected NN is built to represent a PDE equation. When the NN has been trained, partial differential terms are obtained from it. This process is based on the chain rule. The activation function and optimizer of the NN are fixed, which are tanh function and Adam. For each hidden layer, the number of neurons is set in the range of 10 to 40 with step as 10. It has 4 hidden layers in total. About the geometric features, constant type, convex type, concave type, increase type and decrease type are considered. The number of neurons in input layer is connected with an exact PDE. With respect of the output, it has only one neuron that represents a value of exact solution according to an input.

Two candidate libraries that contain multiple partial differential terms wait to be selected while the STRidge regression are built. A minimum library has partial differential terms as same as the PDE. A maximum library has partial differential terms which cover one order higher than the highest order in the PDE. The STRidge is applied to select the candidate term whose coefficient is larger, while the smaller coefficients are omitted. In our case, the initial tolerance is set as 10^{-1}, the maximum iteration of STRidge is set as 10 and the training epoch is 25.

There are NN model error E_{mse}, regularized regression equation error E_{rre}, PDE derivation error E_ϵ, and partial differential term error E_u. We calculate $(E_{mse} + E_{rre}) \times E_\epsilon \times E_u$, refer to as the total error E_{total}, to select the optimal result among different NN structures.

4. Experiments and Results

The advection diffusion equation (ADE) is one of the equations used in physics and chemistry to mathematically model the flow of matter, energy, and other substances.

$$\frac{\partial u}{\partial t} + C\frac{\partial u}{\partial x} - D\frac{\partial^2 u}{\partial x^2} = 0, \quad u|_{x=0} = u_{BC}, \quad u|_{x=\infty} = 0, \quad u|_{t=0} = u_0(x), \tag{1}$$

where, $u_0(x)$ is the step function. We set $u_{BC} = 1$ to get the exact solution, and $C = 1/2$, $D = 1/14$ are used.

The minimum partial differential term candidate library consists of two partial differential terms, which is

$$\Phi(u)_{\min} = [U_x, U_{xx}]. \tag{2}$$

The maximum candidate library is

$$\Phi(u)_{\min} = [U, U_x, U_{xx}, U_{xxx}]. \tag{3}$$

We train the NN with 21000 epochs. Among the minimum and maximum candidate libraries, a champion data is the one that uses convex type layers and increase type layers. Figure 1 shows the parallel coordinates of the NN structure and the E_{total} under the maximum candidate libraries.

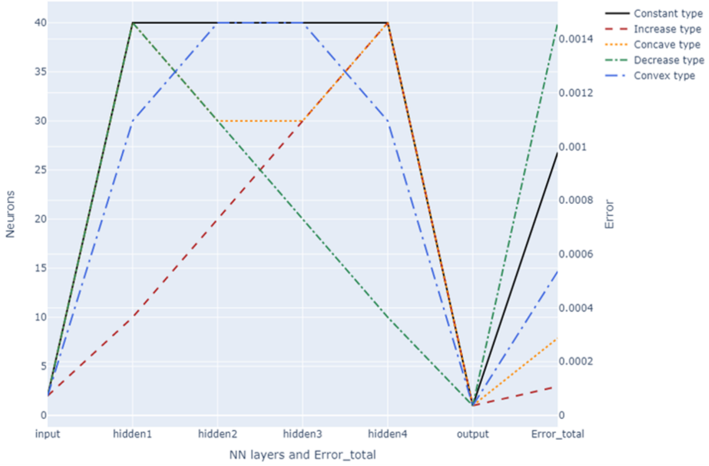

Figure 1: Parallel coordinates graphs of the NN structures and the E_{total} under the maximum candidate libraries. The increase type layers got the best performance.

We also evaluated other one-dimensional equations. Table 1 shows the result together with the ADE result. We will discuss the results in the next section.

	Contant	Increase	Concave	Decrease	Convex
Advection-diffusion equation	3.331	6.164	3.204	**6.294**	**2.463**
	9.780	**1.074**	2.874	**14.605**	5.357
KdV equation	2.791	**8.709**	3.377	**1.354**	2.698
	3.500	**82.349**	25.891	7.037	15.897
Burgers' equation	1.675	**7.012**	2.629	2.727	**1.607**
	5.598	**9.978**	3.133	2.254	**1.533**
Wave equation	**0.103**	**8.821**	0.133	0.371	0.157
	1.695	4.264	**0.585**	**13.201**	4.114

Table 1: Performance evaluation on various one-dimensional equations. The unit is 10^{-4}. Each equation follows two rows. The top row is the result under minimum candidate library, the bottom row is the result under maximum candidate library. The best result is highlighted in green, while the worst result is highlighted in red.

5. Discussion and Conclusion

Regarding the aspect of NN structures, neither the type of increase nor the type of decrease in the number of neurons yielded satisfactory results, as these types involved layers with only a few neurons. Among one-dimensional equations considered, the ADE, Burger's equation and Wave equation, exhibited correct partial differential terms with coefficients that were reasonably close to the expected values. Furthermore, any additional PDE terms included in the identified equations had relatively small coefficients, which aligns with our expectations.

In this paper, we advance the understanding of PDE derivation from big data by employing a NN and exploring different layer structures. Future research can build upon these findings to further enhance the accuracy and efficiency of PDE derivation techniques.

References

[1] A. Koyamada, K., B. Long, Y., C. Kawamura, T., D. Konishi, K. Data-driven derivation of partial differential equations using neural network model, *International Journal of Modeling, Simulation, and Scientific Computing*, (2021), 12.02: 2140001.

[2] A. Maziar Raissi, B. George Em Karniadakis, Hidden physics models: Machine learning of nonlinear partial differential equations, *Journal of Computational Physics*, Vol. 357, (2018), pp. 125–141.

[3] A. Ilknur Icke, B. Joshua C. Bongard, Improving genetic programming based symbolic regression using deterministic machine learning, *IEEE Congress onEvolutionary Computation*, (2013), pp. 1763–1770.

[4] A. Samuel Rudy, B. Alessandro Alla, C. Steven L Brunton, D. J Nathan Kutz Data-driven identification of parametric partial differential equations, *SIAM Journalon Applied Dynamical Systems*, Vol. 18, No. 2, (2019), pp. 643–660.

Understanding of time trend of cesium layer on the plasma grid in ITER scaled negative ion source

Masafumi Yoshida[1,2,*] and Shunsuke Hayashi[2]

[1]Department of Electrical Engineering, National Institute of Technology, Ube College
[2]Advanced Course of Production Systems Engineering, National Institute of Technology, Ube College

*`yoshida-m@ube-k.ac.jp`

The full paper of this paper has been published in Journal of Advanced Simulation in Science and Engineering (JASSE).

DOI: `https://doi.org/10.15748/jasse.11.158`

Elucidation of the fundamental processes in the time evolution of cesium concentration in the water of Lake Onuma

Ikuto Ohtaka[1], Yuko Hatano[2], Makoto Nakamura[3], Seiki Saito[1*]

[1] Department of Information and Electronics, Graduate School of Science and Engineering, Yamagata University

[2]Department of Information, Tsukuba University

[3] Department of Creative Engineering, Kushiro College, National Institute of Technology

*saitos@yz.yamagata-u.ac.jp

Abstract.

In this study, we analyze fluid simulations to determine whether the time evolution of cesium concentration in Lake Onuma in Gunma Prefecture follows a non-integral order diffusion equation with an operator of ${}_0\mathcal{D}_t^{1-\alpha}$. First, seasonal velocity fields in the lake water of Lake Onuma are obtained with relation to the seasonal temperature distribution.

Keywords: Fluid calculation, Computer simulation, Velocity field

1. Introduction

After the Fukushima Daiichi nuclear power plant accident on March 11, 2011, the concentration of radioactive cesium in the water of Lake Onuma in Gunma Prefecture temporarily exceeded the provisional regulatory limit. This resulted in an elevated level of cesium contamination in the local wakasagi population.

It has been demonstrated that the time evolution of cesium concentration in the lake water follows the following non-integer order diffusion equation with α=0.685[1]:

$$\frac{\partial p}{\partial t} = {}_0\mathcal{D}_t^{1-\alpha}\left[K\frac{\partial^2 p}{\partial x^2}\right],\ {}_0\mathcal{D}_t^{\beta} f(t) := \frac{1}{\Gamma(1-\beta)}\int_0^t \frac{f(t')}{(t-t')^{\beta}}\,dt' \qquad (1)$$

p represents concentration, t represents time, and x represents position. Γ is a function expressed by the following equation as a positive real number of x.

$$\Gamma(x) = \int_0^{\infty} t^{x-1}e^{-t}\,dt \qquad (2)$$

Why the time evolution of cesium concentration follows the non-integer order diffusion equation (1) can be analyzed as follows

2. Analysis method

First, we aim to calculate seasonal variations in the velocity field of Lake Onuma. Then, we calculate the velocity field from the temperature distribution data of Lake Onuma for each season (spring, summer, autumn, winter). The governing equations utilized in the analysis account for buoyancy effects and are represented by the Navier-Stokes equations. Fluid simulation software called OpenFOAM is then employed the for the calculations. We first created a mesh of Lake Onuma, which serves as the model to input the seasonal temperature distributions into. Lastly, OpenFOAM is used to compute the velocity fields of each season.

3. Current Research

We examined the differences in the velocity field based on the seasonal temperature distributions. We have calculated the velocity field using a simplified rectangular shape, taking into account the seasonal temperature distribution of Lake Onuma as a precondition. The mesh for the rectangular shape is configured with the following dimensions: x-direction with a length of 10m divided into 20 parts, y-direction with a length of 10m divided into 20 parts, and z-direction with a depth of 18m divided into 36 parts. Note that the z-direction represents the depth.

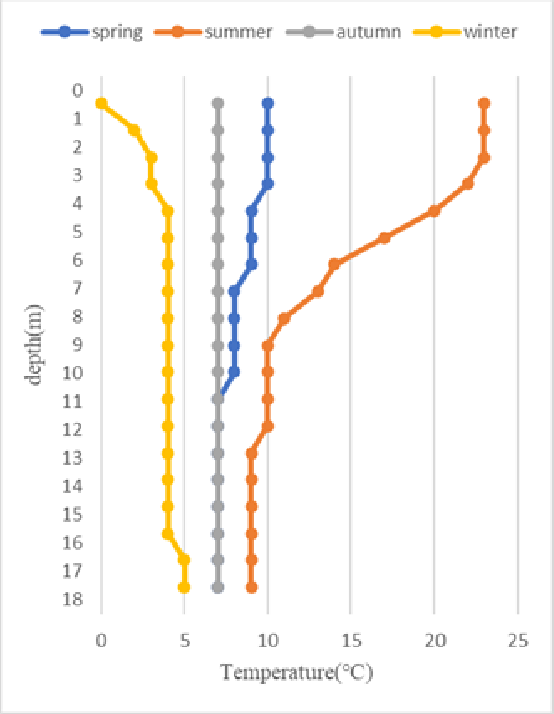

Fig. 1 The temperature distribution of Lake Onuma in relation to depth

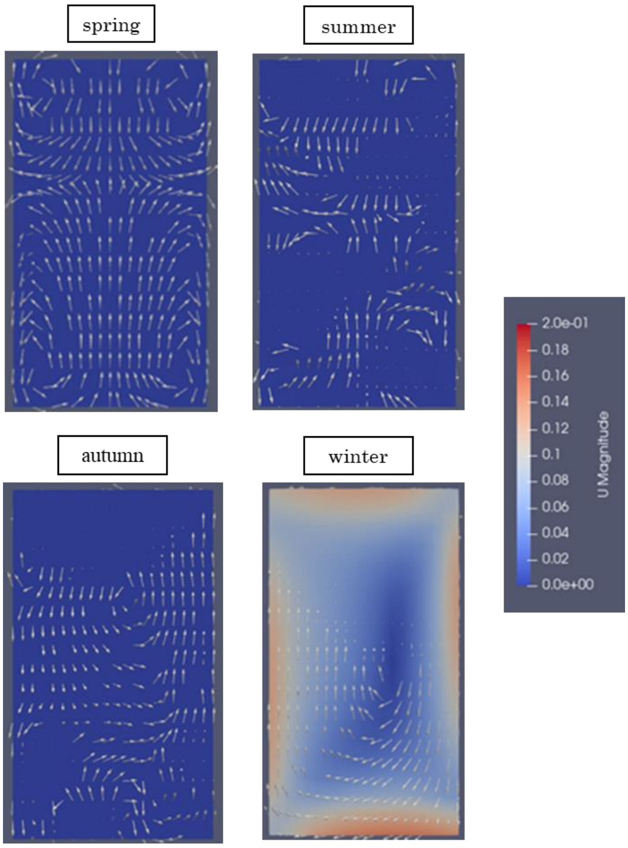

Fig. 2 Velocity fields corresponding to the seasonal temperature distributions.[2]

Figure 1 represents the temperature distribution in relation to the depth of Lake Onuma. Figure 2 shows the velocity fields obtained from fluid calculations using the temperature distribution from Figure 1.

Among the four seasons, it can be observed that during winter, the velocity field is larger.

References

[1] K. Akasaki, Y. Hatano, *et al.*,(2021), "Modeling of Temporal and Vertical Changes in ^{137}Cs Concentration in Lake Onuma", Accepted to Radiation Protection Dosimetry , Radiation Protection Dosimetry , Vol. 0, No. 0, pp. 1–4.

[2] T.Kondo,H.Hiromi,(2011),"Limnological research on Lake Onuma" ,Bulletin of the Faculty of Education, Chiba University,vol.59,319~332.